MARIA CURIE-SKŁODOWSKA UNIVERSITY
LUBLIN
Faculty of Mathematics, Physics and Computer Science

Department of Theoretical Physics

Aksel Kobiałka
Supervisor: prof. dr hab. Tadeusz Domański
Co-supervisor: dr hab. Andrzej Ptok, prof. IFJ PAN

Emergence and nonlocality of Majorana bound states in nanoscopic systems

Emergencja i nielokalność stanów związanych Majorany w układach nanoskopowych

Lublin, Poland (2021)

Acknowledgements

Taking advantage of this opportunity, I would like to show my sincere appreciation for my supervisor and co–supervisor, who have supported me over the years. In the beginning, I would like to thank my supervisor, Tadeusz Domański, for his continual and unwavering support during my PhD studies. His immense knowledge and patience together with valuable ideas and comments greatly inspired my passion in science. Prof. Domański taught me not only about physics, but also the skills of a researcher: attention to detail, critical thinking, modesty, presenting my research to the public, and academic writing. I am delighted that I had a chance to be his student during my masters and PhD studies.

Furthermore, I am grateful for the opportunities that my co–supervisor, Andrzej Ptok, gave to me. Under his guidance, I developed valuable skills and collaborations. His help and patience allowed me to learn and thrive as an aspiring scientist. Additionally, his drive, perpetual push to work harder and passion and for physics greatly influenced and supported my activities during my PhD studies.

Moreover, I express my sincere gratitude to the rest of my co–authors, Nicholas Sedlmayr, Przemysław Piekarz, Andrzej M. Oleś, Maciej M. Maśka, Szczepan Głodzik, Pascal Simon, and David J. Alspaugh, who contributed to the papers building up this Thesis. Their input and discussions were essential in preparing and publishing the presented papers. Additionally, I would like to thank Nicholas Sedlmayr for a careful and meticulous revision of my PhD thesis during its final stage.

Finally, I would like to thank my wife for her love, companionship and motivation during this trying endeavour.

Abstract

Topological superconductors, originating from the interplay between magnetism, spin-orbit coupling, and superconductivity, can host zero energy quasiparticle excitations at the system's edges known as *Majorana bound states*. These states have a peculiar property of being identical with their own antiparticle. Majorana modes, due to their non–Abelian statistics, were proposed to be able to perform *braiding*, a protocol of quantum computation where one quasiparticle revolves in real space around another, allowing to store quantum information. In this thesis, I present an overview of theoretical concepts concerning emergence and nonlocality of Majorana bound states, relying on Bogoliubov–de Gennes formalism. I also focus on experimental development investigating one and two dimensional topological superconductors capable of hosting Majorana states. Additionally, I present methods used for obtaining the results presented in the main part of thesis. Essential part of my thesis has a form of cumulative work – Chapter 4 consists of an aggregate of papers that I coauthored during my PhD, which discuss the mentioned phenomena related to Majorana physics: its emergence and nonlocality. Emergence of Majorana bound states is a fundamental concept that has to be meticulously studied. Development in this case can build an aggregate of the possible ways in which Majoranas can be hosted in the system, and as a result, increase the chances for successful application. In regard to nonlocality, it is a crucial element of braiding, which allows for performing the quantum computation by employing the degenerate states that are spatially separated. It also allows for nontrivial phenomena, like quantum teleportation and nonlocal conductance. Both of these phenomena constitute a fertile ground for theoretical research, not only during my PhD studies but hopefully also in the future to come.

Contents

CHAPTER 1

Introduction

1.1 Historical framework

In 1928 P.A.M. Dirac [1], during an effort of combining quantum mechanics and general relativity, discovered that his formula for electron behaviour implies two solutions. Such positive and negative energy solutions, discussed in greater detail two years later [2], led to discovery that matter should have both positive and negative energy.

As a result, we obtained matter and antimatter, or rather particles and antiparticles. Act of conjugation relates them to each other – in Dirac notation, the creation of an electron is identical to the annihilation of a hole. Few years later, E. Majorana realized that there exists a purely real wave function [3, 4], allowing for such a process to occur. Particle that would behave in such a way, later dubbed as *Majorana fermion*, would be self-conjugated – it would be its own particle. Such a fermion that would behave as a superposition of a particle and antiparticle might seem unlikely, but some schemes like neutrinoless double β decay [5–7] try to find the signature of this exotic particle. Unfortunately, recent news informed that the half-life of such an event would need to be at least 1.8×10^{26} years. As a result, over 80 years of research in the field of high energy and particle physics passed since the inception of this idea that did not achieve any tangible results apart from the belief that sufficient precision of the apparatus for such an experiment can be reached in future [7–11].

However, in superconductors such a linear combination of particle (electron) and antiparticle (hole) can occur in a "natural way" as an object called *Bogoliubov quasiparticle* in the framework of Bogoliubov–de Gennes (BdG) equations [12, 13]. Therefore, before fast forwarding to current times and booming interest in topological phenom-

ena, a notable remark has to be made. Any reference to superconductivity introduces a necessity to recall a remarkable research done by H. K. Onnes in 1911 [14]. By studying the behaviour of mercury, tin, and lead under extremely low temperatures, he noticed that below some temperature T_c, called *critical temperature*, the resistivity of the measured samples dropped to non-measurable values. Before this experiment, the main hypotheses regarding such behaviour supposed a linear increase (W. Thompson), plateau (A. Matthiessen), or decrease (J. Dewar) [15], but as we know now, none of those hypotheses stood the test of time in the case of these novel materials. It is sufficient to say that H. K. Onnes' discovery of superconductivity was a breakthrough in science and opened a vast field of physics.

Superconductivity, in the framework of BCS theory [16] is caused by the attractive electron-phonon interaction, leading to Cooper pair formation due to instability of the Fermi surface [17]. Minimizing the energy of a single interacting electron pair leads to the condition that requires vanishing kinetic energy of the pair center of mass (hence the electron momenta are opposite) and introduces some energy contained within the attractive interaction correlating electrons, which relates to size of *superconducting gap* near the ground state of the system [18]. Mutual relation of an electron and its time–reversed counterpart points to the *s–wave* singlet type of superconducting order.

Excitations inside the superconducting gap described as superposition of electrons and holes are called Bogoliubov quasiparticles or *bogolons*. N. Bogoliubov was studying the general picture of quasiparticle excited states in superfluids. In some situations (which will be discussed in the next paragraphs), we can find these quasiparticles that can be treated as analogues to the Majorana fermions.

In high energy physics, we can find two solutions of the Dirac equation with opposite energy $\pm 2mc^2$, that correspond to a particle and antiparticle [Fig 1.1(a)]. To obtain Majorana fermions, indistinguishability between the particle and antiparticle is necessary, thus the energy should be the same and equal to zero. In similar way, in a superconductor with gap 2Δ, due to the the BdG equations symmetry we can always find two solutions with opposite energies: Γ_{E} and $\Gamma_{\text{-E}} = \Gamma_{\mathrm{E}}^{\dagger}$ [Fig 1.1(b)]. Again, to produce Majorana–like state, it is necessary that $\Gamma_{\text{-E}} = \Gamma_{\mathrm{E}}^{\dagger} = \Gamma_{\mathrm{E}}$, which implies $E = 0$ [Fig 1.1(c)]. Therefore, these solutions of BdG Hamiltonian show that such states are degenerate and symmetric with respect to energy due to particle–hole (charge conjugation) symmetry. As we can see, this type of quasiparticles were extremely close

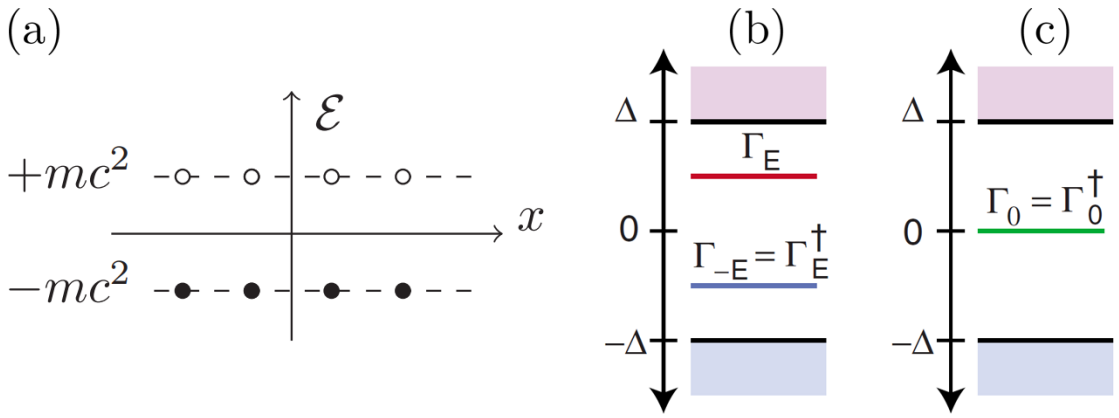

Figure 1.1: Representation of Majorana–like objects in various fields of physics. (a) Majorana fermion native to nuclear and high energy physics as a zero energy solution of the Dirac equation. Condensed matter in–gap states in trivial (b, Andreev bound state) and non–trivial (c, Majorana bound state) topological superconductor. Figures adapted from Refs. [19] and [20], respectively.

to the condensed matter equivalent of Majorana fermions, and are called *Majorana bound state*[1] (MBS). More detailed explanation will be presented in Ch. 2.

Still, in this case, Majorana feature of being a zero energy particle and antiparticle could not be resolved due to the incompatibility of the directions of spin. In order for the above to work, a different superconducting order has to be introduced: triplet *p–wave*[2], in which all electrons have the same spin, to the point that in some models the material can be considered as *spinless*. Over a quarter of a century ago, first premises [22] that *p–wave* order can emerge in Sr_2RuO_4 arose, however further inquiries claim that this is not really the case [23–26] and shift its prediction to *d–wave*[3] [27] type of order instead. Another potential candidate was a He_3, where fermion zero modes in superconducting vortices were predicted [28] and thus started a discussion of quasiparticle zero modes in

[1]There is an apparent naming controversy regarding Majorana objects in condensed matter physics. Initially, it was called Majorana fermion in relation to nuclear physics and if Bogoliubov quasiparticle (which is a fermion) would have equal u and v coefficients it would be a Majorana fermion. However, due to its theoretically predicted properties (described in footnote 5) it certainly cannot be a fermion. Majorana bound state, Majorana zero mode, and Majorana quasiparticle are each zero energy states within a superconducting gap that is bound to some defect in the system (end of one dimensional (1D) nanowire or a vortex core). Those terms are used interchangeably in this thesis. Majorana edge mode is a vortex chirally propagating along the edges of the system, usually in 2D and 3D [21].

[2]Here, by the *p–wave* triplet superconductivity, we should understand a spin–triplet phase with antisymmetric order parameter, i.e. $\Delta(\mathbf{k}) = -\Delta(-\mathbf{k})$.

[3]Contrary to the conventional *s-wave* superconductor, where order parameter is $\Delta(\mathbf{k}) = \text{const}$, in the case of *d-wave* the order parameter has nodal lines in momentum space: $\Delta(\mathbf{k}) \sim \cos(k_x) - \cos(k_y)$.

p–wave type order superfluid. However, this nontrivial *p–wave* superconducting phase can be effectively induced by spin–mixing in the trivial *s–wave* superconductor due to the spin–orbit coupling [29–34]. This will be discussed more closely in Sec. 1.3.

At the end of the previous millennium, two articles on superconductor [35] and quantum Hall effect approach [36], investigated the nature of Majorana zero modes (MZMs)

$$H = \sum_j \left[-w \left(a_j^\dagger a_{j+1} + a_j^\dagger a_{j+1} \right) - \mu \left(a_j^\dagger a_j - \frac{1}{2} \right) + \Delta a_{j+1} a_j + \Delta^* a_j^\dagger a_{j+1}^\dagger \right], \tag{1.1}$$

where $a_j^{(\dagger)}$ is a fermion annihilation (creation) operator on site j, w is hopping integral, μ is chemical potential and Δ is p-wave pairing gap. Various representations of Hamiltonian (1.1) are shown in Fig. 1.2. In panel (a) one can observe a fermionic chain composed of residing on N sites (blue ovals). To continue, one can define new Majorana operators which are a superposition of electron and hole in place of the usual fermion operators,

$$c_{2j-1} = a_j + a_j^\dagger, \quad c_{2j} = \frac{a_j - a_j^\dagger}{i}, \tag{1.2}$$

that fulfil the following conditions:

$$c_m^\dagger = c_m, \quad \{c_m, c_l\} = \delta_{ml}. \tag{1.3}$$

Applying those to Hamiltonian (1.1), we can obtain a new transformed Hamiltonian

$$H = \frac{i}{2} \sum_j \left[-\mu c_{2j-1} c_{2j} + (w + \Delta) c_{2j} c_{2j+1} + (-w + \Delta) c_{2j-1} c_{2j+2} \right]. \tag{1.4}$$

Transformed Hamiltonian can be envisioned by a nanochain of pairs of on–site coupled MQPs (red dots on Fig. 1.2(b)), which in essence is identical to the fermionic nanochain in panel (a) as the two Majoranas fuse into a standard fermion. Substitution mentioned above and a special set of parameters allows for unearthing a significant peculiarity of this model – if one sets $w = \Delta > 0, \mu = 0$, Majorana operators from neighbouring sites become paired together due to the long–range coupling. This can be envisioned by the following Hamiltonian:

$$H = iw \sum_j^{N-1} c_{2j} c_{2j+1}. \tag{1.5}$$

As MZMs become paired, they vanish and form a fermion, annihilating each other due to their inherent self-conjugation. However, when paried between sites of a chain

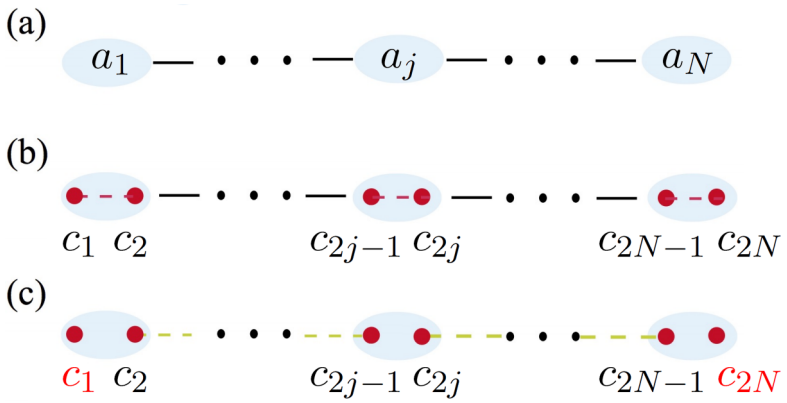

Figure 1.2: (a) Trivial nanowire composed of N aligned fermions. (b) Fermionic chain from (a) represented as pairs of coupled MQPs (red dots). (c) Under the right conditions pairing between Majoranas shifts from on–site to inter–site, leaving two uncoupled MQPs at the ends (red lettering). Figure adapted from Ref. [37].

two MZMs, c_1 and c_{2N}, are left unpaired at the edges of a system. Unpaired Majorana operators do not take part in Hamiltonian due to the fact that they both possess zero energy. Hence, this degeneracy can be explained by the fact that they commute with Hamiltonian ($[H, c_1] = [H, c_{2N}] = 0$). As a result, in the model Kitaev chain model proposes two unpaired zero energy Majorana states, remaining at the edges of the nanowire. These unpaired MQPs are shown in Fig. 1.2(c), and are distinguished by red lettering.

Summarizing, an unpaired Bogoliubov quasiparticle with equal coefficients for both electron and hole components can be an analogue of a Majorana state. Additionally, Kitaev reached conclusions regarding the topological state of MBSs by studying the Pffafian of Hamiltonian of a fermion chain, which is a topological invariant for this system. This article received an extensive praise in the scientific community, much larger than previous Majorana–related articles, that can be attributed to a first application of this phenomenon in technology, namely, in quantum computing.

1.2 A promise of application

Increase of computing power of computers is closely related to an empirical Moore's law, stating that the economically feasible number of transistors in an integrated circuit doubles about every two years, as conceived in 1965 [38]. However, this extrapolation started to level off around the 2000s, as the physical limits of engineering and quantum reality of matter at nanoscopic sizes started to play a major role, dampening the

predicted increase. Since then, an increase in computing power became mainly a result of integrating an increasing number of parallelly working CPUs into supercomputers. As nature abhors a vacuum, new ideas were needed in order to prevent the plateau of progress. This led to inception of the field of quantum computing, that was also kick-started by 1959 R. Feynmann's talk "There's plenty room at the bottom" and later by a paper discussing quantum simulators [39], which could in his belief imitate any quantum system, including the physical world. This was meant to be achievable thanks to the interchangeability between various quantum mechanical systems, even though initially only bosonic particles were considered. Together with other seminal papers [40–47], this led to the first experimental execution of the mentioned ideas, by I.L. Chuang *et al.* [48] on two qubit system. Such a system consisted of carbon and hydrogen nuclei, which spins were manipulated with nuclear magnetic resonance techniques. This allowed to compute Grover's algorithm for searching a distinct entry in a table having N entries – in this case $N = 4$, as a two qubit system allows for four distinct states: $\Psi = (|00\rangle + |10\rangle + |01\rangle + |11\rangle)/2$.

So far, the achievements of quantum computing are rather modest with the largest number factored using Shor's algorithm to be 21 [49] but with use of another schemes this number rises to 1 099 551 473 989 [50]. Such results might seem unimpressive with the feats of digital computing and show that the realm of *quantum supremacy* is still in the future. On the other hand (apart from playing a major role in science–fiction tropes), quantum computers and annealers are already employed in physics [51–53], molecular biology [54], quantum chemistry [55], information processing and cryptography [56–62] and technology[4] [63, 64].

Unfortunately, even the initial studies mentioned above pointed to a potential problem that can thwart the progress of the field – decoherence and other forms of quantum noise. In a qubit system, it leads to an exponential decay of quantum coherence, that in turn leads to the loss of the information stored in a qubit as it returns to the random state, that for some bases can be a superposition [65, 66]. Decoherence time ranges from 10^{10}s in GaAs quantum dots to 1s in microwave cavity-based quantum computers [67, 68]. In digital computing, such errors are mitigated by copying information stored in bits. However, in quantum computing this cannot be done due to *no–cloning* theorem [69, 70]. Currently, an error correction method [71–73] is employed, partially

[4] e.g. Airbus, Boehringer Ingelheim, Volkswagen, Goldman Sachs, JP Morgan and Daimler.

resolving the mentioned issue by leaking the stored information to adjacent qubits that are in a highly entangled state with the initial qubit. This process led to a new form of *noisy* quantum computing, used in contemporary devices [74].

An alternative resolution to the decoherence problem was proposed by A. Kitaev [75]. There, he proposed that encircling non–Abelian anyonic excitations (resulting from the degeneracy of the ground state), with one another on a 2D surface, compels the global wave function to acquire additional phase as the system undergoes some unitary transformation [76, 77]. This process called *braiding*, allows for measurement after fusing two anyons and is inherently fault tolerant, therefore solving the decoherence problem. Non–Abelian anyons are quasiparticles that do not behave according to Fermi–Dirac nor Bose–Einstein statistics as in this case local physics is no longer the same after particle exchange[5]. Instead as anyon location is interchanged, its wave function acquires some phase (Abelian anyons) or is represented by a unitary matrix (non–Abelian anyons) that generates a Berry phase as one anyon winds around another one. Additionally, the matrices describing those unitary matrices for multiple non–Abelian anyons do not commute [81]. Later it was proposed that MBSs are an example of such non–Abelian anyons [82]. Its resistance to decoherence stems from the fact that due to Majorana nonlocality, degenerate ground states which normally form one fermion, are delocalized to the edges of the system. Therefore, only an identical perturbation acting on both ends of the system would lift the degeneracy, fusing Majoranas into a fermion or annihilate [66]. Obviously, one can also destroy MBS in a trivial way by removing some of the necessary symmetries, e.g. destroying the particle hole symmetry by heating up the system over the critical temperature of the superconductor etc.

In Fig. 1.3, we can see an elementary braiding protocol for MBSs. Such an operation consists of following steps: (a $\rightarrow$ b) top left part of the system is transitioned to a trivial state (e.g. with the change of chemical potential due to an external electrostatic gate) and subsequently the bottom part transitions to a nontrivial state. This forces MBS γ_1 to jump to middle of the structure and to the bottom as those are the new edges of

[5] Abelian *anyons* were named due their property of inducing *any* phase after exchange of particles [$\Psi(r_1, r_2) = e^{i\phi}\Psi(r_2, r_1)$] [78]. One can easily see that bosons and fermions are special cases of anyons (with $\phi = 0$ or π, respectively [77]). This results in bosons having a symmetric wave function [$\Psi(r_1, r_2) = \Psi(r_2, r_1)$] and fermions with antisymmetric wave function [$\Psi(r_1, r_2) = -\Psi(r_2, r_1)$], that is a consequence of indistinguishability of particles. However, in case of non–Abelian anyons, it instead generates an unitary $N \times N$ Berry matrix also called non–Abelian Berry phase [$\Psi(r_1, r_2) = U_B\Psi(r_2, r_1)$] [79, 80].

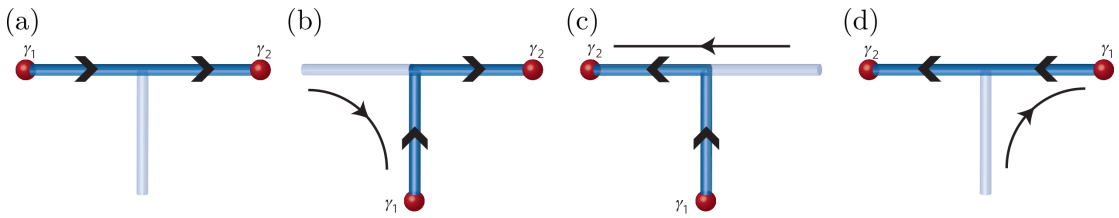

Figure 1.3: Schematics of single qubit Majorana braiding operation using nanowire T–junction device, equal to a half of σ_z gate operation. Dark (light) blue region denotes topologically nontrivial (trivial) region of T–juction. Arrows superimposed on system show the alignment between MBS γ_1 and γ_2. Arrows outside the T–junction point to the direction where the position of MBS is shifted. Figure adapted from Ref. [83].

the system. (b $\rightarrow$ c) as γ_1 is positioned on bottom, one can shift in similar manner γ_2 to the middle and top left of the structure as the distance between MBSs is sufficiently large to avoid any significant overlap and subsequent fusion. (c $\rightarrow$ d) by removing the nontrivial state of bottom part and extending it to top right, γ_2 is placed on the initial position of γ_1. This concludes the braiding protocol as the relative position between both anyons has been reversed, rotating the qubit over in a Bloch sphere from state $|0\rangle$ to superposition of $|0\rangle$ and $|1\rangle$ states. Performing this task a second time flips the qubit state to $|1\rangle$, thus making the whole process equivalent to Z gate: $Z = -i\sigma^z$, where σ^z is a third Pauli matrix.

However, apart from the significant difficulty of experimental realization, Majorana based quantum computing also has potential problems, like delocalisation, quasiparticle poisoning [84–86] and distinguishing from trivial superconductor excitations like Andreev bound states and Yu–Shiba–Rusinov states [87–90]. The first of these problems, delocalisation, is discussed in this thesis.

Non–Abelian braiding properties require that the quasiparticles used for computation possess zero-energy degrees of freedom that nonlocally encode ground-state degeneracy. Conveniently, there is no local perturbation that can split the degeneracy encoded by separate MBSs' since the corresponding ground states are locally indistinguishable [66]. As this feature of nonlocality is a crucial part of a main application of MBSs, driving the research in this branch of study, it is important to investigate the exceptions to this behaviour as well as methods that can allow for its manipulation.

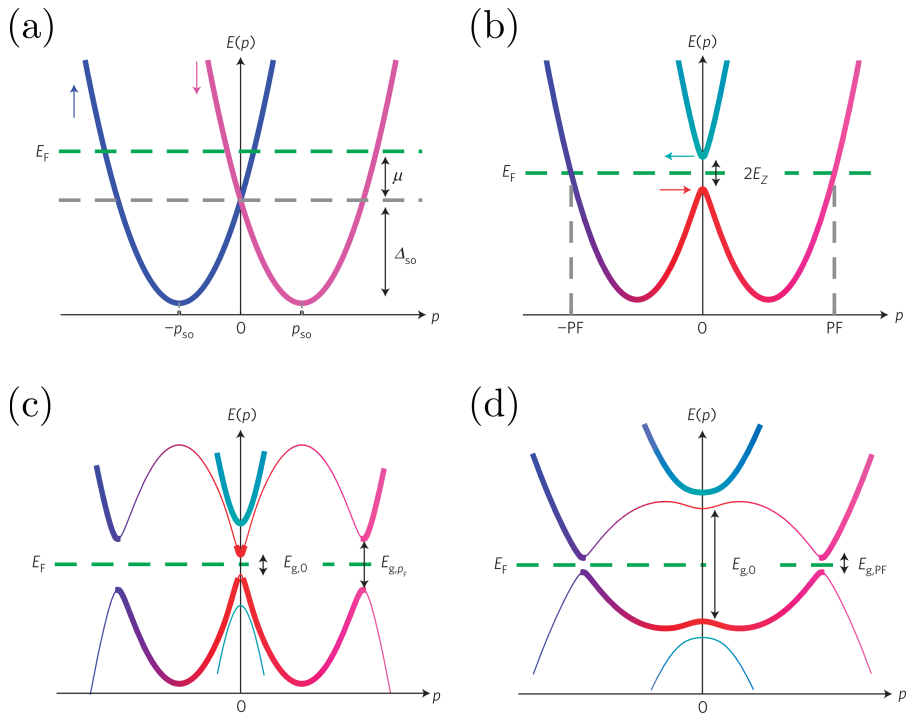

Figure 1.4: A schematic description of the band structure during the MBS emergence in 1D system. (a) Rashba–type spin–orbit cupling lead to the splitting of electronic bands in momentum-domain (two parabolic bands symmetric w.r.t. energy axis). Here, the strength of the spin–orbit coupling is described by $\pm p_{\mathrm{SO}}$ (momentum for which the band has minimum energy). (b) Turning on the external magnetic field leads to opening of Zeeman gap $2E_Z$ at momentum $p = 0$. (c) Proximity induced superconducting gap ($E_{g,p}$ at $p = 0$ or the Fermi points $\pm p_{\mathrm{F}}$) manifested at the crossing of particle– and hole–like bands (thick or thin lines, respectively). (d) When the magnetic field is sufficiently large, the gap at $p = 0$ is bigger then gap at the Fermi point $\pm p_{\mathrm{F}}$. This inverts the order of bands (due to external magnetic field), leading to emergence of the topological phase in the system [20, 91]. In consequence, in open system (without periodic boundary condition), the MBS can emerge. Colors denote opposite spin directions – blue and magenta (spin–orbit) and red and cyan (chiral motion). Figure adapted from Ref. [92].

1.3 Experimental development

In systems more realistic than a toy model, the emergence of MBSs stems from the interplay between three main ingredients: superconductivity, magnetic field, and spin–orbit coupling. This interplay is crucial in inducing the topologically nontrivial phase and is schematically shown in Fig. 1.4 for the case of a 1D system. If a typical parabolic band is affected by the Rashba spin–orbit coupling, the spin degeneracy is lifted and the bands are shifted within the momentum domain in opposite directions (a). Then, if the magnetic field is applied (b), it forces the bands to disjoin, creating

upper and lower Rashba pseudo-spin bands, separated from each other by Zeeman gap $2E_Z$. As we introduce superconductivity by proximity induced superconducting gap 2Δ (c), we enlarge gap at $p = 0$ and obtain an additional gap between bands at $p = p_F$ due to the superconducting proximity effect. Magnetic field has a diminishing effect on the size of the gap and shifts bands changing the relative sizes of gaps around 0 and Fermi momentum (c→d). Further increase of the magnetic field closes the superconducting gap (for critical field H_c), and reopens a new topological gap. This is hallmarked by the inversion of bands, transitioning the system to a topologically non–trivial phase. Interplay between the ingredients mentioned above locks them in a topologically non–trivial phase for $H > H_c$, where

$$H_c^2 = \Delta^2 + \mu^2. \tag{1.6}$$

Here, the chemical potential μ is measured from the bottom of the band. This condition is true, regardless of the dimensionality of the system [31, 93, 94].

Points $p = 0$ and $p = p_F$ are two time-reversal invariant momenta for one-dimensional system that conveniently simplify the above condition by removing any trigonometric dependence resulting from various types of hopping in the system. Thus, by setting the chemical potential μ to cross a Rashba band, and with the superconducting proximity effect, we obtain the situation identical to the pairing of spinless fermions. This is a realistic and experimentally feasible counterpart of *p–wave* Kitaev model [82]. Even though the above description is for an infinite nanowire with periodic boundary conditions, it allows for MBSs to form at zero energy in systems with open boundary conditions, due to the *bulk boundary correspondence* [95–97].

Just over a decade after the theoretical predictions, developments in atomic scale microscopy and manufacturing of nanoscale devices allowed for recording the signatures of MBSs [98, 99]. Some notable examples of such systems in superconductor–semiconductor hybrids [92, 100–117], monoatomic nanowires deposited on superconducting surface [118–122], core of superconducting vortexes [123–129], nanowire coupled to quantum dot [130–132], 2D topological structures [133–143], self assembled pristine nanostructures [144, 145] and quantum Hall systems [146, 147]. A first experimental signs of MBS emergence were recorded by V. Mourik *et al.* [100]. Ingredients mentioned above forced a certain idea of constructing a device capable of perceiving Majorana states [Fig. 1.5(a) and (b)]. Superconductivity was introduced to the system due to the

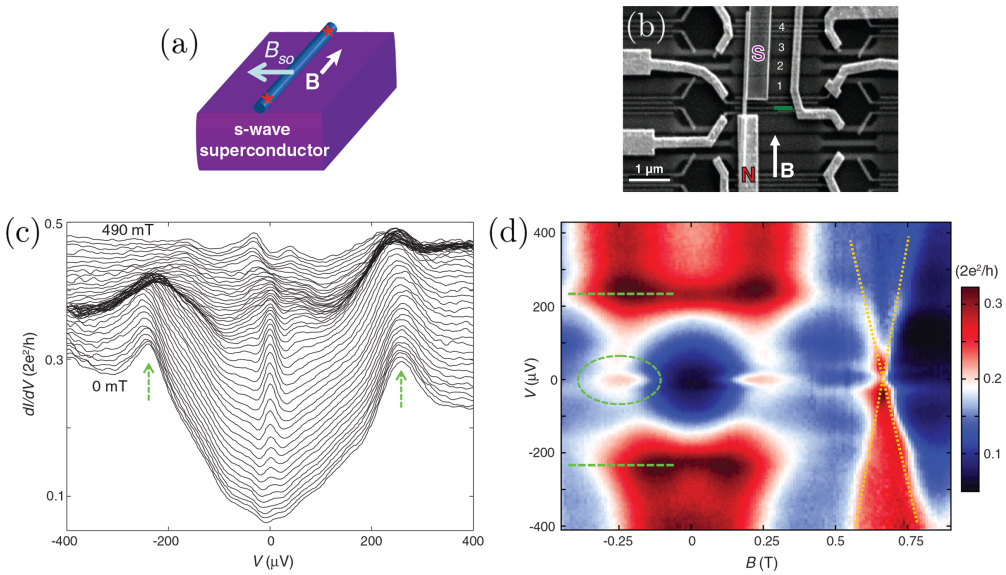

Figure 1.5: Experimental data on differential conductance spectroscopy in hybrid structure and its schematics. (a) Schematic view of device showing a nanowire deposited on a superconducting surface with superimposed directions of magnetic field B and spin–orbit coupling B_{SO}. Red stars specify the probable localisation of MBSs. (b) Scanning electron microscope image of the device with normal (N) and superconducting (S) contacts. (c) Conductance plots as a function of voltage V at 70 mK. Consecutive plots, offset for clarity, were taken at various magnetic fields smaller than 490 mT. Arrows show the peaks of proximity induced gap. (d) Colormap as a function of bias voltage V and magnetic field B at 70 mK, reproducing some of results from (c). Green oval encircles a zero bias peak interpreted as MBSs induced in the system and green lines depict superconducting gap size. Yellow lines show a slope of a non-Majorana state. Figure adapted from Ref. [100].

proximity effect, where Cooper pairs scatter into the semiconducting nanowire. This results in a gapped system with a gap size of approximately 0.65 meV. External magnetic field was applied parallel to the nanowire, with a value of over 0.75 T. Lastly, high spin–orbit coupling is an inherent property of semiconductors. As a result, the interplay between those parameters allows for a transition from a trivial to nontrivial phase.

Usually, local and non–local differential conductance measurements are used in order to probe MBS in condensed matter systems, employing ballistic transport or scanning tunnelling microscopy (STM). MBS localized at the edge of the system that is negligibly coupled to another MBS supports a resonant Andreev process, giving rise to a zero bias differential conductance peak of a single quantum of conductance – $2e^2/h$ [148–150]. Any non–zero coupling between MBSs leads to a decrease of conductance peaks due to MBSs overlap [151]. From the theoretical point of view, local density of states

(LDOS) is analogous to differential conductance, and thus allows for substantial agreement between theory and experiment. In the case of the mentioned experiment and in accordance with the theoretical predictions, an interplay between Majorana ingredients is envisioned by differential conductance measurements showing a zero bias peak [peak at zero energy in Fig. 1.5(c) and green oval in Fig. 1.5(d)] that persists for a range of magnetic field (B from 0.1 to 0.4 T) with intensity of approximately 5% of quantum of conductance, $2e^2/h$. As this experimental effort ruled out other competing phenomena (Andreev bound states, Kondo peaks, weak antilocalization, and reflectionless tunneling), this was the first signature of magnetic field-induced topological phase transition and subsequently, of the emergence of MBSs.

Apart from the nanowires deposited onto the superconductor, there was a competing idea of self-assembled nanowires grown on the surface of superconductor. S. Nadj–Perge *et al.* shown [118] that this is possible in a system, where a fraction of monolayer of iron was deposited on lead surface, resulting in chains stemming from iron nanoislands. In this case, both superconductivity and strong spin–orbit coupling came from the lead surface and the inherent magnetism of ferromagnetic iron atoms resolved the need for an external magnetic field. A topography of the surface of Pb(110) and examples of Fe nanowires can be seen in Fig. 1.6(a). Nanowires of height of approximately 2 Å

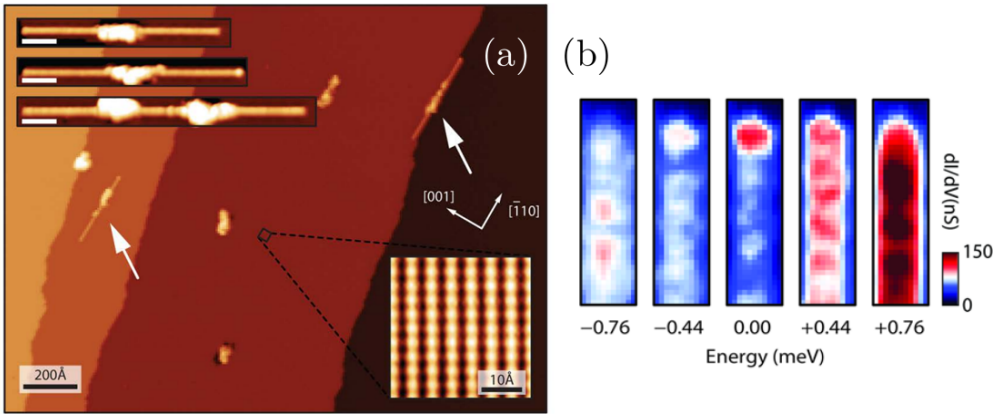

Figure 1.6: Topography of surface of Pb(110) terraces (a) showing self assembled Fe nanowires (white arrows) stemming from Fe islands. Insets show close–ups of nanowires attached to islands (white scale bar spans over 50 Å) and the atomic structure of the Pb(110). (b) STM images of one of the Fe nanowire ends showing color maps of conductance as a function of position for various voltage bias at temperature of 1.4 K. Central image ($V = 0$ eV) shows zero bias peak near the end of nanowire, interpreted as MBS. White scale bar spans over 10 Å. Figure adapted from Ref. [118].

located between Pb atoms, grew from both sides of the seeds that during Fe evaporation transformed into nanoislands. In Fig. 1.6(b) one can see a spatial image of one of the ends of Fe nanowire for various values of voltage applied to the atomic chain. Using STM spectroscopy, they record various excitations for different energies with a clear peak about $15 - 20$ Å from the edge of Fe chain for $E = 0$. This points to the fact that in real systems MBSs are not localised exactly at the very edges of the system but are spread around some distance near the end of the nanowire. Spatial size of MBSs in these systems are over 10 times smaller than the size of the nanowire. As in the previous case, phenomena like Kondo features, gap suppression at the nanowire's end or disorder were ruled out as a potential origin of zero bias peaks. Additionally, very short atomic chains ($\sim 30 - 40$ Å) do not show any edge states in accordance with the prediction that overlapping Majorana states should annihilate each other. It is worth noting that this experimental setup was also probed by superconducting STM tip [152], finding Majorana state as a pair of resonances at $\pm\Delta_{tip}$. An asymmetry in peak intensity was attributed to temperature peak broadening that overlay the additional subgap state in the system (1.1 K).

Another important experimental development from the point of view of this thesis is the work done by M.T. Deng *et al.* [130]. In this study, a hybrid device was manufactured that couples a quantum dot to a semiconducting nanowire. The whole system was created epitaxially, forming an InAs nanowire with Al layer sufficiently thick for a proximity induced superconductivity to occur. Magnetic field in direction along the nanowire axis was obtained with the use of external set of magnets. As a result, this setup should allow for the emergence of MBSs at the ends of nanowire. Interestingly, a small part ($\sim$ 150 nm) of a nanowire was not covered by the superconducting layer, leaving it in a normal state to play a role of quantum dot. Scanning electron microscope picture of the device and exemplary results are shown in Fig. 1.7. By inspecting the differential conductance on the quantum dot part at 20 mK, with changing magnetic field and gate potential, they concluded that MBS forms in the system due to the coalescence of two symmetric Andreev bound states, forming a discrete state at zero energy. Moreover, in the strong coupling regime, MBSs can delocalize from nanowire (nontrivial part) to a quantum dot (trivial part) due to the hybridization between Majorana state and quantum dot. This shows that the indigenous property of being at the edge conquers the need to exist at a topologically nontrivial region of the system. Hence,

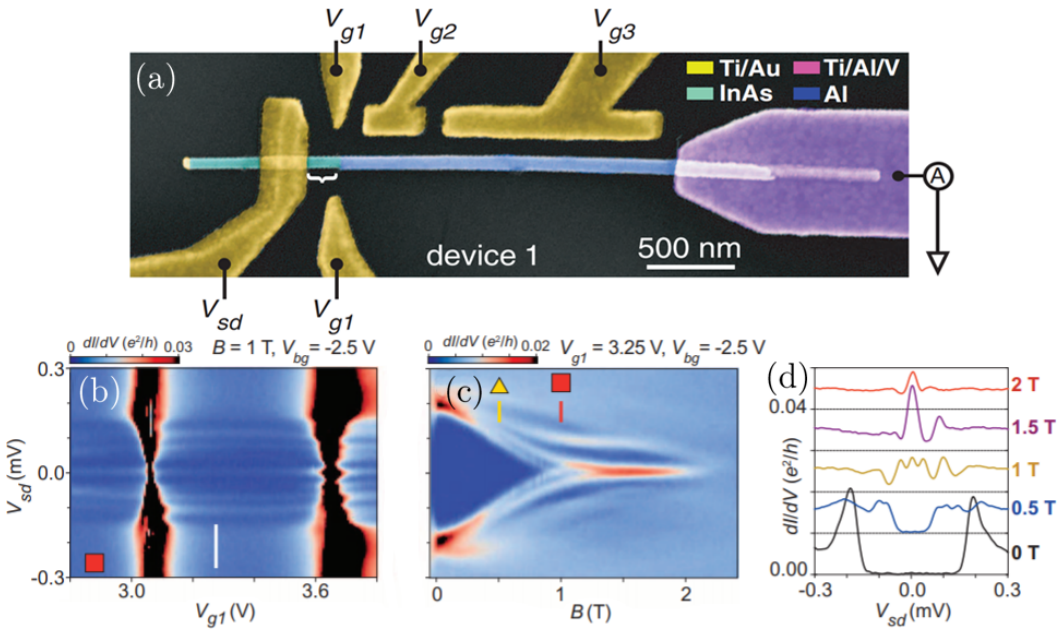

Figure 1.7: A hybrid nanowire–quantum dot device. (a) Scanning electron microscope picture of nanowire–quantum dot hybrid device. Superconducting Al layer is deposited on top of InAs nanowire with quantum dot region being left out without any top layer. Voltage gates V_{g1} control the energy of the quantum dot and V_{g2},V_{g3} control chemical potential of the nanowire. (b) Energy of the system as a function of potential on quantum dot showing persisting zero bias feature. (c) Energy of the system as a function of magnetic field showing a coalescence of Andreev bound states into MBS near B = 1 T. Panels (b) and (c) are each others cross sections (red and white lines, respectively). (d) Differential conductance curves showing zero bias peaks for around $1 - 2$ T. Figure adapted from Ref. [130].

this introduces an interesting problem – if Majorana nonlocality, taken as the ability of MBSs to delocalize to the edges of the system, allows it to spread to its trivial parts, it might threaten the feasibility of topological quantum computation using a braiding protocol. Therefore, it is crucial to investigate the behaviour of this MBS nonlocality for the benefit of technological applications of topological phenomena.

Stepping out of the 1D comfort zone, a significant progress in Majorana emergence has been made in 2D heterostructure systems. In these setups, Majorana nonlocality manifests as a Majorana edge mode, a 1D state along the edge of nanoisland, or other designer systems. In contrast to the 0D case, 1D Majoranas are dispersive and chiral, meaning that they are mobile and revolve along the edge in a magnetic field-dependent direction due to the locking of momentum and spin, analogically to the quantum Hall effect [153]. It is worth mentioning here that there is also a possibility for a helical state with two counter-propagating spin edge states to exist. Still, such phenomena

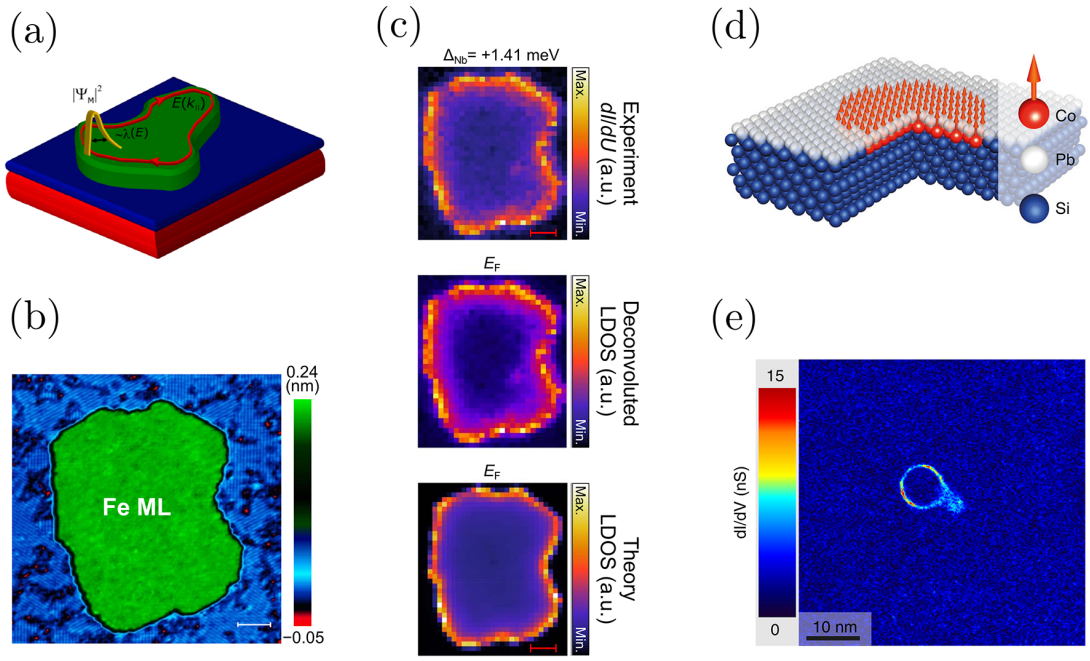

Figure 1.8: Example of the realization of chiral Majorana edge modes around various nanoscale systems. Schematic picture of the the nanoscale magnet-superconductor hybrid system Fe/Re(0001)O (a), indicating the spatial structure of the Majorana edge modes (red line) around Fe nanoisland (green surface). (b) Constant-current STM image of a Fe island located on the O(2×1)-reconstructed surface of Re(0001). Red scale bars show the distance of 5 nm. (c) Comparison between of the differential conductance G, deconvoluted LDOS and theoretical local density of states (LDOS) set to probe Majorana edge mode. (d) Schematic picture of Co nanoisland deposited on top of Si(111) substrate and submerged in Pb. Ferromagnetic Co atoms provide Zeeman energy to the system. (e) Deconvoluted differential conductance map of single Co island at 300 mK. Off–colour ring is the gapless edge state around the edge of island. Panels adapted from Refs. [135, 139].

has not been experimentally confirmed yet. However, chiral Majorana edge state can be probed using STM technique and the subsequent measurements can be expressed as a Chern number which corresponds to the number of edge current channels. Recently, several 2D experimental systems were reported in the form of, e.g. magnetic nanoisland deposited on the superconducting surface (Fe on Re [139], EuS on Au [140, 141], or $CrBr_3$ on $NbSe_2$ [142]) or superconducting Pb monolayer covering Co magnetic island [135, 138]. We can see some notable examples of the emergence of Majorana edge states in condensed matter in Fig. 1.8.

In panels (a) and (b), we can see the schematic and actual image of the Fe island located on the O(2×1)-reconstructed surface of Re(0001). Colour denotes the topography

of the sample. Comparison on panel (c) links the experimental data taken, deconvoluted[6] experimental results and theoretical prediction. It can be seen that the edge state probed by the superconducting tip (Nb) at 360 mK displays an uncanny similarity between experimental and theoretical data, suggesting that this system is indeed a topological superconductor. Even though only a single island is shown, the authors claim that this effect is universal. Topological invariant computations in the theoretical part [lowest part of Fig. 1.8(c)] yield a result of Chern number equal to 20. Red scale bars show the distance of 5 nm. Additionally, a second structure composed of Co nanoisland deposited on top of Si(111) substrate and submerged in Pb is presented (d). Experimental results (e) show an edge state along the nanoisland that can be clearly distinguished from the background noise. Similarly to the previous case, a superconducting tip (Pb) was used to gather data that was later deconvoluted to reveal a gapless ring with sufficiently higher conductance than in the background. This suggests a potential existence of topological superconductivity in Pb/Si(111) heterostructure with Co cluster.

Lastly, an effort by H. Kim *et al.* [145] is worth mentioning. In this work, they firstly deposited a fraction of Fe nanolayer on a superconducting Re(0001) substrate. Inserting an STM tip into Fe nanoisland allowed for recovering some of the atoms from the island by attaching it to the tip and then to release them on the clean surface of Re. Then, by to distinguish Fe atoms from any impurities, they identified Yu–Shiba–Rusinov spectra of Fe atoms. For the identified atoms, a substantial increase in current allowed for picking them up and depositing them at the designated place. Using this process, they were able to create a pristine, 40 atom long nanowire of Fe atoms along the [110] direction of Re substrate. A schematics of this process and STM spectrum of the nanowire as it was grown is shown in Fig. 1.9(a) and Fig. 1.9(b), respectively. In contrast to previous papers, spin–orbit coupling in this system was in the form of spin spiral, originating from Dzyaloshinsky–Moriya interaction, contrary to the situation in Fe atoms on Pb [118]. Reminiscently of previous experimental efforts, differential conductance measurements were performed in order to probe the existence of MBSs. As shown on Fig. 1.9(c), for zero energy, we can see peaks in conductance at both ends of nanowire, as well as diminishing oscillations of Majorana states in the

[6]Deconvolution of the electronic density of states of the tip and sample from STM data is the process used in the case of superconducting tips to subtract background noise and shift energies to the ones actually measured by removing the satellites caused by the tip spectrum [154].

form of lower intensity peaks further from the edge. It is quite often in the theoretical description to model a 1D system that consists solely of a few hundred atoms long nanowire put on top of some superconducting surface. Creating this type of single atom thick pristine nanowires and showing the premises of MBS existence helps in validating the feasibility of theoretical models as well as strengthening the foundations of possible future predictions using similar models.

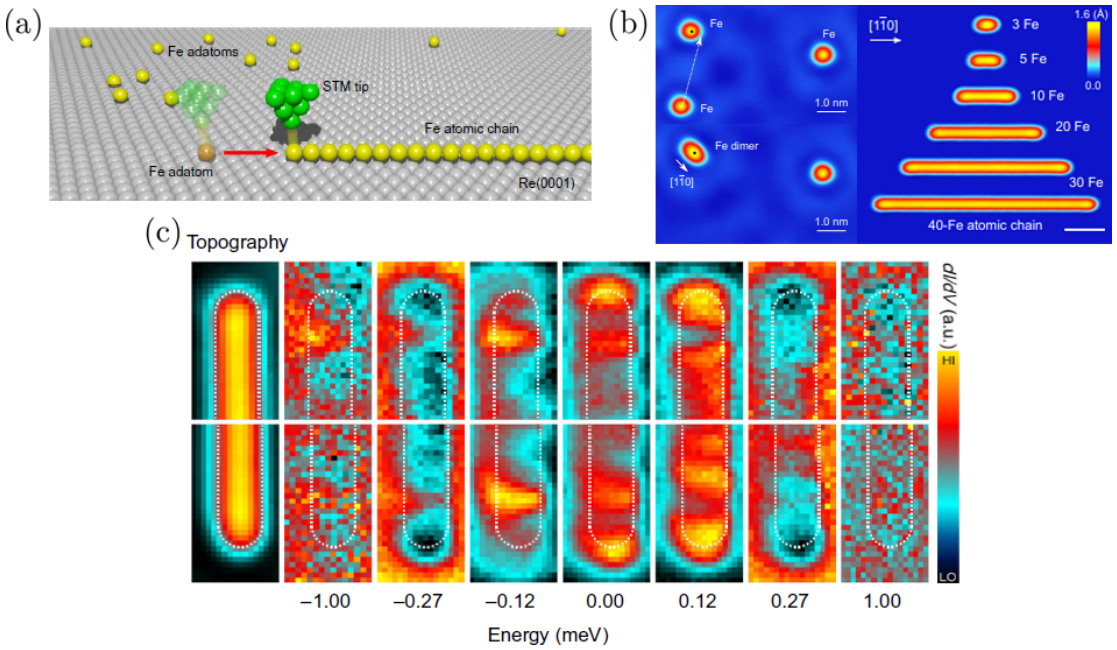

Figure 1.9: Manufacturing of pristine Fe nanowires on Ru(0001) substrate. (a) Schematic picture of lateral manipulation of Fe atoms used in construction of nanowires. (b) STM images of nanowire production process starting with a formation of Fe dimer up until 40 atom long chain. (c) STM measurements showing spatially distributed LDOS of 40 atom nanowire for different energies. Figures show only the ends of nanowire in which one can an alike distribution of states for given energy. On the zero energy, one can see localized states at the edge of nanowire. Left–most figure shows the topography of atomic chain. Figure adapted from Ref. [145].

1.4 Motivation

Quantum computing can be an answer for Moore's law saturation, which is a bottleneck in information processing for our technology. While it is not a universal solution to all of the computational issues, some problems characterized by their extreme complexity (e.g. optimisation, modelling of quantum structures, forecasting) might benefit from such development. As the contemporary quantum computers using superconduct-

ing transmon gates are not yet a gold standard, Majorana–dependent devices still can compete in the race. Even though its one of the many approaches to build a viable quantum computer, the unique features of non–Abelian braiding computation gives this concept a significant edge. As a result, the development of a "braiding–friendly" nanodevices employing MQPs is undoubtedly essential for quantum computing and for the progress of science as a whole. However, before such a device can be constructed, it is imperative to study the fundamentals of MBS behaviour, namely, its emergence and nonlocality (delocalisation). MBSs behaviour in 1D systems can be described by two of its properties – its emergence, a set of premises that coalesce into a working example of this quasiparticle existence and its nonlocality, usually connected with Majoranas being "a half of the fermion", with both "halves" delocalised to the edges of nanowire. In Ch. 2, we will discuss the theoretical background of MBS more closely. In order to successfully produce MBS at the edges of the experimental system in a controllable manner, a substantial work has to be put in theoretical studies of the emergence of MBS – the conditions that drive it in various geometries and settings. At the same time, as the braiding protocols depend on the real space manipulation of MBS location, it is important to investigate Majorana nonlocality. Here, nonlocality separates a fermion into two distinct Majorana anyons, it also can force those anyons to the edges of the system. In most of the braiding schemes proposed in the literature, some adiabatic process shifts the position of MBS due to topological trivialisation of the end parts of the system. Unfortunately, nonlocality has an unfortunate aberration – delocalisation, or *leakage*, that allows MBS to reside in the forbidden regions of the studied devices. Therefore, an inquiry into this property should encompass hybrid devices of mixed dimensionality and composition. Such an investigation can lead to improved control over MBS behaviour in the scope of application in realistic devices.

In this thesis, we investigate these two features with the use of nine articles published in peer-reviewed journals. In Ch. 3, we will present the methods used in order to obtain the results that were shown in the core chapter of this thesis – Ch. 4. There, all of our published papers related to the main two concerns of this thesis, namely, the emergence and nonlocality of MBS are presented with an additional brief description, containing four and five papers respectively. In the first part, we study the emergence of MBSs in various systems and circumstances due to the topological transition, as well as finding new ways to create and manipulate MBSs in the scope of the larger quest of

topological quantum computing. As for the second part, papers regarding this aspect study the extension of nonlocality, where MBS *leaks* from nontrivial to trivial regions but still retains its usual properties. Additionally, we propose multi–dimensional hybrid nanodevices capable of hosting and manipulation of MQPs. We use this as a platform to study both the emergence and nonlocality of MBS. Finally, in the last chapter (Ch. 5), we will summarize our goals, ponder about the state of the field of Majorana physics, and try to look ahead to opportunities and problems that might occur in future. As an aspiring physicist, taking part in an endeavour that might be considered in the future as world–changing as the invention of the Internet was, seems like a dream come true. We were born too late to explore new lands and to early to explore new planets – fortunately, the fact of being the first person in the whole world who is experiencing a just-calculated plot is as close as one can get now to exploring new worlds.

Bibliography

[1] P. Dirac, *The quantum theory of the electron*, Proc. R. Soc. Lond. A **117**, 610 (1928) DOI: 10.1098/rspa.1928.0023

[2] P. Dirac, *A theory of electrons and protons*, Proc. R. Soc. Lond. A **126**, 360 (1930) DOI: 10.1098/rspa.1930.0013

[3] E. Majorana, *Teoria simmetrica dell'elettrone e del positrone*, Il Nuovo Cimento **14**, 171 (1937) DOI: 10.1007/bf02961314

[4] E. Majorana and L. Maiani. *Ettore Majorana Scientific Papers*. Springer Berlin Heidelberg, (2006) 201. DOI: 10.1007/978-3-540-48095-2_10

[5] W. H. Furry, *On Transition Probabilities in Double Beta-Disintegration*, Phys. Rev. **56**, 1184 (1939) DOI: 10.1103/PhysRev.56.1184

[6] M. Agostini *et al.*, *Final Results of GERDA on the Search for Neutrinoless Double-β Decay*, Phys. Rev. Lett. **125**, 252502 (2020) DOI: 10.1103/PhysRevLett.125.252502

[7] M. Agostini *et al.*, *Probing Majorana neutrinos with double-β decay*, Science **365**, 1445 (2019) DOI: 10.1126/science.aav8613

[8] J. B. Albert *et al.*, *Sensitivity and discovery potential of the proposed nEXO experiment to neutrinoless double-β decay*, Phys. Rev. C **97**, 065503 (2018) DOI: 10.1103/PhysRevC.97.065503

[9] G. Anton *et al.*, *Search for Neutrinoless Double-β Decay with the Complete EXO-200 Dataset*, Phys. Rev. Lett. **123**, 161802 (2019) DOI: 10.1103/PhysRevLett.123.161802

[10] S. R. Elliott and M. Franz, *Colloquium: Majorana fermions in nuclear, particle, and solid-state physics*, Rev. Mod. Phys. **87**, 137 (2015) DOI: 10.1103/RevModPhys.87.137

[11] F. T. Avignone, S. R. Elliott, and J. Engel, *Double beta decay, Majorana neutrinos, and neutrino mass*, Rev. Mod. Phys. **80**, 481 (2008) DOI: 10.1103/RevModPhys.80.481

[12] N. N. Bogoliubov and D. V. Shirkov. *Introduction to the theory of quantized fields*. 3rd ed. New York, John Wiley, (1980) ISBN: 978-0471042235.

[13] P. G. D. Gennes. *Superconductivity Of Metals And Alloys (Advanced Books Classics)*. Westview Press, (1999) ISBN: 0738201014.

[14] H. Onnes, *Further experiments with liquid helium. C. On the change of electric resistance of pure metals at very low temperatures etc. IV. The resistance of pure mercury at helium temperatures*, Proc. K. Ned. Akad. Wet. **13**, 1274 (1911).

[15] R. de Bruyn Ouboter, *Heike Kamerlingh Onnes's Discovery of Superconductivity*, Sci. Am. **276**, 98 (1997) DOI: 10.1038/scientificamerican0397-98

[16] J. Bardeen, L. N. Cooper, and J. R. Schrieffer, *Theory of Superconductivity*, Phys. Rev. **108**, 1175 (1957) DOI: 10.1103/PhysRev.108.1175

[17] L. N. Cooper, *Bound Electron Pairs in a Degenerate Fermi Gas*, Phys. Rev. **104**, 1189 (1956) DOI: 10.1103/PhysRev.104.1189

[18] J. Spałek. *Wstęp do fizyki materii skondensowanej*. Warszawa, Wydawnictwo Naukowe PWN, (2015) ISBN: 9788301179731.

[19] F. Queisser, P. Navez, and R. Schützhold, *Sauter-Schwinger-like tunneling in tilted Bose-Hubbard lattices in the Mott phase*, Phys. Rev. A **85**, 033625 (2012) DOI: 10.1103/PhysRevA.85.033625

[20] M. Z. Hasan and C. L. Kane, *Colloquium: Topological insulators*, Rev. Mod. Phys. **82**, 3045 (2010) DOI: 10.1103/RevModPhys.82.3045

[21] C. W. J. Beenakker, *Search for non-Abelian Majorana braiding statistics in superconductors*, SciPost Phys. Lect. Notes, 15 (2020) DOI: 10.21468/SciPostPhysLectNotes.15

[22] Y. Maeno, H. Hashimoto, K. Yoshida, S. Nishizaki, T. Fujita, J. G. Bednorz, and F. Lichtenberg, *Superconductivity in a layered perovskite without copper*, Nature **372**, 532 (1994) DOI: 10.1038/372532a0

[23] K. Deguchi, M. A. Tanatar, Z. Mao, T. Ishiguro, and Y. Maeno, *Superconducting Double Transition and the Upper Critical Field Limit of Sr_2RuO_4 in Parallel Magnetic Fields*, J. Phys. Soc. Jpn **71**, 2839 (2002) DOI: 10.1143/jpsj.71.2839

[24] J. R. Kirtley, C. Kallin, C. W. Hicks, E.-A. Kim, Y. Liu, K. A. Moler, Y. Maeno, and K. D. Nelson, *Upper limit on spontaneous supercurrents in Sr_2RuO_4*, Phys. Rev. B **76**, 014526 (2007) DOI: 10.1103/PhysRevB.76.014526

[25] C. W. Hicks *et al.*, *Strong Increase of T_c of Sr_2RuO_4 Under Both Tensile and Compressive Strain*, Science **344**, 283 (2014) DOI: 10.1126/science.1248292

[26] A. Pustogow *et al.*, *Constraints on the superconducting order parameter in Sr_2RuO_4 from oxygen-17 nuclear magnetic resonance*, Nature **574**, 72 (2019) DOI: 10.1038/s41586-019-1596-2

[27] S. Benhabib *et al.*, *Ultrasound evidence for a two-component superconducting order parameter in Sr_2RuO_4*, Nat. Phys. **17**, 194 (2020) DOI: 10.1038/s41567-020-1033-3

[28] G. E. Volovik, *Fermion zero modes on vortices in chiral superconductors*, J. Exp. Theor. Phys. Lett. **70**, 609 (1999) DOI: 10.1134/1.568223

[29] L. P. Gor'kov and E. I. Rashba, *Superconducting 2D System with Lifted Spin Degeneracy: Mixed Singlet-Triplet State*, Phys. Rev. Lett. **87**, 037004 (2001) DOI: 10.1103/PhysRevLett.87.037004

[30] C. Zhang, S. Tewari, R. M. Lutchyn, and S. Das Sarma, *$p_x + ip_y$ Superfluid from s-Wave Interactions of Fermionic Cold Atoms*, Phys. Rev. Lett. **101**, 160401 (2008) DOI: 10.1103/PhysRevLett.101.160401

[31] M. Sato, Y. Takahashi, and S. Fujimoto, *Non-Abelian topological orders and Majorana fermions in spin-singlet superconductors*, Phys. Rev. B **82**, 134521 (2010) DOI: 10.1103/PhysRevB.82.134521

[32] K. Seo, L. Han, and C. A. R. Sá de Melo, *Topological phase transitions in ultracold Fermi superfluids: The evolution from Bardeen-Cooper-Schrieffer to Bose-Einstein-condensate superfluids under artificial spin-orbit fields*, Phys. Rev. A **85**, 033601 (2012) DOI: 10.1103/PhysRevA.85.033601

[33] T. Yu and M. W. Wu, *Gapped triplet p-wave superconductivity in strong spin-orbit-coupled semiconductor quantum wells in proximity to s-wave superconductor*, Phys. Rev. B **93**, 195308 (2016) DOI: 10.1103/PhysRevB.93.195308

[34] A. Ptok, K. Rodriguez, and K. J. Kapcia, *Superconducting monolayer deposited on substrate: Effects of the spin-orbit coupling induced by proximity effects*, Phys. Rev. Materials **2**, 024801 (2018) DOI: 10.1103/PhysRevMaterials.2.024801

[35] T. Senthil and M. P. A. Fisher, *Quasiparticle localization in superconductors with spin-orbit scattering*, Phys. Rev. B **61**, 9690 (2000) DOI: 10.1103/PhysRevB.61.9690

[36] N. Read and D. Green, *Paired states of fermions in two dimensions with breaking of parity and time-reversal symmetries and the fractional quantum Hall effect*, Phys. Rev. B **61**, 10267 (2000) DOI: 10.1103/PhysRevB.61.10267

[37] R. Aguado, *Majorana quasiparticles in condensed matter*, Riv. del Nuovo Cim. **40**, 523 (2017).

[38] G. Moore, *Cramming more components onto integrated circuits*, Electronics Magazine, (1965). eprint: https://newsroom.intel.com/wp-content/uploads/sites/11/2018/05/moores-law-electronics.pdf.

[39] R. P. Feynman, *Simulating physics with computers*, Int. J. Theor. Phys. **21**, 467 (1982) DOI: 10.1007/bf02650179

[40] R. S. Ingarden, *Quantum information theory*, Rep. Math. Phys. **10**, 43 (1976) DOI: https://doi.org/10.1016/0034-4877(76)90005-7

[41] P. A. Benioff, *Quantum mechanical Hamiltonian models of discrete processes that erase their own histories: Application to Turing machines*, International Journal of Theoretical Physics **21**, 177 (1982) DOI: 10.1007/bf01857725

[42] D. Deutsch, *Quantum theory, the Church–Turing principle and the universal quantum computer*, Proc. R. Soc. Lond. A **400**, 97 (1985) DOI: 10.1098/rspa.1985.0070

[43] W. G. Unruh, *Maintaining coherence in quantum computers*, Phys. Rev. A **51**, 992 (1995) DOI: 10.1103/PhysRevA.51.992

[44] G. M. Palma, K.-A. Suominen, and A. K. Ekert, *Quantum computers and dissipation*, Proc. R. Soc. Lond. A **452**, 567 (1996) DOI: 10.1098/rspa.1996.0029

[45] P. W. Shor, *Polynomial-Time Algorithms for Prime Factorization and Discrete Logarithms on a Quantum Computer*, SIAM J. Comput. **26**, 1484 (1997) DOI: 10.1137/s0097539795293172

[46] L. K. Grover, *Quantum Mechanics Helps in Searching for a Needle in a Haystack*, Phys. Rev. Lett. **79**, 325 (1997) DOI: 10.1103/PhysRevLett.79.325

[47] D. Loss and D. P. DiVincenzo, *Quantum computation with quantum dots*, Phys. Rev. A **57**, 120 (1998) DOI: 10.1103/PhysRevA.57.120

[48] I. L. Chuang, N. Gershenfeld, and M. Kubinec, *Experimental Implementation of Fast Quantum Searching*, Phys. Rev. Lett. **80**, 3408 (1998) DOI: 10.1103/PhysRevLett.80.3408

[49] E. Lucero *et al.*, *Computing prime factors with a Josephson phase qubit quantum processor*, Nat. Phys. **8**, 719 (2012) DOI: 10.1038/nphys2385

[50] A. H. Karamlou, W. A. Simon, A. Katabarwa, T. L. Scholten, B. Peropadre, and Y. Cao. *Analyzing the Performance of Variational Quantum Factoring on a Superconducting Quantum Processor*. (2020) eprint: arXiv:2012.07825.

[51] J. Johansson, P. Nation, and F. Nori, *QuTiP 2: A Python framework for the dynamics of open quantum systems*, Comput. Phys. Commun. **184**, 1234 (2013) DOI: https://doi.org/10.1016/j.cpc.2012.11.019

[52] A. Macridin, P. Spentzouris, J. Amundson, and R. Harnik, *Digital quantum computation of fermion-boson interacting systems*, Phys. Rev. A **98**, 042312 (2018) DOI: 10.1103/PhysRevA.98.042312

[53] H. Abraham *et al. Qiskit: An Open-source Framework for Quantum Computing.* (2019) DOI: 10.5281/zenodo.2562110

[54] C. Outeiral, M. Strahm, J. Shi, G. M. Morris, S. C. Benjamin, and C. M. Deane, *The prospects of quantum computing in computational molecular biology*, Wiley Interdiscip. Rev. Comput. Mol. Sci. **11**, e1481 (2021) DOI: https://doi.org/10.1002/wcms.1481

[55] S. McArdle, S. Endo, A. Aspuru-Guzik, S. C. Benjamin, and X. Yuan, *Quantum computational chemistry*, Rev. Mod. Phys. **92**, 015003 (2020) DOI: 10.1103/RevModPhys.92.015003

[56] A. Kulikov, M. Jerger, A. Potočnik, A. Wallraff, and A. Fedorov, *Realization of a Quantum Random Generator Certified with the Kochen-Specker Theorem*, Phys. Rev. Lett. **119**, 240501 (2017) DOI: 10.1103/PhysRevLett.119.240501

[57] Y. Liu *et al.*, *High-Speed Device-Independent Quantum Random Number Generation without a Detection Loophole*, Phys. Rev. Lett. **120**, 010503 (2018) DOI: 10.1103/PhysRevLett.120.010503

[58] F. Arute *et al.*, *Quantum supremacy using a programmable superconducting processor*, Nature **574**, 505 (2019) DOI: 10.1038/s41586-019-1666-5

[59] E. Pednault, J. A. Gunnels, G. Nannicini, L. Horesh, and R. Wisnieff. *Leveraging Secondary Storage to Simulate Deep 54-qubit Sycamore Circuits*. (2019) eprint: arXiv:1910.09534.

[60] D. Drahi *et al.*, *Certified Quantum Random Numbers from Untrusted Light*, Phys. Rev. X **10**, 041048 (2020) DOI: 10.1103/PhysRevX.10.041048

[61] F. Xu, X. Ma, Q. Zhang, H.-K. Lo, and J.-W. Pan, *Secure quantum key distribution with realistic devices*, Rev. Mod. Phys. **92**, 025002 (2020) DOI: 10.1103/RevModPhys.92.025002

[62] Y.-p. Yuan, C. Du, Q.-q. Shen, J.-d. Wang, Y.-f. Yu, Z.-j. Wei, Z.-x. Chen, and Z.-m. Zhang, *Proof-of-principle demonstration of measurement-device-independent quantum key distribution based on intrinsically stable polarization-modulated units*, Opt. Express **28**, 10772 (2020) DOI: 10.1364/oe.387968

[63] F. Neukart, G. Compostella, C. Seidel, D. von Dollen, S. Yarkoni, and B. Parney, *Traffic Flow Optimization Using a Quantum Annealer*, Front. ICT **4**, 29 (2017) DOI: 10.3389/fict.2017.00029

[64] N. Stamatopoulos, D. J. Egger, Y. Sun, C. Zoufal, R. Iten, N. Shen, and S. Woerner, *Option Pricing using Quantum Computers*, Quantum **4**, 291 (2020) DOI: 10.22331/q-2020-07-06-291

[65] I. L. Chuang, R. Laflamme, P. W. Shor, and W. H. Zurek, *Quantum Computers, Factoring, and Decoherence*, Science **270**, 1633 (1995) DOI: 10.1126/science.270.5242.1633

[66] D. Aasen *et al.*, *Milestones Toward Majorana-Based Quantum Computing*, Phys. Rev. X **6**, 031016 (2016) DOI: 10.1103/PhysRevX.6.031016

[67] M. A. Nielsen. *Quantum Computation and Quantum Information: 10th Anniversary Edition*. Cambridge University Press, (2011) ISBN: 9781107002173.

[68] C. Tutschku, R. W. Reinthaler, C. Lei, A. H. MacDonald, and E. M. Hankiewicz, *Majorana-based quantum computing in nanowire devices*, Phys. Rev. B **102**, 125407 (2020) DOI: 10.1103/PhysRevB.102.125407

[69] W. K. Wootters and W. H. Zurek, *A single quantum cannot be cloned*, Nature **299**, 802 (1982) DOI: 10.1038/299802a0

[70] D. Dieks, *Communication by EPR devices*, Phys. Lett. A **92**, 271 (1982) DOI: https://doi.org/10.1016/0375-9601(82)90084-6

[71] P. W. Shor, *Scheme for reducing decoherence in quantum computer memory*, Phys. Rev. A **52**, R2493 (1995) DOI: 10.1103/PhysRevA.52.R2493

[72] D. G. Cory, M. D. Price, W. Maas, E. Knill, R. Laflamme, W. H. Zurek, T. F. Havel, and S. S. Somaroo, *Experimental Quantum Error Correction*, Phys. Rev. Lett. **81**, 2152 (1998) DOI: 10.1103/PhysRevLett.81.2152

[73] M. D. Reed, L. DiCarlo, S. E. Nigg, L. Sun, L. Frunzio, S. M. Girvin, and R. J. Schoelkopf, *Realization of three-qubit quantum error correction with superconducting circuits*, Nature **482**, 382 (2012) DOI: 10.1038/nature10786

[74] J. Preskill, *Quantum Computing in the NISQ era and beyond*, Quantum **2**, 79 (2018) DOI: 10.22331/q-2018-08-06-79

[75] A. Kitaev, *Fault-tolerant quantum computation by anyons*, Annals Phys. **303**, 2 (2003) DOI: https://doi.org/10.1016/S0003-4916(02)00018-0

[76] D. A. Ivanov, *Non-Abelian Statistics of Half-Quantum Vortices in p-Wave Superconductors*, Phys. Rev. Lett. **86**, 268 (2001) DOI: 10.1103/PhysRevLett.86.268

[77] C. Nayak, S. H. Simon, A. Stern, M. Freedman, and S. Das Sarma, *Non-Abelian anyons and topological quantum computation*, Rev. Mod. Phys. **80**, 1083 (2008) DOI: 10.1103/RevModPhys.80.1083

[78] F. Wilczek, *Quantum Mechanics of Fractional-Spin Particles*, Phys. Rev. Lett. **49**, 957 (1982) DOI: 10.1103/PhysRevLett.49.957

[79] K. Snizhko, R. Egger, and Y. Gefen, *Non-Abelian Berry phase for open quantum systems: Topological protection versus geometric dephasing*, Phys. Rev. B **100**, 085303 (2019) DOI: 10.1103/PhysRevB.100.085303

[80] M. Ezawa, *Non-Abelian braiding of Majorana-like edge states and topological quantum computations in electric circuits*, Phys. Rev. B **102**, 075424 (2020) DOI: 10.1103/PhysRevB.102.075424

[81] V. Lahtinen and J. K. Pachos, *A Short Introduction to Topological Quantum Computation*, SciPost Phys. **3**, 021 (2017) DOI: 10.21468/SciPostPhys.3.3.021

[82] A. Y. Kitaev, *Unpaired Majorana fermions in quantum wires*, Phys.-Usp. **44**, 131 (2001) DOI: 10.1070/1063-7869/44/10s/s29

[83] J. Alicea, Y. Oreg, G. Refael, F. von Oppen, and M. P. A. Fisher, *Non-Abelian statistics and topological quantum information processing in 1D wire networks*, Nat. Phys. **7**, 412 (2011) DOI: 10.1038/nphys1915

[84] G. Goldstein and C. Chamon, *Decay rates for topological memories encoded with Majorana fermions*, Phys. Rev. B **84**, 205109 (2011) DOI: 10.1103/PhysRevB.84.205109

[85] J. C. Budich, S. Walter, and B. Trauzettel, *Failure of protection of Majorana based qubits against decoherence*, Phys. Rev. B **85**, 121405 (2012) DOI: 10.1103/PhysRevB.85.121405

[86] P. P. Aseev, P. Marra, P. Stano, J. Klinovaja, and D. Loss, *Degeneracy lifting of Majorana bound states due to electron-phonon interactions*, Phys. Rev. B **99**, 205435 (2019) DOI: 10.1103/PhysRevB.99.205435

[87] F. Pientka, L. I. Glazman, and F. von Oppen, *Topological superconducting phase in helical Shiba chains*, Phys. Rev. B **88**, 155420 (2013) DOI: 10.1103/PhysRevB.88.155420

[88] C. Moore, C. Zeng, T. D. Stanescu, and S. Tewari, *Quantized zero-bias conductance plateau in semiconductor-superconductor heterostructures without topological Majorana zero modes*, Phys. Rev. B **98**, 155314 (2018) DOI: 10.1103/PhysRevB.98.155314

[89] T. D. Stanescu and S. Tewari, *Robust low-energy Andreev bound states in semiconductor-superconductor structures: Importance of partial separation of component Majorana bound states*, Phys. Rev. B **100**, 155429 (2019) DOI: 10.1103/PhysRevB.100.155429

[90] E. Prada, P. San-Jose, M. W. A. de Moor, A. Geresdi, E. J. H. Lee, J. Klinovaja, D. Loss, J. Nygård, R. Aguado, and L. P. Kouwenhoven, *From Andreev to Majorana bound states in hybrid superconductor–semiconductor nanowires*, Nat. Rev. Phys. 575 (2020) DOI: 10.1038/s42254-020-0228-y

[91] A. Bansil, H. Lin, and T. Das, *Colloquium: Topological band theory*, Rev. Mod. Phys. **88**, 021004 (2016) DOI: 10.1103/RevModPhys.88.021004

[92] A. Das, Y. Ronen, Y. Most, Y. Oreg, M. Heiblum, and H. Shtrikman, *Zero-bias peaks and splitting in an Al–InAs nanowire topological superconductor as a signature of Majorana fermions*, Nat. Phys. **8**, 887 (2012) DOI: 10.1038/nphys2479

[93] M. Sato, Y. Takahashi, and S. Fujimoto, *Non-Abelian Topological Order in s-Wave Superfluids of Ultracold Fermionic Atoms*, Phys. Rev. Lett. **103**, 020401 (2009) DOI: 10.1103/PhysRevLett.103.020401

[94] M. Sato and S. Fujimoto, *Topological phases of noncentrosymmetric superconductors: Edge states, Majorana fermions, and non-Abelian statistics*, Phys. Rev. B **79**, 094504 (2009) DOI: 10.1103/PhysRevB.79.094504

[95] R. S. K. Mong and V. Shivamoggi, *Edge states and the bulk-boundary correspondence in Dirac Hamiltonians*, Phys. Rev. B **83**, 125109 (2011) DOI: 10.1103/PhysRevB.83.125109

[96] T. Fukui, K. Shiozaki, T. Fujiwara, and S. Fujimoto, *Bulk-Edge Correspondence for Chern Topological Phases: A Viewpoint from a Generalized Index Theorem*, J. Phys. Soc. Jpn. **81**, 114602 (2012) DOI: 10.1143/jpsj.81.114602

[97] N. Sedlmayr, V. Kaladzhyan, C. Dutreix, and C. Bena, *Bulk boundary correspondence and the existence of Majorana bound states on the edges of 2D topological superconductors*, Phys. Rev. B **96**, 184516 (2017) DOI: 10.1103/PhysRevB.96.184516

[98] R. M. Lutchyn, E. P. A. M. Bakkers, L. P. Kouwenhoven, P. Krogstrup, C. M. Marcus, and Y. Oreg, *Majorana zero modes in superconductor–semiconductor heterostructures*, Nat. Rev. Materials **3**, 52 (2018) DOI: 10.1038/s41578-018-0003-1

[99] E. Prada, P. San-Jose, M. W. A. de Moor, A. Geresdi, E. J. H. Lee, J. Klinovaja, D. Loss, J. Nygård, R. Aguado, and L. P. Kouwenhoven, *From Andreev to Majorana bound states in hybrid superconductor–semiconductor nanowires*, Nat. Rev. Phys. **2**, 575 (2020) DOI: 10.1038/s42254-020-0228-y

[100] V. Mourik, K. Zuo, S. M. Frolov, S. R. Plissard, E. P. A. M. Bakkers, and L. P. Kouwenhoven, *Signatures of Majorana Fermions in Hybrid Superconductor-Semiconductor Nanowire Devices*, Science **336**, 1003 (2012) DOI: 10.1126/science.1222360

[101] M. T. Deng, C. L. Yu, G. Y. Huang, M. Larsson, P. Caroff, and H. Q. Xu, *Anomalous Zero-Bias Conductance Peak in a Nb–InSb Nanowire–Nb Hybrid Device*, Nano Lett. **12**, 6414 (2012) DOI: 10.1021/nl303758w

[102] H. O. H. Churchill, V. Fatemi, K. Grove-Rasmussen, M. T. Deng, P. Caroff, H. Q. Xu, and C. M. Marcus, *Superconductor-nanowire devices from tunneling to the multichannel regime: Zero-bias oscillations and magnetoconductance crossover*, Phys. Rev. B **87**, 241401 (2013) DOI: 10.1103/PhysRevB.87.241401

[103] A. D. K. Finck, D. J. Van Harlingen, P. K. Mohseni, K. Jung, and X. Li, *Anomalous Modulation of a Zero-Bias Peak in a Hybrid Nanowire-Superconductor Device*, Phys. Rev. Lett. **110**, 126406 (2013) DOI: 10.1103/PhysRevLett.110.126406

[104] F. Nichele *et al.*, *Scaling of Majorana Zero-Bias Conductance Peaks*, Phys. Rev. Lett. **119**, 136803 (2017) DOI: 10.1103/PhysRevLett.119.136803

[105] S. Gazibegovic *et al.*, *Epitaxy of advanced nanowire quantum devices*, Nature **548**, 434 (2017) DOI: 10.1038/nature23468

[106] J. Chen, P. Yu, J. Stenger, M. Hocevar, D. Car, S. R. Plissard, E. P. A. M. Bakkers, T. D. Stanescu, and S. M. Frolov, *Experimental phase diagram of zero-bias conductance peaks in superconductor/semiconductor nanowire devices*, Sci. Adv. **3**, e1701476 (2017) DOI: 10.1126/sciadv.1701476

[107] Ö. Gül *et al.*, *Ballistic Majorana nanowire devices*, Nat. Nanotechnol. **13**, 192 (2018) DOI: 10.1038/s41565-017-0032-8

[108] S. Vaitiekėnas, M.-T. Deng, J. Nygård, P. Krogstrup, and C. M. Marcus, *Effective g Factor of Subgap States in Hybrid Nanowires*, Phys. Rev. Lett. **121**, 037703 (2018) DOI: 10.1103/PhysRevLett.121.037703

[109] D. Laroche *et al.*, *Observation of the 4π-periodic Josephson effect in indium arsenide nanowires*, Nat. Commun. **10**, 245 (2019) DOI: 10.1038/s41467-018-08161-2

[110] H. Zhang, D. E. Liu, M. Wimmer, and L. P. Kouwenhoven, *Next steps of quantum transport in Majorana nanowire devices*, Nat. Commun. **10**, 5128 (2019) DOI: 10.1038/s41467-019-13133-1

[111] J. D. S. Bommer *et al.*, *Spin-Orbit Protection of Induced Superconductivity in Majorana Nanowires*, Phys. Rev. Lett. **122**, 187702 (2019) DOI: 10.1103/PhysRevLett.122.187702

[112] J. Chen, B. D. Woods, P. Yu, M. Hocevar, D. Car, S. R. Plissard, E. P. A. M. Bakkers, T. D. Stanescu, and S. M. Frolov, *Ubiquitous Non-Majorana Zero-Bias Conductance Peaks in Nanowire Devices*, Phys. Rev. Lett. **123**, 107703 (2019) DOI: 10.1103/PhysRevLett.123.107703

[113] G. L. R. Anselmetti *et al.*, *End-to-end correlated subgap states in hybrid nanowires*, Phys. Rev. B **100**, 205412 (2019) DOI: 10.1103/PhysRevB.100.205412

[114] A. Grivnin, E. Bor, M. Heiblum, Y. Oreg, and H. Shtrikman, *Concomitant opening of a bulk-gap with an emerging possible Majorana zero mode*, Nat. Commun. **10**, 1940 (2019) DOI: 10.1038/s41467-019-09771-0

[115] G. C. Ménard *et al.*, *Conductance-Matrix Symmetries of a Three-Terminal Hybrid Device*, Phys. Rev. Lett. **124**, 036802 (2020) DOI: 10.1103/PhysRevLett.124.036802

[116] D. Puglia *et al. Closing of the Induced Gap in a Hybrid Superconductor-Semiconductor Nanowire*. (2020) eprint: arXiv:2006.01275.

[117] H. Zhang *et al. Large zero-bias peaks in InSb-Al hybrid semiconductor-superconductor nanowire devices*. (2021) eprint: arXiv:2101.11456.

[118] S. Nadj-Perge, I. K. Drozdov, J. Li, H. Chen, S. Jeon, J. Seo, A. H. MacDonald, B. A. Bernevig, and A. Yazdani, *Observation of Majorana fermions in ferromagnetic atomic chains on a superconductor*, Science **346**, 602 (2014) DOI: 10.1126/science.1259327

[119] R. Pawlak, M. Kisiel, J. Klinovaja, T. Meier, S. Kawai, T. Glatzel, D. Loss, and E. Meyer, *Probing atomic structure and Majorana wavefunctions in mono-atomic Fe chains on superconducting Pb surface*, Npj Quantum Inf. **2**, 16035 (2016) DOI: 10.1038/npjqi.2016.35

[120] B. E. Feldman, M. T. Randeria, J. Li, S. Jeon, Y. Xie, Z. Wang, I. K. Drozdov, B. A. Bernevig, and A. Yazdani, *High-resolution studies of the Majorana atomic chain platform*, Nat. Phys. **13**, 286 (2016) DOI: 10.1038/nphys3947

[121] M. Ruby, B. W. Heinrich, Y. Peng, F. von Oppen, and K. J. Franke, *Exploring a Proximity-Coupled Co Chain on Pb(110) as a Possible Majorana Platform*, Nano Lett. **17**, 4473 (2017) DOI: 10.1021/acs.nanolett.7b01728

[122] S. Jeon, Y. Xie, J. Li, Z. Wang, B. A. Bernevig, and A. Yazdani, *Distinguishing a Majorana zero mode using spin-resolved measurements*, Science **358**, 772 (2017) DOI: 10.1126/science.aan3670

[123] H.-H. Sun *et al.*, *Majorana Zero Mode Detected with Spin Selective Andreev Reflection in the Vortex of a Topological Superconductor*, Phys. Rev. Lett. **116**, 257003 (2016) DOI: 10.1103/PhysRevLett.116.257003

[124] H.-H. Sun and J.-F. Jia, *Detection of Majorana zero mode in the vortex*, npj Quantum Mater. **2**, 34 (2017) DOI: 10.1038/s41535-017-0037-4

[125] D. Wang *et al.*, *Evidence for Majorana bound states in an iron-based superconductor*, Science **362**, 333 (2018) DOI: 10.1126/science.aao1797

[126] T. Machida, Y. Sun, S. Pyon, S. Takeda, Y. Kohsaka, T. Hanaguri, T. Sasagawa, and T. Tamegai, *Zero-energy vortex bound state in the superconducting topological surface state of Fe(Se, Te)*, Nat. Mater. **18**, 811 (2019) DOI: 10.1038/s41563-019-0397-1

[127] K. Jiang, X. Dai, and Z. Wang, *Quantum Anomalous Vortex and Majorana Zero Mode in Iron-Based Superconductor Fe(Te,Se)*, Phys. Rev. X **9**, 011033 (2019) DOI: 10.1103/PhysRevX.9.011033

[128] C.-K. Chiu, T. Machida, Y. Huang, T. Hanaguri, and F.-C. Zhang, *Scalable Majorana vortex modes in iron-based superconductors*, Sci. Adv. **6**, eaay0443 (2020) DOI: 10.1126/sciadv.aay0443

[129] P. Fan *et al.*, *Observation of magnetic adatom-induced Majorana vortex and its hybridization with field-induced Majorana vortex in an iron-based superconductor*, Nat. Commun. **12**, (2021) DOI: 10.1038/s41467-021-21646-x

[130] M. T. Deng, S. Vaitiekenas, E. B. Hansen, J. Danon, M. Leijnse, K. Flensberg, J. Nygård, P. Krogstrup, and C. M. Marcus, *Majorana bound state in a coupled quantum-dot hybrid-nanowire system*, Science **354**, 1557 (2016) DOI: 10.1126/science.aaf3961

[131] M. T. Deng, S. Vaitiekenas, E. Prada, P. San-Jose, J. Nygård, P. Krogstrup, R. Aguado, and C. M. Marcus, *Nonlocality of Majorana modes in hybrid nanowires*, Phys. Rev. B **98**, 085125 (2018) DOI: 10.1103/PhysRevB.98.085125

[132] Z.-G. Liu, Y.-X. Huang, G.-C. Guo, and M. Gong, *Majorana and non-Majorana modes in a nanowire in partially proximity to a superconductor*, J. Appl. **129**, 094301 (2021) DOI: 10.1063/5.0038612

[133] J. Shabani *et al.*, *Two-dimensional epitaxial superconductor-semiconductor heterostructures: A platform for topological superconducting networks*, Phys. Rev. B **93**, 155402 (2016) DOI: 10.1103/PhysRevB.93.155402

[134] H. J. Suominen, M. Kjaergaard, A. R. Hamilton, J. Shabani, C. J. Palmstrøm, C. M. Marcus, and F. Nichele, *Zero-Energy Modes from Coalescing Andreev States in a Two-Dimensional Semiconductor-Superconductor Hybrid Platform*, Phys. Rev. Lett. **119**, 176805 (2017) DOI: 10.1103/PhysRevLett.119.176805

[135] G. C. Ménard, S. Guissart, C. Brun, R. T. Leriche, M. Trif, F. Debontridder, D. Demaille, D. Roditchev, P. Simon, and T. Cren, *Two-dimensional topological superconductivity in Pb/Co/Si(111)*, Nat. Commun. **8**, 2040 (2017) DOI: 10.1038/s41467-017-02192-x

[136] P. Zhang *et al.*, *Observation of topological superconductivity on the surface of an iron-based superconductor*, Science **360**, 182 (2018) DOI: 10.1126/science.aan4596

[137] B. Jäck, Y. Xie, J. Li, S. Jeon, B. A. Bernevig, and A. Yazdani, *Observation of a Majorana zero mode in a topologically protected edge channel*, Science **364**, 1255 (2019) DOI: 10.1126/science.aax1444

[138] G. C. Ménard, A. Mesaros, C. Brun, F. Debontridder, D. Roditchev, P. Simon, and T. Cren, *Isolated pairs of Majorana zero modes in a disordered superconducting lead monolayer*, Nat. Commun. **10**, 2587 (2019) DOI: 10.1038/s41467-019-10397-5

[139] A. Palacio-Morales, E. Mascot, S. Cocklin, H. Kim, S. Rachel, D. K. Morr, and R. Wiesendanger, *Atomic-scale interface engineering of Majorana edge modes in a 2D magnet-superconductor hybrid system*, Sci. Adv. **5**, eaav6600 (2019) DOI: 10.1126/sciadv.aav6600

[140] P. Wei, S. Manna, M. Eich, P. Lee, and J. Moodera, *Superconductivity in the Surface State of Noble Metal Gold and its Fermi Level Tuning by EuS Dielectric*, Phys. Rev. Lett. **122**, 247002 (2019) DOI: 10.1103/PhysRevLett.122.247002

[141] S. Manna, P. Wei, Y. Xie, K. T. Law, P. A. Lee, and J. S. Moodera, *Signature of a pair of Majorana zero modes in superconducting gold surface states*, Proceedings of the National Academy of Sciences **117**, 8775 (2020) DOI: 10.1073/pnas.1919753117

[142] S. Kezilebieke, M. N. Huda, V. Vaňo, M. Aapro, S. C. Ganguli, O. J. Silveira, S. Głodzik, A. S. Foster, T. Ojanen, and P. Liljeroth, *Topological superconductivity in a van der Waals heterostructure*, Nature **588**, 424 (2020) DOI: 10.1038/s41586-020-2989-y

[143] Z. Wang, J. O. Rodriguez, L. Jiao, S. Howard, M. Graham, G. D. Gu, T. L. Hughes, D. K. Morr, and V. Madhavan, *Evidence for dispersing 1D Majorana channels in an iron-based superconductor*, Science **367**, 104 (2020) DOI: 10.1126/science.aaw8419

[144] R. Drost, T. Ojanen, A. Harju, and P. Liljeroth, *Topological states in engineered atomic lattices*, Nat. Phys. **13**, 668 (2017) DOI: 10.1038/nphys4080

[145] H. Kim, A. Palacio-Morales, T. Posske, L. Rózsa, K. Palotás, L. Szunyogh, M. Thorwart, and R. Wiesendanger, *Toward tailoring Majorana bound states in artificially constructed magnetic atom chains on elemental superconductors*, Sci. Adv. **4**, eaar5251 (2018) DOI: 10.1126/sciadv.aar5251

[146] Q. L. He *et al.*, *Chiral Majorana fermion modes in a quantum anomalous Hall insulator–superconductor structure*, Science **357**, 294 (2017) DOI: 10.1126/science.aag2792

[147] M. Kayyalha *et al.*, *Absence of evidence for chiral Majorana modes in quantum anomalous Hall-superconductor devices*, Science **367**, 64 (2020) DOI: 10.1126/science.aax6361

[148] K. T. Law, P. A. Lee, and T. K. Ng, *Majorana Fermion Induced Resonant Andreev Reflection*, Phys. Rev. Lett. **103**, 237001 (2009) DOI: 10.1103/PhysRevLett.103.237001

[149] M. Wimmer, A. R. Akhmerov, J. P. Dahlhaus, and C. W. J. Beenakker, *Quantum point contact as a probe of a topological superconductor*, New J. Phys. **13**, 053016 (2011) DOI: 10.1088/1367-2630/13/5/053016

[150] J. Kammhuber *et al.*, *Conductance through a helical state in an Indium antimonide nanowire*, Nat. Commun. **8**, 478 (2017) DOI: 10.1038/s41467-017-00315-y

[151] S. Das Sarma, J. D. Sau, and T. D. Stanescu, *Splitting of the zero-bias conductance peak as smoking gun evidence for the existence of the Majorana mode in a superconductor-semiconductor nanowire*, Phys. Rev. B **86**, 220506 (2012) DOI: 10.1103/PhysRevB.86.220506

[152] M. Ruby, F. Pientka, Y. Peng, F. von Oppen, B. W. Heinrich, and K. J. Franke, *End States and Subgap Structure in Proximity-Coupled Chains of Magnetic Adatoms*, Phys. Rev. Lett. **115**, 197204 (2015) DOI: 10.1103/PhysRevLett.115.197204

[153] X.-L. Qi and S.-C. Zhang, *Topological insulators and superconductors*, Rev. Mod. Phys. **83**, 1057 (2011) DOI: 10.1103/RevModPhys.83.1057

[154] P. Wahl, L. Diekhöner, M. A. Schneider, and K. Kern, *Background removal in scanning tunneling spectroscopy of single atoms and molecules on metal surfaces*, Rev. Sci. Instrum. **79**, 043104 (2008) DOI: 10.1063/1.2907533

CHAPTER 2

Theoretical essentials

Pursuit of topological superconductivity in condensed matter physics stems from the great promise of novel physics. Here, MBS can emerge in the topological phase of low dimensional structures, where the mutual interplay between magnetism, spin–orbit coupling, and superconductivity take place. The latter can be described in a convenient manner using Bogoliubov–de Gennes (BdG) approach. In this approach, the equations detailing behaviour of excitations of quasiparticles native to the superconductor and MBS are similar. In this chapter, we will shortly describe this technique.

2.1 Bogoliubov quasiparticles disguised as Majorana zero modes

In this section, we will show that self-conjugate zero energy states are a special version of Bogoliubov quasiparticles. Detailed calculations described in the generic model used for materials constituting this thesis, are presented in Ch. 3. Following that derivation, one arrives at the operators defined by the Bogoliubov–Valatin transformation (3.2) [1, 2], where $\gamma^\dagger$ and γ can be expressed as a linear combination of electrons and holes [3–6]:

$$\gamma_n^\dagger = \sum_i u_{n,\uparrow} c_{i\uparrow}^\dagger + u_{n,\downarrow} c_{i\downarrow}^\dagger - v_{n,\uparrow} c_{i\downarrow} + v_{n,\downarrow} c_{i\uparrow}, \tag{2.1}$$

$$\gamma_n = \sum_i u_{n,\uparrow}^* c_{i\uparrow} + u_{n,\downarrow}^* c_{i\downarrow} - v_{n,\uparrow}^* c_{i\downarrow}^\dagger + v_{n,\downarrow}^* c_{i\uparrow}^\dagger, \tag{2.2}$$

where $c_{i\sigma}$ ($c_{i\sigma}^\dagger$) is an operator describing annihilation (creation) of electron with spin σ on i–th site, while $u_{in\sigma}$ and $v_{in\sigma}$ are components of eigenvectors.

BdG Hamiltonian [e.g. (3.1)] obeys the particle–hole symmetry $\mathcal{P} = \mathcal{C}\mathcal{K}$ [7–9], which is an operator composed of charge conjugation $\mathcal{C}$ and complex conjugation $\mathcal{K}$ operators [10]. Diagonalization of the BdG Hamiltonian can yield a wave function in a form of $\Phi^{\dagger}_{in} = (u_{in\uparrow}, u_{in\downarrow}, v_{in\uparrow}, v_{in\downarrow})$, however it is not a unique choice. The only caveat is that in a different basis, the form of charge conjugation operator $\mathcal{C} = \tau^y \otimes \sigma^y$, would instead employ another combination of Pauli matrices spanning over particle–hole and spin sub–spaces. Particle hole symmetry affects the wave function as $\Phi_{in} = \mathcal{P}\Phi_{im} = \mathcal{C}\Phi^{\dagger}_{im}$ [11], linking two states of opposite energies, symmetrically w.r.t. to Fermi energy (i.e. "zero" energy). Wave function which is a result of the diagonalization of H_{BdG} has the following form, linking particle– and hole–like states in a forthright manner:

$$\Phi_{in} = \begin{pmatrix} u_{in\uparrow} \\ u_{in\downarrow} \\ v_{in\uparrow} \\ v_{in\downarrow} \end{pmatrix} = \mathcal{C}\mathcal{K}\Phi_{im} = \begin{pmatrix} 0 & 0 & 0 & -1 \\ 0 & 0 & 1 & 0 \\ 0 & 1 & 0 & 0 \\ -1 & 0 & 0 & 0 \end{pmatrix} \begin{pmatrix} u^*_{im\uparrow} \\ u^*_{im\downarrow} \\ v^*_{im\uparrow} \\ v^*_{im\downarrow} \end{pmatrix} = \begin{pmatrix} -v^*_{im\downarrow} \\ v^*_{im\uparrow} \\ u^*_{im\downarrow} \\ -u^*_{im\uparrow} \end{pmatrix}. \tag{2.3}$$

Therefore, the solutions of this Hamiltonian come in pairs. Another aspect important here is the fact that the creation of a positive energy particle (electron) is equal to the annihilation of a particle with negative energy (hole):

$$\gamma^{\dagger}_n(E) = \gamma_n(-E). \tag{2.4}$$

From this straightforward contemplation of symmetry within superconductors, one can catch a glimpse of Majorana physics within. In order to put this more clearly, we recall the inherent condition of Majorana objects – namely, its self–conjugation $\gamma^{\dagger}_n = \gamma_n$. However, for this to happen for the same states, they have to be degenerate at zero energy – in such a case these two states (i.e., n–th and m–th) are indistinguishable. Hence, we can set $n \equiv m \equiv 0$ as the energies for both particle and antiparticle in (2.4) have to be zero.

Again, substituting corresponding matrix (2.3) elements into (2.2), while keeping in mind the implied degeneracy, we arrive at:

$$\gamma^{\dagger}_0 = \sum_{i\sigma} u_{0,\sigma} c^{\dagger}_{i\sigma} - \sigma u^*_{0,\sigma} c_{i\bar{\sigma}}, \tag{2.5}$$

which is now clearly a self–adjoint operator that can describe MBS, leading to the existence of two degenerate states at zero energy. However, an ordinary superconductor does not allow for such gapless states – for this superconducting gap should close and

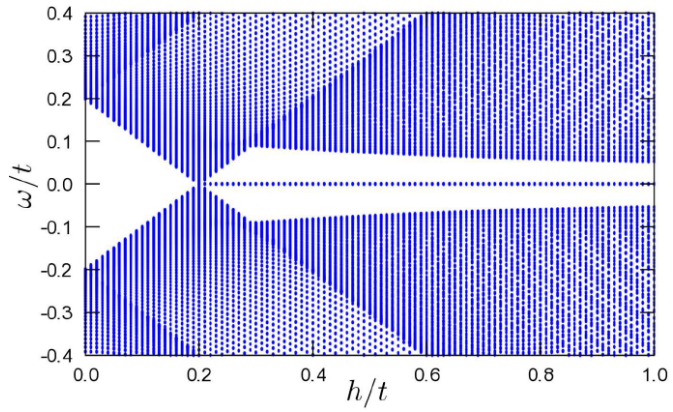

Figure 2.1: Eigenvalue plot showing a magnetic field induced topological transition from trivial to nontrivial phase in a nanowire deposited on a superconducting surface. Before the closing of the gap, we observe trivial superconducting gap. At critical magnetic field $h = 0.2t$, superconducting gap closes, just to reopen with further increase of magnetic field, as a new topological gap. After the transition, two in–gap ABS coalesce into degenerate, zero energy MBS. Even though gap size Δ is not a function of magnetic field h, its increase diminishes the topological gap size. Figure adapted from Ref. [12].

then reopen. Such a process is shown in the Fig. 2.1 and is described as a topological transition from trivial to nontrivial phase as the magnetic field h increases [12]. There one can see that the zero energy state forms from the ABS, coalescing after the reopening of gap. This and other Majorana related topological phenomena will be discussed in the next chapter.

Summarizing, MBS can be treated as a specific part of Bogoliubov–de Gennes formalism that are a result of particle–hole symmetry (also called redundancy in this case, due to the doubling of states [13–15]) inherent to superconductors and stem from the coalescence of two, opposite energy states. This special case allows for their existence, bringing to life a nearly 85 year old idea of Ettore Majorana for a particle which is its own antiparticle.

2.2 Majorana bound states

The cornerstone of Majorana operators' behaviour springs from its property of self–conjugation:

$$\gamma_a = \gamma_a^\dagger, \tag{2.6}$$

which equates a particle with its own antiparticle (this operator acts on the zero energy state, therefore we forgo the previous notation as subscript $n \equiv 0$ and instead, now a enumerates paired MBS). However, as the concept of occupied or unoccupied states is ill defined for Majorana operators, it should rather be considered as a fractionalized zero-mode constructed from a „half" of electron. This, in conjunction with the zero energy requirement from the previous section, leads to a situation where we can suspect that Majorana zero modes exist as two degenerate states, as both $|0\rangle$ and $|\gamma_a^\dagger 0\rangle$ are ground states in this situation [3]. In order to explain that, one can define ordinary spinless fermions in so–called *Majorana basis* [4, 16]

$$c = \frac{\gamma_a + i\gamma_b}{2}, \quad c^\dagger = \frac{\gamma_a - i\gamma_b}{2}. \tag{2.7}$$

Such a pair of MBS that constitutes a fermion is needed to give meaning to the creation and annihilation operators, as for two MBS those operators can be constructed and behave in well known manner [5]. This also forces Majoranas to come in pairs and their parity has severe implications for *braiding* purposes discussed in the following subsection. By inverting this, we can express Majorana operators as a combination of fermions:

$$\gamma_a = c + c^\dagger, \quad \gamma_b = i(c - c^\dagger). \tag{2.8}$$

Through a decomposition of a complex fermion into its real and imaginary parts, Majorana operators further differ themselves from fermions, because their anticommutation relation has an atypical form:

$$[\gamma_a, \gamma_b]_- = 2\delta_{ab}, \tag{2.9}$$

where δ_{ab} is Kronecker delta. Usually, in quantum computing, the information is stored as a state of particle: $|0\rangle, |1\rangle$. In an ingenious idea, Kitaev [17] proposed that MBS can fundamentally influence this due to Majorana nonlocality that sets $|1\rangle = (\gamma_a - i\gamma_b)/2|0\rangle$. Hence, an electron is highly delocalized into two separate MBS existing at the edge of the system, protecting the overall information stored within.

2.2.1 Emergence of Majorana bound states

Kitaev chain model [17] (as described in introduction), proposes a 1D spinless model of fermions, serving as a proof of principle for the emergence of MBS. However, as the publications composing the Ch. 4, do not refer to Kitaev model, we shall focus here on Rashba nanowire model [18–23], also known as Oreg–Lutchyn model.

Rashba nanowire model, proposed in order to achieve some experimental suitability for Majorana emergence, considers a *makeshift* topological superconductor built from several ingredients. These ingredients make up the real space Hamiltonian $\mathcal{H} = \mathcal{H}_0 + \mathcal{H}_{\text{so}} + \mathcal{H}_{\text{prox}}$, which can describe the systems with edges (i.e., without periodic boundary conditions). The first term describes the kinetic behaviour of electrons:

$$\mathcal{H}_{\text{kin}} = \sum_{ij\sigma} \left[-t + (\mu - \sigma h)\delta_{ij}\right] c^{\dagger}_{i\sigma} c_{j\sigma}. \tag{2.10}$$

The operators $c^{\dagger}_{i\sigma}$ ($c_{i\sigma}$) denote creation (annihilation) of the electron with spin σ in i-th site. t is the hopping integral between nearest neighbour sites, μ is the chemical potential and h denotes Zeeman energy induced by the magnetic field. The magnetic field has to be applied along the nanowire, as a sufficiently high deviation from this direction results in an inability of the system to produce nontrivial phase [24].

In the 2D case, Rashba spin orbit coupling term distorts the electron trajectory in the direction of its angular momentum producing spin Hall effect. Its impact can be envisioned by Berry curvature (described in detail in the following section), which plays a role of an effective magnetic field that adds perpendicular velocity to the electron motion. Curiously, this is similar to the Magnus force, where the angular momentum of the spinning ball affects its motion [25]. In 1D of a nanowire system, the spin orbit field is directed perpendicularly to the nanowire and magnetic field (in plane).

$$\mathcal{H}_{\text{so}} = -i \sum_{i\sigma\sigma'} \left[\lambda c^{\dagger}_{i\sigma} (\sigma_y)_{\sigma\sigma'} c_{i\sigma'} + \lambda c^{\dagger}_{i\sigma} (\sigma_y)_{\sigma\sigma'} c_{i-1\sigma'}\right] + \text{h.c.} \tag{2.11}$$

where σ_y is the second Pauli matrix and λ denotes the strength of the spin-orbit coupling.

Last term models the BCS-like superconducting gap, induced in the system due to the proximity effect (Cooper pairs can tunnel from the superconductor to a nanowire.), i.e., forming a tunnel contact by covering the nanowire with a thick superconducting layer or deposition of a nanowire on 2D or 3D superconductor [26]:

$$\mathcal{H}_{\text{prox}} = \sum_{i} \left(\Delta c^{\dagger}_{i\uparrow} c^{\dagger}_{i\downarrow} + \Delta^{*} c_{i\downarrow} c_{i\uparrow}\right). \tag{2.12}$$

In the momentum space (i.e. an infinite system), this Hamiltonian can be represented in matrix form:

$$H_k = \sum_{k} \Psi^{\dagger}_{k} \mathbb{H}(k) \Psi_k, \tag{2.13}$$

where:

$$\mathbb{H}(k) = \begin{pmatrix} \epsilon(k)+h & -iL(k) & \Delta & 0 \\ iL(k) & \epsilon(k)-h & 0 & -\Delta \\ \Delta & 0 & -\epsilon(k)+h & -iL(k) \\ 0 & -\Delta & iL(k) & -\epsilon(k)-h \end{pmatrix}. \tag{2.14}$$

Here, $\Psi_k^\dagger = (c_{k\uparrow}^\dagger, c_{k\downarrow}^\dagger, c_{-k\downarrow}, c_{-k\uparrow})$ is Nambu spinor, $\epsilon(k) = -\mu - 2t\cos(k)$ and $iL(k) = 2\lambda\sin(k)$. This Hamiltonian has the following energy spectrum:

$$E_{k\pm}^2 = \Delta^2 + \epsilon(k)^2 + L(k)^2 + h^2 \pm 2\sqrt{h^2\epsilon(k)^2 + \epsilon(k)^2 L(k)^2 + \Delta^2 h^2}, \tag{2.15}$$

where the difference in energy considering $\pm$ parts is related to the topological gap in the system. Transition to topological space occurs at Majorana condition (1.6) for time reversal invariant momenta (i.e., for a 1D nanowire its $\boldsymbol{k} = 0$ and π) [27–29].

Fig. 2.2 displays the potential of this model to envision the emergence of MBS at the ends of the nanowire. In this case, such a transition happens after the critical value of the magnetic field is surpassed, reopening the quasiparticle gap. Existence of MBS in the system has a few hallmark features sought after in experimental studies: peaks at both ends of the nanowire, reproduction of the theoretical topological phase diagram, and wave function oscillations. Separate peaks are a result of fermionic nonlocality and oscillations are a result of their wave function spatial overlap in finite-length wires. This effect strengthens with increasing magnetic field as the Zeeman energy periodically finetunes the wave function overlap [30–35].

On the first glance, such Hamiltonian should belong to a D class with $\mathbb{Z}_2$ topological invariant [which means it can have two distinct values: trivial (1) and nontrivial (-1)]. It supposedly breaks the time reversal $\mathcal{T}$ and chiral $\mathcal{S}$ symmetries with magnetic field, while upholding particle–hole symmetry $\mathcal{P}$ [37] due to BdG form of Hamiltonian. Operators describing symmetries of Hamiltonian have the following form in Nambu basis [38, 39]:

- The particle hole symmetry is described by antiunitary operator $\mathcal{P} = \tau_y \otimes \sigma_y \otimes \mathcal{K}$, that fulfils anticommutation relation $\mathcal{P}H(k)\mathcal{P}^{-1} = -H(-k)$ and $\mathcal{P}^2 = \mathbb{1}$. τ_i and σ_i are i-th Pauli matrix in particle hole and spin sub–spaces, respectively. $\mathcal{K}$ is the complex conjugation operator.

- The „time reversal" symmetry is described by antiunitary operator $\mathcal{T} = -i\tau_z \otimes \sigma_y\mathcal{K}$, that fulfils commutation relation $\mathcal{T}H(k)\mathcal{T}^{-1} = H(-k)$ and $\mathcal{T}^2 = \mathbb{1}$. Both

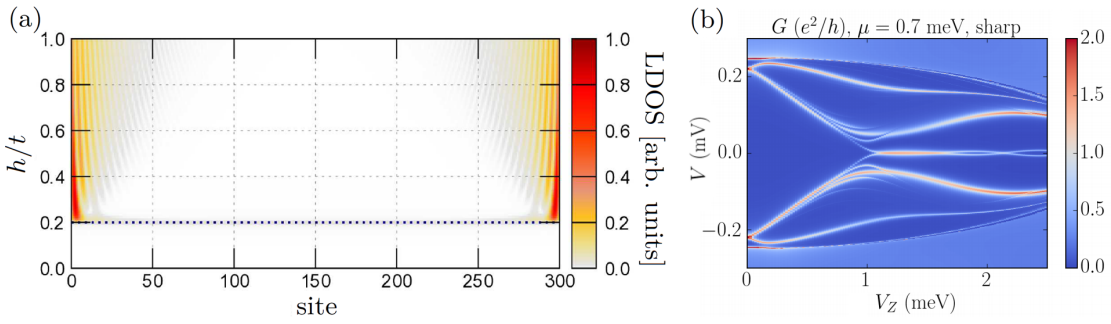

Figure 2.2: (a) Color map of local density of states of MBS as a function of magnetic field h. After a transition to nontrivial state (dotted line) MBS emerge at the ends of nanowire. (b) Emergence of MBS due to the transition to nontrivial state localized at zero energy, visualised by conductance spectrum. Both panels show that with further increase in magnetic field (h/t and V_z respectively), after the topological transition, spatial and energetic Majorana oscillations are revealed. Figures adapted from Refs. [12] and [36].

particle hole and time reversal symmetries have two possible forms of operators that square to -1 or $+1$ due to their antiunitarity [38]. Negative values of those operators lead to CII class and positive values to BDI class. It turns out that in the case of the Rashba Hamiltonian, operators which fulfil both conditions of (anti)commuting and squaring to the positive identity matrix exist. Thus, Rashba Hamiltonian is in fact BDI class. In this class, value of $\mathbb{Z}$ topological invariant corresponds to the winding number that evaluates the number of MBS at the ends of the nanowire [40], and in contrast to D class, both time reversal and chiral symmetries are no longer violated.

- The chiral symmetry is constructed from the previous two, thus it is described by the unitary operator $\mathbb{S} = \mathcal{PT} = \tau_x \otimes \sigma_0$, that fulfils anticommutation relation $\mathcal{S}H(k)\mathcal{S}^{-1} = -H(k)$ and $\mathcal{S}^2 = \mathbb{1}$. σ_0 is identity matrix in spin sub–space. Effect of the mentioned symmetries on the band structure of Hamiltonian is presented on Fig. 2.3.

It is important to point out that in the case where a typical Rashba nanowire model is modified with some sublattice order (Su-Schrieffer-Heeger dimerization or antiferromagnetism, as in Ch. 4) it still remains a member of BDI class with $\mathbb{Z}$ topological invariant.

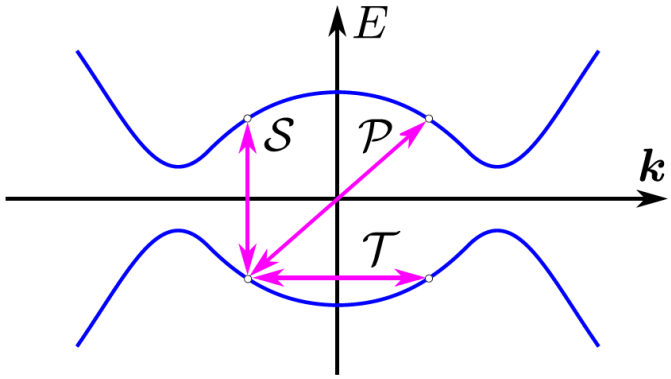

Figure 2.3: Time–reversal symmetry $\mathcal{T}$ relates points in bands of opposite momentum, particle–hole symmetry $\mathcal{P}$ results in the symmetry of the spectrum w.r.p. to the origin point and chiral $\mathcal{S}$ symmetry corresponds to reflection of the bands across the energy axis. Figures adapted from Ref. [41].

2.2.2 Nonlocality of Majorana bound states

Another important property of Majoranas discussed in this thesis is their *nonlocality*. It is inherited from a fermionic state that delocalizes, forming MBS at the edges of the system and can be imagined as the entanglement of those electron parts resulting in degenerate zero energy modes. Therefore, MBS have only half of the regular electron's fermionic degree of freedom. This allows for nontrivial phenomena like teleportation, entanglement, and unique transport signatures [42–45]. Even though a plethora of experimental data suggests the emergence of Majorana zero modes, there is still not enough evidence for an experimental measure of Majorana nonlocality. On the theory side, such phenomena usually require a form of Kitaev model with an additional ϵ_m term, representing the energy equivalent of MBS wave function overlap or their mutual interaction [44–49]. Still, Rashba model also allows for probing of similar phenomena, e.g. registering the change of one MBS while changing the confining potential near the other [50]. As this phenomenon lies in the center of the most important Majorana application – braiding, it is important to point out that there are also aspects of this that might prove detrimental to nanodevices employing MBS. An example of such is Majorana delocalisation, or leakage, which allows MBS to reside in the topologically trivial regions of the studied devices. In real space braiding, any possible inconsistencies in the translation of MBS due to the leakage, might diminish the favourable outcome of quantum computation. These destructive features of Majorana nonlocality are investigated in Ch. 4.

2.3 Nontrivial topology in condensed matter physics

Usually, in order to show that something possesses some properties, we need an indicator of it. In the case of topology, especially in topological superconductors (TSCs), these indicators are called topological invariants. Topological invariants are numbers representing the nontrivial structure of occupied bands in Brillouin zone, which remain constant under smooth deformation (adiabatic evolution) of Hamiltonian. In mathematics, this is exemplified in a popular way by the genus – a number of holes in a surface: a sphere has genus 0, while a donut or a mug have genus 1, etc. Regardless of any transformation that stretches and twists those surfaces, its genus cannot be changed, except for *puncturing* or fusing the surface [51]. Such topological invariants would take various forms due to the symmetries obeyed by the system and its symmetries. In condensed matter physics, values like Chern number, related to conductance in Hall systems, behave in a similar way – until the system transits to another topological phase, in which mathematical *puncturing* occurs when the gap closes, its value is constant during the adiabatic varying of system parameters. This closing is usually an effect of an *unnatural* alliance between Zeeman energy and superconducting gap, which is described by relation (1.6), that marks the transition to nontrivial phase [4, 20, 52]. TSCs possess an odd parity pairing state called *p–wave* or spin triplet. This relates to an odd number of time reversal invariant momenta (TRIM) in the Brillouin zone [5, 13, 53]. A schematic example of low dimensional TSC can be seen in Fig. 2.4. Here, we can observe schematic pictures of edge states for 1D (a) and 2D (d) topological superconductors. Topological transition from trivial to nontrivial state shows the change between (b) and (c), where ABS [visualised by $\Gamma(E)$] are coalescing into the zero energy modes that can be interpreted as Majorana states. In the 2D case, a vortex can form over a flux of magnetic field ϕ allowing for one Majorana state to pin this vortex and the other, envisioned by a metallic state connecting (usually inverted) bands, representing an edge state of 2D topological superconductor [54].

Various types of topological systems were discussed thoroughly in a seminal work by Altland and Zirnbauer [55], where they proposed a part of *periodic table of topological invariants*. There, they describe various topological phases which can arise in condensed matter physics, some of which are related to Majorana research. Typical Hamiltonian H_{BdG} belongs to the class D, due to the existence of particle–hole symmetry within.

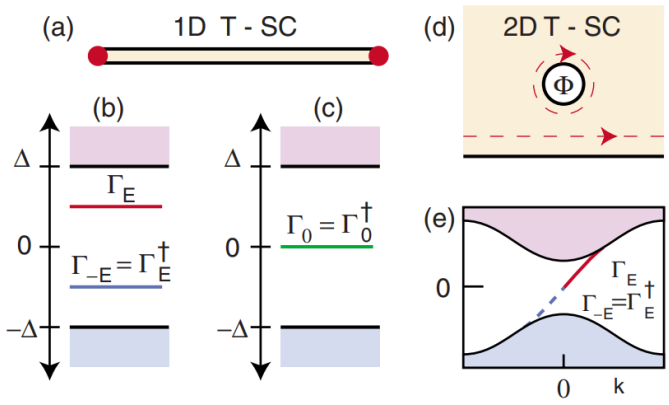

Figure 2.4: Schematic picture of edge states emerging in 1D and 2D topological superconductor (TSC). (a) 1D system hosting bound states at the edges of nanowire. (b) Energy spectrum for edge states for topologically trivial superconductor. (c) Energy spectrum for edge states for topologically nontrivial superconductor – two degenerate zero modes correspond to vortex with flux $\phi = h/2e$ or MBS. (d) Topological 2D superconductor with Majorana zero modes: pinned to vortex and propagating along the edge. (e) Energy spectrum for a chiral Majorana edge mode propagating along the edge of 2D superconductor. Figures adapted from Ref. [13].

This class has a $\mathbb{Z}_2$ topological invariant, which means that the system can have only two values – either a trivial or nontrivial topology. States of opposite energy paired in the spectrum enable us to define a topological number for a given system, such as the geometrical Berry phase [5, 56–58]. In order to probe topological phenomena, a momentum space picture is often beneficial. To start, we first define Berry connection $\mathcal{A}^n(k)$ for our Hamiltonian $H_{BdG}(k)|u_n(k)\rangle = E_n(k)|u_n(k)\rangle$:

$$\mathcal{A}_n(k) = \langle u_n(k)|i\partial_k|u_n(k)\rangle. \tag{2.16}$$

It describes the changes in the wave function as k varies within a Brillouin zone. Solutions of this Hamiltonian can undergo a gauge transformation $|u_n(k)\rangle \to e^{i\theta_n(k)}|u_n(k)\rangle$ which directly affects Berry connection as

$$\mathcal{A}_n(k) - \partial_k\theta_n(k). \tag{2.17}$$

Taking an integral over some closed path O in Brillouin zone gives us Berry phase:

$$\gamma_B = \oint_O \mathcal{A}_n(k)dk \tag{2.18}$$

This scheme yields results of $\gamma_B = n\pi$ for $n \in \mathbb{Z}$. As the phase factor of this gauge-invariant object is 2π periodic, multiples of π define possible values of $\mathbb{Z}$ topological

invariant. Berry phase in 1D is usually called Zak Phase [59]. Additionally, we can employ Berry connection in analogy to electromagnetism and construct a Berry curvature:

$$\mathcal{F}_n(k) = rot[\mathcal{A}_n(k)]. \tag{2.19}$$

This mathematical object relates to the Chern number (called also TKNN[1] invariant) which is a topological invariant for 2D systems. In an infinite and periodic system, one can only experience bulk of the system and all of the exciting topological phenomena happen at the edges and defects of the system. *Bulk-boundary correspondence* aids in remedying that as it relates bulk topology to gapless boundary or defect states. In the case of defects, a nontrivial winding of the bulk topological parameters around the defect gives us information about the phase of the system. A good example of these phenomena is a relation in quantum Hall systems, where Hall conductance is given by Chern number obtained above. On the other hand, if there exists an edge in a system, Hall conductance is described by the number of edge bands propagating along the boundary. Relation constituting the *bulk-boundary correspondence* [62–64] follows from the fact that both of those values need to be precisely the same, and thus forming a *correspondence* between bulk topological invariants and gapless boundary states.

2.3.1 Non–Abelian anyons

The main perspective of MBS in technology, as stated in the introductory part of a seemingly infinite (but still countable!) number of journal articles, is the construction of a topological quantum computer. Its main advantage over regular quantum computers would be its robustness, a resistance to qubit decoherence blurring quantum information with time. At the heart of this concept lies the non–Abelian statistics that lies between Fermi and Bose statistics. In the usual quantum statistical approach, the change in the wave function due to the exchange of particles adds to it an additional phase. As this phase is related to the $U(1)$ symmetry, the order of this exchange does affect the outcome in any way. However, in the case of Majoranas, their non–Abelian behaviour of the degenerate many-body ground state results in a particular change of wave function that is decided by the order of quasiparticle manipulations – *braiding* [56, 65].

[1]Named after authors of paper [60] – Thouless, Kohomoto, Nightingale, and den Nijs investigating quantized Hall conductance in 2D systems. The amount of quanta of conductance measured for edge states corresponds to the Chern number for given system [61].

In the case of braiding, the main properties of MBS are: *(i)* ground state degeneracy due to the lack of energy requirement for creation and annihilation of MBS , and *(ii)* highly nonlocalized entanglement, allowing for robustness of MBS due to the inability to lift the degeneracy by interfering with a single MBS [66–68]. If the manipulation is done adiabatically, for Abelian anyons, the wave function would obtain some phase $e^{i\theta}$ but in case of non–Abelian anyons additional phase is represented by unitary operator U_{ab}. This exchange (or mutual rotation of superconducting vortices) can be envisioned as some integer s_a:

$$s_a\gamma_a = U_{ab}\gamma_b U_{ab}^{\dagger}, \tag{2.20}$$

where a and b are numbered MBS that are exchanged with each other.

Due to the fact that $\gamma_a^{\dagger}\gamma_a = \gamma_a\gamma_a = 1$, $(s_a\gamma_a)^2 = 1$ and thus $s_a^2 = 1 \vee -1$. If we take a look at the number operator $n = c^{\dagger}c$, in Majorana representation it takes a form of $n = (\gamma_a^2 + i\gamma_a\gamma_b - i\gamma_b\gamma_a + \gamma_b^2)/4$. By employing the properties of Majorana operator, we finally obtain:

$$n = (1 + i\gamma_a\gamma_b)/2. \tag{2.21}$$

Our U_{ab}, called also as *generator of the braid group* takes the form of [69, 70]:

$$\begin{aligned} U_{ab} &= exp[-\frac{\pi}{4}\gamma_a\gamma_b] = exp[i\frac{\pi}{4}(2c^{\dagger}c - 1)] && (2.22)\\ &= exp[i\frac{\pi}{4}\sigma_z] = \frac{1}{\sqrt{2}}(1 - \gamma_a\gamma_b). && (2.23) \end{aligned}$$

It is worth noting here that U_{ab} is noncommutative, which is a hallmark of anyonic nature of Majorana operators:

$$[U_{ab}U_{bc}]_{-} = -\gamma_a\gamma_c. \tag{2.24}$$

Now, if we wrap the number operator with our U_{ab}, we exchange both Majoranas – not with respect to each other, but rather with respect to some point in space [65]. Such an operation would not generate any phase or nontrivial objects:

$$\begin{aligned} U_{ab}nU_{ab}^{\dagger} &= \frac{1}{2}\left(1 + iU_{ab}\gamma_a\gamma_b U_{ab}^{\dagger}\right), && (2.25)\\ &= \frac{1}{2}\left(1 + iU_{ab}\gamma_a U_{ab}U_{ab}^{\dagger}\gamma_b U_{ab}^{\dagger}\right),\\ &= \frac{1}{2}\left(1 + is_b\gamma_b s_a\gamma_a\right),\\ &= \frac{1}{2}\left(1 - is_a s_b\gamma_a\gamma_b\right). \end{aligned}$$

In order for the previous remark to be true, we need $s_a s_b = -1$. Hence, $s_{a(b)}$ have to have opposite values of 1. Choosing which $s_{a(b)}$ has which value is arbitrary, but nonetheless this leads to a crucial result enabling braiding of MBS:

$$U_{ab}\gamma_a U_{ab}^\dagger = \gamma_b, \tag{2.26}$$

$$U_{ab}\gamma_b U_{ab}^\dagger = -\gamma_a. \tag{2.27}$$

showing that the exchange of MBS has various results depending on the order of actions taken. Additionally, one can see that performing the braiding operation twice leads to the situation where MBS transforms as $\gamma_a \to -\gamma_a$, showing similarity to the phase gained due to Aharonov-Bohm effect in the case of one vortex pinned with MZM rotating arount another one [69, 71]. Concluding, if one imagines a system where $2N$ MBS exists, there exists a degeneracy of 2^N states at zero energy.

Additionally, one can define the fermion parity operator $P_j = 1 - 2c_j^\dagger c_j = i\gamma_{ja}\gamma_{jb}$ which reminds one that all Majorana operators anticommute with each other, regardless of the fermion from which those originate. However, if two pairs share one of the Majorana operators, they cease to anticommute.

We can obtain the total fermion parity by multiplying all of the P_j operators:

$$P_{tot} = \prod_j^n P_j = i^n \prod_j^n \gamma_{ja}\gamma_{jb} = \pm 1, \tag{2.28}$$

informing us about the total number of occupied fermionic modes being even $(+1)$ or odd (-1), for n MBS pairs (e.g. multi nanowire junction), which is the topologically protected quantity [72–74] that overall reduces ground state degeneracy by factor of 2.

Bibliography

[1] P. G. D. Gennes. *Superconductivity Of Metals And Alloys (Advanced Books Classics)*. Westview Press, (1999) ISBN: 0738201014.

[2] J.-X. Zhu. *Bogoliubov-de gennes method and its applications*. Springer, (2016)

[3] S. R. Elliott and M. Franz, *Colloquium: Majorana fermions in nuclear, particle, and solid-state physics*, Rev. Mod. Phys. **87**, 137 (2015) DOI: 10.1103/RevModPhys.87.137

[4] R. Aguado, *Majorana quasiparticles in condensed matter*, Riv. del Nuovo Cim. **40**, 523 (2017).

[5] M. Sato and Y. Ando, *Topological superconductors: a review*, Reports on Progress in Physics **80**, 076501 (2017) DOI: 10.1088/1361-6633/aa6ac7

[6] M. R. Zirnbauer, *Particle–hole symmetries in condensed matter*, Journal of Mathematical Physics **62**, 021101 (2021) DOI: 10.1063/5.0035358

[7] L. Fu and C. L. Kane, *Probing Neutral Majorana Fermion Edge Modes with Charge Transport*, Phys. Rev. Lett. **102**, 216403 (2009) DOI: 10.1103/PhysRevLett.102.216403

[8] T. Mizushima and M. Sato, *Topological phases of quasi-one-dimensional fermionic atoms with a synthetic gauge field*, New J. Phys. **15**, 075010 (2013) DOI: 10.1088/1367-2630/15/7/075010

[9] Y. Ueno, A. Yamakage, Y. Tanaka, and M. Sato, *Symmetry-Protected Majorana Fermions in Topological Crystalline Superconductors: Theory and Application to* Sr_2RuO_4, Phys. Rev. Lett. **111**, 087002 (2013) DOI: 10.1103/PhysRevLett.111.087002

[10] C.-K. Chiu, J. C. Y. Teo, A. P. Schnyder, and S. Ryu, *Classification of topological quantum matter with symmetries*, Rev. Mod. Phys. **88**, 035005 (2016) DOI: 10.1103/RevModPhys.88.035005

[11] C. Chamon, R. Jackiw, Y. Nishida, S.-Y. Pi, and L. Santos, *Quantizing Majorana fermions in a superconductor*, Phys. Rev. B **81**, 224515 (2010) DOI: 10.1103/PhysRevB.81.224515

[12] A. Kobiałka and A. Ptok, *Leakage of the Majorana Quasiparticles in Rashba Nanowire Deposited on Superconducting–Normal Substrate*, Acta Phys. Pol. A **135**, 64 (2019) DOI: 10.12693/aphyspola.135.64

[13] M. Z. Hasan and C. L. Kane, *Colloquium: Topological insulators*, Rev. Mod. Phys. **82**, 3045 (2010) DOI: 10.1103/RevModPhys.82.3045

[14] B. A. Bernevig and T. L. Hughes. *Topological insulators and topological superconductors*. Princeton University Press, (2013)

[15] L. Fu and C. L. Kane, *Josephson current and noise at a superconductor/quantum-spin-Hall-insulator/superconductor junction*, Phys. Rev. B **79**, 161408 (2009) DOI: 10.1103/PhysRevB.79.161408

[16] C. Beenakker, *Search for Majorana Fermions in Superconductors*, Annu. Rev. Condens. Matter Phys **4**, 113 (2013) DOI: 10.1146/annurev-conmatphys-030212-184337

[17] A. Y. Kitaev, *Unpaired Majorana fermions in quantum wires*, Phys.-Usp. **44**, 131 (2001) DOI: 10.1070/1063-7869/44/10s/s29

[18] L. Fu and C. L. Kane, *Superconducting Proximity Effect and Majorana Fermions at the Surface of a Topological Insulator*, Phys. Rev. Lett. **100**, 096407 (2008) DOI: 10.1103/PhysRevLett.100.096407

[19] J. D. Sau, R. M. Lutchyn, S. Tewari, and S. Das Sarma, *Generic New Platform for Topological Quantum Computation Using Semiconductor Heterostructures*, Phys. Rev. Lett. **104**, 040502 (2010) DOI: 10.1103/PhysRevLett.104.040502

[20] R. M. Lutchyn, J. D. Sau, and S. Das Sarma, *Majorana Fermions and a Topological Phase Transition in Semiconductor-Superconductor Heterostructures*, Phys. Rev. Lett. **105**, 077001 (2010) DOI: 10.1103/PhysRevLett.105.077001

[21] Y. Oreg, G. Refael, and F. von Oppen, *Helical Liquids and Majorana Bound States in Quantum Wires*, Phys. Rev. Lett. **105**, 177002 (2010) DOI: 10.1103/PhysRevLett.105.177002

[22] J. D. Sau, S. Tewari, R. M. Lutchyn, T. D. Stanescu, and S. Das Sarma, *Non-Abelian quantum order in spin-orbit-coupled semiconductors: Search for topological Majorana particles in solid-state systems*, Phys. Rev. B **82**, 214509 (2010) DOI: 10.1103/PhysRevB.82.214509

[23] S. Gangadharaiah, B. Braunecker, P. Simon, and D. Loss, *Majorana Edge States in Interacting One-Dimensional Systems*, Phys. Rev. Lett. **107**, 036801 (2011) DOI: 10.1103/PhysRevLett.107.036801

[24] B. Kiczek and A. Ptok, *Influence of the orbital effects on the Majorana quasiparticles in a nanowire*, Journal of Physics: Condensed Matter **29**, 495301 (2017) DOI: 10.1088/1361-648x/aa93ab

[25] A. Manchon, H. C. Koo, J. Nitta, S. M. Frolov, and R. A. Duine, *New perspectives for Rashba spin–orbit coupling*, Nat. Mater. **14**, 871 (2015) DOI: 10.1038/nmat4360

[26] W. Chang, S. M. Albrecht, T. S. Jespersen, F. Kuemmeth, P. Krogstrup, J. Nygård, and C. M. Marcus, *Hard gap in epitaxial semiconductor–superconductor nanowires*, Nature Nanotech. **10**, 232 (2015) DOI: 10.1038/nnano.2014.306

[27] J. E. Moore and L. Balents, *Topological invariants of time-reversal-invariant band structures*, Phys. Rev. B **75**, 121306 (2007) DOI: 10.1103/PhysRevB.75.121306

[28] F. Zhang, C. L. Kane, and E. J. Mele, *Time-Reversal-Invariant Topological Superconductivity and Majorana Kramers Pairs*, Phys. Rev. Lett. **111**, 056402 (2013) DOI: 10.1103/PhysRevLett.111.056402

[29] C. Dutreix, *Topological spin-singlet superconductors with underlying sublattice structure*, Phys. Rev. B **96**, 045416 (2017) DOI: 10.1103/PhysRevB.96.045416

[30] A. D. K. Finck, D. J. Van Harlingen, P. K. Mohseni, K. Jung, and X. Li, *Anomalous Modulation of a Zero-Bias Peak in a Hybrid Nanowire-Superconductor Device*, Phys. Rev. Lett. **110**, 126406 (2013) DOI: 10.1103/PhysRevLett.110.126406

[31] H. O. H. Churchill, V. Fatemi, K. Grove-Rasmussen, M. T. Deng, P. Caroff, H. Q. Xu, and C. M. Marcus, *Superconductor-nanowire devices from tunneling to the multichannel regime: Zero-bias oscillations and magnetoconductance crossover*, Phys. Rev. B **87**, 241401 (2013) DOI: 10.1103/PhysRevB.87.241401

[32] D. Rainis, L. Trifunovic, J. Klinovaja, and D. Loss, *Towards a realistic transport modeling in a superconducting nanowire with Majorana fermions*, Phys. Rev. B **87**, 024515 (2013) DOI: 10.1103/PhysRevB.87.024515

[33] G. Ben-Shach, A. Haim, I. Appelbaum, Y. Oreg, A. Yacoby, and B. I. Halperin, *Detecting Majorana modes in one-dimensional wires by charge sensing*, Phys. Rev. B **91**, 045403 (2015) DOI: 10.1103/PhysRevB.91.045403

[34] F. Peñaranda, R. Aguado, P. San-Jose, and E. Prada, *Quantifying wave-function overlaps in inhomogeneous Majorana nanowires*, Phys. Rev. B **98**, 235406 (2018) DOI: 10.1103/PhysRevB.98.235406

[35] S. D. Escribano, A. L. Yeyati, and E. Prada, *Interaction-induced zero-energy pinning and quantum dot formation in Majorana nanowires*, Beilstein J. Nanotechnol. **9**, 2171 (2018) DOI: 10.3762/bjnano.9.203

[36] C.-X. Liu, J. D. Sau, and S. Das Sarma, *Distinguishing topological Majorana bound states from trivial Andreev bound states: Proposed tests through differential tunneling conductance spectroscopy*, Phys. Rev. B **97**, 214502 (2018) DOI: 10.1103/PhysRevB.97.214502

[37] P. Kotetes, *Classification of engineered topological superconductors*, New J. Phys. **15**, 105027 (2013) DOI: 10.1088/1367-2630/15/10/105027

[38] S. Ryu, A. P. Schnyder, A. Furusaki, and A. W. W. Ludwig, *Topological insulators and superconductors: tenfold way and dimensional hierarchy*, New J. Phys. **12**, 065010 (2010) DOI: 10.1088/1367-2630/12/6/065010

[39] A. W. W. Ludwig, *Topological phases: classification of topological insulators and superconductors of non-interacting fermions, and beyond*, Phys Scr. **T168**, 014001 (2015) DOI: 10.1088/0031-8949/2015/t168/014001

[40] S. Tewari and J. D. Sau, *Topological Invariants for Spin-Orbit Coupled Superconductor Nanowires*, Phys. Rev. Lett. **109**, 150408 (2012) DOI: 10.1103/PhysRevLett.109.150408

[41] A. Kobiałka, N. Sedlmayr, and A. Ptok, *Majorana bound states in a superconducting Rashba nanowire in the presence of antiferromagnetic order*, Phys. Rev. B **103**, 125110 (2021) DOI: 10.1103/PhysRevB.103.125110

[42] A. M. Turner, F. Pollmann, and E. Berg, *Topological phases of one-dimensional fermions: An entanglement point of view*, Phys. Rev. B **83**, 075102 (2011) DOI: 10.1103/PhysRevB.83.075102

[43] B. Béri and N. R. Cooper, *Topological Kondo Effect with Majorana Fermions*, Phys. Rev. Lett. **109**, 156803 (2012) DOI: 10.1103/PhysRevLett.109.156803

[44] X.-Q. Li and L. Xu, *Nonlocality of Majorana zero modes and teleportation: Self-consistent treatment based on the Bogoliubov–de Gennes equation*, Phys. Rev. B **101**, 205401 (2020) DOI: 10.1103/PhysRevB.101.205401

[45] L. Fu, *Electron Teleportation via Majorana Bound States in a Mesoscopic Superconductor*, Phys. Rev. Lett. **104**, 056402 (2010) DOI: 10.1103/PhysRevLett.104.056402

[46] C. Nayak, S. H. Simon, A. Stern, M. Freedman, and S. Das Sarma, *Non-Abelian anyons and topological quantum computation*, Rev. Mod. Phys. **80**, 1083 (2008) DOI: 10.1103/RevModPhys.80.1083

[47] J. Li, T. Yu, H.-Q. Lin, and J. Q. You, *Probing the non-locality of Majorana fermions via quantum correlations*, Sci. Rep. **4**, 4930 (2014) DOI: 10.1038/srep04930

[48] M.-T. Deng, S. Vaitiek ėnas, E. Prada, P. San-Jose, J. Nygård, P. Krogstrup, R. Aguado, and C. M. Marcus, *Nonlocality of Majorana modes in hybrid nanowires*, Phys. Rev. B **98**, 085125 (2018) DOI: 10.1103/PhysRevB.98.085125

[49] A. Soori, *Transconductance as a probe of nonlocality of Majorana fermions*, Journal of Physics: Condensed Matter **31**, 505301 (2019) DOI: 10.1088/1361-648x/ab3f73

[50] T. D. Stanescu and S. Tewari, *Nonlocality of zero-bias anomalies in the topologically trivial phase of Majorana wires*, Phys. Rev. B **89**, 220507 (2014) DOI: 10.1103/PhysRevB.89.220507

[51] X.-L. Qi and S.-C. Zhang, *Topological insulators and superconductors*, Rev. Mod. Phys. **83**, 1057 (2011) DOI: 10.1103/RevModPhys.83.1057

[52] M. M. Maśka, A. Gorczyca-Goraj, J. Tworzydło, and T. Domański, *Majorana quasiparticles of an inhomogeneous Rashba chain*, Phys. Rev. B **95**, 045429 (2017) DOI: 10.1103/PhysRevB.95.045429

[53] N. P. Armitage, E. J. Mele, and A. Vishwanath, *Weyl and Dirac semimetals in three-dimensional solids*, Rev. Mod. Phys. **90**, 015001 (2018) DOI: 10.1103/RevModPhys.90.015001

[54] A. L. Rakhmanov, A. V. Rozhkov, and F. Nori, *Majorana fermions in pinned vortices*, Phys. Rev. B **84**, 075141 (2011) DOI: 10.1103/PhysRevB.84.075141

[55] A. Altland and M. R. Zirnbauer, *Nonstandard symmetry classes in mesoscopic normal-superconducting hybrid structures*, Phys. Rev. B **55**, 1142 (1997) DOI: 10.1103/PhysRevB.55.1142

[56] M. Sato and S. Fujimoto, *Majorana Fermions and Topology in Superconductors*, Journal of the Physical Society of Japan **85**, 072001 (2016) DOI: 10.7566/JPSJ.85.072001

[57] L. Li, C. Yang, and S. Chen, *Topological invariants for phase transition points of one-dimensional Z2 topological systems*, Eur. Phys. J. B **89**, (2016) DOI: 10.1140/epjb/e2016-70325-x

[58] M. Trif and P. Simon, *Braiding of Majorana Fermions in a Cavity*, Phys. Rev. Lett. **122**, 236803 (2019) DOI: 10.1103/PhysRevLett.122.236803

[59] J. Zak, *Berry's phase for energy bands in solids*, Phys. Rev. Lett. **62**, 2747 (1989) DOI: 10.1103/PhysRevLett.62.2747

[60] D. J. Thouless, M. Kohmoto, M. P. Nightingale, and M. den Nijs, *Quantized Hall Conductance in a Two-Dimensional Periodic Potential*, Phys. Rev. Lett. **49**, 405 (1982) DOI: 10.1103/PhysRevLett.49.405

[61] Y.-F. Zhao *et al.*, *Tuning the Chern number in quantum anomalous Hall insulators*, Nature **588**, 419 (2020) DOI: 10.1038/s41586-020-3020-3

[62] R. S. K. Mong and V. Shivamoggi, *Edge states and the bulk-boundary correspondence in Dirac Hamiltonians*, Phys. Rev. B **83**, 125109 (2011) DOI: 10.1103/PhysRevB.83.125109

[63] T. Fukui, K. Shiozaki, T. Fujiwara, and S. Fujimoto, *Bulk-Edge Correspondence for Chern Topological Phases: A Viewpoint from a Generalized Index Theorem*, J. Phys. Soc. Jpn. **81**, 114602 (2012) DOI: 10.1143/jpsj.81.114602

[64] N. Sedlmayr, V. Kaladzhyan, C. Dutreix, and C. Bena, *Bulk boundary correspondence and the existence of Majorana bound states on the edges of 2D topological superconductors*, Phys. Rev. B **96**, 184516 (2017) DOI: 10.1103/PhysRevB.96.184516

[65] S. D. Sarma, M. Freedman, and C. Nayak, *Majorana zero modes and topological quantum computation*, npj Quantum. Inf. **1**, 15001 (2015) DOI: 10.1038/npjqi.2015.1

[66] J. D. Sau, R. M. Lutchyn, S. Tewari, and S. Das Sarma, *Robustness of Majorana fermions in proximity-induced superconductors*, Phys. Rev. B **82**, 094522 (2010) DOI: 10.1103/PhysRevB.82.094522

[67] J. Alicea, *New directions in the pursuit of Majorana fermions in solid state systems*, Rep. Prog. Phys. **75**, 076501 (2012) DOI: 10.1088/0034-4885/75/7/076501

[68] D. Aasen *et al.*, *Milestones Toward Majorana-Based Quantum Computing*, Phys. Rev. X **6**, 031016 (2016) DOI: 10.1103/PhysRevX.6.031016

[69] D. A. Ivanov, *Non-Abelian Statistics of Half-Quantum Vortices in p-Wave Superconductors*, Phys. Rev. Lett. **86**, 268 (2001) DOI: 10.1103/PhysRevLett.86.268

[70] K. Flensberg, F. von Oppen, and A. Stern. *Engineered platforms for topological superconductivity and Majorana zero modes.* (2021) eprint: arXiv:2103.05548.

[71] X. Ma, C. J. O. Reichhardt, and C. Reichhardt, *Braiding Majorana fermions and creating quantum logic gates with vortices on a periodic pinning structure*, Phys. Rev. B **101**, 024514 (2020) DOI: 10.1103/PhysRevB.101.024514

[72] A. R. Akhmerov, *Topological quantum computation away from the ground state using Majorana fermions*, Phys. Rev. B **82**, 020509 (2010) DOI: 10.1103/PhysRevB.82.020509

[73] T. E. O'Brien, P. Rożek, and A. R. Akhmerov, *Majorana-Based Fermionic Quantum Computation*, Phys. Rev. Lett. **120**, 220504 (2018) DOI: 10.1103/PhysRevLett.120.220504

[74] A. A. M. Irfan, K. Mayer, G. Ortiz, and E. Knill, *Certified quantum measurement of Majorana fermions*, Phys. Rev. A **101**, 032106 (2020) DOI: 10.1103/PhysRevA.101.032106

CHAPTER 3

Theoretical and numerical approach

3.1 Bogoliubov–de Gennes equations

Bogoliubov–de Gennes (BdG) equations have a wide range of applications in the study of the Majorana states. Since its advent, notable examples of the employment of BdG techniques are vortices [1, 2], disordered systems [3–5], non-homogeneous systems [6, 7], quasiparticles native to superconducting state [8–10] and more. Recently, BdG approach was employed in the search for Majorana bound states systems varying in both dimensionality and assembly [11–14], hybrid structures of mixed dimensionality [15, 16], or hybrid structures composed of topological insulator and a superconductor [17, 18]. Additionally, in the framework of tight binding models, its relative simplicity combined with applicability in a vast range of scenarios serves as a great theoretical tool. Moreover, the theoretical calculations are comparable with experimentally obtained results, e.g. via scanning tunnelling microscopy (STM), which allows for reproducing existing and proposing new ideas in condensed matter physics.

Stemming from that below, we will derive the BdG equations in a tight binding setting in an approach similar to that presented in Ref. [19]. The common core of Hamiltonians used in the papers making up this thesis has the following form:

$$\begin{aligned} \mathcal{H} &= \sum_{ij,\sigma} \left[-t_{ij} - (\mu + \sigma h)\,\delta_{ij}\right] c^{\dagger}_{i\sigma} c_{j\sigma} \\ &- \imath\lambda \sum_{\langle ij\rangle,\sigma\sigma'} c^{\dagger}_{i\sigma} \sigma^{y}_{\sigma\sigma'} c_{j\sigma'} + \text{H.c.} \\ &+ \sum_{i} \left(\Delta c^{\dagger}_{i\uparrow} c^{\dagger}_{i\downarrow} + \Delta^{*} c_{i\downarrow} c_{i\uparrow}\right), \end{aligned} \tag{3.1}$$

where t_{ij} is a hopping integral between i–th and j–th site, μ is chemical potential, h is

Zeeman magnetic field. Here, we typically investigate the hopping of electrons between the nearest neighbouring (NN) sites. λ is the strength of Rashba spin orbit coupling, σ_i is i–th Pauli matrix. In practice, this term corresponds to the spin-flip hopping between NN sites. Finally, in the last term concerning the superconducting proximity effect, $\Delta = U\langle c_{i\downarrow}c_{i\uparrow}\rangle$ is order parameter with is pairing potential $U < 0$. To avoid a confusion between site i and imaginary unit, we set the latter to $\imath$.

Bogoliubov–Valatin canonical transformation shows a way to present creation and annihilation operators as a linear function of electron- and hole-like objects. It has the following form:

$$c_{i\sigma} = \sum_n \left(u_{in\sigma}\gamma_{n\sigma} - \sigma v^*_{in\sigma}\gamma^\dagger_{in\bar{\sigma}} \right). \tag{3.2}$$

In order to use it, we first need to calculate the commutators of all variations of electronic operators with Hamiltonian of the system:

$$\begin{aligned}
[c_{i\uparrow}, \mathcal{H}] &= -\sum_j (t_{ij} + h + \mu)c_{j\uparrow} + \imath \sum_j \lambda_{ij}\sigma^y_{\uparrow\downarrow}c_{j\downarrow} + \Delta_i c^\dagger_{i\downarrow}, \\
[c_{i\downarrow}, \mathcal{H}] &= -\sum_j (t_{ij} + h + \mu)c_{j\downarrow} + \imath \sum_j \lambda_{ij}\sigma^y_{\downarrow\uparrow}c_{j\uparrow} + \Delta_i c^\dagger_{i\uparrow}, \\
[c^\dagger_{i\uparrow}, \mathcal{H}] &= \sum_{ij} (t_j + h + \mu)c^\dagger_{j\uparrow} + \imath \sum_j \lambda_{ij}\sigma^y_{\uparrow\downarrow}c^\dagger_{j\downarrow} - \Delta^*_i c_{i\downarrow}, \\
[c^\dagger_{i\downarrow}, \mathcal{H}] &= \sum_{ij} (t_j + h + \mu)c^\dagger_{j\downarrow} + \imath \sum_j \lambda_{ij}\sigma^y_{\downarrow\uparrow}c^\dagger_{j\uparrow} - \Delta^*_i c_{i\uparrow}.
\end{aligned} \tag{3.3}$$

To calculate a commutator of a product of multiple fermionic operators, the following identity is used:

$$[A, BC] = ABC - BCA + BAC - BAC = \{A, B\}\, C - B\, \{C, A\}\,. \tag{3.4}$$

However, instead of using repetitive calculations, we can compute only one of the commutators and while minding the order and interchangeability between the direction of spins, we can take advantage of the fact that $-[c_{i\sigma}, \mathcal{H}]^\dagger = [c^\dagger_{i\sigma}, H]$.

Now, we can compare our Hamiltonian $\mathcal{H}$ with the effective Hamiltonian $H_{eff} = \sum_n E_n \gamma^\dagger_n \gamma_n$. Commutators of H_{eff} have a straightforward form:

$$[\gamma^{(\dagger)}, H_{eff}] = (-)E_n\gamma^{(\dagger)}_n. \tag{3.5}$$

Now, by applying the Bogoliubov–Valatin transformation (3.2) to operators in (3.3), a comparison of Hamiltonians with respect to $\gamma^{(\dagger)}_{i\sigma}$ can be shown in a matrix form as a

set of matrix Bogoliubov–de Gennes equations:

$$\sum_j \mathcal{H}_{ij}\Phi_j = E_n\Phi_i, \tag{3.6}$$

where $\Phi^\dagger_{in} = (u_{in\uparrow}, u_{in\downarrow}, v_{in\uparrow}, v_{in\downarrow})$ is a basis (particle-hole spinor) of Hamiltonian operator $\mathcal{H}_{ij}$:

$$\mathcal{H}_{ij} = \begin{pmatrix} -t_{ij\uparrow} & \imath\lambda_y & 0 & \Delta \\ \imath\lambda_y & -t_{ij\downarrow} & \Delta & 0 \\ 0 & \Delta^* & t_{ij\uparrow} & -\imath\lambda_y \\ \Delta^* & 0 & -\imath\lambda_y & t_{ij\downarrow} \end{pmatrix}. \tag{3.7}$$

where the meaning of the used symbols is the same as in (3.1).

The basic microscopic feature of the condensed matter system is its density of states (DOS) and its local counterpart (LDOS). LDOS is defined by the imaginary part of the retarded Green's function $G^r_{i\sigma}$:

$$G^r_{i\sigma} = -\imath\theta(t-t')\langle[c_{i\sigma}(t), c^\dagger_{i\sigma}(t')]_+\rangle = \langle\langle c_{i\sigma}c^\dagger_{i\sigma}\rangle\rangle, \tag{3.8}$$

where θ is Heavyside function, creation and annihilation operators are represented in Heisenberg picture and $\langle ...\rangle$ is an average over the grand canonical ensemble. This leads to

$$\rho_{i\sigma}(E) = -\frac{1}{\pi}\mathfrak{Im}\left[G^r_{i\sigma}(\omega)\right]. \tag{3.9}$$

If we plug here the Bogoliubov–Valatin transformation (3.2), we obtain [20]:

$$\rho_{i\sigma}(\omega) = \sum_n \left[|u^2_{in\sigma}|\delta(\omega - E_n) + |v^2_{in\sigma}|\delta(\omega + E_n)\right]. \tag{3.10}$$

where $\delta(\omega)$ is Dirac delta function that is usually approximated by a Lorentzian or Gaussian[1] functions.

LDOS envisions a real space picture of the studied system, which is usually modelled by a discrete lattice containing N sites. Necessary components of the above formula, namely, eigenfuctions and eigenvectors, have to be computed numerically for larger systems by diagonalizing $4N \times 4N$ Hamiltonian matrix. Such an assignment might be time consuming by itself. Therefore, any further delay can be mitigated by a substitution of an implementation of realistic Δ obtained from self-consistent methods with a constant value, representing a proximity effect of the superconductor. In order to obtain the band structure of the system, a similar calculation can be performed in momentum space.

[1]Lorentzian can be described by $\delta_L(\omega) = \sigma/[\pi(\omega^2 + \sigma^2)]$ and Gaussian by $\delta_G(\omega) = \exp(-\omega^2/2\sigma^2)/\sigma\sqrt{2\pi}$, where σ is broadening of respective functions.

3.2 Topological Invariants

The topological phase of the system and the transitions between them can be envisioned by the values (topological quantum numbers, topological charge) of topological invariants. Topological phase can be dubbed as nontrivial or trivial, with respect to the possibility of existence of topological phenomena like MBS or a lack thereof. Transition between topological phases occurs in **k**–space as bulk gap is closed for some value of momentum **k**. Usually, it is done with a change in an external parameter that forces the switching of the topological charge in the system, at the moment of gap closing [21]. Below, we will present some of the possible methods of obtaining the charge of topological invariants that directly relate to the topological state of the system and its ability to sustain the emergence of Majorana bound states. Such methods differ with respect to the actual topological class of the system that changes according to the composition of Hamiltonian.

3.2.1 Pfaffian

Pfaffian is a $\mathbb{Z}_2$ invariant of D class of topological systems, in which Rashba nanowire setup resides. It can be defined for any skew symmetric matrix $\mathcal{H}$, resulting with a condition that $\mathrm{Det}(\mathcal{H}) = \mathrm{Pf}(\mathcal{H})^2$. This means that $\mathrm{Pf}(\mathcal{H})$ allows one to obtain a precise sign of the determinant's square root. Such a matrix can be obtained from any Bogoliubov–de Gennes type Hamiltonian H_{BdG} after rotating it with unitary operator $U = exp(-\imath\frac{\pi}{4}\tau_y)$, where τ_y is Pauli y-matrix in particle–hole sub–space [22].

Hamiltonian at TRIM can be represented in a skew symmetric form [23]

$$\mathcal{H}(k) = \begin{pmatrix} 0 & A(k) \\ A^T(-k) & 0 \end{pmatrix}, \tag{3.11}$$

and the invariant mentioned above can be defined for any system of Bogoliubov–de Gennes equations, such as the core Hamiltonian used in this thesis (3.1). After Fourier transform, it can become a skew symmetric matrix, if considered at particle-hole symmetry points $\boldsymbol{k} = 0$ and π [24, 25].

Therefore, using Pfaffians, we can evaluate a topological charge of system Q as

$$\mathcal{Q} = \mathrm{sgn}\frac{\mathrm{Pf}\left[\mathcal{H}(k=\pi)\tau_x\right]}{\mathrm{Pf}\left[\mathcal{H}(k=0)\tau_x\right]}. \tag{3.12}$$

Kitaev [26] has shown that for a chain of atoms with translational symmetry, the topological charge shows the existence ($\mathcal{Q} = -1$) or absence ($\mathcal{Q} = 1$) of topological states at the ends of the system, in this case Majorana bound states. Additionally, the chiral symmetric Hamiltonians obey a simplified formula (3.12):

$$\begin{aligned} \mathrm{Pf}[\mathcal{H}(k)\tau_x] &= \mathrm{Pf}\left[U^\dagger \mathcal{H}(k) U \tau_x U^T U^*\right] \\ &= \mathrm{Pf}\begin{pmatrix} 0 & A(k) \\ -A^T(-k) & 0 \end{pmatrix} = \mathrm{Det}[A(k)]. \end{aligned} \tag{3.13}$$

leading to [23]

$$\mathcal{Q} = \mathrm{sgn}\frac{\mathrm{Det}\left[\mathcal{H}(k=\pi)\tau_x\right]}{\mathrm{Det}\left[\mathcal{H}(k=0)\tau_x\right]} = (-1)^w, \tag{3.14}$$

where w is the winding number for given topological phase, that will be discussed in the next section. Even though our core Hamiltonian (3.1) belongs to the BDI class, its setup does not allow for any higher winding number than ± 1. As a result, instead of simply signifying the parity of winding with Pfaffian, we obtain the correct information about the topological state of the system. In order for our Hamiltonian to allow for a higher winding number, we could, for example, increase the number of hoppings (both spin conserving and spin flipping) to the second nearest neighbours. Numerical calculation of $\mathcal{Q}$ using scattering matrix method is shown in 3.2(a).

3.2.2 Winding number

For a Hamiltonian in skew symmetric form (3.11) a winding number w, being the charge $\mathbb{Z}$ of topological index of BDI topological class, can be found from definition [27]:

$$w = \frac{-\imath}{4\pi}\int_{\frac{-\pi}{2}}^{\frac{\pi}{2}} dk\ \mathrm{Tr}\left[U^\dagger \mathcal{S} U \mathcal{H}(k)\partial_k \mathcal{H}^{-1}(k)\right]. \tag{3.15}$$

Rotating $\mathcal{S}$ with U makes it essentially a $-\tau_z$, and taking the trace of integrand gives a result of $\frac{dA(k)}{A(k)} - \frac{dA^\dagger(-k)}{A^\dagger(-k)}$ which can be wrapped and presented as [28]

$$w = \frac{-\imath}{2\pi}\int_{\frac{-\pi}{2}}^{\frac{\pi}{2}} dk\ \mathrm{Tr}\left[\partial_k \mathcal{A}(k)\right]\mathcal{A}^{-1}(k). \tag{3.16}$$

By using the well known identity $\mathrm{Tr}[\ln(N)] = \ln(\mathrm{Det}[N])$, we get

$$w = \frac{-\imath}{2\pi}\int_{\frac{-\pi}{2}}^{\frac{\pi}{2}} dk\ \partial_k \ln\left[\mathrm{Det}\left(\mathcal{A}(k)\right)\right]. \tag{3.17}$$

It can be seen that winding of $\mathrm{Det}[\ln[A(k)]$ over the complex plane is our new invariant. Considering that $\mathrm{Det}[A(k)] = \mathrm{Det}[A^\dagger(-k)] = Z_k$, by noticing that $z_k = \frac{Z_k}{|Z_k|} = exp(\imath\theta_k)$

due to the fact that the overall magnitude of the integrand vanishes leaving only phase, we can obtain

$$w = \frac{-\imath}{2\pi} \int_{k=\frac{-\pi}{2}}^{k=\frac{\pi}{2}} \frac{dz_k}{z_k} = \frac{1}{2\pi} \int_{\frac{-\pi}{2}}^{\frac{\pi}{2}} dk \frac{d\theta_k}{dk}, \tag{3.18}$$

where angle θ_k *winds* over the origin point of the complex plane. This mathematically translates to winding our phase around the origin point of Riemann surface w times. Behaviour of z_k and its relation to winding over the complex plane is shown in Fig. 3.1. It shows a projection of Z_k (a) on a unit circle that differs upon the system being in the nontrivial (b,d) and trivial (c) phase. This depends on the origin point being contained in a unit circle or not, respectively. Due to the bulk–boundary correspondence, the nonzero result of the above formula informs us about the existence of topological states on the edges of the system and in our case – MBS.

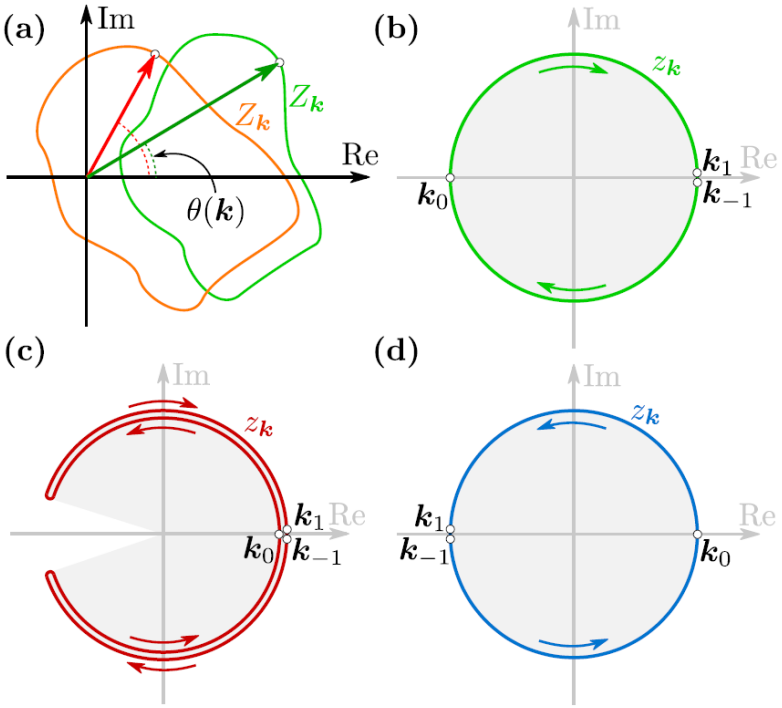

Figure 3.1: Schematic picture of winding number w as described by (3.18). (a) Closed contour Z_k depends on the topological state of the system. In nontrivial (trivial) case, green (orange) contour encircles as angle θ_k changes an origin point (some part) of the complex plane. z_k is a projection of Z_k on unit circle, representing nontrivial phase on panels (b) and (d), and trivial phase on panel (c). Direction of winding between (b) and (d) changes between separate topological branches. White points denote TRIM ($k_0 = 0$ and $k_{\pm 1} = \pm\pi/2$). Figure adapted from Ref. [29].

Another approach is the relation of w to the parity of negative bands at high symmetry points [25]. Parity operator $\mathcal{P}$ is defined as anticommuting with Hamiltonian at

every TRIM and commuting with particle hole symmetry. Usually, Rashba nanowires have only one symmetry point at $k = 0$. Therefore, such Hamiltonian and parity operator share eigenstates. For such, an invariant can be defined:

$$(-1)^w = \prod_{E_n \Gamma_i < 0} \langle n, \Gamma_i | \mathcal{P} | n, \Gamma_i \rangle, \tag{3.19}$$

which determines the product of the parity operator for every i–th energy band below Fermi level and every TRIM, giving knowledge about existence ($w = 1$) or nonexistence ($w = 0$) of MBS [27]. As 1D Rashba nanowires do not require more information than just an existence or nonexistence of topological phase, such parity based method is sufficient for evaluating the emergence of MBS. Winding number w derived analytically is shown in 3.2(b).

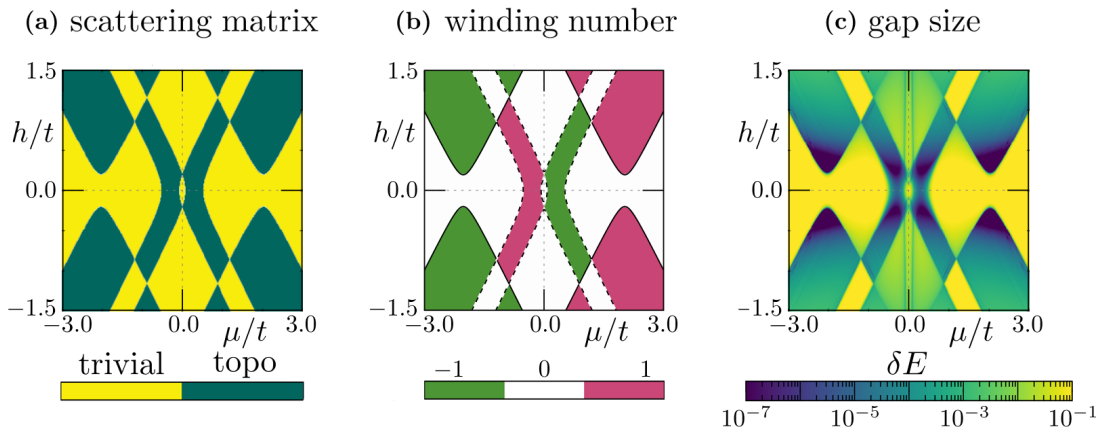

Figure 3.2: Comparison between various methods allowing for probing the topological state of the system. Plots show parameter space of chemical potential μ vs. magnetic field h for Rashba nanowire with superconducting proximity effect and antiferromagnetism for scattering matrix (a), winding number (b) and gap size (c). One can see the sufficient similarity in outline of topological regions between all methods, with slight deviation in *gap size* method as the change is gradual in contrast to other methods. Figures adapted from Ref. [29].

3.2.3 Real space composite measures

Techniques used in the previous sections required a momentum space perspective in order to invent a topological invariant that could show the emergence of MBS in the studied system. However, it is possible to approximate the existence of MBS in real space. This can be done by calculating the energy difference between the two energy levels closest to zero energy [30]. As a result, we probe the gap in energy between

states that could become degenerated at zero energy if Majorana quasiparticles would be present in the system. When this difference is near the order of numerical computing error, one can suspect that MBS emerge in the system for given parameters. Additionally, in contrast to the topological invariants discussed above, such approach has the advantage of being relatively straightforward to measure experimentally [29]. Fig. 3.2, gathers and compares all of the proposed methods for obtaining the information about the topological state of the system. It shows that the composite methods are in sufficient agreement with those relying on topological invariants. Comparison between plots shows that the gap size yields sharp edges of topological phases, however, phases with the same topological charge do not necessarily possess the same gap size. This might lead to ambiguity in deciding whether a nontrivial phase exists for given parameters, still in our case it is apparent which parts of the parameter space belong to which topological phase due to the high contrast between distinct parts in Fig. 3.2(c).

Except for the gap size between the energy levels closest to the Fermi level, we also defined an indicator that shows the distribution of nontrivial topological phases in real space χ_i [31] as

$$\chi_i = \sqrt{\tilde{\mu}_i^2 + \Delta} - h, \tag{3.20}$$

where $\tilde{\mu}_i$ is a chemical potential measured from bottom of band for the homogeneous system, varying from site to site, Δ is gap size and h is the magnetic field. This indicator is based on the topological condition (1.6), that usually describes the magnetic field needed for the gap to close and a new, nontrivial topological phase to emerge in the system. However, as the studied system is under a constant magnetic field, it can be subtracted to show the possible topological state of the system.

3.3 Numerical approach

Numerical simulations in physics allow for studying complex problems for which theoretical models are available, but analytical solutions are computationally impossible. [32]. Most of the data presented in the next chapter was obtained using a Fortran90 code with minor elements obtained using Kwant [33] package for Python. Fortran90 code relies on the diagonalization of BdG Hamiltonian (3.1) using LAPACK/MKL [34, 35] library, from which, after obtaining eigenvalues and eigenvectors one can calculate

observables like LDOS or spectral weight. In Fig. 3.3, one can see a flowchart showing the steps taken in algorithm.

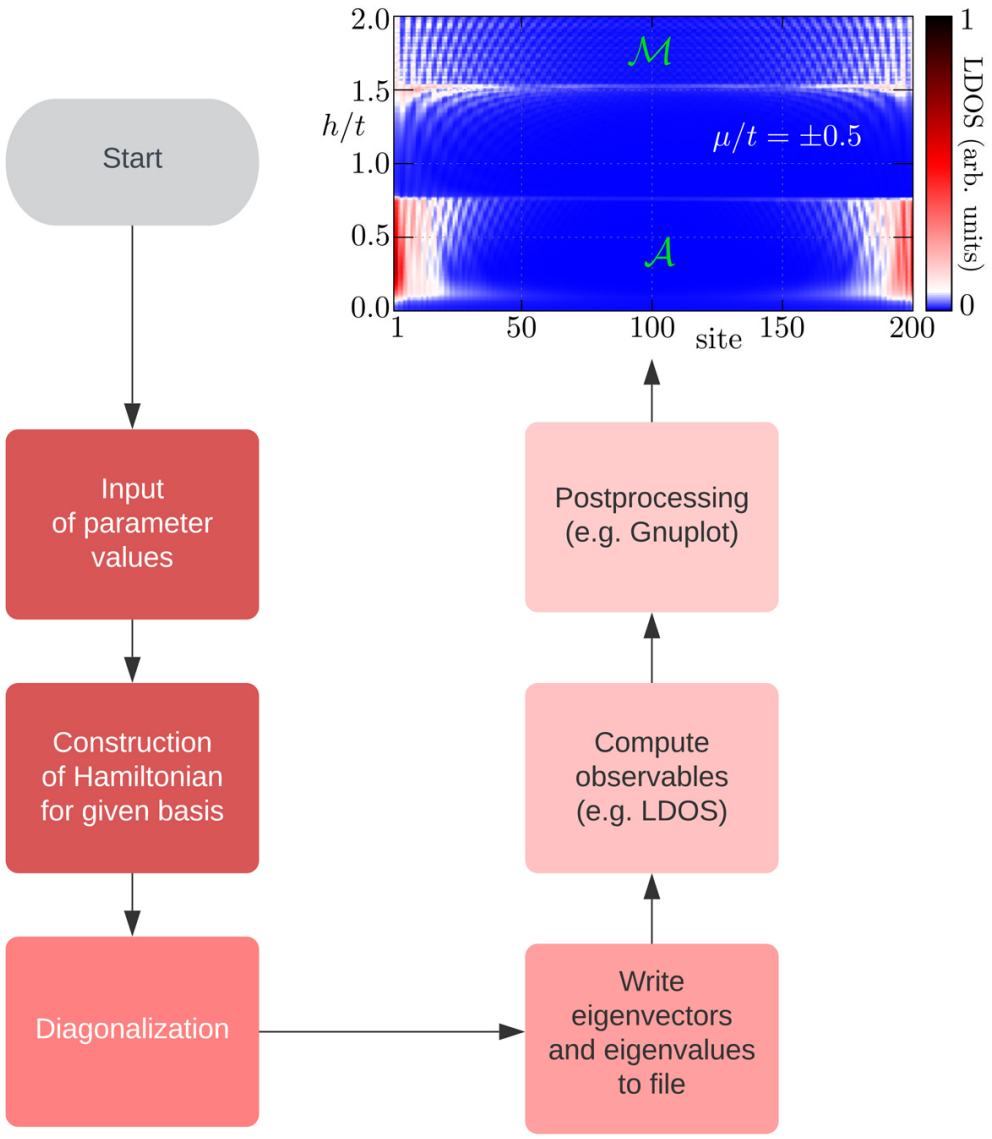

Figure 3.3: Flowchart for typical algorithm used in numerical calculations in this thesis.

This algorithm begins with the input of parameters related to physical values, e.g. chemical potential μ, magnetic field h, spin orbit coupling λ, superconducting order parameter Δ, etc. In order to construct Hamiltonian ready for diagonalization, we combine block matrices, keeping in mind the basis used in the calculations of BdG Hamiltonian. These separate blocks constituting $4N \times 4N$ Hamiltonian are constructed, correlated to the matrix form of Hamiltonian. For example, in a real space picture, each block is built upon iterating over the size of the system, usually the length of

the nanowire (N). Most of the parameters are set on the diagonal of those matrices, with the exception of spin conserving and spin flip hopping which link consecutive sites in system. After diagonalization, and thus solving the eigenequation, we obtain the eigenvalues and eigenvectors, which we write into a file. From those, we can calculate the observables as a function of the system parameters. As a last step, we postprocess our data in some graphics software e.g. GNUPLOT – an open source plotting tool.

Bibliography

[1] M. M. Maśka and M. Mierzejewski, *Vortex structure in the d-density-wave scenario*, Phys. Rev. B **68**, 024513 (2003) DOI: 10.1103/PhysRevB.68.024513

[2] Q. Han, *A method of studying the Bogoliubov–de Gennes equations for the superconducting vortex lattice state*, J. Phys.: Condens. Matter **22**, 035702 (2009) DOI: 10.1088/0953-8984/22/3/035702

[3] H. Mashima, N. Fukuo, Y. Matsumoto, G. Kinoda, T. Kondo, H. Ikuta, T. Hitosugi, and T. Hasegawa, *Electronic inhomogeneity of heavily overdoped* $Bi_{2-x}Pb_xSr_2CuO_y$ *studied by low-temperature scanning tunneling microscopy/spectroscopy*, Phys. Rev. B **73**, 060502 (2006) DOI: 10.1103/PhysRevB.73.060502

[4] M. M. Maśka, Ż. Śledź, K. Czajka, and M. Mierzejewski, *Inhomogeneity-Induced Enhancement of the Pairing Interaction in Cuprate Superconductors*, Phys. Rev. Lett. **99**, 147006 (2007) DOI: 10.1103/PhysRevLett.99.147006

[5] J. Krzyszczak, T. Domański, K. I. Wysokiński, R. Micnas, and S. Robaszkiewicz, *Real space inhomogeneities in high temperature superconductors: the perspective of the two-component model*, **22**, 255702 (2010) DOI: 10.1088/0953-8984/22/25/255702

[6] M. Mierzejewski, A. Ptok, and M. M. Ma ska, *Mutual enhancement of magnetism and Fulde-Ferrell-Larkin-Ovchinnikov superconductivity in* $CeCoIn_5$, Phys. Rev. B **80**, 174525 (2009) DOI: 10.1103/PhysRevB.80.174525

[7] A. Ptok, M. M. Maśka, and M. Mierzejewski, *Coexistence of superconductivity and incommensurate magnetic order*, Phys. Rev. B **84**, 094526 (2011) DOI: 10.1103/PhysRevB.84.094526

[8] O. Dmytruk, D. Loss, and J. Klinovaja, *Pinning of Andreev bound states to zero energy in two-dimensional superconductor- semiconductor Rashba heterostructures*, Phys. Rev. B **102**, 245431 (2020) DOI: 10.1103/PhysRevB.102.245431

[9] E. Prada, P. San-Jose, M. W. A. de Moor, A. Geresdi, E. J. H. Lee, J. Klinovaja, D. Loss, J. Nygård, R. Aguado, and L. P. Kouwenhoven, *From Andreev to Majorana bound states in hybrid superconductor–semiconductor nanowires*, Nat. Rev. Phys. **2**, 575 (2020) DOI: 10.1038/s42254-020-0228-y

[10] R. Hess, H. F. Legg, D. Loss, and J. Klinovaja. *Local and non-local quantum transport due to Andreev bound states in finite Rashba nanowires with superconducting and normal sections*. (2021) eprint: arXiv:2105.02791.

[11] A. Theiler, K. Björnson, and A. M. Black-Schaffer, *Majorana bound state localization and energy oscillations for magnetic impurity chains on conventional superconductors*, Phys. Rev. B **100**, 214504 (2019) DOI: 10.1103/PhysRevB.100.214504

[12] S. Vaitiekenas *et al.*, *Flux-induced topological superconductivity in full-shell nanowires*, Science **367**, (2020) DOI: 10.1126/science.aav3392

[13] R. L. R. C. Teixeira, D. Kuzmanovski, A. M. Black-Schaffer, and L. G. G. V. D. da Silva, *Enhanced Majorana bound states in magnetic chains on superconducting topological insulator edges*, Phys. Rev. B **102**, 165312 (2020) DOI: 10.1103/PhysRevB.102.165312

[14] K. Laubscher and J. Klinovaja. *Majorana bound states in semiconducting nanostructures*. (2021) eprint: arXiv:2104.14459.

[15] A. Kobiałka, T. Domański, and A. Ptok, *Delocalisation of Majorana quasiparticles in plaquette–nanowire hybrid system*, Scientific Reports **9**, 12933 (2019) DOI: 10.1038/s41598-019-49227-5

[16] E. Mascot, S. Cocklin, S. Rachel, and D. K. Morr, *Dimensional tuning of Majorana fermions and real space counting of the Chern number*, Phys. Rev. B **100**, 184510 (2019) DOI: 10.1103/PhysRevB.100.184510

[17] L. Fu and C. L. Kane, *Superconducting Proximity Effect and Majorana Fermions at the Surface of a Topological Insulator*, Phys. Rev. Lett. **100**, 096407 (2008) DOI: 10.1103/PhysRevLett.100.096407

[18] J. R. Williams, A. J. Bestwick, P. Gallagher, S. S. Hong, Y. Cui, A. S. Bleich, J. G. Analytis, I. R. Fisher, and D. Goldhaber-Gordon, *Unconventional Josephson Effect in Hybrid Superconductor-Topological Insulator Devices*, Phys. Rev. Lett. **109**, 056803 (2012) DOI: 10.1103/PhysRevLett.109.056803

[19] J.-X. Zhu. *Bogoliubov-de gennes method and its applications*. Springer, (2016)

[20] H. Matsui, T. Sato, T. Takahashi, S.-C. Wang, H.-B. Yang, H. Ding, T. Fujii, T. Watanabe, and A. Matsuda, *BCS-Like Bogoliubov Quasiparticles in High-T_c Superconductors Observed by Angle-Resolved Photoemission Spectroscopy*, Phys. Rev. Lett. **90**, 217002 (2003) DOI: 10.1103/PhysRevLett.90.217002

[21] S. Murakami, M. Hirayama, R. Okugawa, and T. Miyake, *Emergence of topological semimetals in gap closing in semiconductors without inversion symmetry*, Sci. Adv. **3**, (2017) DOI: 10.1126/sciadv.1602680

[22] B. A. Bernevig and T. L. Hughes. *Topological insulators and topological superconductors*. Princeton University Press, (2013)

[23] S. Tewari and J. D. Sau, *Topological Invariants for Spin-Orbit Coupled Superconductor Nanowires*, Phys. Rev. Lett. **109**, 150408 (2012) DOI: 10.1103/PhysRevLett.109.150408

[24] J. E. Moore and L. Balents, *Topological invariants of time-reversal-invariant band structures*, Phys. Rev. B **75**, 121306 (2007) DOI: 10.1103/PhysRevB.75.121306

[25] C. Dutreix, *Topological spin-singlet superconductors with underlying sublattice structure*, Phys. Rev. B **96**, 045416 (2017) DOI: 10.1103/PhysRevB.96.045416

[26] A. Y. Kitaev, *Unpaired Majorana fermions in quantum wires*, Phys.-Usp. **44**, 131 (2001) DOI: 10.1070/1063-7869/44/10s/s29

[27] M. Sato and S. Fujimoto, *Majorana Fermions and Topology in Superconductors*, Journal of the Physical Society of Japan **85**, 072001 (2016) DOI: 10.7566/JPSJ.85.072001

[28] A. Kobiałka, N. Sedlmayr, M. M. Ma śka, and T. Doma ński, *Dimerization-induced topological superconductivity in a Rashba nanowire*, Phys. Rev. B **101**, 085402 (2020) DOI: 10.1103/PhysRevB.101.085402

[29] A. Kobiałka, N. Sedlmayr, and A. Ptok, *Majorana bound states in a superconducting Rashba nanowire in the presence of antiferromagnetic order*, Phys. Rev. B **103**, 125110 (2021) DOI: 10.1103/PhysRevB.103.125110

[30] A. Kobiałka and A. Ptok, *Electrostatic formation of the Majorana quasiparticles in the quantum dot-nanoring structure*, J. Phys.: Condens. Matter **31**, 185302 (2019) DOI: 10.1088/1361-648x/ab03bf

[31] A. Ptok, D. J. Alspaugh, S. Głodzik, A. Kobiałka, A. M. Ole ś, P. Simon, and P. Piekarz, *Probing the chirality of one-dimensional Majorana edge states around a two-dimensional nanoflake in a superconductor*, Phys. Rev. B **102**, 245405 (2020) DOI: 10.1103/PhysRevB.102.245405

[32] J. Thijssen. *Computational Physics*. 2nd ed. Cambridge University Press, (2007) DOI: 10.1017/CBO9781139171397

[33] C. W. Groth, M. Wimmer, A. R. Akhmerov, and X. Waintal, *Kwant: a software package for quantum transport*, New J. Phys. **16**, 063065 (2014) DOI: 10.1088/1367-2630/16/6/063065

[34] E. Anderson *et al. LAPACK Users' Guide*. Third edition. Philadelphia, Society for Industrial and Applied Mathematics, (1999) ISBN: 0898714478.

[35] *Intel Math Kernel Library. Reference Manual*. (2009)

CHAPTER 4

Cumulative contribution of author

Papers presented in this section are an original contribution of the author of this thesis to the field of condensed matter physics. It consists of two sections that relate to the main topics of the thesis – emergence (4.1) and nonlocality (4.2), containing four and five papers, respectively, published in international journals (including two post–conference articles).

Papers in the first section relate to the first main objective of this thesis: to study the emergence of MBSs in various systems and circumstances, as well as finding new ways to create and manipulate MBSs in the scope of the larger quest of topological quantum computing. These papers focus mainly on inventing new „branches" – regions of a topological parameter space in which MBS can emerge [1, 2]. As the landscape of parameter space for a typical Rashba nanowire deposited onto a superconducting surface is at this time quite barren, one ought to modify the studied system imposing new symetries or conditions on it. Another part related to the emergence is the appearance of Majorana bound states due to the creation of a barrier, playing a role of an artificial end of a system [3]. This section is finished with a study that investigates the differences between free–standing atomic chains and nanowires deposited on the surface. This differences have a profound impact on the formation of the topologically nontrivial phase [4].

A second topic of this thesis, nonlocality, regards the feature of extreme delocalization of degenerate MBSs to the edges of the system. Papers presented in this section study the extension of nonlocality, where MBS *leaks* from nontrivial to trivial regions but still retains its usual properties. This is investigated in hybrid devices where MBS nonlocality manifests in trivial regions of 0D quantum dot [5, 6], 1D normal nanowire

segment [7] and 2D plaquette [8]. Additionally, nonlocality in 2D systems was directly investigated in nanoislands, forming domain walls in which Majorana zero modes could appear [9]. This feature was investigated using nonlocal conductance, which relies on crossed Andreev reflection process to determine the direction of exotic currents in the system.

Papers in both sections are sorted in a chronological order.

4.1 Emergence of Majorana Bound States

4.1.1 Electrostatic formation of the Majorana quasiparticles in the quantum dot–nanoring structure

A. Kobiałka, A. Ptok, J. Phys.: Condens. Matter **31**, 185302 (2019)

In this paper, we applied unconventional methods to describe the emergence of Majorana modes, in the modified Rashba chain model. Usually, such a nanowire is a 1D line element with clearly defined edges. However, here, we instead propose a ring made of Rashba nanowires, that connect both edges which (under proper conditions) would be occupied by MBS. Normally, due to its periodic boundary conditions, such a system could not host MBS as it lacks edges. In order to remedy that, we change the part of the system so it behaves as a quantum dot, transforming the system to one supercell composed of a nanowire and a dot region. Both ABS and MBS can emerge in the vicinity of the quantum dot for some range of parameters. Emergence of MBS in such system happens *on demand*, as it is only a function of quantum dot energy, hence the creation and destruction of MBS does not influence the structural integrity of the system. Such a possibility might be beneficial for quantum computing applications. Building on that, periodic boundary conditions for such supercell can be acquired, which allows momentum space perspective investigation. Band structure study shows the inversion of bands, a hallmark of topological transition, as well as a dispersionless zero–energy flat–band. This flat–band is an aggregate of a range of momenta where MBS form. Additionally, at the topological transition, the spectral weight of MBS is localized around Γ point as with increase of magnetic field, it shifts to Fermi momenta ($\mathbf{k} = \mathbf{k}_F$)

Author's contribution: Partial preparation numerical and analytical calculations, analysi d discussion of obtained results, partial preparation of figures, partial preparation of the manuscript, correspondence with other research groups during the prepublication period, participation in preparing the response for Referees.

IOP Publishing Journal of Physics: Condensed Matter
J. Phys.: Condens. Matter **31** (2019) 185302 (10pp) https://doi.org/10.1088/1361-648X/ab03bf

Electrostatic formation of the Majorana quasiparticles in the quantum dot-nanoring structure

Aksel Kobiałka[1] **and Andrzej Ptok**[2]

[1] Institute of Physics, Maria Curie-Skłodowska University, Plac Marii Skłodowskiej-Curie 1, PL-20031 Lublin, Poland
[2] Institute of Nuclear Physics, Polish Academy of Sciences, ul. W. E. Radzikowskiego 152, PL-31342 Kraków, Poland

E-mail: akob@kft.umcs.lublin.pl and aptok@mmj.pl

Received 18 October 2018, revised 27 January 2019
Accepted for publication 31 January 2019
Published 7 March 2019

Abstract

Zero-energy Majorana quasiparticles can be induced at the edges of low dimensional systems. Non-Abelian statistics of these states make them valid candidates for the realisation of topological quantum computer. From the practical point of view, it is crucial to obtain a system in which an *on demand* creation and manipulation of this type of bound states is feasible. In this article, we show such a possibility in a setup comprising a quantum nanoring in which we specify a quantum dot region via electrostatic means. The presence of quantum dot can lead to the emergence of Andreev and Majorana bound states in the investigated system. We study the differences between those two types of bound states and the possibility of their manipulation. Moreover, the exact calculation method for spectral function has been proposed, which can be used to study the influence of bound states on the band structure of the proposed system. Using this method, it can be shown that the Majorana bound states, induced at the edge of the system, present themselves as a dispersionless zero-energy flat-band.

Keywords: nanoring, quantum dot, band structure, Majorana bound states, Majorana band, spin–orbit coupling, nanostructure

(Some figures may appear in colour only in the online journal)

1. Introduction

Kitaev's depiction of emergence of zero energy Majorana bound states (MBS) in a low dimensional setup [1], ignited the discussion and hopes for creation of topological quantum computers [2–4]. MBS properties are extensively studied due to the possibility of application in quantum computing, as a result of their non-Abelian behaviour [4–12]. Currently, the most promising setups where the emergence of MBS is possible are the semiconductor-superconductor nanostructures [12–18] and ferromagnetic atom chains deposited on the superconductor surface [19–24]. The hard superconducting gap induced by the proximity effect [25, 26] leads to the creation of topologically protected zero energy state.

For practical application of MBS in quantum computing, it is necessary to first invent the feasible way for creation and manipulation of MBS. One of the possible ways to create the MBS in a coupled quantum-dot hybrid-nanowire system is a coalescence of two Andreev bound states (ABS) [17, 27, 28]. Another way would require an external, electrostatic control [29–31], however it requires an additional distinction between trivial and non-trivial zero-energy bound states [23, 32–37].

Interplay between quantum dot and (Andreev or Majorana) bound states is intensively studied [32, 38]. Those types of investigations are focused on the MBS nonlocality and show that MBS, as a topological phenomenon, tends to the edges of the system even if some parts are topologically trivial. This is a result of the hybridisation of quantum dot energy level and

the energy levels of the adjoined topological structure. Such interactions are most commonly realised in semiconductor-superconductor heterostructures [28, 32, 35, 39, 40].

For the reasons described above, we discuss the possibility of inducing the Majorana quasiparticles in the nanoring using electrostatic field. The main idea is presented in figure 1—applying a gate voltage at a part of the semiconducting nanoring located on the superconducting substrate, provides means to change level occupation and effectively creates a barrier. This barrier is treated as the region with properties resembling a quantum dot (QD), because energy levels are associated with small number of states with relation to the rest of the ring. The nanoring structure is advantageous to the nanowire as it allows for *on demand* emergence a pair of MBS in the vicinity of the QD (i.e. at boundary between the QD region and rest of the ring), depending on the gate location. We will show, that the created bound states can form a two non-overlapping MBS, depending on the gate potential. Additionally, the system can be reversed to the topologically trivial state without changing any of the global parameters. Similar nanostructures are experimentally feasible [41, 42].

We consider a realistic microscopic model and investigate the process of emergence of ABS/MBS and their influence on the band structure of the studied system. Using the Bogoliubov–de Gennes formalism, we discuss the possibility of *intentional* creation of zero-energy Majorana bound states. Benefiting from properties of the topologically non-trivial system, we show that such states can be either ABS or MBS, depending on the value of the applied voltage V_{G}. Stemming from this, our purpose is the realisation of MBS within a closed, nanoring structure with QD. We investigate the mechanisms that allow for the emergence of MBS in this setup as the deep understanding of Majorana-hosting devices is essential for further applications. Additionally, we formulate the calculation scheme which allows for obtaining the spectral function. Using this approach, we can describe the properties of the electrons in momentum space from the real space setting of the system. More importantly, in relation to the previous study of the MBS, spectral function technique allows for methodological description of the formation the MBS in momentum space.

This paper is organized as follows. First, we introduce the theoretical model of our system (section 2) and spectral function calculation scheme. Next, we show numerical results and discuss the physical properties of the system in the presence of the QD (section 3). Finally, we summarize our work in section 4.

2. Theoretical model

2.1. Real space description

As mentioned before, we investigate a system in the form of the semiconducting nanoring located on the superconducting substrate (figure 1). This system will be modelled by the one-dimensional Rashba chain with periodic boundary

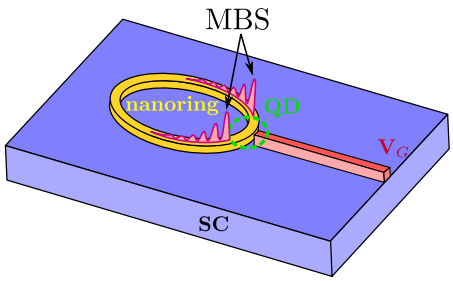

Figure 1. Schematic representation of semiconducting quantum nanoring (yellow) located at the surface of the conventional superconductor (purple). The quantum dot (QD) can be formed due the change of the electron occupation in some part of the nanoring (near the gate) by using the gate voltage (V_{G}). For some value of V_{G}, we can form MBS at the boundary between QD region and rest of ring.

conditions. Thus, it can be described by the Hamiltonian $\mathcal{H} = \mathcal{H}_0 + \mathcal{H}_{\mathrm{SO}} + \mathcal{H}_{\mathrm{QD}} + \mathcal{H}_{\mathrm{prox}}$. The first term describes the mobility of the free electrons in the nanoring:

$$\mathcal{H}_0 = \sum_{ij\sigma} \left(-t\delta_{\langle i,j\rangle} - (\mu + \sigma h)\,\delta_{ij}\right) c^{\dagger}_{i\sigma} c_{j\sigma}, \tag{1}$$

where $c^{\dagger}_{i\sigma}$ ($c_{i\sigma}$) is the creation (annihilation) operator of the electron with spin σ at ith site. Here t denotes a hopping integral between the nearest-neighbour sites, μ is a chemical potential and h denotes the magnetic field in the Zeeman form, which forces the setup to transition to topologically non-trivial phase if the value of critical magnetic value h_c is surpassed. Through the careful choice of the gauge symmetry, we can neglect the diamagnetic (orbital) effects [43]. In the ring structure, the spin–orbit coupling (SOC) is given by the Rashba term:

$$\mathcal{H}_{\mathrm{SO}} = -\mathrm{i}\lambda \sum_{i\sigma\sigma'} c^{\dagger}_{i\sigma} (\sigma_y)_{\sigma\sigma'} c_{i+1,\sigma'} + \mathrm{h.c.}, \tag{2}$$

where σ_y is the second Pauli matrix and λ is the SOC strength. The gate voltage V_{G} can change the occupation of sites. This can create an electrostatic *defect* in the form of the QD in a following way:

$$\mathcal{H}_{\mathrm{QD}} = \sum_{i\in \mathrm{QD}} V_{\mathrm{G}} c^{\dagger}_{i\sigma} c_{i\sigma}, \tag{3}$$

where V_{G} plays the role of the additional potential in a part of ring (sites belonging to the QD region).

As a consequence of placing the nanoring on the superconducting surface, the superconducting gap Δ is induced by the proximity effect, which can be described by the BCS-like term:

$$\mathcal{H}_{\mathrm{prox}} = \Delta \sum_{i} \left(c_{i\downarrow} c_{i\uparrow} + c^{\dagger}_{i\uparrow} c^{\dagger}_{i\downarrow} \right). \tag{4}$$

We assume that the superconducting gap depends on the magnetic field , in the form $\Delta(h) = \Delta_0 \sqrt{1 - (h/h_{c2})^2}$ [32], where h_{c2} is the critical magnetic field of the bulk substrate, while Δ_0 is the superconducting gap induced in the quantum ring, in the absence of the magnetic field h.

2.2. Bogoliubov–de Gennes formalism

The Hamiltonian $\mathcal{H}$ can be diagonalized by the transformation [44]

$$c_{i\sigma} = \sum_n \left(u_{in\sigma}\gamma_n - \sigma v^*_{in\sigma}\gamma^\dagger_n \right), \tag{5}$$

where γ_n and $\gamma^\dagger_n$ are the new quasiparticle fermionic operators, while $u_{in\sigma}$ and $v_{in\sigma}$ are the Bogoliubov–de Gennes (BdG) eigenvectors. This transformation leads to the BdG equations in the form $\mathcal{E}_n\Psi_{in} = \sum_j \mathbb{H}_{ij}\Psi_{jn}$, where

$$\mathbb{H}_{ij} = \begin{pmatrix} H_{ij\uparrow} & D_{ij} & S^{\uparrow\downarrow}_{ij} & 0 \\ D^*_{ij} & -H^*_{ij\downarrow} & 0 & S^{\downarrow\uparrow}_{ij} \\ S^{\downarrow\uparrow}_{ij} & 0 & H_{ij\downarrow} & D_{ij} \\ 0 & S^{\uparrow\downarrow}_{ij} & D^*_{ij} & -H^*_{ij\uparrow} \end{pmatrix} \tag{6}$$

is the matrix representation of Hamiltonian, while $\Psi_{in} = (u_{in\uparrow}, v_{in\downarrow}, u_{in\downarrow}, v_{in\uparrow})^T$. Here the matrix elements are: $H_{ij\sigma} = -t\delta_{\langle i,j\rangle} + [V_G\delta_{i\in QD} - (\mu + \sigma h)]\delta_{ij}$ is the single-particle term, $D_{ij} = \Delta\delta_{ij}$ is the on-site superconducting gap, and $S^{\sigma\sigma'}_{ij} = -\mathrm{i}\lambda(\sigma_y)_{\sigma\sigma'}(\delta_{i+1,j} - \delta_{i-1,j})$ is the SOC term.

2.3. Local density of states

To study our system we will use the spin dependent local density of states (LDOS) $\rho_{i\sigma}(\omega) = -\frac{1}{\pi}\mathrm{Im}\langle\langle c_{i\sigma}|c^\dagger_{i\sigma}\rangle\rangle$, which by using transformation (5) can be expressed in well known form [45]:

$$\rho_{i\sigma}(\omega) = \sum_n \left[|u_{in\sigma}|^2\delta(\omega - \mathcal{E}_n) + |v_{in\sigma}|^2\delta(\omega + \mathcal{E}_n) \right], \tag{7}$$

while the total density of states (DOS) is given by $\rho(\omega) = \sum_{i\sigma}\rho_{i\sigma}(\omega)$. Those physical quantities are measurable by scanning tunneling microscopy (STM) [46–48] and are equivalent to the differential conductance $G_i = \mathrm{d}I_i(V)/\mathrm{d}V$ measurement [49–51].

2.4. Momentum space description

For the system with periodic boundary conditions, (independent of any defects or impurities) we can transform the real space operators to its reciprocal lattice (momentum space) counterparts. Thus, the electrons in Wannier (real space) basis can be expressed by the plane waves in the Bloch (momentum space) basis. Periodicity requirement is fulfilled as our system is periodic with respect to the nanoring length, which implies periodic and continuous wave function required for the Bloch theorem. Similar construction is applied in periodic systems of supercells, which are commonly used in modelling of the defects and impurities in crystals. This can be formally expressed in second quantization as:

$$c_{i\sigma} = \frac{1}{\sqrt{N}}\sum_{\boldsymbol{k}} \exp(\mathrm{i}\boldsymbol{k}\cdot\boldsymbol{R}_i)\, c_{\boldsymbol{k}\sigma}, \tag{8}$$

where $\boldsymbol{R}_i$ and $\boldsymbol{k}$ describe location of the i-th site of the lattice and the momentum, respectively. This unitary transformation connects the real space operator $c_{i\sigma}$ and momentum space operator $c_{\boldsymbol{k}\sigma}$. $c^\dagger_{\boldsymbol{k}\sigma}$ ($c_{\boldsymbol{k}\sigma}$) is the creation (annihilation) operator of electron with the momentum $\boldsymbol{k}$ and spin σ. Transformation (8) conserves the number of states and relates the density in momentum space to the lattice site number.

2.5. Spectral function

To investigate the influence of QD on the band structure of system, we will use the spectral function $\mathcal{A}_{\boldsymbol{k}\sigma}(\omega) = -\frac{1}{\pi}\mathrm{Im}\mathcal{G}_{\boldsymbol{k}\boldsymbol{k}'\sigma}(\omega)$ [52]. $\mathcal{A}_{\boldsymbol{k}\sigma}(\omega)$ is defined in momentum space and can be calculated in two equivalent ways: *(i)* from the Green function equation of motion, which needs the Hamiltonian $\mathcal{H}$ transformed to the momentum representation or *(ii)* transformation of the real space Green function to its momentum representation. The case *(i)* is unfit for a inhomogeneous system. Taking that into account, we present calculation $\mathcal{A}_{\boldsymbol{k}\sigma}(\omega)$ using second method. For this purpose, we must first define the Green functions in the real space $G_{ij\sigma}(\omega) = \langle\langle c_{i\sigma}|c^\dagger_{j\sigma}\rangle\rangle$ and the Green functions in the momentum space $\mathcal{G}_{\boldsymbol{k}\boldsymbol{l}\sigma}(\omega) = \langle\langle c_{\boldsymbol{k}\sigma}|c^\dagger_{\boldsymbol{l}\sigma}\rangle\rangle$. The mutual relation between $G_{ij\sigma}$ and $\mathcal{G}_{\boldsymbol{k}\boldsymbol{l}\sigma}$ functions is given in the periodic system by the Fourier transformation:

$$G_{ij\sigma} = \frac{1}{N}\sum_{\boldsymbol{k}\boldsymbol{l}} \exp(\mathrm{i}\boldsymbol{k}\cdot\boldsymbol{R}_i)\exp(-\mathrm{i}\boldsymbol{l}\cdot\boldsymbol{R}_j)\,\mathcal{G}_{\boldsymbol{k}\boldsymbol{l}\sigma}. \tag{9}$$

Additionally, using transformation (5) we can rewrite $G_{ij\sigma}$ in the form:

$$G_{ij\sigma} = \sum_n \left(u_{in\sigma}u^*_{jn\sigma}\langle\langle\gamma_n|\gamma^\dagger_n\rangle\rangle + v^*_{in\sigma}v_{jn\sigma}\langle\langle\gamma^\dagger_n|\gamma_n\rangle\rangle \right). \tag{10}$$

Then, from equation (9), the spectral function is given as:

$$\mathcal{A}_{\boldsymbol{k}\sigma}(\omega) = \frac{1}{N}\sum_{ij}\exp(-\mathrm{i}\boldsymbol{k}\cdot(\boldsymbol{R}_i - \boldsymbol{R}_j)) \times \sum_n \left(u_{in\sigma}u^*_{jn\sigma}\delta(\omega - \mathcal{E}_n) + v^*_{in\sigma}v_{jn\sigma}\delta(\omega + \mathcal{E}_n) \right). \tag{11}$$

From the solution of the BdG equation (6) in real space, we can numerically obtain the band structure in the form of the spectral function $\mathcal{A}_{\boldsymbol{k}\sigma}(\omega)$. This method can be also generalized to the finite size system (without periodic boundary condition) e.g. in the nanowire form [53].

2.6. Additional remarks

The LDOS shows us how inhomogeneity leads to the localisation of the Andreev and/or Majorana bound states in the real space. In similar way, in the momentum space we can define the spectral function which can show how the same defects influence the band structure of our system [54]. Similarly to the LDOS, the spectral function is a measurable quantity. In this case for visualization of the band structure the angle-resolved photoemission spectroscopy (ARPES) technique [55] can be used, even for the nanostructures [56]. As mentioned previously, in the system with the periodic boundary conditions, the momentum $\boldsymbol{k}$ is a well defined quantity, even in presence of some defects in the nanoring.

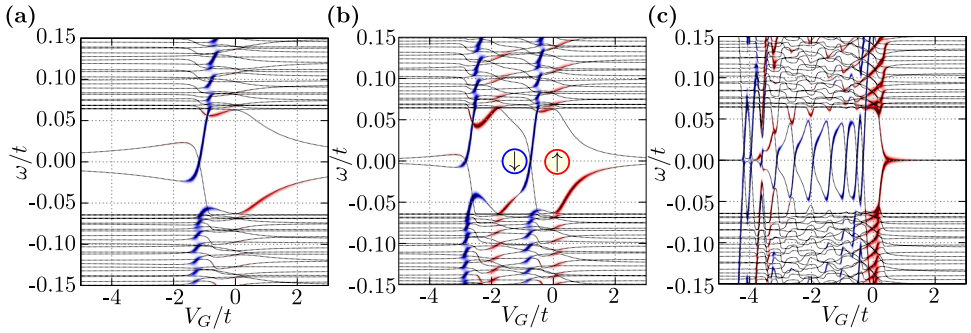

Figure 2. Low energy spectrum of the system for different number of sites $\mathcal{N}_D$ in the quantum dot region (from left to right $\mathcal{N}_D$ is equal to 1, 2 and 10). Line colour denotes spin contribution to the quantum dot states (spin up (red) and down (blue)). Results are in the presence of magnetic field ($h = 0.3t > h_c$).

3. Numerical results

We assume the existence of $\mathcal{N}$ sites in the nanoring and $\mathcal{N}_D$ sites ($\subset \mathcal{N}$) in the QD region. In our calculations we consider $\mathcal{N} = 200$, $\Delta_0/t = 0.2$ and $k_BT/t = 10^{-5}$. Additionally, for the numerical purposes for some type of calculations (e.g. local density of states or spectral function) we replaced the Dirac delta function by a Lorentzian distribution—$\delta(\omega) = \zeta/[\pi(\omega^2 + \zeta^2)]$ with a broadening of $\zeta/t = 0.001$.

3.1. Role of the in-gap spin polarisation

Increase of the gate voltage V_G in the QD region ($\mathcal{N}_D > 0$), leads to the emergence of bound states on the newly created defect in the periodic structure. As we shift the dot energy levels to create a barrier, the change is small with respect to the rest of the band as the barrier height is comparable with the superconducting gap. Its form and influence on the system depends on V_G and $\mathcal{N}_D$. Eigenenergies of QD for the $\mathcal{N}_D$ equal to 1, 2 and 10 are shown in figure 2. Initially, degenerate ABS split under the influence of Zeeman effect. Energy of the ABS is a non-trivial function of the gate potential V_G, that for some values forces ABS to coalesce at the zero-energy [29, 30, 57]. The number of available QD energy levels strongly depends on the value of V_G. The MBS have the spin-polarization similar to the majority spin of the system (i.e. ↑) [58–60]. From this, ordinary zero-energy bound states cannot be MBS, because of the apparent opposite polarization (blue lines represent the eigenstate with minority, ↓ spin). The QD states with the dominant spin-up character are well hybridised with the rest of the ring spin-up states by the spin-conserving hopping (t) [29, 61, 62]. As a consequence, the spin-up QD states do not cross the Fermi level (red lines in figure 2). Situation looks different for the minority spin QD states (blue lines). Hybridisation of spin-down QD states with the rest of ring spin-up states is possible only due to the spin-flip hopping $\lambda \ll t$. As a consequence, the crossing at the Fermi level can be observed. Properties described above are clearly visible in the numerical results, for the case of QD with $\mathcal{N}_D = 10$ sites (figure 2(c)). In the region where the QD energy levels cross the gap, we observe several crossings at the Fermi level by the spin-down QD dot levels ($V_G \sim -4t$) and absence of the spin-up ABS ($V_G \sim 0t$). In relation to the system without periodic boundary conditions e.g. QD-hybrid nanowire system [29], we do not observe any MBS independent of the QD levels in the system (for $-4 < V_G/t < 0$).

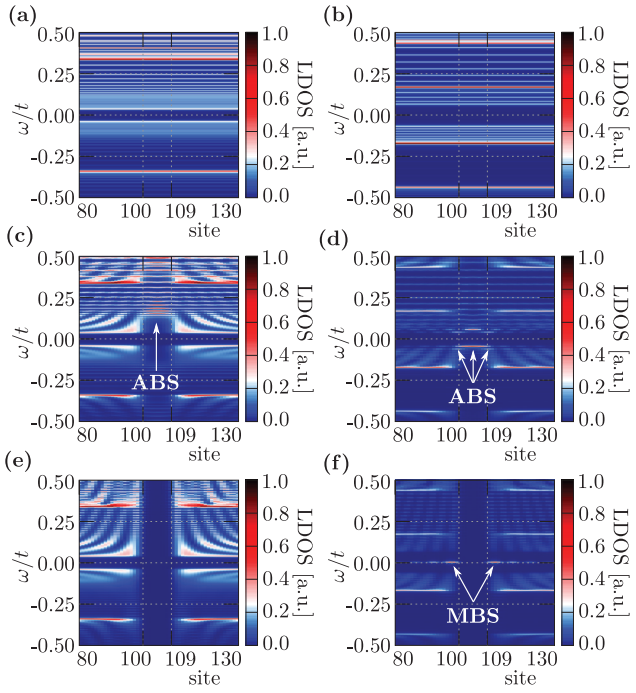

Figure 3. Local density of states (LDOS) around the quantum ring region (for different value of V_G/t equal 0.0, 0.2 and 1.0, from top to bottom). Quantum dot is located within 100 to 109 sites ($\mathcal{N}_Q = 10$). Results for non-topological (trivial) phase ($h = 0.15t < h_c$) and topologically non-trivial phase ($h = 0.3t > h_c$) in left and right row, respectively.

A relatively simple way to show the difference between ordinary ABS and non-trivial MBS is the investigation of the LDOS spectrum around the QD region. Numerical results are shown in figure 3, for a case of the trivial and non-trivial phase (at left and right panels, respectively). In the case of the homogeneous system ($V_G/t = 0$), we see uniform lines independent of the external magnetic field h (figures 3(a) and (b)). The positive gate potential V_G leads to the interplay between the spin-up QD and ring levels. As a consequence of the hybridization described in previous paragraph, we do not observe low energetic ABS localized outside the QD region

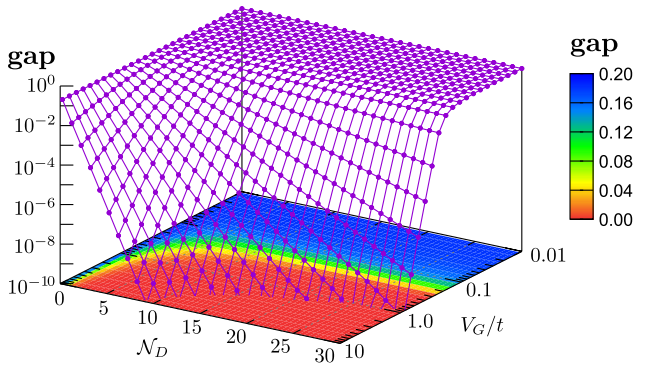

Figure 4. The phase diagram of gate potential V_G versus number of sites $\mathcal{N}_D$ in the quantum dot region. *Z*-axis and background colors show the gap between the two eigenvalues closest to the Fermi level. Results for $h/t = 0.3$.

(figure 3 panels (c) and (d)). The ABS localized inside the QD region are associated with the V_G-shifted spin-up QD energy levels within superconducting gap. For sufficiently large value of V_G, the QD energy levels are located above the gap region (figures 3(e) and (f)). In trivial phase, zero-energy bound states are not observed in vicinity of the QD region (figure 3(e)). In contrast, when the system is in the non-trivial topological phase ($h > h_c$), the bound states are realized in the form of the MBS localized outside the QD region (figure 3(f)). This is possible due to the electrostatic depletion of states which creates barrier high enough, that the probability of the *leakage* of MBS wave function is diminished and in turn prohibits the MBS on both ends of artificial QD to overlap each other. Those properties can be explained by the interplay of the *defect* (in the QD form) with the rest of the system, as well as its influence on the band structure, which will be discussed in next paragraphs.

Increasing the gate potential V_G to relatively large value with respect to the rest of the ring states (in our case below $-4t - h$ and above h), leads to the occurrence of new boundary at the QD-ring transition region. Absence of the ring energy levels in the QD regions leads to the emergence of the (initially Andreev and finally Majorana) bound states [63, 64] localised in the ring region. The relationship between the gate potential V_G and number of sites in the QD region ($\mathcal{N}_D$) (figure 4) can be observed in the dependence of the gap between two bound states closest to zero-energy. Here, $\mathcal{N}_D$ can be understood as the distance between the bound states localised outside of the QD region. The gapless MBS can be realised with smaller value of potential V_G if the size of QD increases. Increase of both $\mathcal{N}_D$ and V_G help in decreasing the probability of annihilation of two Majorana quasiparticles, due to the smaller overlap of Majorana wavefunctions. These properties are similar to the case observed in insufficiently long nanowire, when overlaping between the wavefunction of two bound states is too large and makes it impossible for separate MBS to emerge [30, 31, 65, 66].

Moreover, the ABS transition into MBS around $V_G/t \sim 0.5$ can be observed. An increase of $\mathcal{N}_D$ allows for smaller electrostatic barrier (due to V_G) for which the zero energy ABS transform into MBS. This scheme is essential for an application of

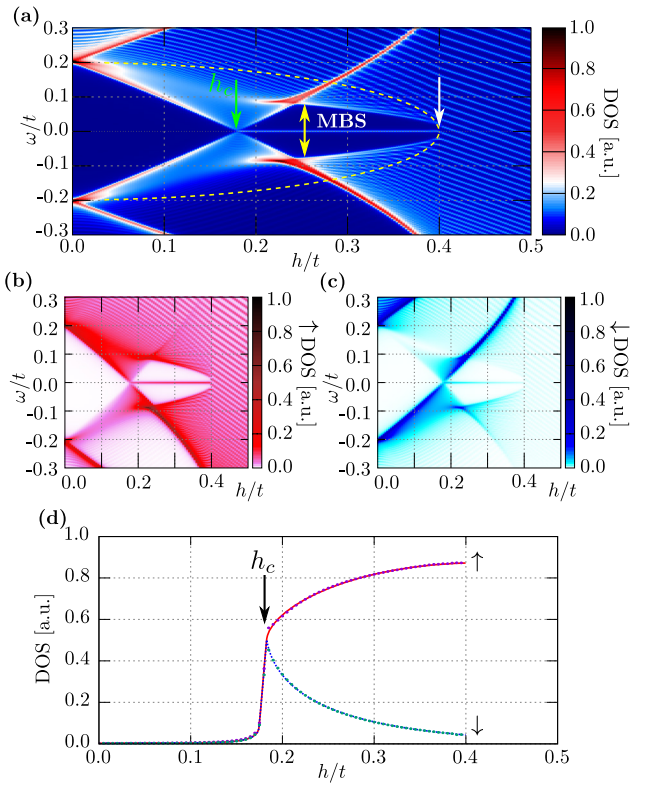

Figure 5. DOS (a) and spin-dependent DOS ((b) and (c)) as a function of the external magnetic field h. (d) Contribution of the spin-dependent DOS to the MBS. Yellow line shows value of magnetic field dependent superconducting gap $\Delta(h) = \Delta_0\sqrt{1-(h/h_{c2})^2}$, while green arrow defines topological phase transition from trivial to non-trivial phase, for magnetic field h_c. Results for $\mathcal{N}_D = 10$ and $V_G/t = 2$.

the studied system in *on-demand* creation of MBS and their manipulation using electrostatic and magnetic fields.

It is important to formulate a description of how the MBS are composed of the spin up and down components. Analysis of the total DOS as a function of the magnetic field h for fixed $\mathcal{N}_D$, shows a characteristic dependence of MBS emergence on magnetic field (figure 5(a)). Increase of h leads to the closing of the trivial gap (associated with Δ_Γ on figure A1), and reopening of the new topological gap at h_c (given by equation (A.4), as marked by yellow arrow). For $h_c < h < h_{c2}$, we can find signatures of the presence of MBS in the system as a form of zero-energy states. The topological gap closes for $h > h_{c_2}$ when the magnetic field destroys the superconductivity in the system, which in turn forbids for MBS to form in the system (white arrow). Analysis of the spin-dependent DOS (figures 5(b) and (c)) clearly shows the band inversion at the h_c. In the topological phase, spectral weight corresponding to the spin-down state is mostly located above the Fermi level (figure 5(c)). Moreover, contribution of the spin-up and spin-down states in the MBS changes (figure 5(d)). As we can see, the MBS is realized above h_c as a zero-energy bound state with unequal composition of the spin-up and spin-down. This effect, while in opposition to the results from Kitaev toy model, is due to MBS emergent nature and thus is a more realistic view of this phenomena. Additionally, ratio between

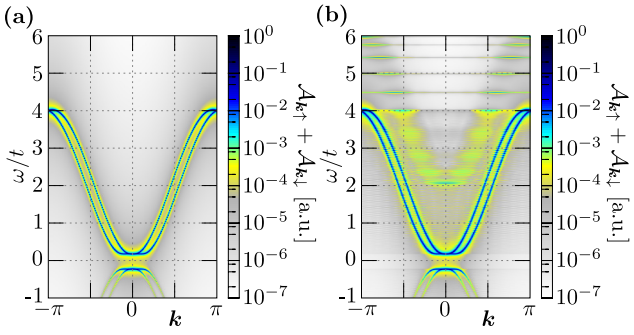

Figure 6. The spectral functions $\mathcal{A}_{k\uparrow}+\mathcal{A}_{k\downarrow}$ of the system in the absence of the magnetic field for the gate potential V_G equal $0t$ (a) and $2t$ (b). Results for a case of the QD with $\mathcal{N}_D = 10$ sites.

spin up and down components of the MBS increases with h. However, it should be noted that the minority spin component is always non-zero. It means that the MBS have 'spin' pointed at the magnetic field direction, which is in agreement with previous theoretical studies [58–60] and experimental measurements [23]. It should be mentioned, that spin properties of the MBS should be always included in the effective *minimal* model of this type of bound states [30, 39].

3.2. Band structure properties

Numerical results for spectral function $\mathcal{A}_{k\sigma}(\omega)$ of studied system in the absence of the magnetic field are shown in figure 6. In the absence of the QD region (figure 6(a)), the band structure (blue line) with SOC is shifted. Two bands with noticeable superconducting gap Δ_0 around the Fermi level can be observed. Adding the QD region (with $\mathcal{N}_D = 10$ and $V_G/t = 2$) leads to the emergence of the ABS at the relatively high energy above the Fermi level ($\omega > V_G \pm h$) (figure 6(b)). Those states can be shown in the total DOS spectrum as *flatbands* of virtual bound states (located outside the gap region) [67]. Additional disorder in the system would lead to the *blurring* of the spectral weight of every state [54, 68–70]. However, the main band structure would still be well visible due to the strongest intensity of the spectral function.

In what follows, we will discuss the influence of magnetic field h on the polarized spectral function $\mathcal{A}_{k\uparrow} - \mathcal{A}_{k\downarrow}$ in a case of the absence and presence of the QD region (shown in figure 7 in the left and right column, respectively). For magnetic field $h < h_c$, we observe typical behaviour of the topologically trivial phase of band polarization at $\mathbf{k} = 0$ (Γ point)—spin order for bands from upper to lower band would be $(\downarrow,\uparrow,\downarrow,\uparrow)$ (figures 7(a) and (b)). At the critical field h_c, closing of the gap at the Γ point occurs. Further increase of the magnetic field h leads to the topological phase transition, which is manifested by the band inversion (see e.g. figures 7(a) and (c)). We observe a new order of the band polarization within non-trivial topological phase $(\downarrow,\downarrow,\uparrow,\uparrow)$ (figures 7(c) and (d)). For the magnetic field $h_c \ll h < h_{c2}$ we can observe qualitative differences in the band structure (figures 7(e) and (f)), while $\Delta_F < \Delta_\Gamma$ (which are the gaps at Fermi and Γ points respectively, see appendix for more details). The only exception occurs just before the destruction of superconducting

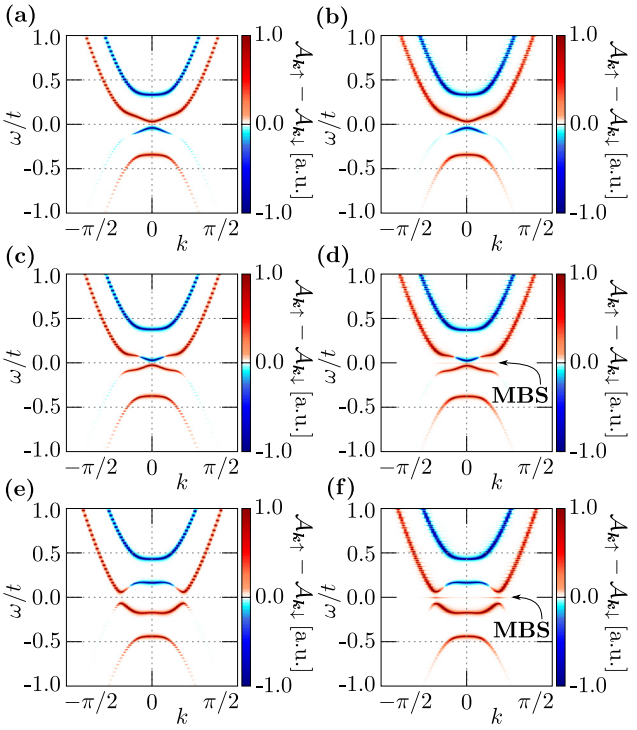

Figure 7. The polarization of the spectral function $\mathcal{A}_{k\uparrow} - \mathcal{A}_{k\downarrow}$ of the system for different values of the external magnetic field h/t equal 0.15, 0.2 and 0.3 (rows from top to bottom). Results for the gate potential V_G equal $0t$ (left column) and $2t$ (right column) Topological phase transition occurs for the magnetic field between $0.15t$ and $0.2t$.

state, when the spectral weight is localised at Fermi point. These characteristic alterations of the band structure (figures 7(c)–(e)) are independent of the SOC λ and gate potential V_G, and the order of the bands is not affected up until the second critical magnetic field h_{c2} which cancels superconductivity in the system.

In the homogeneous system (without the QD) for $h > h_c$, we observe a new gapped non-trivial topological state typical for topological insulators, i.e. gapped state with band inversion present (figures 7(c) and (e)). Due to the existence of the 'edge' of the system, between the ring and the QD region, we can observe a zero-energy dispersionless Majorana flatband (labeled as MBS on panels figures 7(d) and (f)). The Majorana edge states emerge in a topological phase, in the form of Kramer pair with energes $-\mathcal{E}_n = +\mathcal{E}_{n+1} = 0$ [71]. This can be generalized to cases with higher dimensionality. In this sense, MBS are realized in an n-dimensional system as $(n-1)$-dimensional 'surface' states [72–74]. For example, in a three dimensional case, the edge can be realized in a from of the domain wall between topologically non-trivial and trivial system [75]. In our quasi-one-dimensional system, the *surface* is given by the zero-dimensional 'edge' between the QD region and the ring [76].

3.3. Majorana flatband

In this paragraph, the influence of magnetic field h and SOC λ on the Majorana flatband (figure 8) will be discussed. For

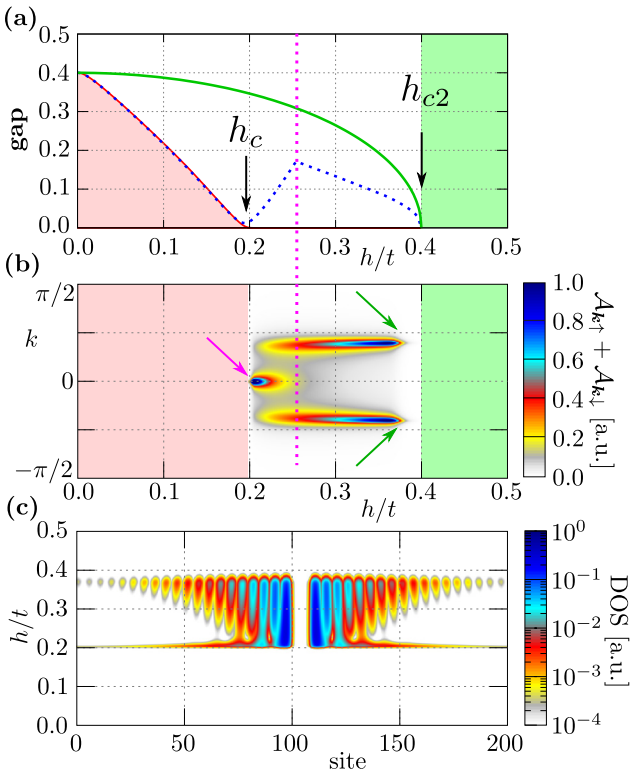

Figure 8. Comparison of the gaps (a), the zero-energy spectral functions $\mathcal{A}_{k\uparrow}+\mathcal{A}_{k\downarrow}$ (b) and the zero-energy local densities of states LDOS (c) as a function of the external magnetic field h. Quantum dot is located between 100th and 109th site ($\mathcal{N}_Q = 10$).

relatively small magnetic field ($0 < h < h_c$), the trivial topological phase exists (figures 8(a) and (b), marked by red region). An increase of magnetic field leads to the closing of the trivial superconducting gap at h_c (A.4). For $h = h_c$ the topological phase transition occurs (see section appendix), which is manifested by the band inversion (described in the previous paragraph). In the presence of the strong 'defect' in the form of the QD, MBS can emerge in the vicinity of QD region. In this state (independent of the boundary condition), the topological gap (shown by blue dashed line) strongly depends on the chosen parameter [5, 77, 78]. Further increase of the magnetic field $h > h_c$ leads to the disappearance of the superconductivity and simultaneous closing of the topological gap at h_{c2}.

Using the notation described in appendix (figure A1), the topological gap is initially given by Δ_Γ and afterwards changed to Δ_F [15] (at the left and right side of the pink dotted line in figure 8(a), respectively). At the same time, increase of the magnetic h field leads to the modification of the spectral weight in the Majorana flatband (figure 8(b)). For the case when the topological gap is given by Δ_Γ, we can see a significant localisation of the spectral weight around $\boldsymbol{k} = 0$ (pink arrow). Similarly, when the topological gap is equal to Δ_F the spectral weight is accumulated around $\boldsymbol{k} = \pm k_F$ (green arrows). However, we must have in mind that the spectral function is non-zero for any $\boldsymbol{k}$. It is an another sign of the emergent nature of MBS, as the whole band of electrons is required to form a single pair of Majorana quasiparticles.

Additionally, the change of the spectral function in Majorana band has its reflection in the LDOS (figure 8(c)). At the magnetic field h_c, we observe maximal delocalisation of the zero-energy bound states in space. Increasing h leads to the localisation of MBS around the QD boundaries in the form of characteristic LDOS oscillation [5, 62, 77]. When $\Delta_\Gamma = \Delta_F$, we can observe the maximally localised MBS, what corresponds to the maximal delocalisation in momentum space (or in other words, a uniform distribution of the spectral weight). These properties can be explained by the manifestation of Heisenberg uncertainty principle—state with well defined momentum $\boldsymbol{k}$ (in the form of band structure, e.g. figure A1) at the same time manifest in the real space as highly delocalised state.

As we can see, the MBS cannot be strictly associated with one specific momentum, like e.g. in the case of the nanowire momentum description around $\boldsymbol{k} = 0$ and $\boldsymbol{k} = \pm k_F$ [79]. In the process of constructing the realistic minimal model of the system capable of hosting MBS, one needs to consider whole Majorana flat band [80]. Moreover, we must keep in mind that the spectral weight of the MBS in momentum space (at zero-energy flat band) strongly depends on the system parameters (see figure 8(b)).

3.4. Outlooks

Localisation of the MBS edge state can be probed by the STM [50]. However, only the spin-resolved measurement of the LDOS [47, 48] can be used to distinguish the real MBS from the trivial zero-energy bound state [58, 59]. These properties of the system with MBS are in agreement with recent expertiments [23]. In a similar way, the spin- and angle-resolved photoemission spectroscopy (sr-ARPES) can be helpful in investigation of the non-topological to topological phase transition [81, 82]. Moreover, the aforementioned properties of the Majorana flatband in the momentum space can be experimentally measured using high quality time- and angle-resolved photoemission spectroscopy (tr-ARPES). Those types of measurements are sensitive to small details of the unoccupied band structure and recently they have been successfully used in the case of topological insulator WTe_2 [83] and Bi_2Se_3 [84] in a study of the non-trivial topological phase. In our case of the nanoring with the QD region, the tr-ARPES technique should be helpful to study states around the Fermi level. Additionally, this type of measurement should allow for for observing the evolution of MBS by tracking the intensity node in the circular dichroism [85–87]. The joint study using those two techniques (sr-ARPES and tr-ARPES) have been already performed [88, 89].

We study realization and differences between the ABS and MBS induced near the boundary between quantum dot area and the rest of the nanoring. Transition to the topologically non-trivial phase was induced by the external Zeeman magnetic field h. However, we must have in mind, that in the presence of the magnetic flux Φ, we can expect realization of the SQUID structure in our setup, with bound states at the Josephson junctions [90–93]. Because MBS is characterized by the fractional a.c. Josephson effect [94], this type of system can be used in distinction between zero-energy MBS and ABS, e.g. by the 4π periodic Josephson currents in a case of dc SQUID [93] or by the MBS existence verified by the Rabi frequency in a case of rf SQUID [90].

4. Summary

Summarising, we proposed the possibility of the creation and manipulation of the Majorana bound states in the nanoring structure, by the electrostatic field in the quantum dot region. In contrast to the other proposed realisations of the Majorana quasiparticles in the nanoring [95], our method is non-invasive. We have shown that the Andreev or Majorana bound states can emerge in the vicinity of potential-induced QD region in the nanoring. Mechanisms that allow for MBS emergence in such system have been analysed—the type of induced bound states depends on the value of the potential, and can be changed *on demand*. Moreover, from practical point of view, this type of the nanostructure can be prepared in relatively simple way.

We have shown that the Majorana bound states can be induced in the system together with Andreev bound states. However, the former states are localised in the vicinity of the quantum dot (i.e. at boundary between quantum dot region and rest of the nanoring), while the latter—the ABS, mostly reside inside. We proposed and discussed a method which allows for interpretation of the existence of the Andreev and/or Majorana bound states in the momentum space. Additionally, we have shown that the Majorana bound states are associated with the dispersionless zero-energy flatband. Spectral function analysis shows that those states cannot exist within a discrete range of some selected momenta, but should be studied in the context of a whole band. It is a consequence of the transfer of the spectral weight within the Majorana flatband from the Γ point ($\mathbf{k}=0$) to the Fermi momenta ($\pm\boldsymbol{k}_{\mathrm{F}}$). Further improvements of our model might help in a formulation of the realistic minimal model of the Majorana bound states.

Acknowledgments

We thank T Domański, Sz Głodzik, P Piekarz and DP Wójcik for careful reading of the manuscript, valuable comments and discussions. AP is grateful to Laboratoire de Physique des Solides (CNRS, Université Paris-Sud) for hospitality during a part of the work on this project. This work was supported by the National Science Centre (NCN, Poland) under grants DEC-2014/13/B/ST3/04451 (AK), UMO-2016/23/B/ST3/00647 (AP).

Appendix. Homogeneous system

In absence of the defect (i.e. for $\mathcal{N}_{\mathrm{D}}=0$ or $V_{\mathrm{G}}/t=0$), the described system is equivalent to the homogeneous ring. In this case, the Hamiltonian $\mathcal{H}$ can be expressed in the momentum space using transformation (8), as:

$$\begin{aligned}\mathcal{H}=&\sum_{\boldsymbol{k}}\left(E_{\boldsymbol{k}}-(\mu+\sigma h)\right)c^{\dagger}_{\boldsymbol{k}\sigma}c_{\boldsymbol{k}\sigma}\\&-i\sum_{\boldsymbol{k}}\mathcal{L}_{\boldsymbol{k}}\sum_{\sigma\sigma'}c^{\dagger}_{\boldsymbol{k}\sigma}\left(\sigma_{y}\right)_{\sigma\sigma'}c_{\boldsymbol{k}\sigma'}\\&+\Delta\sum_{\boldsymbol{k}}\left(c_{\boldsymbol{k}\uparrow}c_{-\boldsymbol{k}\downarrow}+\mathrm{h.c.}\right).\end{aligned}\tag{A.1}$$

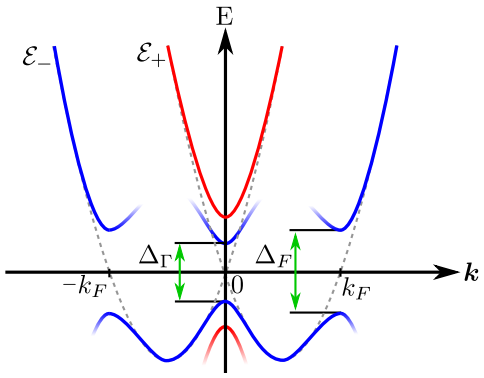

Figure A1. Schematic representation of the band structure of homogeneous system for the superconducting state in the presence of the external magnetic filed. Blue and red solid lines represent lower and upper Rashba bands, respectively. Gray dashed parabolas represent the band structure without the influence of magnetic field and superconductivity, while color insensity corresponds to the spectral weight. We can observe characteristic double-branch structure for the system in the BCS-superconducting state, represented by the gradient from blue/red to white proportional to the decrease in spectral weight.

Here $E_{\boldsymbol{k}}=-2t\cos(k)$ is the dispersion relation for non-interacting electrons, while $\mathcal{L}_{\boldsymbol{k}}=2\lambda\sin(k)$ denotes the spin–orbit coupling in momentum space.

A.1. Band structure

Let us shortly describe the main properties of the band structure in a homogeneous case (figure A1). As a consequence of the SOC ($\lambda>0$) in the normal state ($\Delta_0=0$), the band structure is represented by two shifted parabolas (gray dashed line), crossing the Fermi level ($E=0$) at $\boldsymbol{k}=0$ and $\boldsymbol{k}=\pm k_{\mathrm{F}}$. Proximity effect of the superconductor opens the gap around these two points (marked by Δ_Γ and Δ_{F}, respectively). In the absence of the magnetic field ($h=0$, not shown), both gaps are equal ($\Delta_\Gamma=\Delta_{\mathrm{F}}=\Delta_0$). The increase of the magnetic field leads to the shift of spin up/down energy levels and decreases the gap at $\boldsymbol{k}=0$ (then $\Delta_\Gamma=\Delta(h)-h$). If the superconducting gap is large enough, increasing the magnetic field leads to the closing of the gap at $\boldsymbol{k}=0$ for some critical magnetic field h_c and a reopening of the new *topological gap*. Closing trivial (superconducting) gap is associated with the topological phase transition. The band inversion is a consequence of transition from trivial to non-trival topological phase [71, 96].

A.2. Topological phase transition

For the homogeneous system, we can calculate the condition for the topological phase transition while the gap of the system closes. This is equivalent to the condition [97–99]:

$$\begin{aligned}&\left(E_{\boldsymbol{k}}-\mu\right)^2+h^2+|\mathcal{L}_{\boldsymbol{k}}|^2+|\Delta|^2\\&=2\sqrt{\left(E_{\boldsymbol{k}}-\mu\right)^2|\mathcal{L}_{\boldsymbol{k}}|^2+\left(\left(E_{\boldsymbol{k}}-\mu\right)^2+|\Delta|^2\right)h^2}\end{aligned}\tag{A.2}$$

which yields [100]:

$$(E_{\boldsymbol{k}} - \mu)^2 + |\Delta|^2 = h^2 + |\mathcal{L}_{\boldsymbol{k}}|^2, \quad \Delta\mathcal{L}_{\boldsymbol{k}} = 0. \quad \text{(A.3)}$$

The second condition is satisfied by $\boldsymbol{k} = 0$ and $\boldsymbol{k} = \pm\pi$, which are two time-reversal-invariant momenta for one-dimensional system [73]. By inserting those values to (A.3), we get:

$$h_c = \sqrt{(2t \pm \mu)^2 + |\Delta|^2}, \quad \text{(A.4)}$$

where $\Delta = \Delta(h)$. For this value of the magnetic field, the trivial energy gap closes and the new topological gap opens.

ORCID iDs

Aksel Kobiałka https://orcid.org/0000-0003-2881-8253
Andrzej Ptok https://orcid.org/0000-0002-5566-2656

References

[1] Kitaev A Y 2001 *Phys.—Usp.* **44** 131
[2] Nayak C, Simon S H, Stern A, Freedman M and Das Sarma S 2008 *Rev. Mod. Phys.* **80** 1083
[3] Liu X J, Wong C L M and Law K T 2014 *Phys. Rev.* X **4** 021018
[4] Sarma S D, Freedman M and Nayak C 2015 *NPJ Quantum Inf.* **1** 15001
[5] Stanescu T D, Lutchyn R M and Das Sarma S 2011 *Phys. Rev.* B **84** 144522
[6] Alicea J 2012 *Rep. Prog. Phys.* **75** 076501
[7] Leijnse M and Flensberg K 2012 *Semicond. Sci. Technol.* **27** 124003
[8] Stanescu T D and Tewari S 2013 *J. Phys.: Condens. Matter* **25** 233201
[9] De-Ping Z and Guang-Shan T 2015 *Chin. Phys.* B **24** 080401
[10] Elliott S R and Franz M 2015 *Rev. Mod. Phys.* **87** 137
[11] Aguado R 2017 *Riv. Nuovo Cimento* **40** 523
[12] Lutchyn R M, Bakkers E P A M, Kouwenhoven L P, Krogstrup P, Marcus C M and Oreg Y 2018 *Nat. Rev. Mater.* **3** 52
[13] Mourik V, Zuo K, Frolov S M, Plissard S R, Bakkers E P A M and Kouwenhoven L P 2012 *Science* **336** 1003
[14] Deng M T, Yu C L, Huang G Y, Larsson M, Caroff P and Xu H Q 2012 *Nano Lett.* **12** 6414
[15] Das A, Ronen Y, Most Y, Oreg Y, Heiblum M and Shtrikman H 2012 *Nat. Phys.* **8** 887
[16] Finck A D K, Van Harlingen D J, Mohseni P K, Jung K and Li X 2013 *Phys. Rev. Lett.* **110** 126406
[17] Deng M T, Vaitiekenas S, Hansen E B, Danon J, Leijnse M, Flensberg K, Nygård J, Krogstrup P and Marcus C M 2016 *Science* **354** 1557
[18] Nichele F *et al* 2017 *Phys. Rev. Lett.* **119** 136803
[19] Nadj-Perge S, Drozdov I K, Li J, Chen H, Jeon S, Seo J, MacDonald A H, Bernevig B A and Yazdani A 2014 *Science* **346** 602
[20] Pawlak R, Kisiel M, Klinovaja J, Meier T, Kawai S, Glatzel T, Loss D and Meyer E 2016 *npj Quantum Inf.* **2** 16035
[21] Ruby M, Heinrich B W, Peng Y, von Oppen F and Franke K J 2017 *Nano Lett.* **17** 4473
[22] Feldman B E, Randeria M T, Li J, Jeon S, Xie Y, Wang Z, Drozdov I K, Bernevig B A and Yazdani A 2017 *Nat. Phys.* **13** 286
[23] Jeon S, Xie Y, Li J, Wang Z, Bernevig B A and Yazdani A 2017 *Science* **358** 772
[24] Kim H, Palacio-Morales A, Posske T, Rózsa L, Palotás K, Szunyogh L, Thorwart M and Wiesendanger R 2018 *Sci. Adv.* **4** eaar5251
[25] Chang W, Albrecht S M, Jespersen T S, Kuemmeth F, Krogstrup P, Nygård J and Marcus C M 2015 *Nat. Nanotechnol.* **10** 232
[26] Gül O *et al* 2017 *Nano Lett.* **17** 2690
[27] Suominen H J, Kjaergaard M, Hamilton A R, Shabani J, Palmstrøm C J, Marcus C M and Nichele F 2017 *Phys. Rev. Lett.* **119** 176805
[28] Reeg C, Dmytruk O, Chevallier D, Loss D and Klinovaja J 2018 *Phys. Rev.* B **98** 245407
[29] Ptok A, Kobiałka A and Domański T 2017 *Phys. Rev.* B **96** 195430
[30] Prada E, Aguado R and San-Jose P 2017 *Phys. Rev.* B **96** 085418
[31] Escribano S D, Yeyati A L and Prada E 2018 *Beilstein J. Nanotechnol.* **9** 2171
[32] Liu C X, Sau J D, Stanescu T D and Das Sarma S 2017 *Phys. Rev.* B **96** 075161
[33] Chevallier D, Szumniak P, Hoffman S, Loss D and Klinovaja J 2018 *Phys. Rev.* B **97** 045404
[34] Hell M, Flensberg K and Leijnse M 2018 *Phys. Rev.* B **97** 161401
[35] Moore C, Stanescu T D and Tewari S 2018 *Phys. Rev.* B **97** 165302
[36] Cayao J, San-José P, Black-Schaffer A M, Prada E and Aguado R 2018 *Beilstein J. Nanotechnol.* **9** 1339
[37] Fleckenstein C, Domínguez F, Traverso Ziani N and Trauzettel B 2018 *Phys. Rev.* B **97** 155425
[38] Silva J F and Vernek E 2016 *J. Phys.: Condens. Matter* **28** 435702
[39] Deng M T, Vaitiekėnas S, Prada E, San-Jose P, Nygård J, Krogstrup P, Aguado R and Marcus C M 2018 *Phys. Rev.* B **98** 085125
[40] Kobiałka A, Domański T and Ptok A 2018 Delocalisation of Majorana quasiparticles in plaquette-nanowire hybrid system preprint (arXiv:1808.05281)
[41] Spathis P, Biswas S, Roddaro S, Sorba L, Giazotto F and Beltram F 2011 *Nanotechnology* **22** 105201
[42] Fornieri A, Amado M, Carillo F, Dolcini F, Biasiol G, Sorba L, Pellegrini V and Giazotto F 2013 *Nanotechnology* **24** 245201
[43] Kiczek B and Ptok A 2017 *J. Phys.: Condens. Matter* **29** 495301
[44] de Gennes P G 1989 *Superconductivity of Metals and Alloys* (Reading, MA: Addison-Wesley)
[45] Matsui H, Sato T, Takahashi T, Wang S C, Yang H B, Ding H, Fujii T, Watanabe T and Matsuda A 2003 *Phys. Rev. Lett.* **90** 217002
[46] Hofer W A, Foster A S and Shluger A L 2003 *Rev. Mod. Phys.* **75** 1287
[47] Wiesendanger R 2009 *Rev. Mod. Phys.* **81** 1495
[48] Oka H, Brovko O O, Corbetta M, Stepanyuk V S, Sander D and Kirschner J 2014 *Rev. Mod. Phys.* **86** 1127
[49] Figgins J and Morr D K 2010 *Phys. Rev. Lett.* **104** 187202
[50] Chevallier D and Klinovaja J 2016 *Phys. Rev.* B **94** 035417
[51] Stenger J and Stanescu T D 2017 *Phys. Rev.* B **96** 214516
[52] Mayr M, Alvarez G, Moreo A and Dagotto E 2006 *Phys. Rev.* B **73** 014509
[53] Winkler G W, Ganahl M, Schuricht D, Evertz H G and Andergassen S 2017 *New J. Phys.* **19** 063009
[54] Xu Y, Chiu J, Miao L, He H, Alpichshev Z, Kapitulnik A, Biswas R R and Wray L A 2017 *Nat. Commun.* **8** 14081
[55] Damascelli A, Hussain Z and Shen Z X 2003 *Rev. Mod. Phys.* **75** 473

[56] Snijders P C and Weitering H H 2010 *Rev. Mod. Phys.* **82** 307
[57] Cayao J, Prada E, San-Jose P and Aguado R 2015 *Phys. Rev.* B **91** 024514
[58] Sticlet D, Bena C and Simon P 2012 *Phys. Rev. Lett.* **108** 096802
[59] Maśka M M and Domański T 2017 *Sci. Rep.* **7** 16193
[60] Serina M, Loss D and Klinovaja J 2018 *Phys. Rev.* B **98** 035419
[61] Guigou M, Sedlmayr N, Aguiar-Hualde J M and Bena C 2016 *Europhys. Lett.* **115** 47005
[62] Kobiałka A and Ptok A 2019 *Acta Phys. Pol.* A accepted (https://doi.org/10.12693/APhysPolA.135.64)
[63] Das Sarma S, Sau J D and Stanescu T D 2012 *Phys. Rev.* B **86** 220506
[64] Albrecht S M, Higginbotham A P, Madsen M, Kuemmeth F, Jespersen T S, Nygård J, Krogstrup P and Marcus C M 2016 *Nature* **531** 206
[65] Stenger J P T, Woods B D, Frolov S M and Stanescu T D 2018 *Phys. Rev.* B **98** 085407
[66] Peñaranda F, Aguado R, San-Jose P and Prada E 2018 *Phys. Rev.* B **98** 235406
[67] Balatsky A V, Vekhter I and Zhu J X 2006 *Rev. Mod. Phys.* **78** 373
[68] Medeiros P V C, Stafström S and Björk J 2014 *Phys. Rev.* B **89** 041407
[69] Skachkov D, Quayle P C, Kash K and Lambrecht W R L 2016 *Phys. Rev.* B **94** 205201
[70] Sun Y, Xi L, Yang J, Wu L, Shi X, Chen L, Snyder J, Yang J and Zhang W 2017 *J. Mater. Chem.* A **5** 5098
[71] Hasan M Z and Kane C L 2010 *Rev. Mod. Phys.* **82** 3045
[72] Fu L and Kane C L 2007 *Phys. Rev.* B **76** 045302
[73] Moore J E and Balents L 2007 *Phys. Rev.* B **75** 121306
[74] Teo J C Y and Kane C L 2010 *Phys. Rev.* B **82** 115120
[75] Weithofer L and Recher P 2013 *New J. Phys.* **15** 085008
[76] Fu L and Kane C L 2008 *Phys. Rev. Lett.* **100** 096407
[77] Sau J D, Tewari S, Lutchyn R M, Stanescu T D and Das Sarma S 2010 *Phys. Rev.* B **82** 214509
[78] Sau J D, Lutchyn R M, Tewari S and Das Sarma S 2010 *Phys. Rev. Lett.* **104** 040502
[79] Klinovaja J and Loss D 2012 *Phys. Rev.* B **86** 085408
[80] Lee S P, Lutchyn R M and Maciejko J 2017 *Phys. Rev.* B **95** 184506
[81] Jozwiak C *et al* 2013 *Nat. Phys.* **9** 293
[82] Zhu Z H *et al* 2014 *Phys. Rev. Lett.* **112** 076802
[83] Crepaldi A *et al* 2017 *Phys. Rev.* B **96** 241408
[84] Soifer H *et al* 2017 Band resolved imaging of photocurrent in a topological insulator preprint (arXiv:1712.08694)
[85] Park S R *et al* 2012 *Phys. Rev. Lett.* **108** 046805
[86] Zhu Z H, Veenstra C N, Levy G, Ubaldini A, Syers P, Butch N P, Paglione J, Haverkort M W, Elfimov I S and Damascelli A 2013 *Phys. Rev. Lett.* **110** 216401
[87] Kondo T, Nakashima Y, Ishida Y, Kikkawa A, Taguchi Y, Tokura Y and Shin S 2017 *Phys. Rev.* B **96** 241413
[88] Sánchez-Barriga J, Golias E, Varykhalov A, Braun J, Yashina L V, Schumann R, Minár J, Ebert H, Kornilov O and Rader O 2016 *Phys. Rev.* B **93** 155426
[89] Bugini D, Boschini F, Hedayat H, Yi H, Chen C, Zhou X, Manzoni C, Dallera C, Cerullo G and Carpene E 2017 *J. Phys.: Condens. Matter* **29** 30LT01
[90] Veldhorst M, Molenaar C G, Verwijs C J M, Hilgenkamp H and Brinkman A 2012 *Phys. Rev.* B **86** 024509
[91] Lucignano P, Tafuri F and Tagliacozzo A 2013 *Phys. Rev.* B **88** 184512
[92] Wang Z, Liang Q F, Yao D X and Hu X 2015 *Sci. Rep.* **5** 11686
[93] Huang W C, Liang Q F, Yao D X and Wang Z 2015 *Europhys. Lett.* **110** 37010
[94] Rokhinson L P, Liu X and Furdyna J K 2012 *Nat. Phys.* **8** 795
[95] van Miert G, Ortix C and Smith C M 2017 *2D Mater.* **4** 015023
[96] Bansil A, Lin H and Das T 2016 *Rev. Mod. Phys.* **88** 021004
[97] Sato M and Fujimoto S 2009 *Phys. Rev.* B **79** 094504
[98] Sato M, Takahashi Y and Fujimoto S 2009 *Phys. Rev. Lett.* **103** 020401
[99] Sato M, Takahashi Y and Fujimoto S 2010 *Phys. Rev.* B **82** 134521
[100] Sato M 2006 *Phys. Rev.* B **73** 214502

4.1.2 Dimerization–induced topological superconductivity in a Rashba nanowire

A. Kobiałka, N. Sedlmayr, M.M. Maśka, T. Domański, Phys. Rev. B **101**, 085402 (2020)

Typical Rashba nanowire model has well defined boundaries of a topologically nontrivial phase. In order to peer through those boundaries, we modify this model in Su-Schrieffer-Heeger like system. Such a periodic modulation of spin conserving and spin flipping hopping leads to band inversion, allowing for the emergence of MBS in a unusual region of topological phase space. We call this region *topological branch* induced by the dimerization in the system. Additionally, some parts of the topologically nontrivial phase disappear due to the overlap of topological phases with different value of winding number. However, in the extreme limit of strong dimerization because the topological gap is closed, the system becomes a set of two–atom dimers. We also tested the robustness of the topological superconducting phases to disorder modelled by a variation of chemical potential. Surprisingly, the topological phase native to dimerization is actually more robust to disorder than the uniform Rashba nanowire.

Author's contribution: Partial preparation of numerical and analytical calculations, partial preparation of figures, analysis and discussion of obtained results, partial preparation of the manuscript, participation in preparing the response for Referees.

Dimerization-induced topological superconductivity in a Rashba nanowire

Aksel Kobiałka,[1,*] Nicholas Sedlmayr,[1,†] Maciej M. Maśka,[2,‡] and Tadeusz Domański[1,§]
[1]*Institute of Physics, M. Curie-Skłodowska University, 20-031 Lublin, Poland*
[2]*Department of Theoretical Physics, Wrocław University of Science and Technology, 50-370 Wrocław, Poland*

(Received 2 October 2019; revised manuscript received 7 January 2020; accepted 7 January 2020; published 3 February 2020)

We analyze the influence of dimerization on the topological phases of a Rashba nanowire proximitized to a superconducting substrate. We find that periodic alternations of the hopping integral and spin-orbit coupling can lead to band inversion, inducing a transition to the topologically nontrivial superconducting phase that hosts Majorana zero-energy modes. This "dimerization-induced topological superconductivity" completely repels the topological phase of the uniform nanowire, whenever they happen to overlap. We provide an analytical justification for this puzzling behavior based on symmetry and parity considerations, and discuss feasible spectroscopic methods for its observation. We also test stability of the topological superconducting phases against electrostatic disorder.

DOI: 10.1103/PhysRevB.101.085402

I. INTRODUCTION

The topological superconducting phase of finite length one-dimensional systems with *p*-wave electron pairing enables the realization of Majorana-type quasiparticles that are immune to decoherence [1], hence being ideal candidates for constructing stable qubits. Spectroscopic signatures of such Majorana zero-energy modes (MZMs) have been so far observed in semiconducting nanowires proximitized to superconductors [2–9], nanoscopic chains of magnetic atoms deposited on superconducting surfaces [10–15], lithographically fabricated nanostructures [16], and narrow metallic stripes embedded between two external superconductors differing in phase [17,18].

Electron pairing of these one-dimensional systems is driven via the proximity effect, whereas the topological phase originates either (a) from the spin-orbit coupling (SOC) combined with a sufficiently strong Zeeman field [19–23] or (b) from spiral magnetic textures [24–33]. In both cases MZMs are localized on the most peripheral sites of such nanowires or nanochains [34–40] or separated by an artificial barrier [41]. Their robustness against various types of *perturbations* has been extensively explored, considering, e.g., internal disorder [42–48], disordered superconducting substrates [49], noise [50], inhomogeneous spin-orbit coupling [51], thermal fluctuations [30,52–54], reorientation of the magnetic field [55,56], and correlations [57,58].

Here we consider a *stress test* for topological superconductivity in the Rashba nanowire that might be encountered due to dimerization. The seminal papers by Su, Schrieffer, and Heeger (SSH) [59,60] have firmly established that dimerization itself can induce a topological insulating phase in one-dimensional fermion systems. Interplay between dimerization and superconductivity would be currently of great importance because of its potential effect on the Majorana quasiparticles. Some aspects of the Kitaev combined with SSH scenarios have been recently addressed in Refs. [61–66]. To the best of our knowledge, however, any systematic study of more realistic topologically superconducting nanowires is missing. For this reason we analyze here the role played by alternations of the hopping integral in a Rashba nanowire proximitized to an isotropic superconductor.

This paper is organized as follows. In Sec. II we introduce the microscopic model describing the dimerized nanowire in the presence of the Rashba and Zeeman terms that are crucial for inducing the topological superconductivity. In Sec. III we present the topological phase originating solely from the dimerization, and discuss its spectroscopic signatures such as the emerging Majorana quasiparticles. In Sec. IV we address the electrostatic disorder and its influence on the topological phases. Section V summarizes our results and gives a brief outlook.

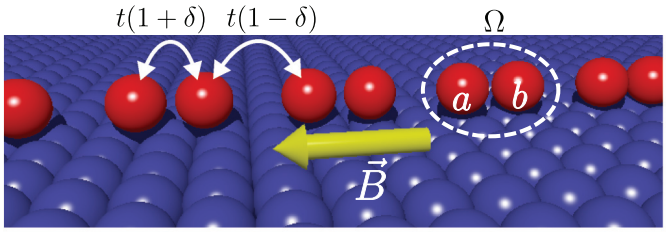

FIG. 1. Schematic of the dimerized nanowire (red) deposited on the superconducting substrate (blue). Modulation of the hopping integral $t(1 \pm \delta)$ is related to shifts in the positions between neighboring a and b atoms forming a two-site unit cell Ω. The (yellow) arrow shows the direction of the applied magnetic field $\vec{B}$.

*akob@kft.umcs.lublin.pl
†sedlmayr@umcs.pl
‡maciej.maska@pwr.edu.pl
§doman@kft.umcs.lublin.pl

II. FORMULATION OF THE PROBLEM

We consider a semiconducting nanowire deposited on a superconductor with an alternating set of strong and weak bonds (Fig. 1). Modulation δ of the hopping integral and spin-orbit coupling can originate either from a mismatch of the lattice constants or due to misalignment of the nanowire with respect to the main crystallographic axes of the superconducting substrate. Neighboring atoms of the nanowire (denoted by a and b) are not equidistant, so formally the *unit cell* Ω comprises two sites.

The Hamiltonian of our setup, $\mathcal{H} = \mathcal{H}_0 + \mathcal{H}_{\rm so} + \mathcal{H}_{\rm prox}$, consists first of the single-particle term

$$\mathcal{H}_0 = -t\sum_{i,\sigma}[(1+\delta)c^\dagger_{ia\sigma}c_{ib\sigma} + (1-\delta)c^\dagger_{ia\sigma}c_{i-1b\sigma} + \text{H.c.}] - \sum_{\Omega=a,b}\sum_{i,\sigma}\left(\mu + \sigma^z_{\sigma\sigma}h\right)c^\dagger_{i\Omega\sigma}c_{i\Omega\sigma}, \quad (1)$$

describing electrons moving along the periodically deformed nanowire. The second quantization operators $c^\dagger_{i\Omega\sigma}$ ($c_{i\Omega\sigma}$) create (annihilate) an electron with spin σ at site $\Omega = a$ or b of the ith unit cell, μ is the chemical potential, and h stands for the Zeeman shift induced by the magnetic field. The hopping integral $t(1\pm\delta)$ between the nearest-neighbor sites periodically varies with a relative amplitude δ. The same modulation is also imposed in the spin-orbit Rashba term

$$\mathcal{H}_{\rm so} = -i\lambda\sum_{i\sigma\sigma'}\left[(1+\delta)c^\dagger_{ia\sigma}\sigma^y_{\sigma\sigma'}c_{ib\sigma'} + (1-\delta)c^\dagger_{ia\sigma}\sigma^y_{\sigma\sigma'}c_{i-1b\sigma'}\right] + \text{H.c.}, \quad (2)$$

where $\sigma^{x,y,z}$ are the Pauli matrices. The last part $\mathcal{H}_{\rm prox}$ accounts for the proximity induced on-site electron pairing. For simplicity we describe it by the BCS-like term

$$\mathcal{H}_{\rm prox} = \sum_i\sum_{\Omega=a,b}(\Delta c^\dagger_{i\Omega\uparrow}c^\dagger_{i\Omega\downarrow} + \Delta^* c_{i\Omega\downarrow}c_{i\Omega\uparrow}). \quad (3)$$

Previous considerations of the uniform Rashba nanowire have established that the topologically nontrivial superconducting phase is realized for magnetic fields obeying the constraint [19]

$$\sqrt{(2t-\mu)^2+|\Delta|^2} < h < \sqrt{(2t+\mu)^2+|\Delta|^2}. \quad (4)$$

The topological phase transition occurs when the quasiparticle spectrum closes and reopens the soft gap [67]. In Sec. III we shall revisit this criterion in the presence of dimerization δ and determine the topological phase diagram with respect to the model parameters h, λ, δ, Δ, and μ.

A. Formalism

The Hamiltonian $\mathcal{H}$ can be recast in the Nambu basis

$$\Psi_i = (c_{ia\uparrow}, c_{ib\uparrow}, c_{ia\downarrow}, c_{ib\downarrow}, c^\dagger_{ia\downarrow}, c^\dagger_{ib\downarrow}, -c^\dagger_{ia\uparrow}, -c^\dagger_{ib\uparrow})^T \quad (5)$$

using the Bogoliubov–de Gennes procedure. We then diagonalize the matrix H_{ij} defined via $\mathcal{H} = \frac{1}{2}\sum_{i,j}\Psi^\dagger_i H_{ij}\Psi_j$. Its Fourier transform $\mathcal{H}_k$ takes the form

$$H_k = -h\sigma^z - \mu\tau^z - t\gamma^+_k\tau^z - i\lambda\gamma^-_k\sigma^y\tau^z + \Delta\tau^x, \quad (6)$$

where $\tau^{x,y,z}$ are Pauli matrices acting within the particle-hole subspace, and we have assumed (without loss of generality) that Δ is real. We have additionally introduced the matrices acting in the sublattice space

$$\gamma^\pm_k = \begin{pmatrix} 0 & (1+\delta)\pm(1-\delta)e^{ik} \\ \pm[(1+\delta)\pm(1-\delta)e^{-ik}] & 0 \end{pmatrix}. \quad (7)$$

By convention identity matrices are not explicitly shown and a tensor product over the matrices is implied.

B. Experimentally accessible observables

In specific numerical computations we have considered a finite length nanowire consisting of 200 sites and used $\Delta = 0.2t$, $\lambda = 0.15t$, and $h = 0.3t$ (unless stated otherwise). Typical values of the hopping integral between the nearest-neighbor atoms on superconducting surface are $t \sim 10$ meV [27,68], whereas their spacing varies between 0.3 and 0.6 nm, see Table 1 in Ref. [30]. The eigenvalues ε_n and eigenvectors in Nambu space $(u^n_{ia\uparrow}, u^n_{ib\uparrow}, u^n_{ia\downarrow}, u^n_{ib\downarrow}, v^n_{ia\downarrow}, v^n_{ib\downarrow}, v^n_{ia\uparrow}, v^n_{ib\uparrow})^T$ [see Eq. (5)] are determined by numerical diagonalization, from which we construct the local density of states

$$\rho_{i\Omega}(\omega) = \sum_{\sigma,n}|u^n_{i\Omega\sigma}|^2\delta(\omega-\varepsilon_n) + |v^n_{i\Omega\sigma}|^2\delta(\omega+\varepsilon_n). \quad (8)$$

This local density of states (LDOS) is measurable by scanning tunneling microscopy (STM) [69] and, at low temperatures, is equivalent to the differential conductance $G_{i\Omega} = dI_{i\Omega}(V)/dV$ of the tunneling current $I_{i\Omega}(V)$ induced by a voltage V [70]. In special cases it is useful to inspect the total density of states (DOS) obtained from the summation $\rho(\omega) = \sum_{i\Omega}\rho_{i\Omega}(\omega)$. Since our numerical solution is obtained for a finite size nanowire we shall illustrate the resulting spectra replacing the Dirac delta functions by Gaussian distributions $\delta(\omega-\varepsilon_n) = \frac{1}{\sigma\sqrt{2\pi}}\exp\left(\frac{-(\omega-\varepsilon_n)^2}{2\sigma^2}\right)$, with a small broadening $\sigma = 0.0035t$.

III. TOPOLOGICAL SUPERCONDUCTIVITY

The dimerized nanowire still retains the symmetries of the homogeneous wire, namely particle-hole $[H,\mathcal{C}]_+ = 0$, where $\mathcal{C} = \sigma^y\tau^y\hat{K}$, and a "time-reversal" symmetry $[H,\mathcal{T}]_- = 0$, where $\mathcal{T} = \sigma^x\hat{K}$ and $\mathcal{T}^2 = 1$. $\hat{K}$ is the complex conjugation operator. Hence the Hamiltonian also possesses their composite symmetry $\mathcal{TC}$, often referred to as chiral symmetry. The Hamiltonian is therefore in the BDI class [71] and has a $\mathbb{Z}$ topological index, the winding number ν. However, for this particular Hamiltonian we find that this index does not obtain magnitudes larger than 1, and hence all interesting information from this index can also be contained in its parity $(-1)^\nu$. This is relatively straightforward to calculate, using either the Pfaffian [1], scattering matrices [72,73], or a suitable parity operator [19,20,74]. Here we will focus on the last option, as this also allows us to understand the phase diagrams inferred from band inversions.

The index ν can be related directly to an appropriately defined parity of the negative energy bands at the time-reversal invariant momenta $\{\Gamma_1,\Gamma_2\} = \{0,\pi\}$. The parity operator $\mathcal{P}$ must satisfy $[\mathcal{P},\mathcal{C}]_+ = 0$ and $[\mathcal{P},H_{\Gamma_i}]_- = 0$. In that case

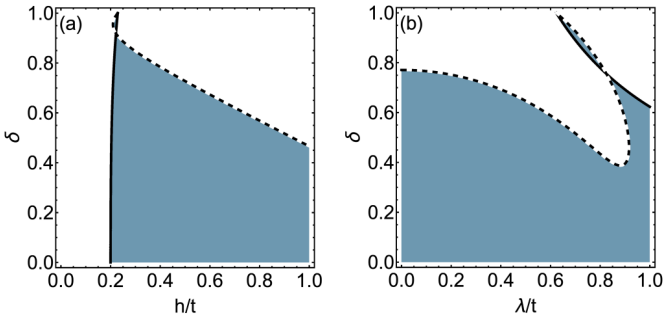

FIG. 2. Topological phase diagram of the dimerized nanowire. (a) The phase diagram with respect to the magnetic field h and the hopping integral modulation δ, obtained for $\lambda = 0.3t$; (b) with respect to the spin-orbit coupling λ and the hopping integral modulation δ, for $h = 0.3t$. The dark (blue) regions have a parity of $(-1)^{\nu} = -1$ and are topologically nontrivial, the white regions are topologically trivial. Gap closings at $k = 0$ are marked with solid black lines and at $k = \pi$ with dashed black lines. Parameters used for both plots are: $\Delta = 0.2t$, $\mu = -2t$.

the eigenstates $|n, k\rangle$ at the time-reversal invariant points are eigenstates also of the parity operator and have a definite parity $\Pi_{n,\Gamma_i} \equiv \langle n, \Gamma_i | \mathcal{P} | n, \Gamma_i \rangle = \pm 1$. One can then demonstrate that [74,75]

$$(-1)^{\nu} = \prod_{\varepsilon_{n,\Gamma_i}<0} \Pi_{n,\Gamma_i}. \tag{9}$$

Calculation of the topological phase is therefore reduced to finding a suitable parity operator. Following the methods of Refs. [37,75–77] we find $\mathcal{P} = \lambda^x \sigma^z$, where $\lambda^{x,y,z}$ are Pauli matrices acting in the sublattice subspace.

Finally one finds

$$\begin{aligned}(-1)^{\nu} = \mathrm{sgn}[&(h^2 - \mu^2)^2 + (4t^2 + 4\lambda^2\delta^2 + \Delta^2)^2 \\ &- 2\mu^2(4t^2 + 4\lambda^2\delta^2 - \Delta^2) \\ &- 2h^2(4t^2 - 4\lambda^2\delta^2 + \Delta^2)] \\ &\times \mathrm{sgn}[(h^2 - \mu^2)^2 + (4\lambda^2 + 4t^2\delta^2 + \Delta^2)^2 \\ &- 2\mu^2(4\lambda^2 + 4t^2\delta^2 - \Delta^2) \\ &+ 2h^2(4\lambda^2 - 4t^2\delta^2 - \Delta^2)].\end{aligned} \tag{10}$$

The first terms change sign when the gap closes at $k = 0$, and the second when it closes at $k = \pi$. These two conditions are marked separately in Figs. 2–4. The gap closing lines separating topologically trivial and nontrivial regions are given in the Appendix, as well as the expression in the limit $h, \mu \to \infty$. For $\delta = 0$ one finds

$$\begin{aligned}(-1)^{\nu} = \mathrm{sgn}[&(4t^2 - h^2 + \Delta^2)^2 \\ &- 2\mu^2(4t^2 + h^2 - \Delta^2) + \mu^4],\end{aligned} \tag{11}$$

which reproduces the well-known result for a homogeneous wire. In that limit the second term in (10) becomes positive definite and no longer contributes. As for some quasi-one-dimensional wires [37] and hexagonal lattices [75,77], which are related to the dimerized wire, the topological phase now depends explicitly on the strength of the spin-orbit coupling λ. The additional conditions for topology also indicate, as we shall see, that there are new topologically nontrivial phases appearing.

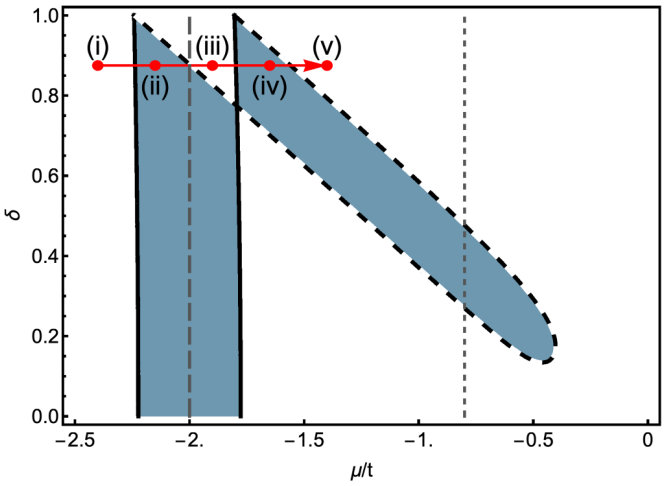

FIG. 3. Topological phase diagram of the dimerized nanowire with respect to the chemical potential μ and the modulation of the hopping integral δ. The dark (blue) regions have a parity of $(-1)^{\nu} = -1$ and are topologically nontrivial, the white regions are topologically trivial. The dimerization introduces a new region of topology at smaller chemical potential than in the homogeneous case. The band structures at the points (i)–(v), demonstrating the band inversion, are shown in Fig. 5. The dashed lines correspond to the calculations of the DOS and LDOS, see Figs. 6 to 9. Results calculated for $\Delta = 0.2t$, $h = 0.3t$, and $\lambda = 0.15t$.

Examples of the phase diagrams are displayed in Figs. 2–4. Stability of the topological superconducting state of the proximitized Rashba nanowire is very sensitive to magnetic field. Figure 2(a) depicts the phase diagram with respect to the applied magnetic field h and the hopping modulation δ. The lowest critical field is $h \simeq 0.2t$ and it is rather unaffected by dimerization. Contrary to this, the upper critical field is considerably suppressed by dimerization. The lower and upper critical magnetic fields merge at sufficiently strong dimerization ($\delta \approx 0.95$).

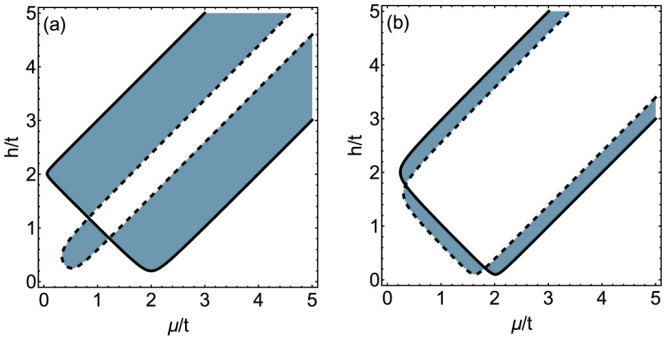

FIG. 4. Topological phase diagram of the dimerized nanowire with respect to the chemical potential μ and the magnetic field h. The dark (blue) regions have a parity of $(-1)^{\nu} = -1$ and are topologically nontrivial, the white regions are topologically trivial. (a) $\delta = 0.2$ and (b) $\delta = 0.8$. The dimerization destroys a part of the topological phase and at a critical value there is no topologically nontrivial phase left, as seen also in Figs. 2 and 3. Gap closings at $k = 0$ are marked with solid black lines and at $k = \pi$ with dashed black lines. Both results were obtained for $\Delta = 0.2t$, $h = 0.3t$, and $\lambda = 0.15t$.

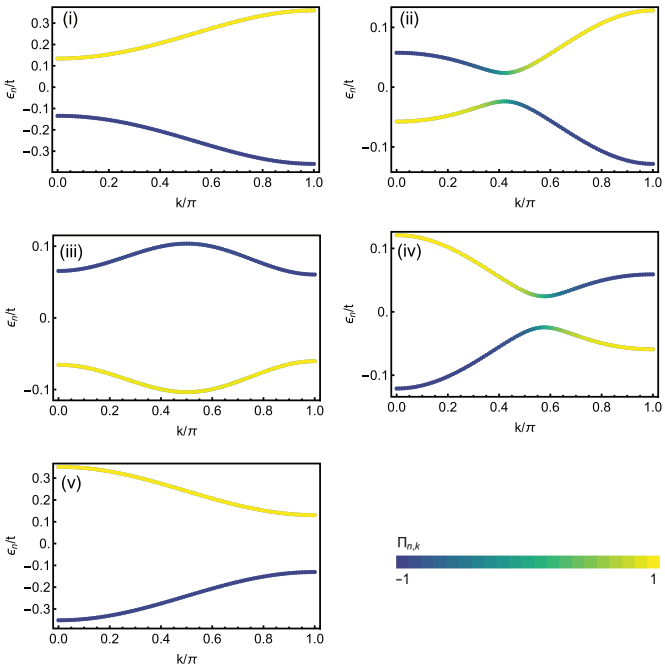

FIG. 5. Band inversion demonstrating the topological phases. Shown are the lowest negative and positive energy bands between the time-reversal invariant momenta 0 and π. Between each panel is a gap closing (at either $k = 0$ or $k = \pi$) which inverts the parity of the bands (see main text for more details). Parameters in (i)–(v) are indicated in Fig. 3, with $\delta = 0.875$ and the chemical potential: (i) $\mu = -2.4t$, (ii) $\mu = -2.15t$, (iii) $\mu = -1.9t$, (iv) $\mu = -1.65t$, and (v) $\mu = -1.4t$ Rest of the parameters are as follows: $\Delta = 0.2t$, $h = 0.3t$, and $\lambda = 0.15t$.

Furthermore, we would like to emphasize the appearance of the additional topological phase induced solely by the dimerization as can be seen in Fig. 3. Such additional topological phase forms away from the usual topological phase of the uniform nanowire existing around $\mu = -2t$. This dimerization induced topologically nontrivial phase nonetheless still requires spin-orbit coupling to be present.

A. Band inversion

Using the parity operator from which the topological index was calculated, one can demonstrate the topology by considering band inversion. One can define the parity of a band at a momentum k as

$$\Pi_{n,k} \equiv \langle n, k|\mathcal{P}|n, k\rangle. \tag{12}$$

At $k = 0, \pi$ the energy eigenstate is also an eigenvector of parity with eigenvalues ± 1. From the definition of the index Eq. (9) it should be apparent that the system is in a topologically nontrivial phase when the parity of the negative energy bands switches an odd number of times between the time-reversal invariant momenta.

We can check this explicitly for the phases shown in Fig. 3, see Fig. 5. Between panels (i) and (ii) the gap closes and opens with band inversion occurring. The gap closing associated with the new topological phase re-inverts these bands and the system becomes trivial again for (iii). The subsequent gap closing and opening from (iii) to (iv) pushes the system into the new topological phase. This phase has the bands inverted along a different orientation of k, which is why these two phases destroy each other, becoming topologically trivial, when they cross (see Figs. 3 and 4 and additionally, videos of band inversion for parameters chosen along the lines in those phase diagrams [78]).

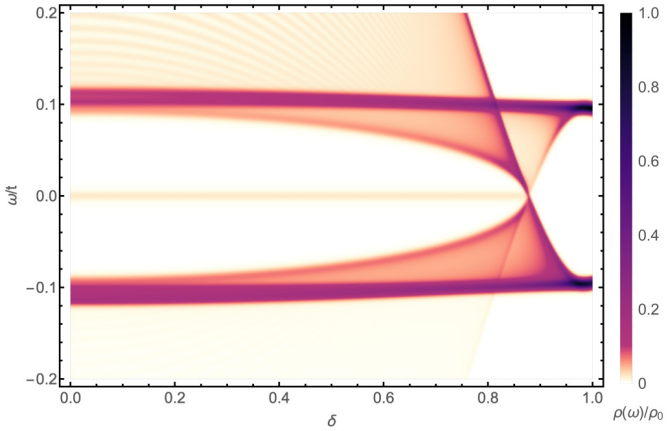

FIG. 6. Evolution of the density of states $\rho(\omega)$ upon the modulation δ obtained for $\mu = -2t$, $h = 0.3t$, $\lambda = 0.15t$, and $\Delta = 0.2t$. The density of states is scaled by $\rho_0 = 1.26 \times 10^4 t^{-1}$.

B. Quasiparticle spectra

Let us now inspect the evolution of the quasiparticle spectra driven by dimerization. In Fig. 6 we show the density of states obtained for the model parameters $\mu = -2t$, $h = 0.3t$, $\lambda = 0.15t$. We can notice that the soft gap gradually closes upon approaching the critical $\delta = 0.87$, and the system evolves into the topologically trivial phase. Traversing this critical dimerization we clearly observe signatures of the band inversion accompanied by disappearance of the Majorana quasiparticles. Ultimately, for $\delta \to 1$ the nanowire becomes entirely dimerized, therefore its spectrum evolves to the bonding and antibonding states. We have checked that for larger values of the magnetic field, the topological phase, and hence the MZMs, are destroyed at considerably lower dimerization strengths (Fig. 2).

In Fig. 7 we illustrate the changeover of the Majarona profile driven by dimerization. For this purpose we display the LDOS at zero energy $\rho_{i\Omega}(\omega{=}0)$ with respect to sites $\{i, \Omega\} \in \langle 1; N/2\rangle$ and for varying δ. The spatial profile of the MZM is rather stable for a wide range of the hopping integral modulation δ. Upon approaching the critical value $\delta \approx 0.87t$ the topological transition, caused by the band inversion, occurs. The zero-energy Majorana modes then cease to exist and merge back into the bulk states.

Figure 8 shows the density of states obtained for $\mu = -1t$, corresponding to the topologically nontrivial phase driven by dimerization. In this case the MZMs are present over a finite dimerization regime, between the subsequent gap closing points signaling the change in topology, as can be clearly seen in Fig. 9.

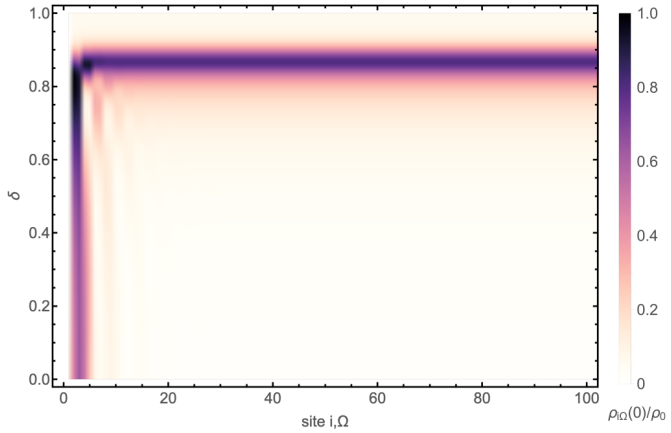

FIG. 7. The local density of states at zero energy $\rho_{i\Omega}(\omega)$ as a function of the hopping integral modulation δ obtained for the same model parameters as in Fig. 6. The MZMs can be clearly seen at the edges of the wire, until the critical dimerization closes the gap. The normalization is $\rho_0 = 4.65t^{-1}$. Only data for the left half of the nanowire (first 100 sites) is shown, as the nanowire is symmetric.

IV. ROBUSTNESS TO DISORDER

Finally we check whether the topological phase driven solely by dimerization is equally stable against disorder, as the topological phase of the homogeneous nanowire. We thus introduce a random on-site term

$$\mathcal{H}_{\rm dis} = \frac{W}{2}\sum_i \xi_i \Psi_i^\dagger \tau^z \Psi_i, \tag{13}$$

where W stands for the disorder amplitude and $-1 \leqslant \xi_i \leqslant 1$ are random numbers. We have diagonalized the system using the Bogoliubov–de Gennes technique and computed the quasiparticle spectra as well as the topological invariant averaged over 10^5 different distributions $\{\xi_i\}$.

Figure 10 illustrates the effect of the disorder on the averaged topological invariant obtained at three representative points in the phase diagram. We have evaluated the

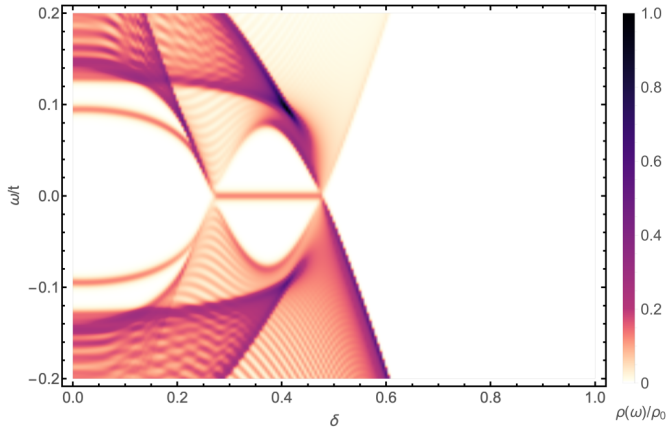

FIG. 8. Evolution of the density of states $\rho(\omega)$ driven by the hopping integral modulation δ obtained for $\mu = -0.8t$, $h = 0.3t$, $\lambda = 0.15t$, and $\Delta = 0.2t$, i.e., within the new topological phase induced by the dimerization. The density of states is scaled by $\rho_0 = 1.89 \times 10^3 t^{-1}$.

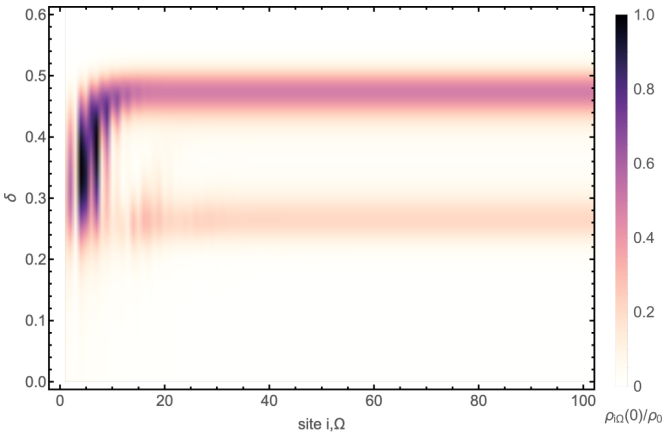

FIG. 9. The local density of states at zero energy $\rho_{i\Omega}(\omega)$ as a function of the hopping integral modulation δ obtained for the same model parameters as in Fig. 8. The MZMs can be clearly seen at the edges of the wire, until the critical dimerization closes the gap. The normalization is $\rho_0 = 2.14t^{-1}$. Only data for the left half of the nanowire are shown, the right half are symmetric. The very faint edge states that can be seen for small dimerization are traces of the trivial nonzero energy subgap states which are clearly visible in Fig. 8.

topological index using the scattering method [72,73] and averaged it over 10^5 configurations of the electrostatic disorder. Although the index is constrained to be either -1 or 1 for any particular disorder realization, upon averaging it shows a smooth crossover between these values. No substantial difference in the robustness to disorder can be seen for the three cases considered by us, i.e., (i) the homogeneous nontrivial phase; (ii) a point in the continuation of this phase in the dimerized case; and (iii) a point in the dimerization induced topologically nontrivial phase. We noticed that compared to (i), case (ii) tends towards the topological crossover at smaller disorder strengths. More surprisingly in case (iii) the topological phase survives on average to larger disorder strengths. This

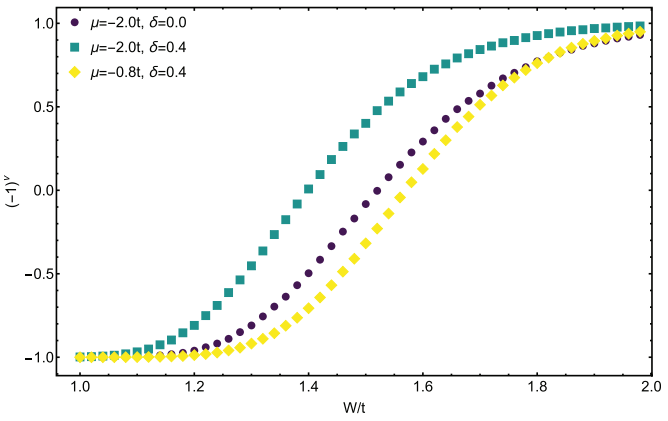

FIG. 10. Topological transition driven by the electrostatic disorder for three representative values of μ and δ, as indicated. Perhaps unsurprisingly introducing dimerization to the completely homogeneous case, causes the transition to occur for smaller disorder strengths. However in the dimerization-induced phase (yellow diamonds) the transition occurs at slightly larger disorder values. The rest of the parameters used in calculation were $h = 0.3t$, $\lambda = 0.15t$, and $\Delta = 0.2t$.

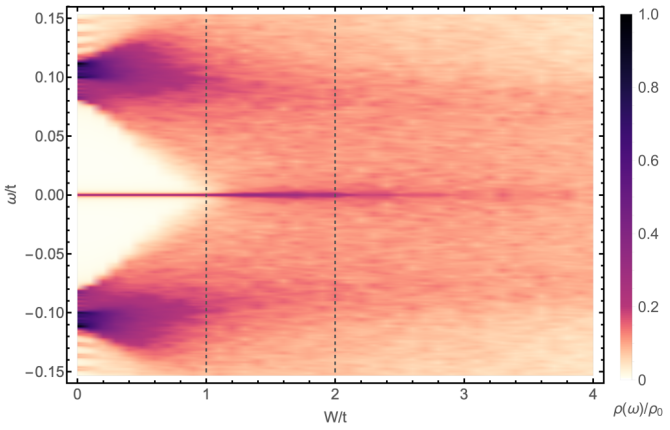

FIG. 11. Changeover of the global density of states averaged over electrostatic disorder versus its amplitude W obtained for $\mu = -2t$, $\delta = 0.4t$, $h = 0.3t$, $\lambda = 0.15t$, and $\Delta = 0.2t$. The dashed lines show the limits in which the disorder induced transition occurs on average. The MZMs can still be seen in this regime, although on average the gap has already been closed. The density of states is scaled by $\rho_0 = 1.26 \times 10^4 t^{-1}$.

is despite the size of the gap being slightly smaller in case (iii) than either (i) or (ii).

The change of the averaged topological index is simultaneously reflected in the local density of states (Fig. 11). The gap closes, on average, at the same disorder amplitude where the topological index begins to change its value between -1 and 1. In this region, however, there still exist realizations of the random electrostatic fields (13) when the MZMs survive, as is evidenced by the well pronounced spectral weight at $\omega = 0$ (Fig. 11). This phenomenon partly resembles the role played by thermal effects, as has been recently predicted for the uniform Rashba nanowires using the Monte Carlo studies [54].

V. SUMMARY AND PERSPECTIVES

We have studied the influence of dimerization on the topological phases of a Rashba nanowire proximitized to a superconducting substrate. We have found that sufficiently strong alternation of the hopping integral is detrimental to the topological superconducting phase, as evidenced by closing of the protecting gap and subsequent disappearance of the Majorana zero modes. Besides this detrimental role, however, we have also predicted an additional topological phase appearing well outside the usual regions typical for the uniform Rashba nanowires. Inspecting symmetries of the system and the related band inversion we have analytically determined the topological invariant and constructed the phase diagrams with respect to all parameters of the model.

Our results indicate that dimerization might be beneficial for realization of the topological superconducting phase in the proximitized Rashba nanowires. In practice such a situation might be encountered, for instance, in extremely narrow metallic strips (comprising a ladder of itinerant electrons) sandwiched between two external superconducting reservoirs, analogous to what has been recently experimentally reported in Refs. [17,18]. The dimerized Rashba systems could also be realized using either double- (or multi-) chain arrangements of some magnetic atoms, such as Co and Fe, weakly interconnected between themselves and deposited on surfaces of superconducting substrates [79]. A general approach for such tailor-made band structures could be practically achieved through atom manipulation using STM [80].

Another feasible version of an emergent symmetry protection due to dimerization manifested in the structure of the $\mathbb{Z}_2$ fields can be related with the topological bond order of the interacting (correlated) ultracold atom systems [81,82].

Further theoretical studies would be useful to verify whether a tendency towards the chain dimerization is energetically favorable or unfavorable. Experimental fabrication and detection of the resulting quasiparticles in such dimerized nanosystems is also welcome and may enable a new route towards controllable manipulation of the Majorana zero modes.

ACKNOWLEDGMENTS

We thank M. Lewenstein for pointing out to us the important role of dimerization and its influence on topological phases. This work was supported by the National Science Centre (NCN, Poland) under Grants 2018/31/N/ST3/01746 (A.K.), 2018/29/B/ST3/01892 (M.M.M.), 2017/27/B/ST3/01911 (T.D.), and 2017/27/B/ST3/02881 (N.S.).

APPENDIX: GAP CLOSING LINES FOR THE TOPOLOGICAL PHASE TRANSITIONS

The topological phase diagram of our dimerized Rashba nanowire is given by Eq. (10). Its topologically trivial and nontrivial phases must be separated by gap closing points at either $k = 0$ or $k = \pi$. For $k = 0$ one finds such closing at

$$h^2 = 4t^2 - 4\lambda^2\delta^2 + \Delta^2 + \mu^2 \pm 4\sqrt{t^2\mu^2 - (4t^2 + \Delta^2)\lambda^2\delta^2} \tag{A1}$$

or, solving for the chemical potential,

$$\mu^2 = 4t^2 + h^2 + 4\lambda^2\delta^2 - \Delta^2 \pm 4\sqrt{t^2h^2 - \Delta^2(t + \lambda^2\delta^2)}. \tag{A2}$$

The other closing, at $k = \pi$, occurs when

$$h^2 = 4t^2\delta^2 - 4\lambda^2 + \Delta^2 + \mu^2 \pm 4\sqrt{t^2\delta^2\mu^2 - \lambda^2(4t^2\delta^2 + \Delta^2)} \tag{A3}$$

or, for the chemical potential,

$$\mu^2 = h^2 + 4\lambda^2 + 4t^2\delta^2 - \Delta^2 \pm 4\sqrt{t^2h^2\delta^2 - \Delta^2(\lambda^2 + t^2\delta^2)}. \tag{A4}$$

In the limit of large $\mu, h \gg t, \Delta, \lambda$ these expressions simplify to

$$\mu^2 - h^2 \approx \pm 4|th|, \tag{A5}$$

at $k = 0$, and

$$\mu^2 - h^2 \approx \pm 4|th\delta|, \tag{A6}$$

at $k = \pi$. The condition to be in the topologically nontrivial phase therefore becomes

$$4|th\delta| \leqslant |\mu^2 - h^2| \leqslant 4|th| \tag{A7}$$

in this limit.

[1] A. Y. Kitaev, Phys.-Usp. **44**, 131 (2001).
[2] M. T. Deng, C. L. Yu, G. Y. Huang, M. Larsson, P. Caroff, and H. Q. Xu, Nano Lett. **12**, 6414 (2012).
[3] V. Mourik, K. Zuo, S. M. Frolov, S. R. Plissard, E. P. A. M. Bakkers, and L. P. Kouwenhoven, Science **336**, 1003 (2012).
[4] A. Das, Y. Ronen, Y. Most, Y. Oreg, M. Heiblum, and H. Shtrikman, Nat. Phys. **8**, 887 (2012).
[5] A. D. K. Finck, D. J. Van Harlingen, P. K. Mohseni, K. Jung, and X. Li, Phys. Rev. Lett. **110**, 126406 (2013).
[6] M. T. Deng, S. Vaitiekenas, E. B. Hansen, J. Danon, M. Leijnse, K. Flensberg, J. Nygård, P. Krogstrup, and C. M. Marcus, Science **354**, 1557 (2016).
[7] J. E. Sestoft, T. Kanne, A. N. Gejl, M. von Soosten, J. S. Yodh, D. Sherman, B. Tarasinski, M. Wimmer, E. Johnson, M. Deng, J. Nygård, T. S. Jespersen, C. M. Marcus, and P. Krogstrup, Phys. Rev. Materials **2**, 044202 (2018).
[8] R. M. Lutchyn, E. P. A. M. Bakkers, L. P. Kouwenhoven, P. Krogstrup, C. M. Marcus, and Y. Oreg, Nat. Rev. Mater. **3**, 52 (2018).
[9] O. Gül, H. Zhang, J. Bommer, M. de Moor, D. Car, S. Plissard, E. Bakkers, A. Geresdi, K. Watanabe, T. Taniguchi, and L. Kouwenhoven, Nat. Nanotechnol. **13**, 192 (2018).
[10] S. Nadj-Perge, I. K. Drozdov, J. Li, H. Chen, S. Jeon, J. Seo, A. H. MacDonald, B. A. Bernevig, and A. Yazdani, Science **346**, 602 (2014).
[11] R. Pawlak, M. Kisiel, J. Klinovaja, T. Meier, S. Kawai, T. Glatzel, D. Loss, and E. Meyer, npj Quantum Inform. **2**, 16035 (2016).
[12] B. E. Feldman, M. T. Randeria, J. Li, S. Jeon, Y. Xie, Z. Wang, I. K. Drozdov, B. A. Bernevig, and A. Yazdani, Nat. Phys. **13**, 286 (2016).
[13] M. Ruby, B. W. Heinrich, Y. Peng, F. von Oppen, and K. J. Franke, Nano Lett. **17**, 4473 (2017).
[14] S. Jeon, Y. Xie, J. Li, Z. Wang, B. A. Bernevig, and A. Yazdani, Science **358**, 772 (2017).
[15] H. Kim, A. Palacio-Morales, T. Posske, L. Rózsa, K. Palotás, L. Szunyogh, M. Thorwart, and R. Wiesendanger, Sci. Adv. **4**, eaar5251 (2018).
[16] F. Nichele, A. C. C. Drachmann, A. M. Whiticar, E. C. T. O'Farrell, H. J. Suominen, A. Fornieri, T. Wang, G. C. Gardner, C. Thomas, A. T. Hatke, P. Krogstrup, M. J. Manfra, K. Flensberg, and C. M. Marcus, Phys. Rev. Lett. **119**, 136803 (2017).
[17] A. Fornieri, A. Whiticar, F. Setiawan, E. Portoles, A. Drachmann, A. Keselman, S. Gronin, C. Thomas, T. Wang, R. Kallaher, G. Gardner, E. Berg, M. Manfra, A. Stern, C. Marcus, and F. Nichele, Nature (London) **569**, 89 (2019).
[18] H. Ren, F. Pientka, S. Hart, A. Pierce, M. Kosowsky, L. Lunczer, R. Schlereth, B. Scharf, E. Hankiewicz, L. Molenkamp, B. Halperin, and A. Yacoby, Nature (London) **569**, 93 (2019).
[19] M. Sato and S. Fujimoto, Phys. Rev. B **79**, 094504 (2009).
[20] M. Sato, Y. Takahashi, and S. Fujimoto, Phys. Rev. Lett. **103**, 020401 (2009).
[21] M. Sato, Y. Takahashi, and S. Fujimoto, Phys. Rev. B **82**, 134521 (2010).
[22] R. M. Lutchyn, J. D. Sau, and S. Das Sarma, Phys. Rev. Lett. **105**, 077001 (2010).
[23] Y. Oreg, G. Refael, and F. von Oppen, Phys. Rev. Lett. **105**, 177002 (2010).
[24] T.-P. Choy, J. M. Edge, A. R. Akhmerov, and C. W. J. Beenakker, Phys. Rev. B **84**, 195442 (2011).
[25] I. Martin and A. F. Morpurgo, Phys. Rev. B **85**, 144505 (2012).
[26] M. Kjaergaard, K. Wölms, and K. Flensberg, Phys. Rev. B **85**, 020503(R) (2012).
[27] S. Nadj-Perge, I. K. Drozdov, B. A. Bernevig, and A. Yazdani, Phys. Rev. B **88**, 020407(R) (2013).
[28] B. Braunecker and P. Simon, Phys. Rev. Lett. **111**, 147202 (2013).
[29] F. Pientka, L. I. Glazman, and F. von Oppen, Phys. Rev. B **88**, 155420 (2013).
[30] J. Klinovaja, P. Stano, A. Yazdani, and D. Loss, Phys. Rev. Lett. **111**, 186805 (2013).
[31] M. M. Vazifeh and M. Franz, Phys. Rev. Lett. **111**, 206802 (2013).
[32] M. Schecter, K. Flensberg, M. H. Christensen, B. M. Andersen, and J. Paaske, Phys. Rev. B **93**, 140503(R) (2016).
[33] R. L. R. C. Teixeira, D. Kuzmanovski, A. M. Black-Schaffer, and L. G. G. V. Dias da Silva, Phys. Rev. B **99**, 035127 (2019).
[34] A. C. Potter and P. A. Lee, Phys. Rev. Lett. **105**, 227003 (2010).
[35] A. C. Potter and P. A. Lee, Phys. Rev. B **83**, 094525 (2011).
[36] N. Sedlmayr, J. M. Aguiar-Hualde, and C. Bena, Phys. Rev. B **91**, 115415 (2015).
[37] N. Sedlmayr, J. M. Aguiar-Hualde, and C. Bena, Phys. Rev. B **93**, 155425 (2016).
[38] A. Ptok, A. Kobiałka, and T. Domański, Phys. Rev. B **96**, 195430 (2017).
[39] A. Kobiałka, T. Domański, and A. Ptok, Sci. Rep. **9**, 12933 (2019).
[40] A. Kobiałka, P. Piekarz, A. M. Oleś, and A. Ptok, arXiv:1911.13039.
[41] A. Kobiałka and A. Ptok, J. Phys.: Condens. Matter **31**, 185302 (2019).
[42] P. W. Brouwer, M. Duckheim, A. Romito, and F. von Oppen, Phys. Rev. B **84**, 144526 (2011).
[43] W. DeGottardi, D. Sen, and S. Vishveshwara, Phys. Rev. Lett. **110**, 146404 (2013).
[44] H.-Y. Hui, J. D. Sau, and S. Das Sarma, Phys. Rev. B **92**, 174512 (2015).
[45] S. Hoffman, J. Klinovaja, and D. Loss, Phys. Rev. B **93**, 165418 (2016).
[46] S. S. Hegde and S. Vishveshwara, Phys. Rev. B **94**, 115166 (2016).
[47] B. Pekerten, A. Teker, O. Bozat, M. Wimmer, and I. Adagideli, Phys. Rev. B **95**, 064507 (2017).
[48] M. M. Maśka, A. Gorczyca-Goraj, J. Tworzydło, and T. Domański, Phys. Rev. B **95**, 045429 (2017).
[49] W. S. Cole, J. D. Sau, and S. Das Sarma, Phys. Rev. B **94**, 140505(R) (2016).
[50] Y. Hu, Z. Cai, M. A. Baranov, and P. Zoller, Phys. Rev. B **92**, 165118 (2015).
[51] J. Klinovaja and D. Loss, Eur. Phys. J. B **88**, 62 (2015).
[52] B. Braunecker and P. Simon, Phys. Rev. B **92**, 241410(R) (2015).
[53] W. Hu, R. T. Scalettar, and R. R. P. Singh, Phys. Rev. B **92**, 115133 (2015).
[54] A. Gorczyca-Goraj, T. Domański, and M. M. Maśka, Phys. Rev. B **99**, 235430 (2019).
[55] B. Kiczek and A. Ptok, J. Phys.: Condens. Matter **29**, 495301 (2017).

[56] V. Kaladzhyan, J. Despres, I. Mandal, and C. Bena, Eur. Phys. J. B **90**, 211 (2017).
[57] A. Wieckowski, M. M. Maśka, and M. Mierzejewski, Phys. Rev. Lett. **120**, 040504 (2018).
[58] C. Monthus, J. Phys. A: Math. Theor. **51**, 115304 (2018).
[59] W. P. Su, J. R. Schrieffer, and A. J. Heeger, Phys. Rev. Lett. **42**, 1698 (1979).
[60] A. J. Heeger, S. Kivelson, J. R. Schrieffer, and W. P. Su, Rev. Mod. Phys. **60**, 781 (1988).
[61] R. Wakatsuki, M. Ezawa, Y. Tanaka, and N. Nagaosa, Phys. Rev. B **90**, 014505 (2014).
[62] Y. Wang, J.-J. Miao, H.-K. Jin, and S. Chen, Phys. Rev. B **96**, 205428 (2017).
[63] M. Ezawa, Phys. Rev. B **96**, 121105(R) (2017).
[64] G. Y. Chitov, Phys. Rev. B **97**, 085131 (2018).
[65] W. C. Yu, P. D. Sacramento, Y. C. Li, D. G. Angelakis, and H.-Q. Lin, Phys. Rev. B **99**, 115113 (2019).
[66] C.-B. Hua, R. Chen, D.-H. Xu, and B. Zhou, Phys. Rev. B **100**, 205302 (2019).
[67] J. E. Moore and L. Balents, Phys. Rev. B **75**, 121306(R) (2007).
[68] M. Menzel, Y. Mokrousov, R. Wieser, J. E. Bickel, E. Vedmedenko, S. Blügel, S. Heinze, K. von Bergmann, A. Kubetzka, and R. Wiesendanger, Phys. Rev. Lett. **108**, 197204 (2012).
[69] R. Wiesendanger, Rev. Mod. Phys. **81**, 1495 (2009).
[70] J. Figgins and D. K. Morr, Phys. Rev. Lett. **104**, 187202 (2010).
[71] S. Ryu, A. Schnyder, A. Furusaki, and A. Ludwig, New J. Phys. **12**, 65010 (2010).
[72] A. R. Akhmerov, J. P. Dahlhaus, F. Hassler, M. Wimmer, and C. W. J. Beenakker, Phys. Rev. Lett. **106**, 057001 (2011).
[73] I. C. Fulga, F. Hassler, A. R. Akhmerov, and C. W. J. Beenakker, Phys. Rev. B **83**, 155429 (2011).
[74] M. Sato, Phys. Rev. B **79**, 214526 (2009).
[75] C. Dutreix, Phys. Rev. B **96**, 045416 (2017).
[76] N. Sedlmayr and C. Bena, Phys. Rev. B **92**, 115115 (2015).
[77] N. Sedlmayr, V. Kaladzhyan, C. Dutreix, and C. Bena, Phys. Rev. B **96**, 184516 (2017).
[78] See Supplemental Material at http://link.aps.org/supplemental/10.1103/PhysRevB.101.085402 for videos illustrating the band inversion with the change of chemical potential μ and magnetic field h.
[79] S. Franca, D. V. Efremov, and I. C. Fulga, Phys. Rev. B **100**, 075415 (2019).
[80] R. Drost, T. Ojanen, A. Harju, and P. Liljeroth, Nat. Phys. **13**, 668 (2017).
[81] D. González-Cuadra, P. R. Grzybowski, A. Dauphin, and M. Lewenstein, Phys. Rev. Lett. **121**, 090402 (2018).
[82] D. González-Cuadra, A. Dauphin, P. R. Grzybowski, P. Wójcik, M. Lewenstein, and A. Bermudez, Phys. Rev. B **99**, 045139 (2019).

4.1.3 First–principles study of the nontrivial topological phase in chains of *3d* transition metals

A. Kobiałka, P. Piekarz, A. M. Oleś, A. Ptok, Phys. Rev. B **101**, 205143 (2020)

One of the many platforms, where MBS emergence can be expected are magnetic atoms deposited on a superconducting surface. Here, we investigate *3d* transition metal chains, their possibility for hosting the topological superconductivity as well as the effect of deposition of magnetic atom chains on the superconducting Pb surface. Usually, Slater-Koster parameters for bulk systems were used in order to model 1D systems. Except for the finite size effect, change in the number of next neighbours and the length of lattice constant show crucial differences between 1D and bulk systems. Stemming from this, we developed a tight binding model in Wannier orbitals, obtained from DFT calculations. This allowed us to compute the values of Pfaffians for a set of freestanding chains (i.e., Mn, Cr, Fe, and Co) suspended in vacuum, and chains deposited on the superconductor, from which we can infer the topological state of the system. Change in parameters has a substantial effect on the band structure that resulted in our findings standing in opposition to previous studies on similar freestanding systems. Moreover, the inclusion of superconducting surface into DFT calculations, turned out to infer a topologically nontrivial state existing regardless of the type of *3d* metal used in calculations. These findings show importance of the substrate on the topological properties of the *3d* metallic chains.

Author's contribution: Analysis and discussion of obtained results, partial preparation of manuscript, participation in preparing the response for Referees.

First-principles study of the nontrivial topological phase in chains of 3*d* transition metals

Aksel Kobiałka,[1,*] Przemysław Piekarz,[2,†] Andrzej M. Oleś,[3,4,‡] and Andrzej Ptok[2,§]

[1]*Institute of Physics, Maria Curie-Skłodowska University, Plac Marii Skłodowskiej-Curie 1, PL-20031 Lublin, Poland*
[2]*Institute of Nuclear Physics, Polish Academy of Sciences, ulica W. E. Radzikowskiego 152, PL-31342 Kraków, Poland*
[3]*Institute of Theoretical Physics, Jagiellonian University, Profesora Stanisława Łojasiewicza 11, PL-30348 Kraków, Poland*
[4]*Max Planck Institute for Solid State Research, Heisenbergstrasse 1, D-70569 Stuttgart, Germany*

(Received 29 November 2019; accepted 5 May 2020; published 22 May 2020)

Recent experiments have shown the signatures of Majorana bound states at the ends of magnetic chains deposited on a superconducting substrate. Here, we employ first-principles calculations to directly investigate the topological properties of 3*d* transition metal nanochains (i.e., Mn, Cr, Fe and Co). In contrast to the previous studies [Nadj-Perge *et al.*, Science **346**, 602 (2014) and Ruby *et al.*, Nano Lett. **17**, 4473 (2017)], we found the exact tight-binding models in the Wannier orbital basis for the isolated chains as well as for the surface–deposited wires. Based on these models, we calculate the topological invariant of $\mathbb{Z}_2$ phases for all systems. Our results for the isolated chains demonstrate the existence of the topological phase only in Mn and Co systems. We also considered a noncollinear magnetic order as a source of the nontrivial topological phase and found that this type of magnetic order is not a stable ground state in the Fe and Co isolated chains. Further studies showed that a coupling between the chain and substrate leads to strong modification of the band structure. Moreover, the analysis of the topological invariant indicates the possibility of emergence of the topological phase in all studied nanochains deposited on the Pb surface. Therefore, our results demonstrate an important role of the coupling between deposited atoms and a substrate for topological properties of nanosystems.

DOI: 10.1103/PhysRevB.101.205143

I. INTRODUCTION

Prediction of localization of the Majorana bound states (MBSs) at the ends of the one-dimensional chain [1] initiated intensive studies of this phenomenon in a wide array of systems [2–5]. Typically, to generate MBSs, a mutual interplay between the conventional *s-wave* superconductivity, Zeeman magnetic field, and strong spin-orbit coupling (SOC) is essential [6,7]. This condition can be achieved in semiconductor–superconductor nanostructures, where a semiconducting nanowire is deposited on a conventional superconductor [8–15]. Other theoretically predicted possibilities of the emergence of MBSs are chains of the magnetic atoms [16–19] or nanoparticles [20] located on a superconductor. The interplay between the magnetic moments and proximity-induced superconductivity can drive the system into a topological phase [21,22].

Scanning tunneling microscopy (STM) technique has been proven to be an excellent tool in this venue. An experiment based on the theoretical prediction was carried out in 2014 by Yazdani group [23]—the authors presented evidence of the forming of topological Majorana zero modes in iron chains on the superconducting Pb(110) surface. Additionally, high-resolution experiments with superconducting tips confirmed the existence of zero-energy excitations in this type of chain [24] and also in the form of zero-energy local density of states measurements [25]. More recently, spin-dependent experiments [26] demonstrated the emergence of the MBS in this system [27].

The mentioned experiments are based on the existence of the Yu–Shiba–Rusinov (YSR) in-gap bound states induced by a magnetic impurity [28–30]. The interaction of the local spin of impurity with the Cooper pairs in superconductors gives rise to a low-lying excited state within the gap of the quasiparticle excitation spectrum [31,32]. Progress in experimental techniques allows the study of the YSR bound states of individual magnetic atoms [33]. Such studies of the YSR bound states were performed for many 3*d* transition metal adatoms, e.g., Ti [34], Mn [33,35–39], Cr [38–41], Fe [42,43], or Co [44]. Forming a chain of magnetic adatoms can lead to the evolution of the YSR bound states to the zero-energy MBS [45–47]. In the case of the chains of magnetic atoms, the rich spectrum of the in-gap states can be observed [48,49].

Experimentally, the monoatomic chains are usually prepared by the electron beam evaporation technique. This method was used successfully in the case of the Fe [23–25,27,50] and Co [51] chains. However, recent progress in atomic engineering [52–57] allows for *in situ* construction of the magnetic atomic chains [58–66]. This technique can help to produce monoatomic chains on the superconducting surfaces (Fig. 1). In relation to chains prepared by electron beam technique [23–25,27,50,51], artificial magnetic chains can have predetermined parameters, such as distance between atoms. An additional advantage of this technique is the possibility for preparation of ideally homogeneous systems. By pushing this idea further, the pristine, homogeneous chains

*akob@kft.umcs.lublin.pl
†piekarz@wolf.ifj.edu.pl
‡a.m.oles@fkf.mpg.de
§aptok@mmj.pl

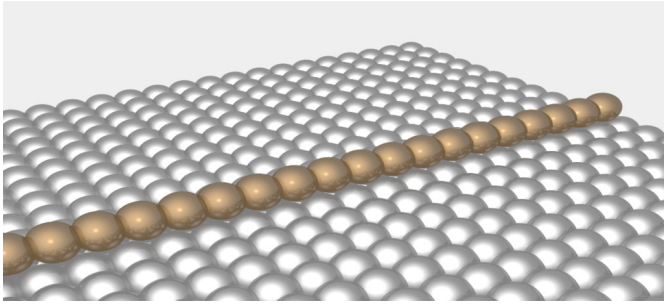

FIG. 1. Schematic representation of the discussed system: The monoatomic magnetic chain of 3*d* transition metal (brown atoms) at the surface of superconductor (gray atoms).

of 40 atoms and longer were produced [66] by Wiesendanger group, using an *in situ* STM assembly [64]. The zero-energy MBS at the Fe chain ends became more stable with increase of the nanochain length.

In the context of the mentioned experiments, in this paper we study the physical properties of monoatomic chains of magnetic 3*d* transition metal atoms, i.e., Mn, Cr, Fe, and Co. Our studies take advantage of first-principles calculations and the parameters obtained using this method are applied in a tight-binding model (TBM) to calculate topological invariants of the investigated systems. In previous studies, the analysis of topological properties of monoatomic chains was based on TBMs with the hopping parameters taken from bulk crystals [23,51]. Since the electronic band structures of monoatomic chains significantly differ from those of crystals, such a simplified approach may lead to wrong conclusions. Surprisingly, our calculations for the 3*d* monoatomic chains show that a nontrivial topological phase may exist only in Mn and Co free-standing nanowires, while this phase is excluded in Fe or Cr chains. These results for isolated chains are incompatible with previous studies. We also study noncollinear magnetic order as a possible origin of topological phases as well as the impact of the substrate on electronic band structures of monoatomic chains. Additionally, we investigate the influence of the substrate on topological properties of magnetic chains. In this case, we show that regardless of the modeled metal atom set, the system supports a topological phase. Therefore, the substrate plays a crucial role in the emergence of topological properties of the studied systems.

This paper is organized as follows. First, we describe in detail the methods of investigation (Sec. II). Next, we present and discuss our numerical results (Sec. III). Results for the isolated chains are presented in Sec. III A and for the chains deposited on the substrate in Sec. III B. The latter is supplemented by the magnetic order reported in Sec. III C. Finally, we summarize the results in Sec. IV.

II. METHODS

The ground state of electronic structure can be described by density functional theory (DFT) [67]. Typically, the electronic band structure is in a good agreement with experimental data given by, e.g. angle-resolved photoemission spectroscopy. In our paper, we adopt the following method of investigation: (i) DFT calculations of electronic properties and (ii) construction of a realistic TBM.

This allows for the comparison of the parameters obtained for bulk crystals with the results from calculations for isolated nanowires, i.e., an atomic chain in the absence of substrate. The parameters calculated for the atomic chains are used to obtain the topological invariants for the isolated nanochains. Next, we find the band structure for the chains deposited on a superconducting substrate, which corresponds to a realistic situation where the orbitals of atoms from the chain hybridize with the substrate orbitals (cf. Fig. 1). Finally, we derive the TBM and obtain the topological invariants for the nanochains deposited on the Pb surface.

A. *Ab initio* calculations

The DFT calculations were performed using the QUANTUM ESPRESSO code [68,69]. The exchange-correlation functional was calculated within the generalized gradient approximation [70] developed by Perdew, Burke, and Enzerhof [71]. The wave functions in the core region were evaluated using the full potential projector augmented-wave method [72,73]. We performed calculations in the absence and in the presence of the SOC, using pseudopotentials developed in frame of PSLIBRARY [74]. Within the DFT calculations, we executed a full optimization of the structural parameters for conventional cells (for bcc and hcp structures) and primitive cells (for an isolated chain with the vacuum layer of 10 Å).

Additionally, to study the impact of the additional neighbors in the chain states, we modeled a system with the substrate in approximated form, where the chain is coupled to one layer of superconducting substrate (containing three atoms of Pb) with vacuum layer of 10 Å. In the calculations, we used the Monkhorst-Pack scheme [75] with $12 \times 12 \times 12$ ($12 \times 12 \times 4$) **k** grid in the case of Fe-bcc (Co-hcp) and $4 \times 4 \times 12$ for isolated nanowires and nanowires deposited on the Pb substrate. We have also used the cutoff for charge density with the value suggested by using pseudopotentials increased by 100 Ry and cutoff for wave functions with the value equal to a quarter of the charge density cutoff.

B. Tight-binding model

Using the band structure obtained from the DFT calculations, we can find the realistic TBM of the monoatomic chains in the basis of the maximally localized Wannier functions (MLWFs) [76–78]. We perform this part of the calculations using the WANNIER90 software [79–81]. This allows for description of our system by using TBM in the form

$$\mathcal{H}_0 = \sum_{\boldsymbol{R}\boldsymbol{R}',\mu\nu,\sigma\sigma'} T_{\mu\nu}^{\sigma\sigma'}(\boldsymbol{R},\boldsymbol{R}') c_{\boldsymbol{R}\mu\sigma}^{\dagger} c_{\boldsymbol{R}'\nu\sigma'}, \tag{1}$$

where $c_{\boldsymbol{R}\mu\sigma}^{\dagger}$ ($c_{\boldsymbol{R}\mu\sigma}$) is the creation (annihilation) operator in the MLWF basis. Here $T_{\mu\nu}^{\sigma\sigma'}(\boldsymbol{R},\boldsymbol{R}')$ is the matrix describing the electron hopping from orbital ν located at $\boldsymbol{R}'$ with spin σ' to orbital μ located at $\boldsymbol{R}$ with spin σ. In this description, the hopping without and with the spin-flip component corresponds to the kinetic and SOC term, respectively.

When the chain is coupled to the superconductor, the superconducting gap Δ can be induced by the proximity effect of

superconducting substrate (Pb in our case). Then, our system can be described by the Hamiltonian,

$$\mathcal{H} = \mathcal{H}_0 + \mathcal{H}_{\mathrm{SC}}, \tag{2}$$

where the first term denotes the "free" electrons (band structure), i.e., the Hamiltonian Eq. (1) in momentum space,

$$\mathcal{H}_0 = \sum_{\boldsymbol{k}} H_{\mu\nu}^{\sigma\sigma'}(\boldsymbol{k}) c_{\boldsymbol{k}\mu\sigma}^{\dagger} c_{\boldsymbol{k}'\nu\sigma'}, \tag{3}$$

where $H_{\mu\nu}^{\sigma\sigma'}(\boldsymbol{k}) = \sum_{\boldsymbol{R},\boldsymbol{R}'} \exp[i\boldsymbol{k}\cdot(\boldsymbol{R}-\boldsymbol{R}')] T_{\mu\nu}^{\sigma\sigma'}(\boldsymbol{R},\boldsymbol{R}')$. The second term describes superconductivity and can be written in the BCS-like form

$$\mathcal{H}_{\mathrm{SC}} = \Delta \sum_{\boldsymbol{k}\nu} (c_{-\boldsymbol{k}\nu\downarrow} c_{\boldsymbol{k}\nu\uparrow} + \mathrm{H.c.}), \tag{4}$$

where Δ is half of the superconducting gap (for lead $2\Delta \sim 2.7$ meV [38,82–84]). Now, $c_{\boldsymbol{k}\mu\sigma}^{\dagger}$ ($c_{\boldsymbol{k}\mu\sigma}$) is the creation (annihilation) operator of the electron with spin σ and momentum $\boldsymbol{k}$ in orbital μ.

C. Nontrivial topological phase

In the case of the one-dimensional hybrid semiconductor-superconductor nanowires [5,8–15], the phase transition from a trivial to topological phase can occur when splitting of the bands given by the SOC is larger than the superconducting gap [85–87],

$$\mu_B H_z = \sqrt{\tilde{\mu}^2 + \Delta^2}, \tag{5}$$

where μ_B is the Bohr magneton, H_z is the magnetic field parallel to the nanowire, Δ is the superconducting gap, while $\tilde{\mu}$ is the Fermi energy computed at the bottom of the band. In our case, the magnetic moment plays the role of the effective "magnetic field." Here, it should be noted that in contrast to the hybrid nanostructure, realization of the topological phase is given only by the intrinsic properties of the monoatomic chain, e.g., magnetic order or the position of Fermi level (which strongly depends on the type of atoms and the lattice parameters). Therefore, it is crucial to obtain the correct TBM of the studied system and our proposed solution is to use the method described in the previous section.

The topological phase can be described by a topological invariant, e.g., the winding number w [88]. However, in our case, we describe the topological phase by the Pfaffian of the transformed Hamiltonian, which is a $\mathbb{Z}_2$ invariant [1]. This type of invariant can be defined for any system described by the Bogoliubov–de Gennes equations [89], which is equivalent to the Hamiltonian $\mathcal{H}$. Because our system has the particle-hole symmetry, i.e., $\boldsymbol{k} = 0, \pi$ are the particle-hole symmetric points in the Brillouin zone [90], the Pfaffian is given by [89]

$$\mathcal{Q} = \mathrm{sgn}\left[\frac{\mathrm{Det}(A(\boldsymbol{k}=\pi))}{\mathrm{Det}(A(\boldsymbol{k}=0))}\right] = (-1)^{w}. \tag{6}$$

Here, $A(\boldsymbol{k})$ denotes the element of Hamiltonian matrix in the block off-diagonal form [91], which can be derived from the unitary transformation $\mathcal{U}$ [92],

$$\mathcal{U}\mathcal{H}\mathcal{U}^{\dagger} = \begin{pmatrix} 0 & A(\boldsymbol{k}) \\ A^{T}(-\boldsymbol{k}) & 0 \end{pmatrix}, \tag{7}$$

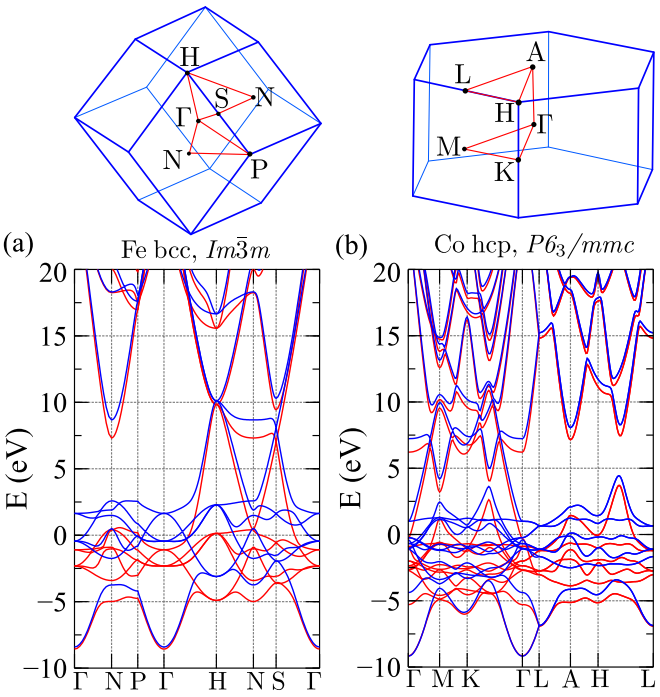

FIG. 2. First Brillouin zone and band structures of the Fe bcc and Co hcp crystals. Results in the absence of the SOC. Red and blue colors denote the states with spin ↑ and ↓, respectively. Fermi level is located at zero energy.

where $A_{\sigma\sigma'}^{\mu\nu}(\boldsymbol{k}) = H_{\sigma\sigma'}^{\mu\nu}(\boldsymbol{k}) + \Delta\delta_{\bar{\sigma}\sigma'}\delta_{\mu\nu}$. The topological phase is realized when $\mathcal{Q} = -1$.

III. NUMERICAL RESULTS

We start from a short description of the Fe bcc and Co hcp bulk systems. From the DFT self-consistent calculations, we find that the Fe bcc (Co hcp) structures have magnetic moments equal to 2.1988 μ_B (1.6693 μ_B) and lattice constant of 2.4512 Å (2.4881 Å). For the optimized systems, we find the electronic band structures (Fig. 2). In both cases, the $3d$ orbitals are accumulated around the Fermi level, while the rest of states (unoccupied $4p$ states) are located far above the Fermi level (approximately above 7.5 eV).

A. Isolated chains

Now we discuss the results for the isolated magnetic chains. Here, we performed the volume relaxation of one magnetic atom with the 15 Å of vacuum in $\hat{x}$ and $\hat{y}$ directions (chain is aligned along the $\hat{z}$ direction). From this, we find the distances between atoms in the isolated nanowires (see Table I). The obtained distances in both Fe and Co chains are approximately 0.2 Å smaller than those in the bulk materials, while magnetic moments are larger. Modification of these two quantities must have a substantial impact on the parameters of the model describing the atomic chains. It is clearly visible in the band structures of the isolated chains (see Fig. 3). We observe a strong shift of the p-orbital states to lower energies (cf. Figs. 2 and 3, states initially located above 10 eV are shifted to energies around 4 eV). This leads to the strong hybridization between these states with the $3d$ levels. More

TABLE I. Distances between atoms (in Å) and magnetic moments (in μ_B) in the isolated chains.

3*d* element	Cr	Mn	Fe	Co
distance	2.07	2.30	2.23	2.15
mag. mom. w/o SOC	1.94	3.50	2.89	2.05
mag. mom. w/SOC	1.78	3.55	2.94	2.05

importantly, one additional band crosses the Fermi level. As a consequence, isolated monoatomic chains cannot be described—not only by a simple single-orbital TBM but even by a model incorporating as much as ten 3*d* orbitals.

The shapes of the obtained bands associated with 3*d* orbitals are approximately given as a cosinelike function of momentum (see Fig. 3), which is typical for a one-dimensional chain. However, when 3*d* states hybridize with other orbitals, a relatively large "deformation" of this shape (marked by green circle) takes place. Therefore, the band structure cannot be approximated by the dispersion relation of a simple one-dimensional lattice anymore. The other consequence is an avoided crossing behavior of the hybridized bands (marked by pink circle).

Introduction of the SOC in the calculations does not change the results qualitatively. As usual, the band degeneracy is lifted thanks to SOC, however, the shape of band dispersion is not influenced. The magnetic moments found in noncollinear calculations have approximately similar values, independent

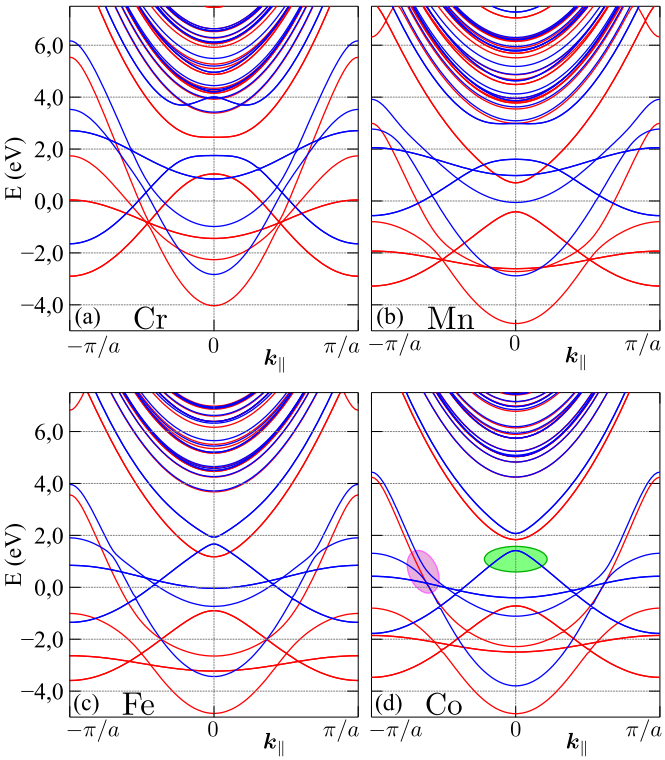

FIG. 3. Electron band structures of Cr, Mn, Fe, and Co nanowires as labeled. Results obtained at absence of the SOC. Red and blue colors denote states with the spin ↑ and ↓, respectively. Fermi level is located at zero energy.

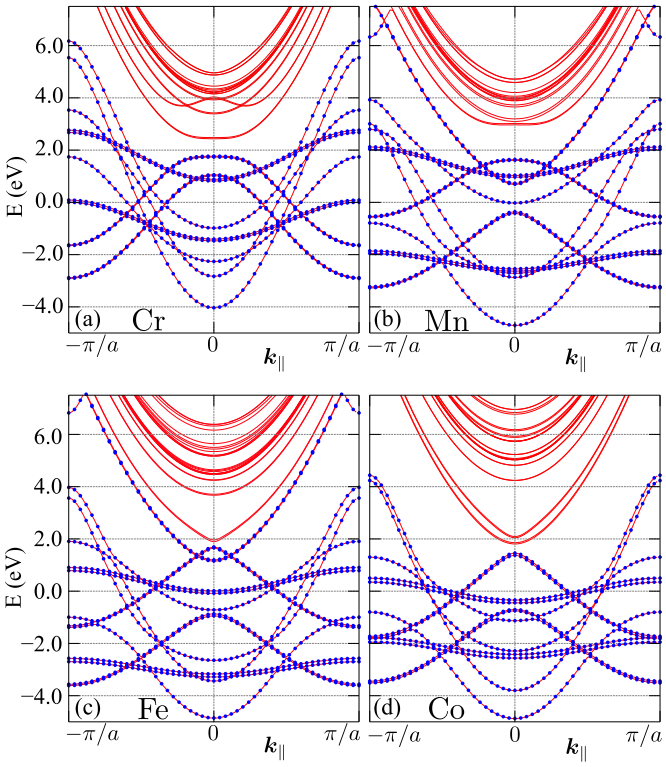

FIG. 4. The same as in Fig. 3 in the presence of the SOC and magnetic moment parallel to the nanowire. Solid red lines and blue dots correspond to band structures obtained from the DFT and TBM calculations, respectively. Fermi level is located at zero energy.

of its direction. Still, the largest splitting of the bands can be found when the magnetic moments are parallel to the nanowire. Even though splitting of the bands due to the SOC depends on the atomic mass [93], it is much smaller for isolated nanowires than in the bulk. Here it should be mentioned that in the previous studies of isolated Fe and Co free-standing chains [23,51], a value of the SOC was overestimated.

In conclusion, a difference in the distance between atoms in the chain and in the bulk, as well as a reduced number of neighboring atoms, leads to severe modification of most of the system parameters, e.g., hoping integrals, magnetic moments, or SOC. Additionally, *p*-type orbitals play an important role in a proper description of the isolated chains.

1. Realization of a nontrivial topological phase

In the previous studies of the magnetic monoatomic chains, to describe isolated nanowires capable of hosting the topologically nontrivial phase, the Slater-Koster TBM parameters for bulk were used [23,51]. In the case of the Fe chain, the hopping integral values were taken for the nearest-neighbor distance of the bulk Fe (bcc, $Im\bar{3}m$, space group 229), which is 2.383 Å [94]. Similarly, in the case of the Co chain, the hopping integral was calculated for the nearest neighbor distance of the bulk Co (hcp, $P6_3/mmc$, space group 194) with $a = 2.486$ Å [95]. Taking into account strong modifications of the band structure in the isolated chains (see Figs. 3 and 4), in particular, a different number of bands crossing the Fermi level, such assumptions can lead to incorrect conclusions

TABLE II. Signs of the Pfaffians in the time-reversal invariant momenta and values of the topological number $\mathcal{Q}$. Results obtained for the isolated chains.

	3*d* element			
k	Cr	Mn	Fe	Co
0	+	+	−	+
π	+	−	−	−
$\mathcal{Q}$	+1	−1	+1	−1

regarding the existence of the nontrivial topological phase. Moreover, in the general case, fitting the band structure with the Slater-Koster parameters can give incorrect results in comparison with the *ab initio* band structure [96].

To precisely describe the band structures of isolated chains, we found the TBM in the MLWF based on the DFT calculations (cf. Fig. 4). In a general case, the TBM model describing our system around the Fermi level is mostly composed of *d*-like orbitals (typical for transition metals). However, contrary to the bulk models, additional *p*-like orbitals should be included in the model.

Next, by employing these models, we calculate the topological number $\mathcal{Q}$ given by Eq. (6). Additionally, we assume that the superconducting gap induced by the proximity effect in nanowires is equal to 3 meV (which is close to the experimental result of 2.7 meV). That small, qualitative, difference does not change results, which are presented in Table II. As we mentioned before, the topological phase can be realized only when $\mathcal{Q} = -1$. From our calculations, we can conclude that the topological phase can be induced only in the Mn and Co nanowires.

Information about the realization of a nontrivial phase can be attained from the number of the bands crossing the Fermi level within a half of the Brillouin zone [97]. If the number of crossing bands is odd, then the realization of the MBSs at the ends of the finite nanowire is expected. In the case of the Fe chain described by the model with bulk parameters [23], this number was almost always odd, making the presence of MBSs at the ends of the chains almost guaranteed. On the other hand, for the Co chain with the SOC, the number of crossings was even [51]. From our results (cf. Fig. 4), an even number of bands crossing the Fermi level within half of the Brillouin zone are realized in the Cr and Fe nanowire. These analyses yield comparable results to those obtained from $\mathcal{Q}$, supporting the hypothesis about realization of the nontrivial topological phase in Mn and Co nanowires.

The obtained results contradict the previous studies of Fe and Co chains [23,51], where the topological phase was found only in the Fe chain. Here we must keep in mind that such results are extremely sensitive to parameters used in calculations. For instance, distances between atoms can modify the band structure by changing the overlap between orbitals. Similarly, the number of occupied bands for momentum 0 or π can strongly depend on a position of the Fermi level—this should be important in the case of Mn, Fe, or Cr isolated chains, where bands at momentum 0 or π are located close to the Fermi level. In such case, a small modification of the hopping integrals, as well as the SOC or magnetic moments, can change a value of $\mathcal{Q}$ drastically and, as a consequence, topological properties of the system.

2. Noncollinear magnetic moments

A topologically nontrivial phase is not exclusive to a ferromagnetic chain—in some situations, topological effects can also be induced by noncollinear magnetic moments. In the chain of one-orbital magnetic "atoms," the spiral order can minimize the free energy of the system, leading to the emergence of a topological phase [98,99]. In this situation, the Majorana quasiparticles can be found at the ends of the chain [21,22,46,100]. This is possible due to the fact that the spiral magnetic order leads to the same effects as the SOC together with the external magnetic field [101,102].

In a more realistic situation of a multiorbital chain, the description using only a simple model may not be sufficient [17]. However, the DFT calculations allow for a comparison of the energies of the chains with different noncollinear magnetic orders (Table III). From this comparison, we can find the order which minimizes the energy of the system (values in the box). As we can see, in the case of Fe and Co atoms, the ferromagnetic order is more favorable. In the Fe chain, the magnetic moment should be perpendicular to the chain, in contrast to the parallel moment in the Co chain. Interestingly, in the Cr chain, the antiferromagnetic order is the most stable one, while in the Mn chain a chiral order with the $2\pi/3$ period is the lowest energy state. Thus, we do not expect the noncollinear magnetic order as a probable source of the Majorana quasiparticles in Fe and Co magnetic chains.

B. Chains deposited on the substrate

Now we will discuss the results obtained for the chains deposited on a substrate for the system presented in Fig. 1. To simulate the measurements described in Refs. [23,51], we take the Pb(110) surface as the substrate. To simplify the band structure and make it more readable, in the calculations we have used a system shown in the inset of Fig. 5 containing one transition metal atom and three lead atoms in the unit cell. In the first approximation, such a system can help us to describe the influence of neighboring Pb atoms on the transition metal chain.

Figure 6 presents the density of states (DOS) in the case of the isolated chain (dashed line) and the chain deposited on the substrate (solid line). In the latter case, contributions of the deposited atoms to the total DOS are shown by solid-colored areas. Comparing to the isolated chains, all 3*d*-orbital bands are modified and become narrower. The weakest effect of the substrate is observed for the Fe chain, where the positions of spin-up states very well correspond to those in the isolated chain. Analyzing the electron DOS, we can also explain the modification of the magnetic moments induced by the substrate. In the case of Cr and Mn, the atoms are nearly fully spin polarized (all $\downarrow$ states are above the Fermi level, while $\uparrow$ below). In contrast, a small magnetic moment of Co results from the shift of the $\downarrow$ states to energies below the Fermi level.

Deposition of the chains on the substrate changes the system symmetry and allows for the hybridization between the orbitals in the chain and the substrate. These properties lead to the modification of the band structure of the studied system

TABLE III. Comparison of the energies between noncollinear magnetic orders with magnetic moments lying in the plane containing the chain ($E_\parallel$) and in the plane perpendicular to the chain ($E_\perp$), $\delta E = E_\parallel - E_\perp$, which plays the role of the magnetic anisotropy energy. The angle of the magnetic moment rotation in space is given by φ, which depends on the number of atoms in the magnetic unit cell n, i.e., $\varphi = 2\pi/n$. Results obtained in the presence of SOC, in eV per atom.

φ	Cr		Mn		Fe		Co	
	$E_\parallel - E_0$	$E_\perp - E_0$	$E_\parallel - E_0$	$E_\perp - E_0$	$E_\parallel - E_0$	$E_\perp - E_0$	$E_\parallel - E_0$	$E_\perp - E_0$
0	-6.5×10^{-4}	4.2×10^{-6}	−1.538	−1.538	−1.101	**−1.108**	**−0.491**	−0.470
	$\delta E = -6.5 \times 10^{-4}$		$\delta E = 7.8 \times 10^{-7}$		$\delta E = 3.4 \times 10^{-6}$		$\delta E = -0.020$	
π	**−1.057**	−1.056	−1.794	−1.794	−0.800	−0.799	−0.074	−0.025
	$\delta E = -8.3 \times 10^{-4}$		$\delta E = 3.0 \times 10^{-5}$		$\delta E = -1.3 \times 10^{-3}$		$\delta E = -0.049$	
$2\pi/3$	−0.582	−0.582	−1.828	**−1.828**	−0.923	−0.923	−0.144	−0.149
	$\delta E = -4.3 \times 10^{-8}$		$\delta E = 1.3 \times 10^{-4}$		$\delta E = -1.7 \times 10^{-6}$		$\delta E = 0.006$	
$\pi/2$	−0.420	−0.420	−1.766	−1.766	−1.047	−1.015	−0.310	−0.318
	$\delta E = 0.0$		$\delta E = 3.2 \times 10^{-8}$		$\delta E = -0.032$		$\delta E = 0.008$	
$2\pi/5$	−0.914	−0.366	−1.707	−1.707	−1.089	−1.089	−0.460	−0.349
	$\delta E = -1.6 \times 10^{-7}$		$\delta E = -4.0 \times 10^{-7}$		$\delta E = -2.8 \times 10^{-7}$		$\delta E = 0.041$	

(Fig. 7). To increase the readability of the band structure, the projection of the states into transition-metal atoms are shown by colors in the background. From the comparison of the band structures of the isolated chain and the deposited chain, see Figs. 3 and 7, respectively), we can find the influence of the substrate on the chain bands. The bands associated with transition-metal atoms have narrower bandwidth with respect to the isolated nanowire. This is equivalent to the modification of the hopping integrals between the atomic orbitals.

1. Nontrivial topological phase

Now we perform the analysis of existence of the topological phase in the chains deposited on the Pb surface. Similarly, like in the previous case, in the first step, we found the TBM in MLWF based on the DFT calculations (cf. Fig. 8). In contrast to the models of isolated chains, here TBMs are based on $3d$ orbitals of transition metals and $6p$ orbitals of Pb. In total, our models take into account 30 orbitals and reproduce band structures around the Fermi level very well. As we can see, in every case, around 4 eV, we can observe strong interplay between orbitals included in the model and those excluded (at the Γ point). For the developed models, we calculate topological number $\mathcal{Q}$ (results are included in Table IV). Surprisingly, in contrast to the isolated chains, topological phase is supported in every case of the chains

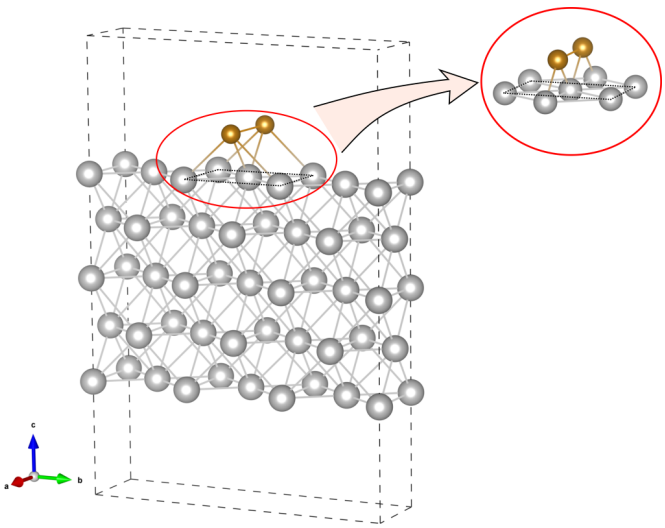

FIG. 5. Schematic representation of the unit cell (black dashed line) in the case of a monoatomic chain deposited on the Pb(110) surface. To check the influence of the neighboring atoms on the band structure of the chain, for simplicity we consider a system in the form presented in the inset (containing one transition metal atom and three lead atoms in the unit cell). The image was rendered using VESTA software [103].

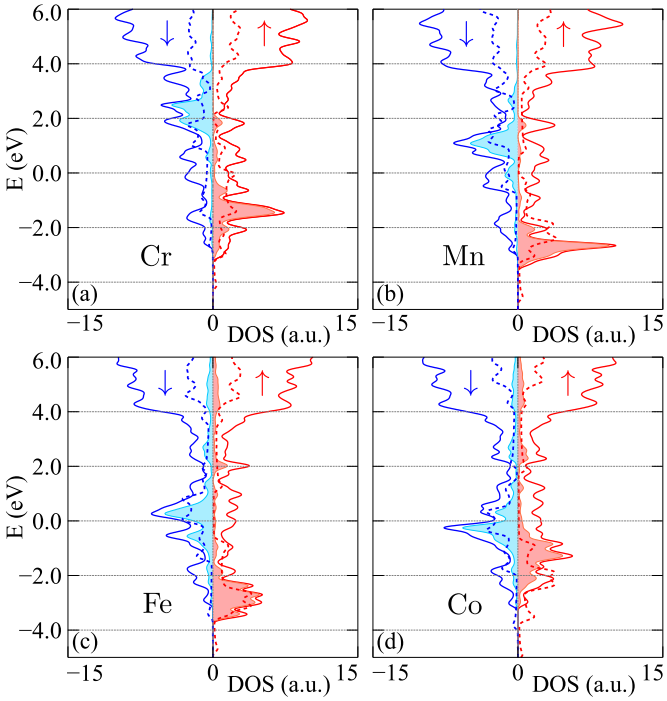

FIG. 6. Comparison of the electronic density of states (DOS) for chains (as labeled) isolated and deposited on the substrate in the approximated case (as shown in Fig. 5). Red and blue lines denote states with ↑ and ↓ spin, respectively. Solid areas show contribution of the deposited atoms. Fermi level is located at zero energy.

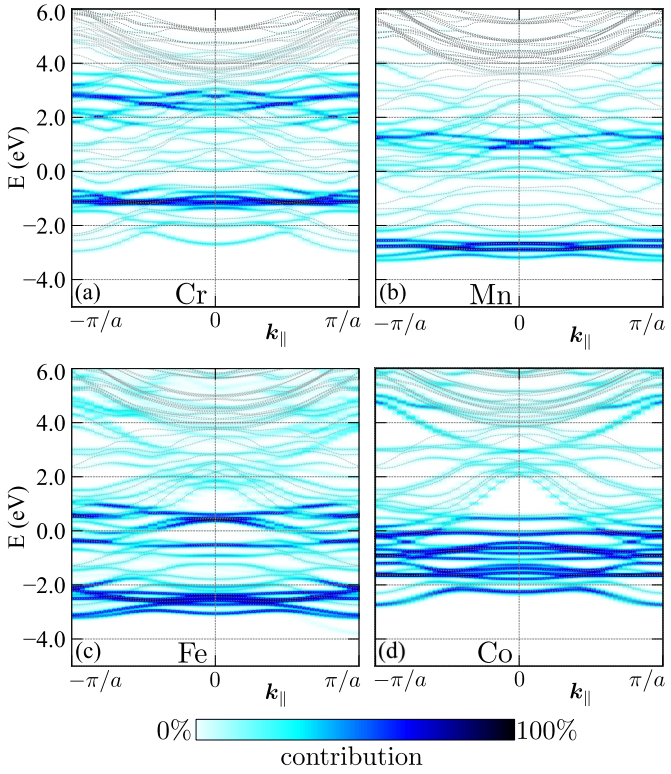

FIG. 7. Electronic band structures of nanowires (as labeled) deposited on the substrate (as shown in Fig. 5). Results in the presence of the SOC. Background color shows contribution of the deposited atoms. Fermi level is located at zero energy.

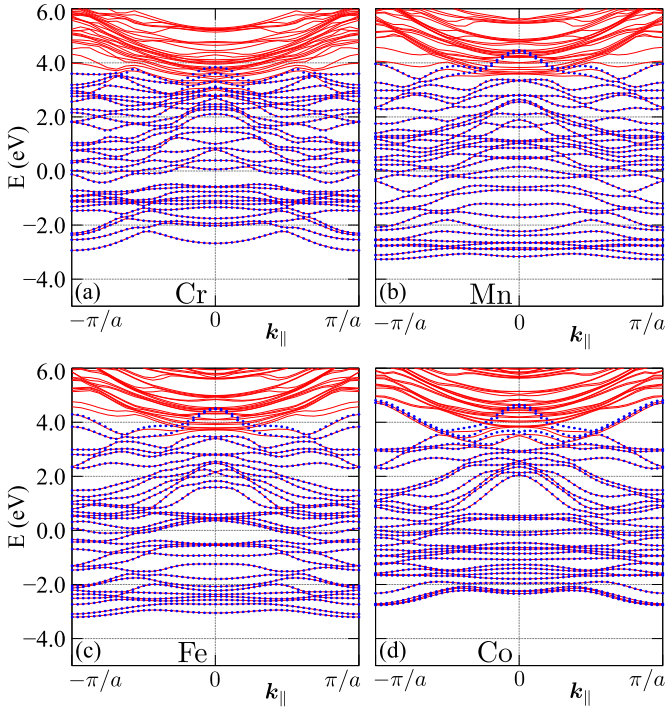

FIG. 8. Comparison of the band structures obtained from the DFT and TBM calculations (red lines and blue dots, respectively). Results for nanowires deposited on Pb(110) surface (as shown in Fig. 5). Fermi level is located at zero energy.

TABLE IV. Signs of the Pfaffians in the time-reversal invariant momenta and values of the topological number $\mathcal{Q}$. Results for nanowires deposited on Pb(110) surface (as shown in Fig. 5).

	3*d* element			
k	Cr	Mn	Fe	Co
0	−	+	−	−
π	+	−	+	+
$\mathcal{Q}$	−1	−1	−1	−1

deposited on the substrate. These results show an important role of the substrate in stabilization of the topological phase.

C. Magnetic order

Now we will shortly discuss the magnetic order of the chains deposited on the substrate. Coupling the chain to the Pb atoms leads to the increase of the magnetic moments only in the case of Cr atom (cf. Tables I and V). One should also notice the strong suppression of the magnetic moment in the Co chain.

As we mentioned in previous paragraphs, noncollinear magnetic moments can be a source of the topological phase. This type of magnetic structure can be stabilized by the conduction-electron-mediated Ruderman–Kittel–Kasuya–Yosida (RKKY) interaction [104]. For instance, early studies of the RKKY mechanism shown that the ferromagnetic (FM) order in Fe chains is unstable [105]. However, more recent theoretical studies allow for existence of the FM, antiferromagnetic (AFM), or noncollinear magnetic orders [106,107], depending on the system parameters. Additionally, it was experimentally shown that the small cluster of magnetic atoms can exhibit AFM instability [61,62]. Similarly, the noncollinear magnetic order in Fe double chains [108] have been reported. Here, the RKKY interaction can lead to stabilization of the noncollinear magnetic orders [109]. On the other hand, a role of the Dzyaloshinskii–Moriya interaction (DMI) can be important [65] in the case of the chain deposited on a substrate, due to an interface between these two systems [110]. Additionally, the strength of DMI can depend on the position of a chain with respect to a surface [111]. In conclusion, both types of interactions, as well as a its mutual interplay, have an important role in adjusting the interatomic iron distance, which enables tailoring of the rotational period of the spin-spiral [65]. The inclusion of these interactions in calculations with the substrate may change the ground state and support the topological phase. However, unfortunately, such long-range interactions like RKKY cannot be included in our calculations due to a small size of the cell.

TABLE V. Magnetic moments (in μ_B) in the monoatomic chain deposited on the Pb surface (as shown in Fig. 5). Results in the absence and in the presence of SOC.

3*d* element	Cr	Mn	Fe	Co
mag. mom. without SOC	4.16	3.91	2.78	1.08
mag. mom. with SOC	4.18	3.99	2.77	1.12

Here, we should also remember about a general form of the interaction between electrons inside 3*d* atoms chains [112], which include intra- and interorbital Coulomb repulsions, as well as the Hund's exchange and the pair-hopping term. The existence of strong magnetic moments in 3*d* transition metals cannot be correctly captured within the single-band model. From this, the stabilization of the topological phase should depend not only on the Hund's exchange in partly filled 3*d* orbital states [113,114] but also on other interactions which have negative impact on the emergence of MBSs [115–117].

IV. SUMMARY

In summary, Majorana quasiparticles constitute a very interesting concept of particles, which are indistinguishable from their antiparticles. One of the many platforms in which we expect the emergence of bound states with such properties are systems of magnetic atomic chains deposited on a surface of the conventional superconductor [16–19]. In this paper, we studied the topological phase of the 3*d* transition metal chains, in the form of (i) isolated chains and (ii) chains deposited on the Pb surface.

In Sec. III A, we discussed the freestanding chains which should be treated as a first step in a theoretical description of the experimental system. Previous studies of the 3*d* transition-metal chains [23,51] were based on the Slater-Koster parameters of the bulk systems [118]. Unfortunately, such an approach does not correctly describe the physical properties of the freestanding chains, mostly due to a different number of neighboring sites in chains comparing to a bulk. Additionally, different distances between atoms in both systems lead to the strong modification of the band structure (i.e., hopping integrals between orbitals). To verify this, we developed the TBM in the Wannier orbitals, based on the *ab initio* (DFT) band structures. We have shown that in the case of isolated chains, the additional band crossing the Fermi level exists, which cannot be captured by the simple TBM derived from the bulk electronic structure. Using the obtained TBM, we also calculated the topological quantum number. Hence, we concluded that in the case of isolated chains, the nontrivial topological phase can exist only in the Mn and Co chains. These results are in opposition to previous studies of the Fe and Co chains [23,51], where nontrivial topological phase was reported only in the case of the iron chain.

Next, we performed similar analysis for the chains deposited on the Pb surface (Sec. III B). In this case, we studied the impact of the substrate on topological properties of the system. The interplay between the atoms of the substrate and the chains leads to strong modifications of the electronic properties of the chains. It is clearly visible in the band structure projected onto the chain atoms, as well as in the density of states. Here, we also developed a TBM of this system to calculate the topological index. In contrast to the isolated chains where the influence of the substrate is described only by one parameter (superconducting gap), the incorporation of the surface states in the system leads to the emergence of the nontrivial phase, regardless of the used transition metal. Finally, we have shown in Sec. III C that the magnetic order in the chains deposited on the substrate is a subtle problem and the final order depends on the electronic filling which decides about the RKKY interaction.

We hope that our studies will provide substantial information about the properties of magnetic chains and will stimulate further research in this field. Our findings demonstrate significant influence of the substrate on topological properties of the magnetic chains. Therefore, we conclude that a substrate constitutes a crucial part for a correct description of nanosystems and should be included in future studies based on *ab initio* methods.

ACKNOWLEDGMENTS

We thank Pascal Simon and Wojciech Tabiś for inspiring discussions and valuable comments. A.P. is grateful to Laboratoire de Physique des Solides (CNRS, Université Paris-Sud) for hospitality during a part of the work on this project. This work was supported by the National Science Centre (NCN, Poland) under Projects No. 2018/31/N/ST3/01746 (A.K.), No. 2017/25/B/ST3/02586 (P.P.), No. 2016/23/B/ST3/00839 (A.M.O.), and No. 2016/23/B/ST3/00647 (A.P.). A.M.O. is grateful for the Alexander von Humboldt Foundation Fellowship (Humboldt-Forschungspreis).

[1] A. Y. Kitaev, Unpaired Majorana fermions in quantum wires, Phys. Usp. **44**, 131 (2001).

[2] C. W. J. Beenakker, Search for Majorana fermions in superconductors, Annu. Rev. Condens. Matter Phys. **4**, 113 (2013).

[3] T. D. Stanescu and S. Tewari, Majorana fermions in semiconductor nanowires: Fundamentals, modeling, and experiment, J. Phys.: Condens. Matter **25**, 233201 (2013).

[4] C. W. J. Beenakker, Random-matrix theory of Majorana fermions and topological superconductors, Rev. Mod. Phys. **87**, 1037 (2015).

[5] R. M. Lutchyn, E. P. A. M. Bakkers, L. P. Kouwenhoven, P. Krogstrup, C. M. Marcus, and Y. Oreg, Majorana zero modes in superconductor-semiconductor heterostructures, Nat. Rev. Mater. **3**, 52 (2018).

[6] Y. Oreg, G. Refael, and F. von Oppen, Helical Liquids and Majorana Bound States in Quantum Wires, Phys. Rev. Lett. **105**, 177002 (2010).

[7] R. M. Lutchyn, J. D. Sau, and S. Das Sarma, Majorana Fermions and a Topological Phase Transition in Semiconductor-Superconductor Heterostructures, Phys. Rev. Lett. **105**, 077001 (2010).

[8] V. Mourik, K. Zuo, S. M. Frolov, S. R. Plissard, E. P. A. M. Bakkers, and L. P. Kouwenhoven, Signatures of Majorana fermions in hybrid superconductor-semiconductor nanowire devices, Science **336**, 1003 (2012).

[9] M. T. Deng, C. L. Yu, G. Y. Huang, M. Larsson, P. Caroff, and H. Q. Xu, Anomalous zero-bias conductance peak in a Nb–InSb nanowire–Nb hybrid device, Nano Lett. **12**, 6414 (2012).

[10] A. Das, Y. Ronen, Y. Most, Y. Oreg, M. Heiblum, and H. Shtrikman, Zero-bias peaks and splitting in an Al-InAs nanowire topological superconductor as a signature of Majorana fermions, Nat. Phys. **8**, 887 (2012).

[11] A. D. K. Finck, D. J. Van Harlingen, P. K. Mohseni, K. Jung, and X. Li, Anomalous Modulation of a Zero-Bias Peak in a Hybrid Nanowire-Superconductor Device, Phys. Rev. Lett. **110**, 126406 (2013).

[12] E. J. H. Lee, X. Jiang, M. Houzet, R. Aguado, Ch. M. Lieber, and S. De Franceschi, Spin-resolved Andreev levels and parity crossings in hybrid superconductor-semiconductor nanostructures, Nat. Nanotech. **9**, 79 (2013).

[13] M. T. Deng, S. Vaitiekenas, E. B. Hansen, J. Danon, M. Leijnse, K. Flensberg, J. Nygård, P. Krogstrup, and C. M. Marcus, Majorana bound state in a coupled quantum-dot hybrid-nanowire system, Science **354**, 1557 (2016).

[14] S. M. Albrecht, A. P. Higginbotham, M. Madsen, F. Kuemmeth, T. S. Jespersen, J. Nygård, P. Krogstrup, and C. M. Marcus, Exponential protection of zero modes in Majorana islands, Nature **531**, 206 (2016).

[15] F. Nichele, A. C. C. Drachmann, A. M. Whiticar, E. C. T. O'Farrell, H. J. Suominen, A. Fornieri, T. Wang, G. C. Gardner, C. Thomas, A. T. Hatke, P. Krogstrup, M. J. Manfra, K. Flensberg, and Ch. M. Marcus, Scaling of Majorana Zero-Bias Conductance Peaks, Phys. Rev. Lett. **119**, 136803 (2017).

[16] S. Nadj-Perge, I. K. Drozdov, B. A. Bernevig, and A. Yazdani, Proposal for realizing Majorana fermions in chains of magnetic atoms on a superconductor, Phys. Rev. B **88**, 020407(R) (2013).

[17] J. Li, H. Chen, I. K. Drozdov, A. Yazdani, B. A. Bernevig, and A. H. MacDonald, Topological superconductivity induced by ferromagnetic metal chains, Phys. Rev. B **90**, 235433 (2014).

[18] Y. Peng, F. Pientka, L. I. Glazman, and F. von Oppen, Strong Localization of Majorana End States in Chains of Magnetic Adatoms, Phys. Rev. Lett. **114**, 106801 (2015).

[19] R. Pawlak, S. Hoffman, J. Klinovaja, D. Loss, and E. Meyer, Majorana fermions in magnetic chains, Progr. Part. Nucl. Phys. **107**, 1 (2019).

[20] T.-P. Choy, J. M. Edge, A. R. Akhmerov, and C. W. J. Beenakker, Majorana fermions emerging from magnetic nanoparticles on a superconductor without spin-orbit coupling, Phys. Rev. B **84**, 195442 (2011).

[21] B. Braunecker and P. Simon, Interplay between Classical Magnetic Moments and Superconductivity in Quantum One-Dimensional Conductors: Toward a Self-Sustained Topological Majorana Phase, Phys. Rev. Lett. **111**, 147202 (2013).

[22] J. Klinovaja, P. Stano, A. Yazdani, and D. Loss, Topological Superconductivity and Majorana Fermions in RKKY Systems, Phys. Rev. Lett. **111**, 186805 (2013).

[23] S. Nadj-Perge, I. K. Drozdov, J. Li, H. Chen, S. Jeon, J. Seo, A. H. MacDonald, B. A. Bernevig, and A. Yazdani, Observation of Majorana fermions in ferromagnetic atomic chains on a superconductor, Science **346**, 602 (2014).

[24] M. Ruby, F. Pientka, Y. Peng, F. von Oppen, B. W. Heinrich, and K. J. Franke, End States and Subgap Structure in Proximity-Coupled Chains of Magnetic Adatoms, Phys. Rev. Lett. **115**, 197204 (2015).

[25] R. Pawlak, M. Kisiel, J. Klinovaja, T. Meier, S. Kawai, T. Glatzel, D. Loss, and E. Meyer, Probing atomic structure and Majorana wavefunctions in mono-atomic Fe chains on superconducting Pb surface, Npj Quantum Inf. **2**, 16035 (2016).

[26] R. Wiesendanger, Spin mapping at the nanoscale and atomic scale, Rev. Mod. Phys. **81**, 1495 (2009).

[27] S. Jeon, Y. Xie, J. Li, Z. Wang, B. A. Bernevig, and A. Yazdani, Distinguishing a Majorana zero mode using spin-resolved measurements, Science **358**, 772 (2017).

[28] L. Yu, Bound state in superconductors with paramagnetic impurities, Acta Phys. Sin. **21**, 75 (1965).

[29] H. Shiba, Classical spins in superconductors, Progr. Theor. Exp. Phys. **40**, 435 (1968).

[30] A. I. Rusinov, Theory of gapless superconductivity in alloys containing paramagnetic impurities, Sov. JETP Lett. **9**, 85 (1969).

[31] A. V. Balatsky, I. Vekhter, and J.-X. Zhu, Impurity-induced states in conventional and unconventional superconductors, Rev. Mod. Phys. **78**, 373 (2006).

[32] B. W. Heinrich, J. I. Pascual, and K. J. Franke, Single magnetic adsorbates on *s*-wave superconductors, Progr. Surf. Sci. **93**, 1 (2018).

[33] A. Yazdani, B. A. Jones, C. P. Lutz, M. F. Crommie, and D. M. Eigler, Probing the local effects of magnetic impurities on superconductivity, Science **275**, 1767 (1997).

[34] K. Yang, Y. Bae, W. Paul, F. D. Natterer, P. Willke, J. L. Lado, A. Ferrón, T. Choi, J. Fernández-Rossier, A. J. Heinrich, and Ch. P. Lutz, Engineering the Eigenstates of Coupled Spin-1/2 Atoms on a Surface, Phys. Rev. Lett. **119**, 227206 (2017).

[35] C. P. Moca, E. Demler, B. Jankó, and G. Zaránd, Spin-resolved spectra of shiba multiplets from Mn impurities in MgB_2, Phys. Rev. B **77**, 174516 (2008).

[36] M. Ruby, Y. Peng, F. von Oppen, B. W. Heinrich, and K. J. Franke, Orbital Picture of Yu-Shiba-Rusinov Multiplets, Phys. Rev. Lett. **117**, 186801 (2016).

[37] M. Ruby, B. W. Heinrich, Y. Peng, F. von Oppen, and K. J. Franke, Wave-Function Hybridization in Yu-Shiba-Rusinov Dimers, Phys. Rev. Lett. **120**, 156803 (2018).

[38] S.-H. Ji, T. Zhang, Y.-S. Fu, X. Chen, X.-C. Ma, J. Li, W.-H. Duan, J.-F. Jia, and Q.-K. Xue, High-Resolution Scanning Tunneling Spectroscopy of Magnetic Impurity Induced Bound States in the Superconducting Gap of Pb Thin Films, Phys. Rev. Lett. **100**, 226801 (2008).

[39] S.-H. Ji, T. Zhang, Y.-S. Fu, X. Chen, J.-F. Jia, Q.-K. Xue, and X.-C. Ma, Application of magnetic atom induced bound states in superconducting gap for chemical identification of single magnetic atoms, Appl. Phys. Lett. **96**, 073113 (2010).

[40] D.-J. Choi, C. Rubio-Verdú, J. de Bruijckere, M. M. Ugeda, N. Lorente, and J. I. Pascual, Mapping the orbital structure of impurity bound states in a superconductor, Nat. Commun. **8**, 15175 (2017).

[41] D.-J. Choi, C. G. Fernández, E. Herrera, C. Rubio-Verdú, M. M. Ugeda, I. Guillamón, H. Suderow, J. I. Pascual, and N. Lorente, Influence of Magnetic Ordering between Cr Adatoms on the Yu-Shiba-Rusinov States of the β-Bi_2Pd Superconductor, Phys. Rev. Lett. **120**, 167001 (2018).

[42] G. C. Ménard, S. Guissart, Ch. Brun, S. Pons, V. S. Stolyarov, F. Debontridder, M. V. Leclerc, E. Janod, L. Cario, D. Roditchev, P. Simon, and T. Cren, Coherent long-range magnetic bound states in a superconductor, Nat. Phys. **11**, 1013 (2015).

[43] L. Cornils, A. Kamlapure, L. Zhou, S. Pradhan, A. A. Khajetoorians, J. Fransson, J. Wiebe, and R. Wiesendanger, Spin-Resolved Spectroscopy of the Yu-Shiba-Rusinov States of Individual Atoms, Phys. Rev. Lett. **119**, 197002 (2017).

[44] F. Meier, L. Zhou, J. Wiebe, and R. Wiesendanger, Revealing magnetic interactions from single-atom magnetization curves, Science **320**, 82 (2008).

[45] D. Chevallier, P. Simon, and C. Bena, From Andreev bound states to Majorana fermions in topological wires on superconducting substrates: A story of mutation, Phys. Rev. B **88**, 165401 (2013).

[46] F. Pientka, L. I. Glazman, and F. von Oppen, Topological superconducting phase in helical Shiba chains, Phys. Rev. B **88**, 155420 (2013).

[47] G. M. Andolina and P. Simon, Topological properties of chains of magnetic impurities on a superconducting substrate: Interplay between the Shiba band and ferromagnetic wire limits, Phys. Rev. B **96**, 235411 (2017).

[48] K. Björnson, A. V. Balatsky, and A. M. Black-Schaffer, Superconducting order parameter π-phase shift in magnetic impurity wires, Phys. Rev. B **95**, 104521 (2017).

[49] N. Mohanta, A. P. Kampf, and T. Kopp, Supercurrent as a probe for topological superconductivity in magnetic adatom chains, Phys. Rev. B **97**, 214507 (2018).

[50] B. E. Feldman, M. T. Randeria, J. Li, S. Jeon, Y. Xie, Z. Wang, I. K. Drozdov, B. A. Bernevig, and A. Yazdani, High-resolution studies of the Majorana atomic chain platform, Nat. Phys. **13**, 286 (2016).

[51] M. Ruby, B. W. Heinrich, Y. Peng, F. von Oppen, and K. J. Franke, Exploring a proximity-coupled Co chain on Pb(110) as a possible Majorana platform, Nano Lett. **17**, 4473 (2017).

[52] D. M. Eigler and E. K. Schweizer, Positioning single atoms with a scanning tunneling microscope, Nature **344**, 524 (1990).

[53] A. A. Khajetoorians, J. Wiebe, B. Chilian, S. Lounis, S. Blügel, and R. Wiesendanger, Atom-by-atom engineering and magnetometry of tailored nanomagnets, Nat. Phys. **8**, 497 (2012).

[54] K. Morgenstern, N. Lorente, and K.-H. Rieder, Controlled manipulation of single atoms and small molecules using the scanning tunneling microscope, Phys. Status Solidi B **250**, 1671 (2013).

[55] A. Spinelli, M. P. Rebergen, and A. F. Otte, Atomically crafted spin lattices as model systems for quantum magnetism, J. Phys.: Condens. Matter **27**, 243203 (2015).

[56] D.-J. Choi, N. Lorente, J. Wiebe, K. von Bergmann, A. F. Otte, and A. J. Heinrich, Colloquium: Atomic spin chains on surfaces, Rev. Mod. Phys. **91**, 041001 (2019).

[57] L. Schneider, S. Brinker, M. Steinbrecher, J. Hermenau, T. Posske, M. dos Santos Dias, S. Lounis, R. Wiesendanger, and J. Wiebe, Controlling in-gap end states by linking nonmagnetic atoms and artificially-constructed spin chains on superconductors, arXiv:2002.12294.

[58] C. F. Hirjibehedin, Ch. P. Lutz, and A. J. Heinrich, Spin coupling in engineered atomic structures, Science **312**, 1021 (2006).

[59] T. Matsui, Chr. Meyer, L. Sacharow, J. Wiebe, and R. Wiesendanger, Electronic states of Fe atoms and chains on InAs(110) from scanning tunneling spectroscopy, Phys. Rev. B **75**, 165405 (2007).

[60] S. Fölsch, J. Yang, Ch. Nacci, and K. Kanisawa, Atom-by-atom Quantum State Control in Adatom Chains on a Semiconductor, Phys. Rev. Lett. **103**, 096104 (2009).

[61] S. Loth, S. Baumann, Ch. P. Lutz, D. M. Eigler, and A. J. Heinrich, Bistability in atomic-scale antiferromagnets, Science **335**, 196 (2012).

[62] S. Yan, L. Malavolti, J. A. J. Burgess, A. Droghetti, A. Rubio, and S. Loth, Nonlocally sensing the magnetic states of nanoscale antiferromagnets with an atomic spin sensor, Sci. Adv. **3**, e1603137 (2017).

[63] S. Rolf-Pissarczyk, S. Yan, L. Malavolti, J. A. J. Burgess, G. McMurtrie, and S. Loth, Dynamical Negative Differential Resistance in Antiferromagnetically Coupled Few-Atom Spin Chains, Phys. Rev. Lett. **119**, 217201 (2017).

[64] H. Kim, A. Palacio-Morales, T. Posske, L. Rózsa, K. Palotás, L. Szunyogh, M. Thorwart, and R. Wiesendanger, Toward tailoring Majorana bound states in artificially constructed magnetic atom chains on elemental superconductors, Sci. Adv. **4**, eaar5251 (2018).

[65] M. Steinbrecher, R. Rausch, K. T. That, J. Hermenau, A. A. Khajetoorians, M. Potthoff, R. Wiesendanger, and J. Wiebe, Non-collinear spin states in bottom-up fabricated atomic chains, Nat. Commun. **9**, 2853 (2018).

[66] A. Kamlapure, L. Cornils, J. Wiebe, and R. Wiesendanger, Engineering the spin couplings in atomically crafted spin chains on an elemental superconductor, Nat. Commun. **9**, 3253 (2018).

[67] K. Lejaeghere, G. Bihlmayer, T. Björkman, P. Blaha, S. Blügel, V. Blum, D. Caliste, I. E. Castelli, S. J. Clark, A. Dal Corso, S. de Gironcoli, T. Deutsch, J. K. Dewhurst, I. Di Marco, C. Draxl, M. Dułak, O. Eriksson, J. A. Flores-Livas, K. F. Garrity, L. Genovese, P. Giannozzi, M. Giantomassi, S. Goedecker, X. Gonze, O. Grånäs, E. K. U. Gross, A. Gulans, F. Gygi, D. R. Hamann, P. J. Hasnip, N. A. W. Holzwarth, D. Iuşan, D. B. Jochym, F. Jollet, D. Jones, G. Kresse, K. Koepernik, E. Küçükbenli, Y. O. Kvashnin, I. L. M. Locht, S. Lubeck, M. Marsman, N. Marzari, U. Nitzsche, L. Nordström, T. Ozaki, L. Paulatto, Ch. J. Pickard, W. Poelmans, M. I. J. Probert, K. Refson, M. Richter, G.-M. Rignanese, S. Saha, M. Scheffler, M. Schlipf, K. Schwarz, S. Sharma, F. Tavazza, P. Thunström, A. Tkatchenko, M. Torrent, D. Vanderbilt, M. J. van Setten, V. Van Speybroeck, J. M. Wills, J. R. Yates, G.-X. Zhang, and S. Cottenier, Reproducibility in density functional theory calculations of solids, Science **351**, aad3000 (2016).

[68] P. Giannozzi, S. Baroni, N. Bonini, M. Calandra, R. Car, C. Cavazzoni, D. Ceresoli, G. L Chiarotti, M. Cococcioni, I. Dabo, A. Dal Corso, S. de Gironcoli, S. Fabris, G. Fratesi, R. Gebauer, U. Gerstmann, Ch. Gougoussis, A. Kokalj, M. Lazzeri, L. Martin-Samos, N. Marzari, F. Mauri, R. Mazzarello, S. Paolini, A. Pasquarello, L. Paulatto, C. Sbraccia, S. Scandolo, G. Sclauzero, A. P. Seitsonen, A. Smogunov, P. Umari, and R. M. Wentzcovitch, QUANTUM ESPRESSO: A modular and open-source software project for quantum simulations of materials, J. Phys.: Condens. Matter **21**, 395502 (2009).

[69] P. Giannozzi, O. Andreussi, T. Brumme, O. Bunau, M. B. Nardelli, M. Calandra, R. Car, C. Cavazzoni, D. Ceresoli, M. Cococcioni, N. Colonna, I. Carnimeo, A. Dal Corso, S. de Gironcoli, P. Delugas, R. A. DiStasio, A. Ferretti, A. Floris, G. Fratesi, G. Fugallo, R. Gebauer, U. Gerstmann, F. Giustino,

T. Gorni, J. Jia, M. Kawamura, H.-Y. Ko, A. Kokalj, E. Küçükbenli, M. Lazzeri, M. Marsili, N. Marzari, F. Mauri, N. L. Nguyen, H.-V. Nguyen, A. Otero de-la Roza, L. Paulatto, S. Poncé, D. Rocca, R. Sabatini, B. Santra, M. Schlipf, A. P. Seitsonen, A. Smogunov, I. Timrov, T. Thonhauser, P. Umari, N. Vast, X. Wu, and S. Baroni, Advanced capabilities for materials modeling with QUANTUM ESPRESSO, J. Phys.: Condens. Matter **29**, 465901 (2017).

[70] J. P. Perdew, J. A. Chevary, S. H. Vosko, K. A. Jackson, M. R. Pederson, D. J. Singh, and C. Fiolhais, Atoms, molecules, solids, and surfaces: Applications of the generalized gradient approximation for exchange and correlation, Phys. Rev. B **46**, 6671 (1992).

[71] J. P. Perdew, K. Burke, and M. Ernzerhof, Generalized Gradient Approximation Made Simple, Phys. Rev. Lett. **77**, 3865 (1996).

[72] P. E. Blöchl, Projector augmented-wave method, Phys. Rev. B **50**, 17953 (1994).

[73] G. Kresse and D. Joubert, From ultrasoft pseudopotentials to the projector augmented-wave method, Phys. Rev. B **59**, 1758 (1999).

[74] A. Dal Corso, Pseudopotentials periodic table: From H to Pu, Comput. Mater. Sci. **95**, 337 (2014).

[75] H. J. Monkhorst and J. D. Pack, Special points for Brillouin-zone integrations, Phys. Rev. B **13**, 5188 (1976).

[76] N. Marzari and D. Vanderbilt, Maximally localized generalized Wannier functions for composite energy bands, Phys. Rev. B **56**, 12847 (1997).

[77] I. Souza, N. Marzari, and D. Vanderbilt, Maximally localized Wannier functions for entangled energy bands, Phys. Rev. B **65**, 035109 (2001).

[78] N. Marzari, A. A. Mostofi, J. R. Yates, I. Souza, and D. Vanderbilt, Maximally localized Wannier functions: Theory and applications, Rev. Mod. Phys. **84**, 1419 (2012).

[79] A. A. Mostofi, J. R. Yates, Y.-S. Lee, I. Souza, D. Vanderbilt, and N. Marzari, WANNIER90: A tool for obtaining maximally-localised Wannier functions, Comput. Phys. Commun. **178**, 685 (2008).

[80] A. A. Mostofi, J. R. Yates, G. Pizzi, Y.-S. Lee, I. Souza, D. Vanderbilt, and N. Marzari, An updated version of WANNIER90: A tool for obtaining maximally-localised Wannier functions, Comput. Phys. Commun. **185**, 2309 (2014).

[81] G. Pizzi, V. Vitale, R. Arita, S. Blügel, F. Freimuth, G. Géranton, M. Gibertini, D. Gresch, Ch. Johnson, T. Koretsune, J. Ibañez-Azpiroz, H. Lee, J.-M. Lihm, D. Marchand, A. Marrazzo, Y. Mokrousov, J. I Mustafa, Y. Nohara, Y. Nomura, L. Paulatto, S. Poncé, T. Ponweiser, J. Qiao, F. Thöle, S. S. Tsirkin, M. Wierzbowska, N. Marzari, D. Vanderbilt, I. Souza, A. A. Mostofi, and J. R. Yates, WANNIER90 as a community code: New features and applications, J. Phys.: Condens. Matterr **32**, 165902 (2020).

[82] C Kittel, *Introduction to Solid State Physics*, Vol. 8 (Wiley, New York, 1976).

[83] P. Townsend and J. Sutton, Investigation by electron tunneling of the superconducting energy gaps in Nb, Ta, Sn, and Pb, Phys. Rev. **128**, 591 (1962).

[84] M. Ruby, B. W. Heinrich, J. I. Pascual, and K. J. Franke, Experimental Demonstration of a Two-Band Superconducting State for Lead Using Scanning Tunneling Spectroscopy, Phys. Rev. Lett. **114**, 157001 (2015).

[85] M. Sato, Y. Takahashi, and S. Fujimoto, Non-Abelian Topological Order in *s*-Wave Superfluids of Ultracold Fermionic Atoms, Phys. Rev. Lett. **103**, 020401 (2009).

[86] M. Sato and S. Fujimoto, Topological phases of noncentrosymmetric superconductors: Edge states, Majorana fermions, and non-Abelian statistics, Phys. Rev. B **79**, 094504 (2009).

[87] M. Sato, Y. Takahashi, and S. Fujimoto, Non-Abelian topological orders and Majorana fermions in spin-singlet superconductors, Phys. Rev. B **82**, 134521 (2010).

[88] Ch.-K. Chiu, J. C. Y. Teo, A. P. Schnyder, and S. Ryu, Classification of topological quantum matter with symmetries, Rev. Mod. Phys. **88**, 035005 (2016).

[89] S. Tewari and J. D. Sau, Topological Invariants for Spin-Orbit Coupled Superconductor Nanowires, Phys. Rev. Lett. **109**, 150408 (2012).

[90] J. E. Moore and L. Balents, Topological invariants of time-reversal-invariant band structures, Phys. Rev. B **75**, 121306(R) (2007).

[91] A. P. Schnyder, S. Ryu, A. Furusaki, and A. W. W. Ludwig, Classification of topological insulators and superconductors in three spatial dimensions, Phys. Rev. B **78**, 195125 (2008).

[92] S. Ryu, A. P. Schnyder, A. Furusaki, and A. W. W. Ludwig, Topological insulators and superconductors: Tenfold way and dimensional hierarchy, New J. Phys. **12**, 065010 (2010).

[93] K. V. Shanavas, Z. S. Popović, and S. Satpathy, Theoretical model for Rashba spin-orbit interaction in *d* electrons, Phys. Rev. B **90**, 165108 (2014).

[94] See Supplementary Materials for Ref. [23].

[95] See Supporting Information for Ref. [51].

[96] R. Roldán, L. Chirolli, E. Prada, J. A. Silva-Guillén, P. San-Jose, and F. Guinea, Theory of 2D crystals: graphene and beyond, Chem. Soc. Rev. **46**, 4387 (2017).

[97] M. Z. Hasan and C. L. Kane, *Colloquium:* Topological insulators, Rev. Mod. Phys. **82**, 3045 (2010).

[98] M. M. Vazifeh and M. Franz, Self-Organized Topological State with Majorana Fermions, Phys. Rev. Lett. **111**, 206802 (2013).

[99] I. Reis, D. J. J. Marchand, and M. Franz, Self-organized topological state in a magnetic chain on the surface of a superconductor, Phys. Rev. B **90**, 085124 (2014).

[100] Y. Kim, M. Cheng, B. Bauer, R. M. Lutchyn, and S. Das Sarma, Helical order in one-dimensional magnetic atom chains and possible emergence of Majorana bound states, Phys. Rev. B **90**, 060401(R) (2014).

[101] B. Braunecker, G. I. Japaridze, J. Klinovaja, and D. Loss, Spin-selective Peierls transition in interacting one-dimensional conductors with spin-orbit interaction, Phys. Rev. B **82**, 045127 (2010).

[102] J. Klinovaja and D. Loss, Composite Majorana fermion wave functions in nanowires, Phys. Rev. B **86**, 085408 (2012).

[103] K. Momma and F. Izumi, VESTA3 for three-dimensional visualization of crystal, volumetric and morphology data, J. Appl. Crystallogr. **44**, 1272 (2011).

[104] L. Zhou, J. Wiebe, S. Lounis, E Vedmedenko, F. Meier, S. Blügel, P. H. Dederichs, and R. Wiesendanger, Strength and directionality of surface Ruderman-Kittel-Kasuya-Yosida interaction mapped on the atomic scale, Nat. Phys. **6**, 187 (2010).

[105] P. W. Anderson and H. Suhl, Spin alignment in the superconducting state, Phys. Rev. **116**, 898 (1959).

[106] F. Schubert, Y. Mokrousov, P. Ferriani, and S. Heinze, Noncollinear magnetism in freestanding and supported monatomic Mn chains, Phys. Rev. B **83**, 165442 (2011).

[107] M. Tanveer, P. Ruiz-Díaz, and G. M. Pastor, Environment-dependent noncollinear magnetic orders and spin-wave spectra of Fe chains and stripes, Phys. Rev. B **87**, 075426 (2013).

[108] M. Menzel, Y. Mokrousov, R. Wieser, J. E. Bickel, E. Vedmedenko, S. Blügel, S. Heinze, K. von Bergmann, A. Kubetzka, and R. Wiesendanger, Information Transfer by Vector Spin Chirality in Finite Magnetic Chains, Phys. Rev. Lett. **108**, 197204 (2012).

[109] J. Hermenau, S. Brinker, M. Marciani, M. Steinbrecher, M. dos Santos Dias, R. Wiesendanger, S. Lounis, and J. Wiebe, Stabilizing spin systems via symmetrically tailored RKKY interactions, Nat. Commun. **10**, 2565 (2019).

[110] A. Belabbes, G. Bihlmayer, F. Bechstedt, S. Blügel, and A. Manchon, Hund's Rule-Driven Dzyaloshinskii-Moriya Interaction at 3*d*-5*d* Interfaces, Phys. Rev. Lett. **117**, 247202 (2016).

[111] B. Schweflinghaus, B. Zimmermann, M. Heide, G. Bihlmayer, and S. Blügel, Role of Dzyaloshinskii-Moriya interaction for magnetism in transition-metal chains at Pt step edges, Phys. Rev. B **94**, 024403 (2016).

[112] A. M. Oleś, Antiferromagnetism and correlation of electrons in transition metals, Phys. Rev. B **28**, 327 (1983).

[113] A. M. Oleś and G. Stollhoff, Correlation effects in ferromagnetism of transition metals, Phys. Rev. B **29**, 314 (1984).

[114] G. Stollhoff, A. M. Oleś, and V. Heine, Stoner exchange interaction in transition metals, Phys. Rev. B **41**, 7028 (1990).

[115] H. T. Ng, Decoherence of interacting Majorana modes, Sci. Rep. **5**, 12530 (2015).

[116] H. Katsura, D. Schuricht, and M. Takahashi, Exact ground states and topological order in interacting Kitaev/Majorana chains, Phys. Rev. B **92**, 115137 (2015).

[117] A. Więckowski and A. Ptok, Influence of long-range interaction on Majorana zero modes, Phys. Rev. B **100**, 144510 (2019).

[118] D. A. Papaconstantopoulos, *Handbook of the Band Structure of Elemental Solids* (Springer US, New York, 2015).

4.1.4 Majorana bound states in a superconducting Rashba nanowire in the presence of antiferromagnetic order

A. Kobiałka, N. Sedlmayr, A. Ptok, Phys. Rev. B **103**, 125110 (2021)

Emergence of MBS in unconventional regions of topological phase space was studied in the case of SSH model in Sec. 4.1.2. Here, we impose a different modification upon Rashba nanowire – we force the nanowire into an antiferromegnetic setting, where the system is composed of two spin polarized sublattices. In this setting, using various methods showing the existence of topological supercondictivity, we find that MBS emerge away from the typical region at the bottom of the band. Indeed, this new AFM order-related topological branch emerges close to half–filling and what is more interesting, without any external magnetic field. Competition between overlapping topological phases leads to the destruction of the normal Rashba topological branch, which is proportional to strength of antiferromagnetic order. We also investigate real and momentum space of this system, finding edge state delocalisation and band inversion. Additionally, the value of the zero–bias local differential conductance correlates with our results from topological invariant calculations, showing zero–bias conductance peak at nontrivial parts of the topological diagram. Similarly to our study of dimerization, extra topological branches are more resistant to disorder than the typical bottom–of–the–band Rashba branch.

Author's contribution: Partial preparation of numerical and analytical calculations, partial preparation of figures, analysis and discussion of obtained results, partial preparation of the manuscript, participation in preparing the response for Referees.

Majorana bound states in a superconducting Rashba nanowire in the presence of antiferromagnetic order

Aksel Kobiałka,[1,*] Nicholas Sedlmayr,[1,†] and Andrzej Ptok[2,‡]

[1]*Institute of Physics, Maria Curie-Skłodowska University, Plac Marii Skłodowskiej-Curie 1, PL-20031 Lublin, Poland*

[2]*Institute of Nuclear Physics, Polish Academy of Sciences, ul. W. E. Radzikowskiego 152, PL-31342 Kraków, Poland*

(Received 3 August 2020; revised 19 February 2021; accepted 19 February 2021; published 4 March 2021)

Theoretical studies have shown that Majorana bound states can be induced at the ends of a one-dimensional wire, a phenomenon possible due to the interplay between *s*-wave superconductivity, spin-orbit coupling, and an external magnetic field. These states have been observed in superconductor-semiconductor hybrid nanostructures in the presence of a Zeeman field, and in the limit of a low density of particles. In this paper, we demonstrate and discuss the possibility of the emergence of Majorana bound states in a superconducting Rashba nanowire deposited on an antiferromagnetically ordered surface. We calculate the relevant topological invariant in several complementary ways. Studying the topological phase diagram reveals two branches of the nontrivial topological phase—the main branch, which is typical for Rashba nanowires, and an additional branch emerging due to the antiferromagnetic order. In the case of the additional topological branch, Majorana bound states can also exist close to half-filling, obviating the need for either doping or gating the nanowire to reach the low-density regime. Moreover, we show the emergence of the Majorana bound states in the absence of the external magnetic field, which is possible due to the antiferromagnetic order. We also discuss the properties of the bound states in the context of real-space localization and the spectral function of the system. This allows one to perceive the band inversion within the spin and sublattice subspaces in the additional branch, contrary to the main branch, where the only band inversion reported in previous studies exists in the spin subspace. Finally, we demonstrate how these topological phases can be confirmed experimentally in transport measurements.

DOI: 10.1103/PhysRevB.103.125110

I. INTRODUCTION

The possibility for topologically protected localized zero-energy states to form in a superconducting nanowire was first proposed in a seminal paper by Kitaev [1] and opened a period of intense study of these Majorana bound states (MBS) [2–4]. The states are of particular interest because they are non-Abelian anyons, and thus potentially of interest for topological quantum computing [5]. In the last decade, potential signatures of MBS have been detected in low-dimensional structures, e.g., semiconducting-superconducting hybrid nanostructures [6–13] and chains of magnetic atoms deposited on a superconducting surface [14–19]. In the first case, it is the interplay between intrinsic spin-orbit coupling (SOC), proximity induced superconductivity, and an external magnetic field, which leads to the emergence of MBS [3]. In the second case, MBS are expected due to the helical ordering of magnetic moments in the monoatomic chains [20–25].

MBS emerge in these systems when they are in a topologically nontrivial phase. In a typical situation, the phase transition from topologically trivial to nontrivial is induced by the magnetic field [26–28]. Increasing the applied magnetic field leads to a closing of the trivial superconducting gap and the reopening of a new, nontrivial, gap [29]. This is true for a system with a relatively small density of particles, i.e., when the Fermi level is near the bottom of the band. If the splitting of the bands by the external magnetic field is larger than the superconducting gap, pairing occurs in the one-band channel [8,29–31]. This "one" type quasiparticle paring arises as an effect of the spin mixing by the SOC, corresponding to *p*-wave inter-site pairing in real space [32–34].

However, state of the art experiments also allow one to create inhomogeneous periodic magnetic fields. For example, carbon nanotubes coupled to an antiferromagnetic substrate [35] lead to a *synthetic magnetic field* [36]. Similar solutions were proposed theoretically in the form of nanomagnets [37–39], which have also been executed experimentally with an arrangement of alternating magnetization [40–42]. Just like in the case of the magnetic moments with helical order [20–23], this magnetic field can be the source of an effective spin-orbit coupling. Another possibility consists of magnetic nanopillars producing magnetic textures, which can be tuned by passing currents [43]. Similar types of architecture based on magnetic tunnel junctions can be used to perform braiding operations [44]. Last, but not least, coupling a nanowire to a magnetic Co/Pt multilayer [45] can achieve a similar goal.

New perspectives for a system with antiferromagnetic (AFM) order were brought about by recent progress in experimental techniques allowing for the preparation of atomic chains [19]. In such a case a self-organized spin helix order [20–22] can be stabilized via the Ruderman-Kittel-

*akob@kft.umcs.lublin.pl
†sedlmayr@umcs.pl
‡aptok@mmj.pl

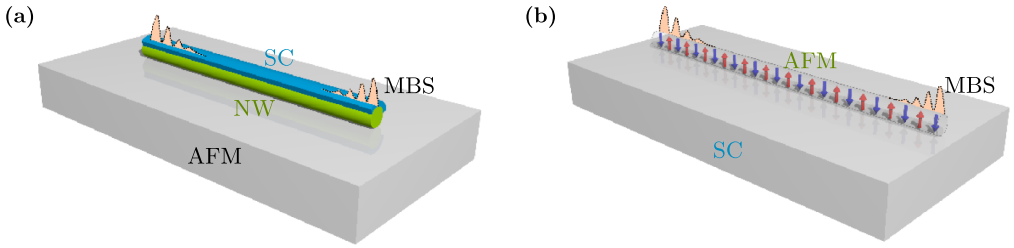

FIG. 1. A Schematic representation of the described systems: in the case (a), a semiconducting nanowire (NW) is deposited on the surface of an antiferromagnetic (AFM) base, partially covered by a superconductor (SC); similarly, in case (b) an AFM chain is deposited on a SC surface. In both cases, at the ends of the nanowire, Majorana bound states (MBS) can be induced due to the interplay between intrinsic spin orbit coupling, superconductivity, external Zeeman field (along the nanowire), and antiferromagnetism (induced by the proximity effect).

Kasuya-Yosida (RKKY) mechanism [46–48]. Moreover, ideal monoatomic chains can be crafted with atoms one by one [49], which allows for the existence of various types of magnetic order in the chain [48,50,51]. For example, AFM order was observed experimentally in sufficiently short Fe chains [51–53] [cf. Fig. 1(b)]. Additionally, the proximity effect can relay the AFM order to the nanowire, e.g., by contact with a strong AFM system [cf. Fig. 1(a)]. Strong antiferromagnets such as $YbCo_2Si_2$ [54], VBr_3 [55], Mn_2C [56], $NiPS_3$ [57], or most promisingly V_5S_8 [58,59], can be good candidates for the substrate in the investigated system. In such a case, topological phase can emerge due to the tuning of the external magnetic field, without destroying the AFM order in the substrate.

In the case of a semiconducting-superconducting hybrid nanowire, the nontrivial topological phase is expected when the Fermi level is located near the bottom of the band. Otherwise, too large a magnetic field is required. As a result, the MBS is strongly restricted to the case of a low density of particles in the system. Contrary to this, we discuss a scenario for MBS in the nearly-half-filled case. The presence of MBS without any *additional* external magnetic field applied, but instead only due to the AFM order, which we demonstrate here, has previously received only scant attention, see, for example, Refs. [60,61].

This paper is organized as follows. In Sec. II, we describe our model and the techniques used to investigate it. In Sec. III, we derive the topological phase diagram of the system in the presence of AFM order and external magnetic field. We also discuss the origin of the nontrivial topological phase. In Sec. IV, we discuss electronic properties of the system in both real and reciprocal spaces. Next, in Sec. V, we discuss the proposal of an experimental examination of this phase diagram via the differential conductance. Finally, in Sec. VII, we summarize the results.

II. MODEL AND TECHNIQUES

A. Real-space description

In our calculations, we model the system shown schematically in Fig. 2. We consider a one-dimensional Rashba nanowire with superconducting and antiferromagnetic order both induced by proximity effects (cf. Fig. 1), in the presence of an external magnetic field directed along the nanowire. The low-energy physics of such a system can be described by the Hamiltonian $\mathcal{H} = \mathcal{H}_0 + \mathcal{H}_{\rm SC} + \mathcal{H}_{\rm AFM}$.

The Rashba nanowire itself is described by

$$\mathcal{H}_0 = \sum_{ij,ss',\sigma} \left[-t_{ij}^{ss'} - (\mu + \sigma h)\delta_{ij}\delta_{ss'}\right] c_{is\sigma}^\dagger c_{js'\sigma} - i\lambda \sum_{i,\sigma\sigma'} [c_{iA\sigma}^\dagger \sigma_{\sigma\sigma'}^y c_{iB\sigma'} + c_{iB\sigma}^\dagger \sigma_{\sigma\sigma'}^y c_{i+1,A\sigma'}] + \text{H.c.}, \quad (1)$$

where $c_{is\sigma}^\dagger$ ($c_{is\sigma}$) describes the creation (annihilation) of an electron with spin $\sigma \in \{\uparrow, \downarrow\}$ in sublattice $s \in \{A, B\}$ of the ith unit cell. We assume equal hopping between the nearest-neighbor sites (when $t_{ij}^{ss'} = t = 1$ in appropriate energy units) and zero otherwise. As usual, μ is the chemical potential, and h is the external Zeeman magnetic field. In our calculations, we neglect the orbital effect [62], assuming the magnetic field is parallel to the nanowire. The term in the second line describes the SOC with strength λ, where σ_y is the second Pauli matrix. Superconductivity, which is induced in a nanowire due to the proximity effect, can be described by the BCS-like term:

$$\mathcal{H}_{\rm SC} = \Delta \sum_{is} (c_{is\uparrow}^\dagger c_{is\downarrow}^\dagger + c_{is\downarrow} c_{is\uparrow}), \quad (2)$$

where Δ is the superconducting order parameter, proportional to the induced superconducting gap. The AFM order in the nanowire is described by

$$\mathcal{H}_{\rm AFM} = -m_0 \sum_{i\sigma} \sigma (c_{iA\sigma}^\dagger c_{iA\sigma} - c_{iB\sigma}^\dagger c_{iB\sigma}), \quad (3)$$

where m_0 denotes the amplitude of the AFM order.

Finite size system. Properties of the finite size system (with open boundary conditions), can be analyzed in real space. In this case, the Hamiltonian $\mathcal{H}$ can be diagonalized by the transformation $c_{is\sigma} = \sum_n (u_{isn\sigma}\gamma_n - \sigma v_{isn\sigma}^* \gamma_n^\dagger)$ [63], where γ_n

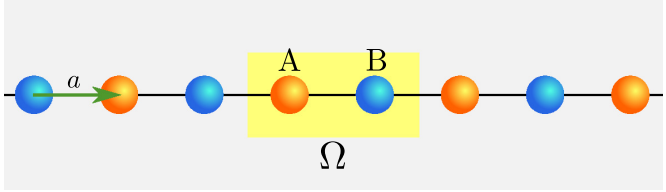

FIG. 2. The one-dimensional AFM lattice discussed in this paper. The unit cell Ω contains two non-equivalent sites with opposite magnetic moments (orange and blue) belonging to sublattices A and B. The lattice spacing $a \equiv 1$ is taken as the distance between two nearest-neighbor sites.

and $\gamma_n^\dagger$ are fermionic operators. Such a transformation leads to the real-space Bogoliubov-de Gennes (BdG) equations [64], in the form $\mathcal{E}_n\Psi_{isn} = \sum_{js'} \mathbb{H}_{is,js'}\Psi_{js'n}$, where $\mathbb{H}_{is,js'}$ is the Hamiltonian in the matrix form, given in Appendix B.

From solving the BdG equations, we can determine the site-dependent average number of particles:

$$\begin{aligned} n_{is\sigma} &= \langle c_{is\sigma}^\dagger c_{is\sigma}\rangle \\ &= \sum_n \left[|u_{isn\sigma}|^2 f(\mathcal{E}_n) + |v_{isn\sigma}|^2 f(-\mathcal{E}_n)\right], \end{aligned} \tag{4}$$

where $f(\omega) = 1/[1+\exp(-\omega/k_BT)]$ is the Fermi-Dirac distribution. From this, *effective* site-dependent magnetization is given as $m_{is} = n_{is\uparrow} - n_{is\downarrow}$. In a similar way, we can determine the local density of states (LDOS) [65]:

$$\begin{aligned} \rho_{is}(\omega) &= -\frac{1}{\pi}\sum_\sigma \mathrm{Im}\, G_{is\sigma}(\omega + \mathrm{i}0^+) \\ &= \sum_{n\sigma}\left[|u_{isn\sigma}|^2\delta(\omega+\mathcal{E}_n) + |v_{isn\sigma}|^2\delta(\omega-\mathcal{E}_n)\right], \end{aligned} \tag{5}$$

where $G_{is\sigma} = \langle c_{is\sigma}|(\omega - H)^{-1}|c_{is\sigma}^\dagger\rangle$ and $\delta(\omega)$ is the Dirac delta function. The LDOS represents quantities experimentally measured by scanning tunneling microscope (STM) [66–69], and can give information about the emergence of the zero-energy states [14]. In the numerical calculations, we replace the delta function by the Lorentzian $\delta(\omega) = \xi/[\pi(\omega^2 + \xi^2)]$, with a small broadening $\xi/t = 0.001$.

B. Reciprocal space description

From the explicit form of the Fourier transform of operators:

$$c_{is\sigma}^\dagger = \frac{1}{\sqrt{N}}\sum_{\boldsymbol{k}} c_{ks\sigma}^\dagger \exp(-i\boldsymbol{k}\cdot\boldsymbol{R}_{is}), \tag{6}$$

where $\boldsymbol{R}_{is}$ denotes position of ith sites in sublattice s (cf. Fig. 2), the Hamiltonian in momentum space can be found:

$$\begin{aligned} \mathcal{H}_0 &= \sum_{\boldsymbol{k}\sigma}\mathcal{E}_{\boldsymbol{k}}(c_{\boldsymbol{k}A\sigma}^\dagger c_{\boldsymbol{k}B\sigma} + \mathrm{H.c.}) \\ &\quad - \sum_{\boldsymbol{k}s\sigma}(\mu - \sigma h)c_{\boldsymbol{k}s\sigma}^\dagger c_{\boldsymbol{k}s\sigma} \\ &\quad + \sum_{\boldsymbol{k}\sigma\sigma'} i\mathcal{L}_{\boldsymbol{k}}(c_{\boldsymbol{k}A\sigma}^\dagger \sigma_{\sigma\sigma'}^y c_{\boldsymbol{k}B\sigma'} + \mathrm{H.c.}), \end{aligned} \tag{7}$$

$$\mathcal{H}_{\mathrm{SC}} = \Delta\sum_{\boldsymbol{k}s}(c_{\boldsymbol{k}s\uparrow}^\dagger c_{-\boldsymbol{k}s\downarrow}^\dagger + c_{-\boldsymbol{k}s\downarrow}c_{\boldsymbol{k}s\uparrow}), \tag{8}$$

$$\mathcal{H}_{\mathrm{AFM}} = -m_0\sum_{\boldsymbol{k}s\sigma}\sigma(c_{\boldsymbol{k}A\sigma}^\dagger c_{\boldsymbol{k}A\sigma} - c_{\boldsymbol{k}B\sigma}^\dagger c_{\boldsymbol{k}B\sigma}), \tag{9}$$

where $c_{\boldsymbol{k}s\sigma}^\dagger$ ($c_{\boldsymbol{k}s\sigma}$) describes the creation (annihilation) operator of an electron with momentum $\boldsymbol{k}$ and spin σ in sublattice s. Additionally, $\mathcal{E}_{\boldsymbol{k}} = -2t\cos(k)$ denotes the dispersion relation of noninteracting electrons in a 1D chain, while $\mathcal{L}_{\boldsymbol{k}} = -2i\lambda\sin(k)$ is SOC in momentum space.

For the following, we will use a more convenient representation for the Hamiltonian. We introduce Pauli matrices that act in the particle-hole subspace $\boldsymbol{\tau}^{0,x,y,z}$, spin subspace $\boldsymbol{\sigma}^{0,x,y,z}$, and sublattice subspace $\boldsymbol{\rho}^{0,x,y,z}$. The "0" superscript labels the identity matrix for any given subspace. Then, following the Bogoliubov transform, the Hamiltonian in the Nambu basis,

$$\psi_{\boldsymbol{k}}^\dagger = (c_{\boldsymbol{k}A\uparrow}^\dagger\, c_{\boldsymbol{k}B\uparrow}^\dagger\, c_{\boldsymbol{k}A\downarrow}^\dagger\, c_{\boldsymbol{k}B\downarrow}^\dagger\, c_{-\boldsymbol{k}A\uparrow}\, c_{-\boldsymbol{k}B\uparrow}\, c_{-\boldsymbol{k}A\downarrow}\, c_{-\boldsymbol{k}B\downarrow}), \tag{10}$$

takes the form $\mathcal{H} = \sum_{\boldsymbol{k}}\psi_{\boldsymbol{k}}^\dagger\mathcal{H}(\boldsymbol{k})\psi_{\boldsymbol{k}}$, where

$$\begin{aligned} \mathcal{H}(\boldsymbol{k}) &= \mathcal{E}_{\boldsymbol{k}}\boldsymbol{\tau}^z\boldsymbol{\sigma}^0\boldsymbol{\rho}^x - \mu\boldsymbol{\tau}^z\boldsymbol{\sigma}^0\boldsymbol{\rho}^0 + i\mathcal{L}_{\boldsymbol{k}}\boldsymbol{\tau}^z\boldsymbol{\sigma}^y\boldsymbol{\rho}^x \\ &\quad - \Delta\boldsymbol{\tau}^y\boldsymbol{\sigma}^y\boldsymbol{\rho}^0 - h\boldsymbol{\tau}^z\boldsymbol{\sigma}^z\boldsymbol{\rho}^0 - m_0\boldsymbol{\tau}^z\boldsymbol{\sigma}^z\boldsymbol{\rho}^z. \end{aligned} \tag{11}$$

We will use this form of the Hamiltonian to calculate the bulk topological properties. In turn, due to the bulk-boundary correspondence [70,71], this tells us when there will be MBS in the finite length nanowire. More details can be found in Sec. III.

The band structure of the system can be found by diagonalizing the Hamiltonian (11). Each block $\mathcal{H}_{\boldsymbol{k}}$ has eight eigenvalues $\mathcal{E}_{\boldsymbol{k}}^n$ (for $n = 1, 2, \ldots, 8$) associated with eigenvectors

$$\varphi_{\boldsymbol{k}} = \left(u_{\boldsymbol{k}A\uparrow}^n\, u_{\boldsymbol{k}B\uparrow}^n\, u_{\boldsymbol{k}A\downarrow}^n\, u_{\boldsymbol{k}B\downarrow}^n\, v_{\boldsymbol{k}A\uparrow}^n\, v_{\boldsymbol{k}B\uparrow}^n\, v_{\boldsymbol{k}A\downarrow}^n\, v_{\boldsymbol{k}B\downarrow}^n\right)^T. \tag{12}$$

Due to the existence of the AFM order in the system, the unit cell Ω contains two non-equivalent sites. Increasing the size of the unit cell twice leads to the folding of the Brillouin zone (BZ) to $\boldsymbol{k} \in [-\pi/2, \pi/2)$. As a result the two time-reversal invariant momenta (TRIM) [72,73] are $\boldsymbol{k} = 0$ and $\boldsymbol{k} = \pi/2$. The impact of each parameter of the Hamiltonian on the band structure is described in detail in Appendix A). As the AFM order introduces a band splitting at lower energies than in the standard scenario, we may expect that we can drive the chain into the nontrivial phase at densities closer to the half-filling case. As we shall see in the following, this is indeed the case.

III. TOPOLOGICAL PHASE DIAGRAM

In this section, we will discuss the topological phase diagrams obtained from analytical calculations of the invariants and numerical calculations. We will also consider them in the context of the localization of the Majorana zero modes at the ends of the system. Based on the symmetries of the system, we will discuss the origin of the topological phase and the impact of the AFM order.

A. System symmetries

The BdG Hamiltonian (11) can possess several symmetries important for its topological properties [74,75]. Of interest are antiunitary symmetries and we have the following.

(1) The particle-hole (PH) symmetry described by the antiunitary operator $\mathcal{P} = \boldsymbol{\tau}^x\boldsymbol{\sigma}^0\boldsymbol{\rho}^0\mathcal{K}$, such that $\mathcal{P}H_{\boldsymbol{k}}\mathcal{P}^{-1} = -H_{-\boldsymbol{k}}$ and $\mathcal{P}^2 = 1$. $\mathcal{K}$ is the complex conjugation operator. It is worth mentioning, that all BdG Hamiltonians satisfy PH symmetry by construction [75].

(2) The "time-reversal" (TR) symmetry described by the antiunitary operator $\mathcal{T} = \lambda\mathcal{K}$, where $\lambda = \boldsymbol{\tau}^0\boldsymbol{\sigma}^0\boldsymbol{\rho}^0$, and $\mathcal{T}H_{\boldsymbol{k}}\mathcal{T}^{-1} = H_{-\boldsymbol{k}}$ with $\mathcal{T}^2 = 1$. Note that this is not the physical time-reversal operator for the electrons.

(3) Finally, we have the composite of these, the sublattice (SL) or "chiral" symmetry described by the unitary operator $\mathcal{S} = \mathcal{P}\mathcal{T} = \boldsymbol{\tau}^x\boldsymbol{\sigma}^0\boldsymbol{\rho}^0$, with $\mathcal{S}^{-1}H_{\boldsymbol{k}}\mathcal{S} = -H_{\boldsymbol{k}}$.

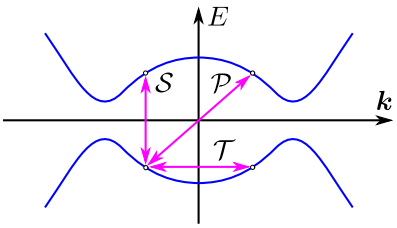

FIG. 3. Schematic representation of the roles played by the symmetries possessed by the considered Hamiltonian. The particle-hole symmetry $\mathcal{P}$ results in the symmetry of the spectrum (solid blue line) with respect of the point "zero," while time-reversal symmetry $\mathcal{T}$ and chiral (sublattice) symmetry $\mathcal{S}$ correspond to reflection of the spectrum across the momentum and energy axes, respectively.

The impact of these symmetries on the Hamiltonian is schematically shown in Fig. 3. With all of these symmetries present, which is the case for the Hamiltonian (11), we find ourselves in the BDI symmetry class in the Altland-Zirnbauer periodic-table of topological classes [75–77]. From this, the $\mathbb{Z}$ invariant (i.e., the winding number w) can be studied in order to discuss the topological phase diagram. We can also construct a $\mathbb{Z}_2$ invariant (e.g., from the Pfaffian) which measures the parity of w. Both topological indices will be discussed below.

B. Origin of the topological phase

First we note that a chiral Hamiltonian (11) can be rewritten in purely off-diagonal form [78] using the rotation $\tilde{\mathcal{H}}(\boldsymbol{k}) = \mathcal{U}_\pi^\dagger \mathcal{H}(\boldsymbol{k})\mathcal{U}_\pi$ where $\mathcal{U}_\pi = \mathrm{e}^{\mathrm{i}\frac{\pi}{4}\tau^y}\boldsymbol{\sigma}^0\boldsymbol{\rho}^0$. This results in

$$\begin{aligned}\tilde{\mathcal{H}}(\boldsymbol{k}) = {}& \mathcal{E}_{\boldsymbol{k}}\boldsymbol{\tau}^x\boldsymbol{\sigma}^0\boldsymbol{\rho}^x - \mu\boldsymbol{\tau}^x\boldsymbol{\sigma}^0\boldsymbol{\rho}^0 + \mathrm{i}\mathcal{L}_{\boldsymbol{k}}\boldsymbol{\tau}^x\boldsymbol{\sigma}^y\boldsymbol{\rho}^x \\ & - \Delta\boldsymbol{\tau}^y\boldsymbol{\sigma}^y\boldsymbol{\rho}^0 - h\boldsymbol{\tau}^x\boldsymbol{\sigma}^z\boldsymbol{\rho}^0 - m_0\boldsymbol{\tau}^x\boldsymbol{\sigma}^z\boldsymbol{\rho}^z, \end{aligned} \tag{13}$$

which has the form

$$\tilde{\mathcal{H}}(\boldsymbol{k}) = \begin{pmatrix} 0 & \mathcal{A}(\boldsymbol{k}) \\ \mathcal{A}^\dagger(-\boldsymbol{k}) & 0 \end{pmatrix}, \tag{14}$$

where

$$\begin{aligned}\mathcal{A}(\boldsymbol{k}) = {}& \mathcal{E}_{\boldsymbol{k}}\boldsymbol{\sigma}^0\boldsymbol{\rho}^x - \mu\boldsymbol{\sigma}^0\boldsymbol{\rho}^0 + \mathrm{i}\mathcal{L}_{\boldsymbol{k}}\boldsymbol{\sigma}^y\boldsymbol{\rho}^x \\ & + \mathrm{i}\Delta\boldsymbol{\sigma}^y\boldsymbol{\rho}^0 - h\boldsymbol{\sigma}^z\boldsymbol{\rho}^0 - m_0\boldsymbol{\sigma}^z\boldsymbol{\rho}^z. \end{aligned} \tag{15}$$

Now because

$$\det\mathcal{H}(\boldsymbol{k}) = \det\tilde{\mathcal{H}}(\boldsymbol{k}) = \det\mathcal{A}(\boldsymbol{k})\cdot\det\mathcal{A}^\dagger(-\boldsymbol{k}), \tag{16}$$

the sign of the gap is encoded by the function $Z_{\boldsymbol{k}} = \det\mathcal{A}(\boldsymbol{k}) = \det\mathcal{A}^\dagger(-\boldsymbol{k})$, where from Eq. (15), we find

$$\begin{aligned} Z_{\boldsymbol{k}} = {}& (h_+^2 - \mu^2 - \Delta^2)(h_-^2 - \mu^2 - \Delta^2) \\ & + 8t^2(2t^2\cos^2(k) - h_-h_+ - \mu^2 + \Delta^2)\cos^2(k) \\ & + 8\lambda^2(2\lambda^2\sin^2(k) + h_-h_+ - \mu^2 + \Delta^2)\sin^2(k) \\ & - 16t^2\lambda^2\sin^2(k)\cos^2(k) + 32\mathrm{i}t\Delta\lambda\mu\cos(k)\sin(k), \end{aligned} \tag{17}$$

with $h_\pm = h \pm m_0$.

The nontrivial topological phase can be found by calculating the topological invariant (see Appendix C for more details). In order to do that, we first define $z_{\boldsymbol{k}} = Z_{\boldsymbol{k}}/|Z_{\boldsymbol{k}}|$. As

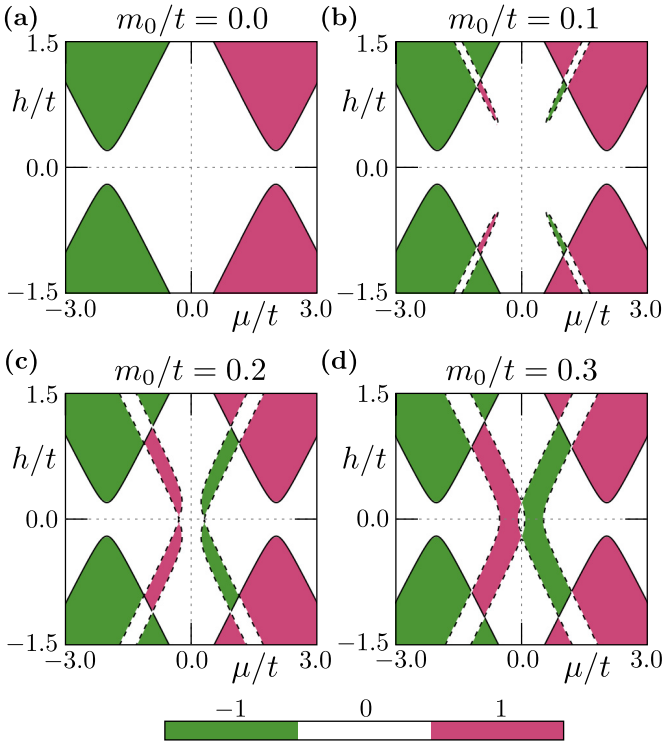

FIG. 4. Topological phase diagrams obtained from the winding number w, given by Eq. (C2), for different amplitudes of the AFM order m_0 (as labeled). Color denotes the trivial phase, $w = 0$, (white) and the nontrivial phases with $w = -1$ (green) and $w = 1$ (red). Solid black lines show gap closings at $k = 0$ and dashed lines show gap closings at $k = \pm\pi/2$. Results are for $\Delta/t = 0.2$ and $\lambda/t = 0.15$.

$\mathcal{A}(\boldsymbol{k})$ also has the time-reversal asymmetry $\mathcal{K}\mathcal{H}_{\boldsymbol{k}}\mathcal{K} = \mathcal{H}_{-\boldsymbol{k}}$, at the TRIM $\mathcal{A}(0)$ and $\mathcal{A}(\pi/2)$ must be real, and hence so must $z_{0,\pi/2}$. Therefore, for the topological index w to change one of $z_{0,\pi/2}$ must pass through zero, corresponding to a gap closing. The relative signs of $z_{0,\pi/2}$ therefore encode some information about the topological index, its parity $(-1)^w$. We can therefore construct a $\mathbb{Z}_2$ topological index [1]:

$$\mathcal{Q} = (-1)^w = \mathrm{sgn}(z_{\boldsymbol{k}=0})\cdot\mathrm{sgn}(z_{\boldsymbol{k}=\pi/2}), \tag{18}$$

which is equivalent to the index based on the Pfaffian [1]

$$\mathcal{Q} = \mathrm{sgnPf}[\mathcal{W}(0)]\cdot\mathrm{sgnPf}[\mathcal{W}(\pi/2)], \tag{19}$$

where $\mathcal{W}(k) = \mathcal{H}(k)\lambda$. Moreover, from the Hamiltonian (14), one finds

$$\begin{aligned}\mathrm{Pf}[\mathcal{W}(0)] = {}& (h_+^2 - \mu^2 - \Delta^2)(h_-^2 - \mu^2 - \Delta^2) \\ & + 8t^2(2t^2 - h_-h_+ - \mu^2 + \Delta^2) \end{aligned} \tag{20}$$

and

$$\begin{aligned}\mathrm{Pf}[\mathcal{W}(\pi/2)] = {}& (h_+^2 - \mu^2 - \Delta^2)(h_-^2 - \mu^2 - \Delta^2) \\ & + 8\lambda^2(2\lambda^2 + h_-h_+ - \mu^2 + \Delta^2). \end{aligned} \tag{21}$$

Topological phase diagrams obtained from Eq. (18) are in agreement with those ones obtained from the winding number (Fig. 4), as well as from scattering matrix technique (Fig. 5, cf. Sec. III C).

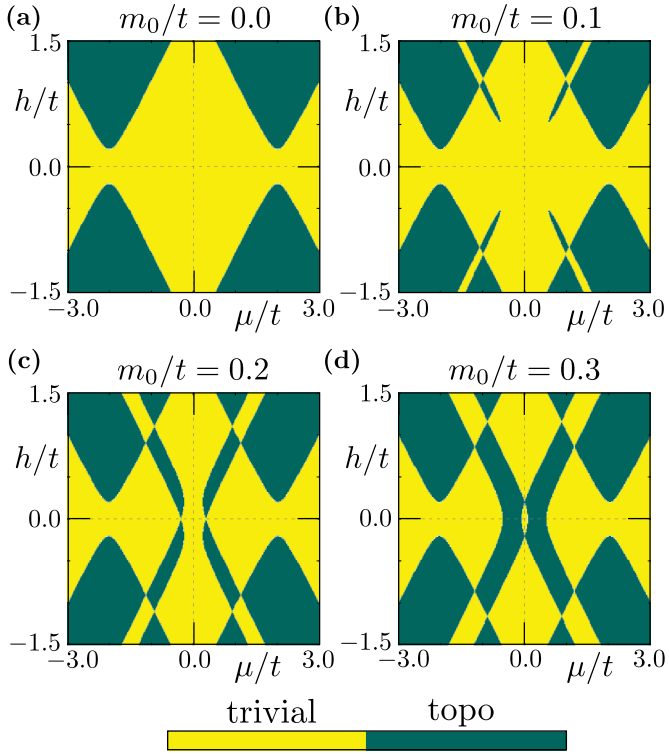

FIG. 5. Topological phase diagrams, obtained from the topological index $\mathcal{Q}$ calculated numerically using the S matrix method (cf. Sec. III C) for different amplitudes of the AFM order m_0 (as labeled). Color denotes trivial (yellow) and nontrivial (green) topological phase. Results from $\Delta/t = 0.2$ and $\lambda/t = 0.15$ for lattice with 200 sites without periodic boundary conditions.

There exists a direct relation between the $\mathbb{Z}$ invariant w and the Pfaffian $\mathbb{Z}_2$ invariant: $\mathcal{Q} = (-1)^w$ [78]. As for this model $w \in \{-1, 0, 1\}$ then $\mathcal{Q} = 1$ refers to a topologically trivial phase and $\mathcal{Q} = -1$ refers to a topologically nontrivial phase. It is then straightforward to find the exact relation between both invariants for our model:

$$w = \frac{\mathrm{sgn}(\Delta\lambda\mu)}{2}\{\mathrm{sgnPf}[\mathcal{W}(\pi/2)] - \mathrm{sgnPf}[\mathcal{W}(0)]\}, \quad (22)$$

which follows from Eq. (17) and Eq. (C3). Topological phase diagrams obtained from the winding number calculations are shown in Fig. 4.

Changes in $\mathcal{Q}$ are related to changes in the sign of $\mathrm{Pf}[\mathcal{W}(\boldsymbol{k})]$ at TRIM. In the absence of the AFM order ($h_\pm \to h$), only $\mathrm{Pf}[\mathcal{W}(0)]$ changes sign with changes in h. This is shown as the typical form of the parabolic-like part on phase diagram [Fig. 4(a)]. However, the existence of the AFM order alone can also force the emergence of an additional branch in the topologically nontrivial phase. This is possible due to the sign change of $\mathrm{Pf}[\mathcal{W}(\pi/2)]$ at the second TRIM $\pi/2$. When the magnitude of the AFM order m_0 is significantly large, additional topological branches emerge from main branches (along $|\mu| \approx |h|$ line) [cf. Figs. 4(a) and 4(b)]. If this occurs, for a range of parameters inside the main branches, the topological phase is destroyed as these phases have opposite chirality. Further increasing of m_0 joins the AFM branches and leads to a destructive overlap and emergence of a trivial phase around $\mu = h = 0$ [Fig. 4(d)]. When the AFM amplitude is relatively large, the nontrivial phase can exist around $\mu \approx 0$, i.e., in the nearly-half-filling limit $n \approx 1$ [cf. Figs. 4(c) and 4(d)].

Summarizing this part, the topological phase diagram is composed of two branches of the nontrivial phase – the main branch associated with TRIM at $\boldsymbol{k} = 0$ and the additional branch connected with the second TRIM at $\boldsymbol{k} = \pm\pi/2$. The main branch has properties which can be typically observed in the standard Rashba nanowire scenario, while the non trivial phase originating in the additional branch can be compared to the nontrivial phase induced by dimerization [79].

C. Scattering matrix method

As an independent check of the preceding analytical calculations the behavior of the topological properties can be investigated by studying the scattering matrix S, which relates the incoming and outgoing wave amplitudes (further discussion on this point can be found in Sec. V) [80–84]. In this method, the $\mathbb{Z}_2$ topological quantum number can be found from $\mathcal{Q} = \mathrm{sgn}\det R$, where R denotes the reflection submatrix of S. The scattering matrix can be calculated exactly from the real-space Hamiltonian in the frame of the transfer-matrix scheme, described in detail in Ref. [84–86]. Using this method, we evaluated the topological phase diagram numerically.

Topological phase diagrams found with this method are shown in Fig. 5. The (non)trivial topological phase covers the (green) yellow regions. It can be seen that in the absence of the AFM order, the boundary of the nontrivial phase in the μ-h space, is given by the known characteristic parabolas [Fig. 5(a)]. The existence of the AFM order, modifies the boundaries of the nontrivial phase around diagonal lines $|\mu| \approx |h|$ [Fig. 5(b)], such a modification is a result of the presence of the sublattice in the system. These phase diagram were obtained numerically and are in complete agreement with the previous results obtained from analytical calculations (Fig. 4).

D. Topological phase without a Zeeman field

Analysis of these phase diagrams show important features of the described system: first with the increase of the amplitude of m_0, we can see the emergence of additional branches of the nontrivial phase. Moreover, for some range of parameters the nontrivial topological phase can emerge without any external magnetic field but instead, only due to the existence of the AFM order in the system. This is manifested in the additional branch of the topological phase caused by the band inversion at the $\mathbf{k} = \pi/2$ TRIM [cf. Fig. 4(d)].

Due to fact that the additional branch is connected with $\boldsymbol{k} = \pi/2$ TRIM, let us analyze the properties of $\mathrm{Pf}[\mathcal{W}(\pi/2)]$ for $h = 0$. In this case, $h_\pm = \pm m_0$, which gives

$$\mathrm{Pf}[\mathcal{W}(\pi/2)]\big|_{h=0} = \left[\Delta^2 - m_0^2 + (\mu + 2\lambda)^2\right] \times\left[\Delta^2 - m_0^2 + (\mu - 2\lambda)^2\right]. \quad (23)$$

One should note that in the limit $\lambda \to 0$, we have

$$\mathrm{Pf}[\mathcal{W}(\pi/2)] \to \left(m_0^2 - \mu^2 - \Delta^2\right)^2 \geqslant 0. \quad (24)$$

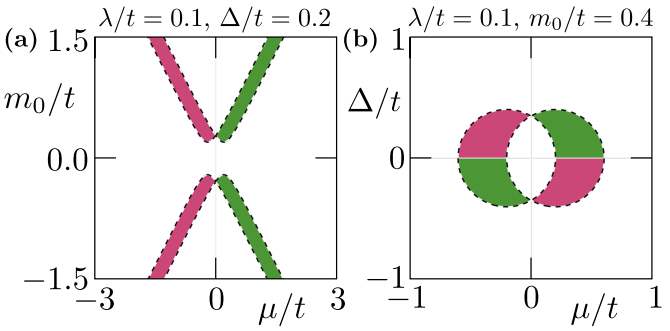

FIG. 6. Topological phase diagram in the absence of the magnetic field. Results are shown as a function of the amplitude of the AFM order and chemical potential (a) and of the SC order and and chemical potential (b). The boundaries of the nontrivial topological phases are given by the dashed lines. The winding number w color scheme is as in Fig. 4. In (b), the circles are centered on $\pm 2\lambda$ with a radius $|m_0|$.

As we can see, SOC is still a mandatory ingredient of the nontrivial topological phase.

The impact of the AFM order amplitude and the SOC on the emergence of the nontrivial topological phase is shown in Fig. 6. Interestingly, the boundaries of the nontrivial topological phase are given exactly by two circles centered on $\pm 2\lambda$ with a radius $|m_0|$ [Fig. 6(b)]. When the circles overlap each other, the overlapping region is in the trivial phase (no coloring).

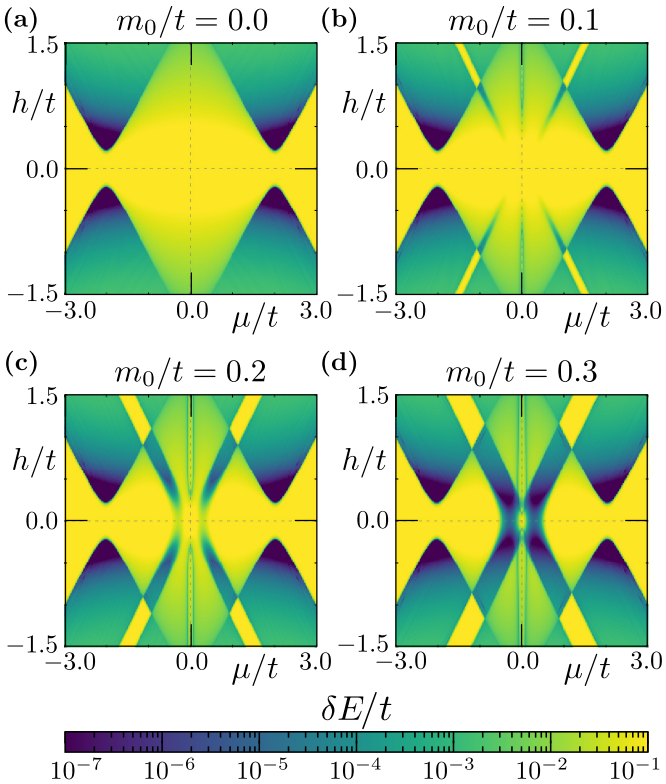

FIG. 7. Values of the "gap" δE defined as the difference between the energies of the two eigenstates which are nearest to the Fermi level for different amplitudes of the AFM order m_0 (as labeled).

IV. ELECTRONIC PROPERTIES

In this section, we will discuss the electronic properties of the system. The numerical results presented in this section were obtained for a nanowire with $N = 200$ sites and fixed values of $\Delta/t = 0.2$ and $\lambda/t = 0.15$. Our tight binding parameters can be related to real quantities via $t = 1/2ma^2$ and $\lambda \sim \alpha/a$, where m is the electron's effective mass, a is the lattice constant, and α is the physical spin-orbit coupling value. However, any experimental realization of this system (cf. discussion in Sec. I) can force particular system parameters. For example [21], in the case of semiconducting wires, $a \sim 0.6$ nm while $m = 0.027\ m_e$, which gives $t \sim 10$ meV. Induction of the superconducting gap by proximity effect is approximately given by $\Delta = 0.1$ meV. In this case, the Fermi level is located around the bottom of the band and can be tuned by doping or electrostatic gating. Contrary to this, in the multiband monoatomic chains [87], hoppings are in range of 0.5 eV. Additionally $\Delta \simeq 1$ meV [21], while the Fermi level is located around half-filling.

A. Topological gap and zero-energy states

In the absence of symmetry breaking, a topological phase transition from a trivial to a nontrivial phase is associated with closing of the trivial gap and reopening of a new topological gap. In the case of the system without periodic boundary conditions, i.e., with edges, the existence of MBS is equivalent to the existence of the nearly-zero-energy state after the phase transition to the nontrivial topological phase. However, a small value of the energy gap δE (defined as a difference between energies nearest to the Fermi level in the spectrum of the system) is not a good indicator of the existence of MBS (Fig. 7). Still, a substantial decrease of δE can indicate a clearly visible boundary between two topological phases, and has the advantage of being relatively straightforward to measure experimentally, in contrast to the invariants. For instance, in the absence of the AFM order [Fig. 7(a)], the phase boundary of the nontrivial topological phase is visible in the form of characteristic parabolas. An identical shape can be found in the corresponding topological phase diagram [cf. with Fig. 4(a)].

The phase diagrams prove to be more complicated in the presence of the AFM order. For some values of μ, we can observe additional regions with extremely small values of δE, e.g., vertical lines around $\mu/t = 0$ at Figs. 7(c) and 7(d). This behavior is associated with crossing of the Fermi level by the separate energy levels and can be noticed in the spectrum of the system [cf. red arrows at Figs. 8(a) and 8(b)]. Moreover, as these states exist in the trivial phase, they can not generate MBS at the end of the chain.

Energy spectra of the system are shown in Fig. 8. For half-filling (i.e., $\mu = 0$), some midgap states can cross the Fermi level $E = 0$ [shown by A red arrow in Figs. 8(a) and 8(b)]. However, a nontrivial topological phase is not present and these states are not MBS. In the nontrivial topological phase, MBS are visible in the spectrum of the system in the form of two close to degenerate zero-energy states (the range of h corresponding to the nontrivial phase is marked by the green color in Fig. 8). Similar to the nanowire without AFM

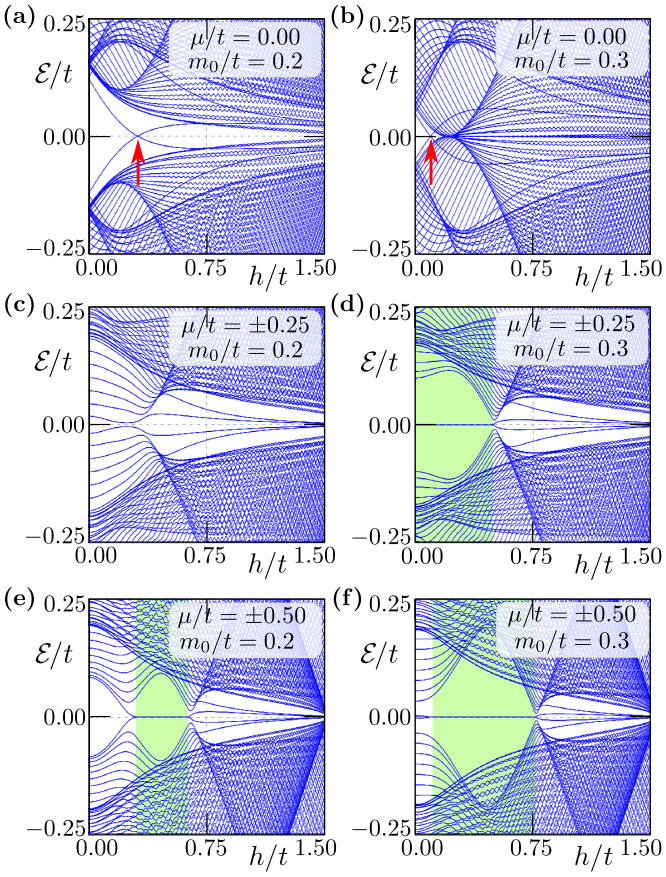

FIG. 8. The spectrum of the system for various values of the chemical potential μ and the AFM amplitude m_0 (as labeled) as a function of the magnetic field h. The range of h marked by the green color corresponds to the nontrivial topological phase.

order, eigenvalues show oscillations as a function of magnetic field h [88,89].

Additional features of the system can be visible in the energy spectrum for constant field h (Fig. 9). The well known transition to the nontrivial topological phase in the main branch is marked by the green areas. The situation is more complicated in the case of the additional branch (marked by the orange areas in Fig. 9). When m_0 is too small, the MBS do not fully emerge even if the nontrivial topological phase due to finite size effects [cf. Fig. 9(b)]. Increasing m_0 increases the gap and the MBS can then form at the same system sizes [Fig. 9(d)]. In the case of the longer chains, the MBS exist even for smaller m_0 (cf. Appendix D). This shows the importance of the length scale ζ_M (denoting the exponential decay of the Majorana wave function in space [30]), on the additional branch of the topological phase diagram. The splitting of the MBS energy depends on the mutual relation between the chain length L and ζ_M, and in practice the emergence of a zero-energy MBS is possible when $L \gg \zeta_M$ [90].

B. Localization of the Majorana modes

Localization of the Majorana states can be studied via the zero-energy LDOS (5). Exemplary results for several values of the chemical potential μ as the magnetic field h is increased are shown in Fig. 10. The MBS emerging within the main

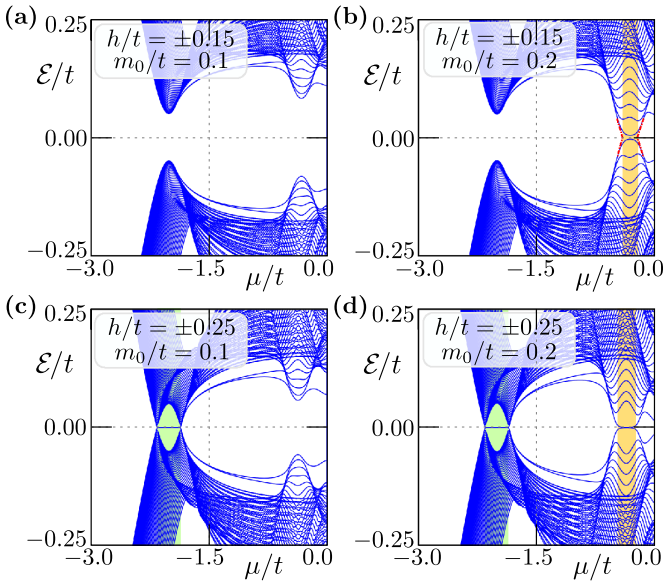

FIG. 9. The spectrum of the system for various values of the magnetic field h and the AFM amplitude m_0 (as labeled) as a function of the chemical potential μ. The range of h is marked by the green and orange color, in correspondence with the nontrivial topological phase in the main and additional branches, respectively.

and additional branches of the topological phase diagram are marked by $\mathcal{M}$ and $\mathcal{A}$, respectively. In each topological phase, independently of the topological branch, the MBS are well localized around each end of the chain. We can also observe the exponential decay of the MBS starting near the end of the chain and decaying to the middle. Moreover, for sufficiently

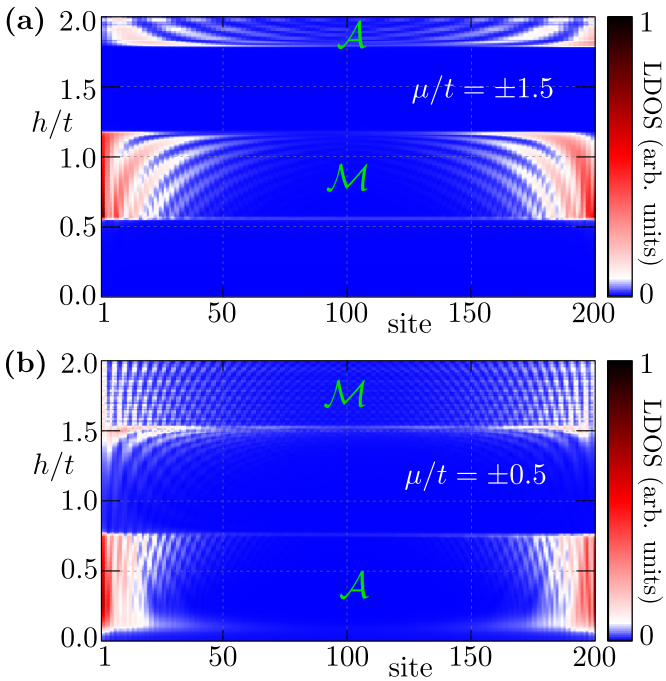

FIG. 10. Zero-energy local density of states (LDOS) as a function of the magnetic field h. Results are for AFM order with an amplitude $m_0/t = 0.3$. Edge states localized within the main and additional topological branches are marked by $\mathcal{M}$ and $\mathcal{A}$, respectively.

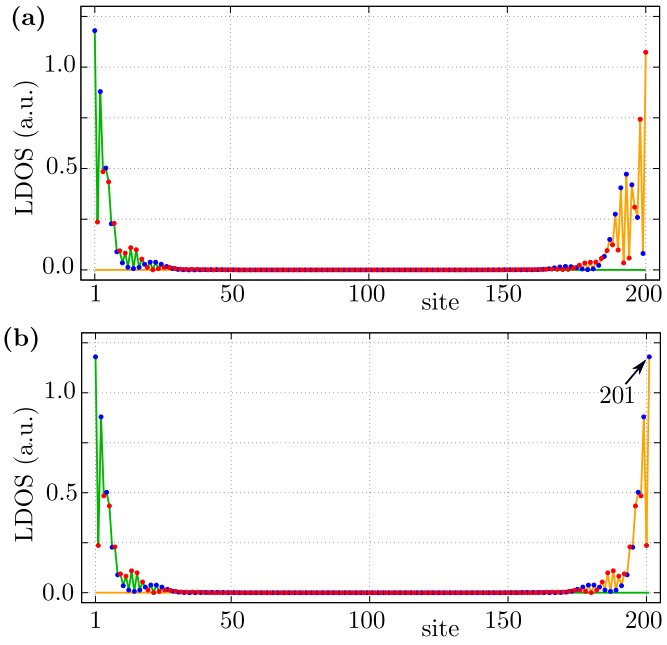

FIG. 11. The zero-energy local density of states (LDOS) corresponding to the MBS. Blue and red dots represent the A and B sublattice sites, respectively. Results for $\mu/t = -0.3$, $h/t = 0.2$, and $m_0/t = 0.3$. A comparison of results for chains with (a) 200 and (b) 201 sites.

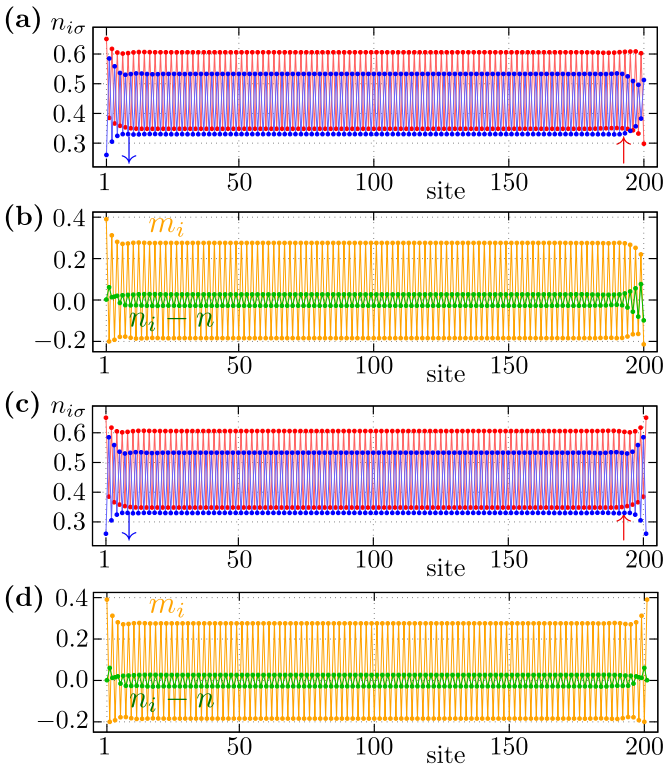

FIG. 12. The distribution of particles $n_{i\sigma}$ with spin ↑ (red) and ↓ (blue) in the system, as well as magnetization m_i (orange) and the difference between the average number of particles on a particular site and the average number per site in the system as a whole, $n_i - n$ (green). A comparison of results for the chains with 200 [(a) and (b)] and 201 [(c) and (d)] sites is shown. Same parameters as Fig. 11 for $\mu/t = -0.3$, $h/t = 0.2$, and $m_0/t = 0.3$.

high h, alternating oscillations of the Majorana bound states energies around the Fermi level are observed in the form of horizontal lines that represent the distribution of zero-energy states on the entire nanowire. The same behavior has been discussed in the context of the energy gap in the previous section. With increasing magnetic field, we can observe a series of topological phase transitions from trivial to nontrivial and vice versa as one would cross the branches of the topological phase diagram (cf. Fig. 4).

C. Influence of the sublattices

From a diagonalization of the Hamiltonian in real space (cf. Sec. II A) using the BdG formalism, in the nontrivial topological phase, we can find two zero-energy fermionic modes $\Psi^{\pm}$ at exponentially small energies $\pm\delta\epsilon$. From this, using a simple rotation:

$$\begin{pmatrix}\Psi^{L}_{is}\\ \Psi^{R}_{is}\end{pmatrix} = \frac{1}{\sqrt{2}}\begin{pmatrix}1 & 1\\ -\mathrm{i} & \mathrm{i}\end{pmatrix}\begin{pmatrix}\Psi^{+}_{is}\\ \Psi^{-}_{is}\end{pmatrix}, \tag{25}$$

we can find Majorana modes localized exactly at the left Ψ^{L} or the right Ψ^{R} side of the chain. Note that $\Psi^{L/R}$ are eigenstates of the particle-hole operator and therefore represent true Majorana modes. In a similar way, using a site-dependent unitary transformation, we can find the representation of the Majorana wave function $\Psi^{A/B}$ in each sublattice (A and B). Exemplary results are shown in Fig. 11, where left (right) modes are show by green (orange) solid lines, while the color of the dots (red and blue) represents the sublattices.

We will focus our analysis on the Majorana bound states manifesting in the additional branch of the topological phase diagram. In the absence of the external magnetic field, the site-dependent distribution of the particles with opposite spins $n_{i\sigma}$ is given only by the AFM order. The total average number of particles per site $\langle n\rangle = \sum_{i\sigma} n_{i\sigma}/2N$ is always fixed by the chemical potential. The distribution of particles with spin ↑ and ↓ has a reflection symmetry with respect to the center of the system (see Fig. 12). The average number of particles in each site is approximately constant, however, the AFM order introduced a distinguishability of the sublattices via magnetization—in other words, magnetization in sublattice A is different to B. Additionally, the Majorana wave functions $\Psi^{L/R}$, as well as $\Psi^{A/B}$, show the reflection symmetry with respect to the center of the chain. Here, it should be mentioned that the properties described above in the absence of the magnetic field do not depend on the parity of the number of sites.

The situation looks different in the presence of the magnetic field. In the case of the system with even number of sites [Fig. 11(a)], this leads to a loss of the reflection symmetry. This is a consequence of the modification of the $n_{i\sigma}$ distribution due to interplay between the AFM order and magnetic field. In fact, the effective magnetic field $h_{\pm}$ at the first and last sites of the chain are not identical. The reflection symmetry can be recovered by elongating the nanowire by one site, which yields an odd total number of sites [Fig. 11(b)]. As a

result, the first and last sites belong to the same sublattice. Similar modification of the mirror symmetry by the odd or even number of sites in the system is also observed in the particle distributions. However, the bound states have only a very small influence on the particle distribution in the central region of the nanowire.

Properties similar to those described above are exhibited by the Majorana wave function. When the number of sites is even [Fig. 11(a)], the reflection symmetry is destroyed regardless of the basis ($\Psi^{L/R}$ or $\Psi^{A/B}$). The reflection symmetry of the Majorana wave functions is restored when the system has odd sites [Fig. 11(b)]. In this case, the Ψ^{L} is a reflection of Ψ^{R}, while $\Psi^{A/B}$ has a reflection symmetry with respect to the symmetry center. Moreover, one of the $\Psi^{A/B}$ is greatly suppressed in one of the sublattices [in our case, it is the sublattice marked by red points on Fig. 11(b)].

D. Spectral function analysis

The origin of the main and additional AFM branches in the topological phase diagram can be studied in the context of the spectral function:

$$\mathcal{A}_{\boldsymbol{k}}(\omega) = -\frac{1}{\pi}\sum_{s\sigma}\mathrm{Im}G_{\boldsymbol{k}s\sigma}(\omega + \mathrm{i}0^{+}), \tag{26}$$

where $G_{\boldsymbol{k}s\sigma} = \langle c_{\boldsymbol{k}s\sigma}|(\omega - H)^{-1}|c^{\dagger}_{\boldsymbol{k}s\sigma}\rangle$. In practice, the spectral function can be re-expressed in terms of the BdG coefficients:

$$\begin{aligned}\mathcal{A}_{\boldsymbol{k}}(\omega) &= \sum_{\boldsymbol{k}s\sigma}\mathcal{A}_{\boldsymbol{k}s\sigma} \qquad (27)\\ &= \sum_{\boldsymbol{k}s\sigma}\left[|u^{n}_{\boldsymbol{k}s\sigma}|^{2}\delta(\omega - \mathcal{E}_{\boldsymbol{k}n}) + |v^{n}_{\boldsymbol{k}s\sigma}|^{2}\delta(\omega + \mathcal{E}_{\boldsymbol{k}n})\right],\end{aligned}$$

where $u^{n}_{\boldsymbol{k}s\sigma}$ and $v^{n}_{\boldsymbol{k}s\sigma}$ are components of the nth eigenvector of the Hamiltonian (11). Here we have introduced the sublattice- and spin-dependent spectral function $\mathcal{A}_{\boldsymbol{k}s\sigma}$. The topological phase transition is associated with a band inversion during the transition. To study this behavior in our system, we can define

$$\delta\mathcal{A}^{s}_{\boldsymbol{k}} = \mathcal{A}_{\boldsymbol{k}A\uparrow} + \mathcal{A}_{\boldsymbol{k}A\downarrow} - \mathcal{A}_{\boldsymbol{k}B\uparrow} - \mathcal{A}_{\boldsymbol{k}B\downarrow}, \tag{28}$$

$$\delta\mathcal{A}^{\sigma}_{\boldsymbol{k}} = \mathcal{A}_{\boldsymbol{k}A\uparrow} - \mathcal{A}_{\boldsymbol{k}A\downarrow} + \mathcal{A}_{\boldsymbol{k}B\uparrow} - \mathcal{A}_{\boldsymbol{k}B\downarrow}. \tag{29}$$

$\delta\mathcal{A}^{s}_{\boldsymbol{k}}$ and $\delta\mathcal{A}^{\sigma}_{\boldsymbol{k}}$ describe the imbalance in the sublattice and spin subspace at momentum $\boldsymbol{k}$, respectively.

Let us start with an analysis of the spectral function in the case when the topological phase arises in the main branch of the topological phase diagram (Fig. 13). As written previously, these topologically nontrivial phases occur due to the band gap closing at the TRIM $\boldsymbol{k} = 0$. Increasing the magnetic field, for fixed chemical potential, leads to a topological phase transition from the trivial to nontrivial phase. During this transition the band inversion is observed in both (sublattice and spin) subspaces. Before the topological phase transition, i.e., $h < h_c$, and in both subspaces, we observe the order of the bands "polarization": to be $(+,-,+,-)$, ordering from negative to positive energy [Figs. 13(e) and 13(f)]. For the chosen parameters, topological phase transition occurs at the critical magnetic field $h_c/t \simeq 0.2$. When $h = h_c$, the gap is closed and two bands touch each other at $\boldsymbol{k} = 0$ [Figs. 13(c) and 13(d)]. Further increase of h leads to a changing of the "polarization" order to $(+,+,-,-)$ at $\boldsymbol{k} = 0$ [Figs. 13(a) and 13(b)]. At $\boldsymbol{k} = \pi/2$ the ordering remains $(+,-,+,-)$ and hence there is band inversion. This inversion occurs in both sublattice and spin subspaces at the same time. From this, we can conclude that the main branch of the topological phase emerges as an effect of the external magnetic field, independently of the AFM order.

Now, we turn to analyze the inversion of the bands in the case of the additional, AFM-related, branch of the topological phase diagram (Fig. 14). In this case, the existence of the topological phase is associated with the system properties at the TRIM $\boldsymbol{k} = \pm\pi/2$. As previously, increasing the magnetic field leads to the topological phase transition. However, during this transition, in the spin sector we do not observe band inversion, i.e., the spin polarization for each band is the same and positive (Fig. 14, right panels), the spin imbalance in the system is unchanged due to the presence of a relatively strong magnetic field. The situation looks different in the sublattice sector. In the trivial phase [Fig. 14(e)], we observe band ordering as in the previous case, i.e., $(+,-,+,-)$. At $h = h_c$, we observe a closing of the gap at the TRIM $\boldsymbol{k} = \pi/2$ [Fig 14(c)]. A further increase of h leads to a band inversion in sublattice frame and the polarization order—$(+,+,-,-)$ at $\boldsymbol{k} = \pi/2$ [Fig. 14(a)]. From this we can conclude, that the key role of AFM order is key in the emergence of the additional branch in the topological phase diagram. Moreover, the introduction of the sublattice imbalance by the AFM order is the main source of the nontrivial band topology.

Band inversion is a very typical signature of a topological phase transition in these systems [91–93] and was also reported as a signature of the topological phase transition in the case of the Rashba chain [29,94,95]. The spectral function can be measured in angle-resolved photoemission spectroscopy (ARPES) experiments [65]. The properties described above open a new way for the experimental examination of the construction of the additional topological branches in the AFM chain, and their comparison with the standard branch.

Summarizing, we would like to point out that the emergence of the topological branch in the phase diagram is a consequence of the band inversion located around half-filing ($\mu/t = 0$). Here, we should remember that a similar behavior can also be observed in the systems exhibiting folding of the Brillouin zone due to an increase in the sites/atoms in the "primitive" unit cell [96–100]. Therefore increasing the number of allowed subbands leads to more complicated forms of the topological phase diagram. However, in contrary to those systems, in our case the magnetic order can lead to an emergence of MBS even in the absence of the external magnetic field. This behavior can be crucial in the experimental realization of the MBS in the chains with chiral magnetic order [19,48,50,101] or spin-block systems [102].

V. TRANSPORT PROPERTIES

Here, we show the results of numerical calculations of the differential conductance of the studied system using the scattering formalism [80–84]. Our system can be treated as a superconducting chain connected to normal leads (cf. Fig. 15),

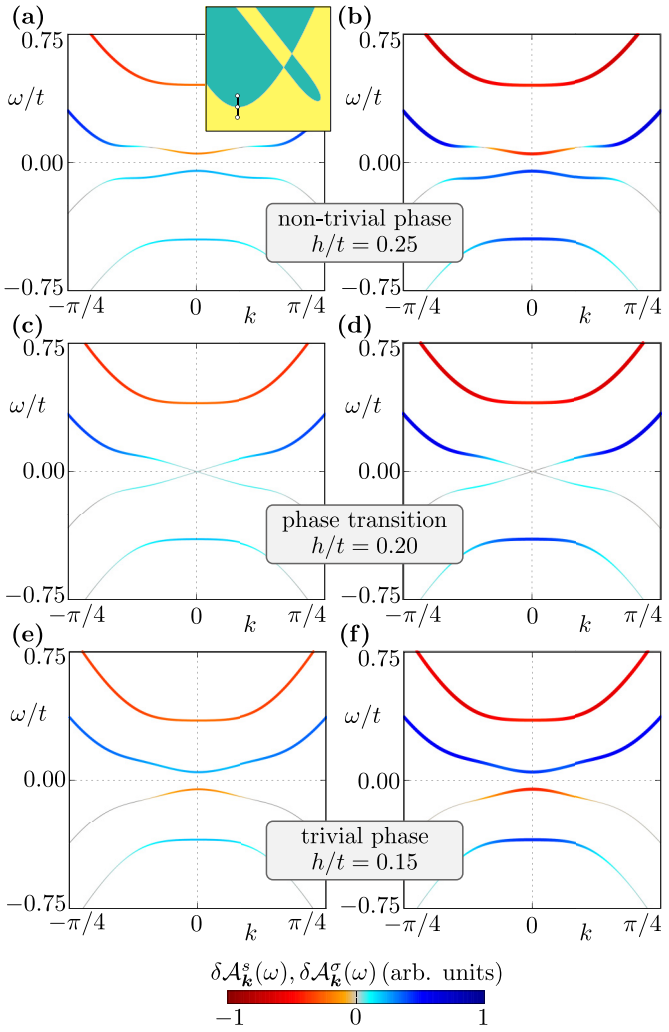

FIG. 13. Distinctions in the sublattice and spin dependent spectral functions, $\delta\mathcal{A}^s_{\boldsymbol{k}}$ (left) and $\delta\mathcal{A}^\sigma_{\boldsymbol{k}}$ (right). Results for $m_0/t = 0.1$, $\mu/t = -2.0$, and $h/t = 0.15$, 0.20, and 0.25 (panels from bottom to top) showing the topological phase transition from the trivial to the nontrivial topological phase along the main branch (the black line is not in scale, shown in the inset).

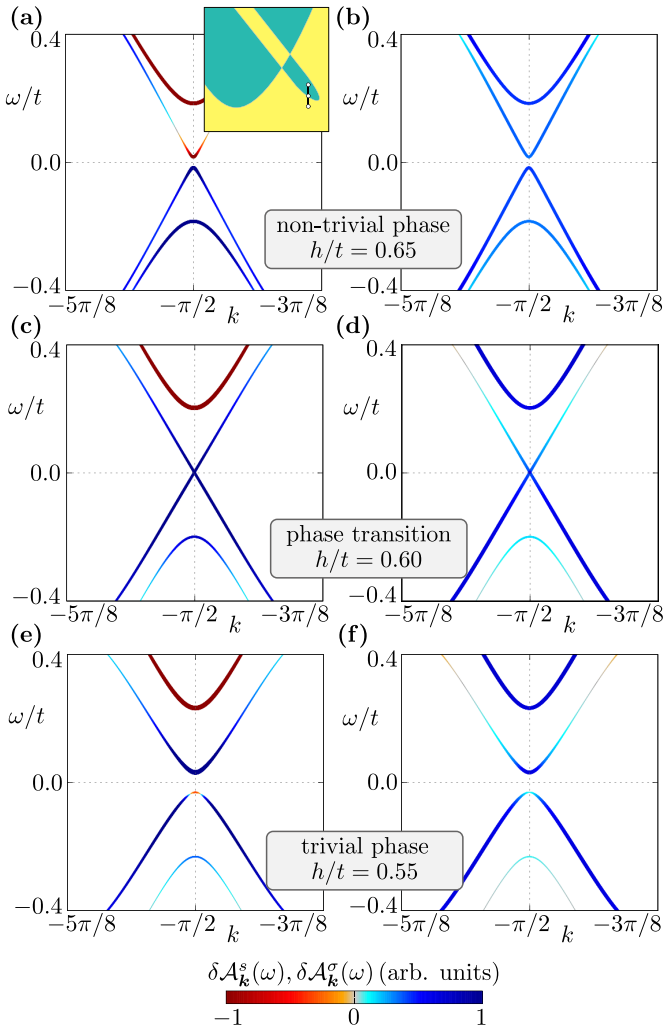

FIG. 14. Distinctions in the sublattice and spin dependent spectral function, $\delta\mathcal{A}^s_{\boldsymbol{k}}$ (left) and $\delta\mathcal{A}^\sigma_{\boldsymbol{k}}$ (right), respectively. Results for $m_0/t = 0.1$, $\mu/t = -0.7$, and h/t equal 0.55, 0.60, and 0.65 (from bottom to top) topological phase transition from trivial to nontrivial topological phase along additional branch (the green line is not in scale, shown at inset).

i.e., and N/S/N junction. Then the scattering matrix relating all incident and outgoing modes in this system is

$$S = \begin{pmatrix} S_{11} & S_{12} \\ S_{21} & S_{22} \end{pmatrix}, \quad S_{ij} = \begin{pmatrix} S^{ee}_{ij} & S^{eh}_{ij} \\ S^{he}_{ij} & S^{hh}_{ij} \end{pmatrix}. \tag{30}$$

The S^{ab}_{ij} is the block of scattering amplitudes of incident particles of type b in lead j to particles of type a in lead i [83]. The zero-temperature differential conductance matrix is

$$G_{ij}(E) \equiv \frac{\partial I_i}{\partial V_j} = G_0\left(T^{ee}_{ij} - T^{he}_{ij} - \delta_{ij}N^e_i\right), \tag{31}$$

where I_i is the current entering terminal i from the scattering region, while V_j is the voltage applied to terminal j. Here $G_0 = e^2/\hbar$ is the conductance quantum without the spin degeneracy taken into account. N^e_i is the number of electron modes at energy E in terminal i. The energy transmission is given as

$$T^{ab}_{ij} = \mathrm{Tr}\left(\left[S^{ab}_{ij}\right]^\dagger S^{ab}_{ij}\right). \tag{32}$$

We performed the calculation in the case of the N/S/N system shown in Fig. 15, using the KWANT [103] code to numerically obtain the scattering matrix.

An experimental study of the MBS emergence in the system can be performed by local differential conductance G_{ii} measurements (for $i = 1, 2$). In the tunneling regime, the local conductance G_{ii} in a normal lead probes the density of states

FIG. 15. Schematic representation of system used in the differential conductance G calculation—AFM chain connected to two normal leads. Due to the Coulomb blockade between leads and chains, a barrier region exists in the system (gray area).

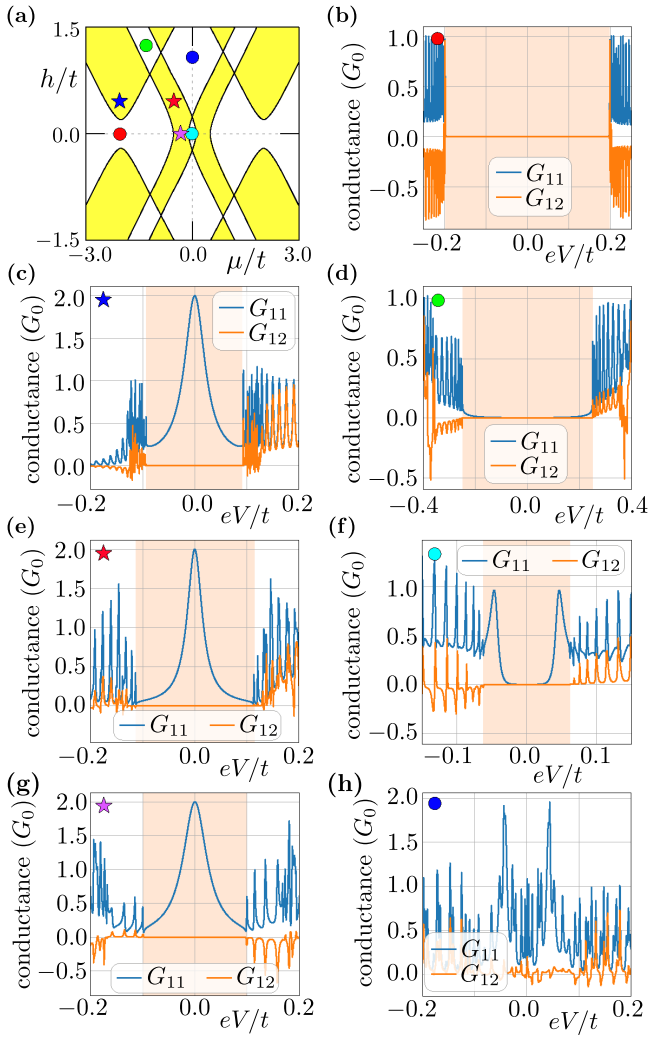

FIG. 16. Local (G_{11}) and nonlocal (G_{12}) differential conductance for different sets of the system parameters μ and h (marked by colored points—the stars and circles correspond to the nontrivial and trivial phases, respectively). Results for a finite size chain with 200 sites and fixed $m_0/t = 0.3$, $\Delta/t = 0.2$, and $\lambda/t = 0.15$.

in the proximitized region.[1] From this, one can obtain information about the in-gap states close to the i-th normal lead. In a typical situation, the local conductance G_{ii} is quantized by G_0 [104] (if spin degeneracy is not present). However, for "true" zero-energy bound states, the local conductance G_{ii} should be equal to $2G_0$ (per each MBS) [105–107]. A measurement of G_{ii} in such a case can yield important information about the existence of the MBS and can be used in the experimental "testing" of the topological phase diagram [108]. Contrary to this, non-local conductance G_{12} (or G_{21}) can give information about the nontrivial topological gap [83,109] and be helpful in distinguishing between nontrivial in-gap states and the "bulk" states. The induced gap matches the energies at which the nonlocal conductance becomes finite [83].

[1]We assume chemical potential $\mu/t = 0$ in leads and a barrier potential which is equal to $3t$.

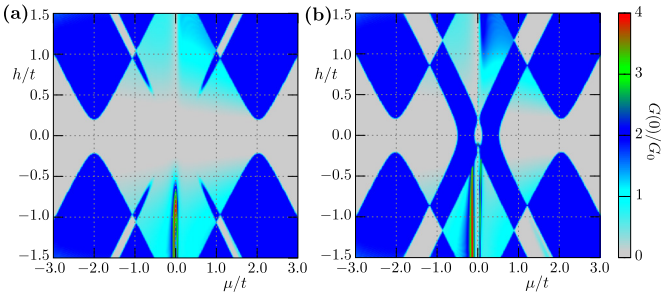

FIG. 17. Value of the zero-bias local differential conductance $G_{11}(0)$ in the case of AFM nanowire with $m_0/t = 0.1$ (a) nad $m_0/t = 0.3$ (b). Results for a finite chain with 200 sites, $\Delta/t = 0.2$, and $\lambda/t = 0.15$.

First, we evaluate the local G_{11} and nonlocal G_{12} conductance for several fixed values of chemical potential μ and magnetic field h (Fig. 16). We assume $m_0/t = 0.3$, which corresponds to a rich topological phase diagram, cf. Fig. 16(a). In the simplest case, in the absence of the magnetic field, for chemical potential near the bottom of band ($\mu/t = -2$), i.e., Fig. 16(b), G_{11} takes maximal values around G_0, while G_{12} correctly shows the value of the gap (marked by the shaded orange background). The transition to the topological phase by increasing the magnetic field leads to the emergence of MBS associated with the zero-bias peak of $G_{11} = 2G_0$, cf. Fig. 16(b). At the same time the nonzero value of G_{12} shows the induced topological gap. In the intermediate trivial region, Fig. 16(c) for $\mu/t = -1.5$ and $h/t = 1.25$, the results looks similar to the first case. Results obtained within the additional branch of the topological phase diagram, i.e., Fig. 16(e), look similar to the main branch. G_{12} indicate the values of the small topological gap with clearly visible zero-bias MBS peak $G_{11} = 2G_0$. These features are also conserved in the absence of the external magnetic field [Fig. 16(g), for $\mu/t = -0.25$]. Finally, in the central trivial region of the phase diagram, for $\mu/t = 0$ and $h/t = 0$, i.e., Fig. 16(f), again a typical signature of the trivial phase can be seen. Additionally, due to the closeness to the boundary of the topological phase, we observe a signature of the extremely small gap in G_{12}. Similar behavior can be observed for larger values of h [Fig. 16(h), for $h/t = 1$], where in practice the gap is negligible.

Analogously to the experimental venue [108], we can try to reproduce the shape of the topological phase diagram by studying the zero-bias local conductance G_{11} (Fig. 17). The conductance quanta $2G_0$ (the blue color) reproduce the main features of the topological phase diagram. The calculations have been performed for a finite size system, in the case of a chain with 200 sites. For shorter chains, a vanishing of the MBS in some parts of the diagram can be observed. This effect is associated with the splitting of the in-gap energies [110] and is similar to the situation previously described in Sec. III A.

A. Distinguishing trivial and topological zero-energy states

Although the existence of the $2G_0$ quantized conductance is often considered as a good indication of the presence of MBS, it should be noted that this can be mimicked by non-Majorana states [111,112], and hence is not an unambiguous

detection of a MBS. The nonlocal conductance G_{ij} can give some information about the realization of the nontrivial topological gap [83,109]. A similar situation can also be found in hybrid systems, e.g., in a nanowire with a quantum dot region, leading to the realization of nontopological zero-energy states [112–115], which has also been reported experimentally [12].

Recently, there have been a host of methods introduced for distinguishing trivial zero-energy (Andreev or Yu-Shiba-Rushinov) bound states from the topological MBS. Those which may be directly applicable to the system we are considering include several theoretical predictions about nontrivial spin signatures of MBS [29,95,116–119] and spin selective Andreev reflection [120,121]. Such ideas were successfully applied within a spin polarized STM experiment as a diagnostic tool [18]. However due to the AFM background the spin polarization of the MBS is unlikely to show such clear results in this case.

Another way of observing a signature of MBS can be achieved, via coupling the topological nanowire to a quantum dot, by spin-resolved current shot-noise measurements [117,122–126] or finite-frequency current shot-noise [127]. An interesting alternative is possible due to the Majorana entropy study [128], which was successfully applied experimentally in the low temperature regime [129]. The MBS may also be distinguished from other trivial bound states using supercurrents and critical currents measurements in superconductor-normal-superconductor junctions [130–132]. These proposals all require significant modifications to the setup under scrutiny here, and we will not consider them further in this work.

VI. TOPOLOGICAL PROTECTION

From a practical point of view, one of the most important properties of the MBS is their robustness due to the topological protection, which is manifested in the absence of an impact of any form of external "disorder" on the degeneration of MBS (provided the disorder neither closes the gap nor destroys the relevant symmetries). We study this property in our system in the presence of several different types of perturbation: (i) a random or (ii) homogeneous tilt of the AFM magnetic moments, and (iii) random variations in the SOC coupling strength (i.e., off-diagonal disorder). First, we modify the magnetic moment by a site-dependent perturbation δm_i perpendicular to the initial AFM magnetic moments m_0. We substitute:

$$m_0\hat{e}_z \rightarrow \frac{m_0\,\hat{e}_z + \delta m_i\,\hat{e}_x}{\sqrt{1+\delta m_i^2/m_0^2}}, \tag{33}$$

which conserves the norm of the magnetic moment on each site as equal to m_0. In case (i), δm_i varies randomly for each site, whereas for *(ii)* the change in magnetization direction was homogeneous $\delta m_i \rightarrow \delta m$. For (i), we define the angle $\sin\alpha_i = \delta m_i/m_0$, and for (ii), we define the angle $\sin\beta = \delta m/m_0$. Secondly, we assume for (iii) off-diagonal disorder as a perturbation of the SOC value:

$$\lambda_{ij} \rightarrow \lambda + \delta\lambda_{ij}, \tag{34}$$

where $\delta\lambda_{ij} = \delta\lambda_{ji}$ denotes the change in the SOC amplitude between neighboring sites.

To study the influence of these perturbations on the robustness of the MBS, we calculated the DOS of the disordered system. For cases (i) and (iii), we average over 10^2 different distribution of α_i and $\delta\lambda_{ij}$, respectively. The parameters vary such that $\alpha_i \in [-\alpha, \alpha]$ (analogically for angle β) and $\delta\lambda_{ij} \in [-\delta\lambda, \delta\lambda]$. We compare the effects of the perturbations for both a point in the main topologically nontrivial phase, and the additional topologically nontrivial phase (blue and violet stars in Fig. 16, respectively).

As may be expected, MBS emerging within the main topological branch are stable to random variations in the AFM direction, case *(i)*, [Fig. 18(a)]. In contrast, if one is in the additional branch, which is related to the AFM order, one can see that the MBS are destroyed for large enough variations in the AFM field direction [Fig. 18(b)]. One can compare this to tilting of magnetic field in the normal nanowire set-up, which also destroys the topological phase [62]. For case (ii), again tilting the direction of the AFM order has no effect on the main topological phase [Fig. 18(c)]. For the additional branch of the phase diagram tilting the AFM order drives the system through a topological phase transition to a trivial phase [Fig. 18(d)]. This happens for a smaller value of β than α [compare Figs. 18(b) and 18(d)].

The situation is different in the case of the off-diagonal disorder [Fig. 18(e) and 18(f)]. For the main branch, Fig. 18(e), the value of the SOC is not important for the existence of the topological phase, and so the topological phase remains robust. One can see that eventually disorder will close the gap for sufficiently large values of $\delta\lambda$. The additional branch, Fig. 18(f), has a phase transition to the topologically trivial regime for $\lambda/t \approx 0.21$ and $\lambda/t = 0.15$ in the results of Fig. 18(e). We are therefore not far from the topological phase transition and may expect the disorder to fully close the gap. However, for the disorder values considered this has not yet occurred. This situation is similar to the dimerized branch which occurs in a similar nanowire with SSH ordering, where the MBS should be destroyed when the amplitude of the perturbation is on the order of the hopping t [79].

VII. SUMMARY

In this paper, we studied the possibility of the emergence of Majorana bound states in a nanowire with antiferromagnetic and superconducting order induced by proximity effects. We found that the topological phase diagram is composed of two branches of the nontrivial topological phase. The main branch has the typical properties characteristic for a superconducting Rashba nanowire, while the second additional branch is associated with the existence of the antiferromagnetic order. Moreover, for some range of the parameters, the additional branch of the nontrivial topological phase can "survive" even in the absence of the external magnetic field. In such a case, antiferromagnetic order is the source of the nontrivial phase near the half-filling limit.

These results show an emergence of a new, antiferromagnetic topological phase that can be contrasted with the typical situation, when the Majorana bound states can emerge only if the density of the particles is sufficiently low (i.e., when

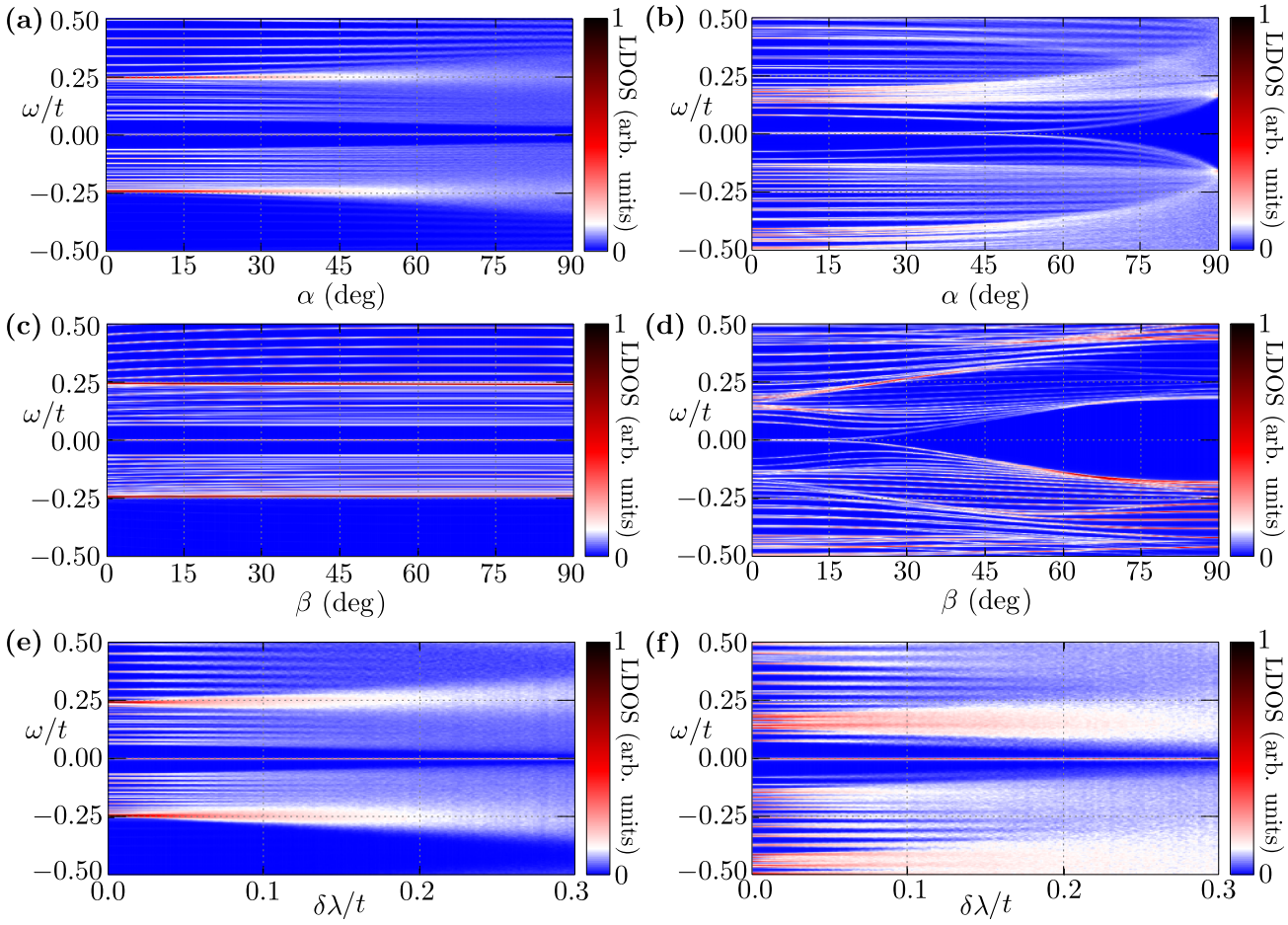

FIG. 18. Comparison of the MBS stability due to different types of perturbation: a random tilt of the magnetic moments [(a) and (b)], a constant tilt of magnetic moments [(c) and (d)], and random perturbations of the SOC [(e) and (f)]. Degree value describes magnetic moments tilt from $\hat{e}_z$ to $\hat{e}_x$. The color corresponds to the average LDOS under several configurations. Left and right panels show results within the main branch ($\mu/t = -2$, $h/t = 0.5$, and $m_0/t = 0.3$, blue star in Fig. 16) and the additional branch ($\mu/t = -0.2$, $h/t = 0.0$, and $m_0/t = 0.3$, violet star in Fig. 16), respectively.

the Fermi level is located near the bottom of the band) and the system is under the effect of an external magnetic field. However, the phase transition to the nontrivial topological phase can still induced by the external magnetic field or by changing of the chemical potential, i.e., by doping. We show that the standard nontrivial phase of such a nanowire has a different band inversion signature to that of the novel phase, which could be measured in ARPES experiments. We also explored experimental signatures of the MBS and topological gap in the local and nonlocal differential conductance.

ACKNOWLEDGMENTS

We kindly thank Pascal Simon for fruitful discussions. This work was supported by the National Science Centre (NCN, Poland) under the grants UMO-2018/31/N/ST3/01746 (A.K.), UMO-2018/29/B/ST3/01892 (N.S.), and UMO-2017/24/C/ST3/00276 (A.P.). Additionally, A.P. appreciates funding in the frame of scholarships of the Minister of Science and Higher Education (Poland) for outstanding young scientists (2019 edition, No. 818/STYP/14/2019).

APPENDIX A: BAND STRUCTURE

Here we discuss the impact of the model parameters on the band structure of the chain without superconductivity ($\Delta = 0$). The band structure is presented in Fig. 19. In the case of a "free standing" chain (i.e., in the absence of magnetic field, AFM order, and SOC), the bands contain two spin degenerate branches due to the unit cell containing two, in this case identical, atoms - upward and downward parabolic bands (dashed green line in every panel). These two branches are a result of the folding of the $\mathcal{E}_{\boldsymbol{k}} = -2t\cos(k_x a)$ dispersion relation, intersecting at $\boldsymbol{k} = \pm\pi/2$. The external magnetic field h leads to a shifting of the bands in the energy domain due to the Zeeman effect [Fig. 19(a)]. The Rashba type SOC leads to a shifting of bands in the momentum domain,, while preserving the band degeneracy at $k = 0$ (indicated by blue arrows) [Fig. 19(b)]. Here, it should be mentioned that this effect is typical in the Rashba chain [133,134]. Introduction of AFM order into the system allows for band gap to emerge at $\boldsymbol{k} = \pi/2$ [Fig. 19(c)], marked by red background color. This behavior has been also reported in the case of the Su-Schrieffer-Heeger (SSH) model, with two nonequivalent

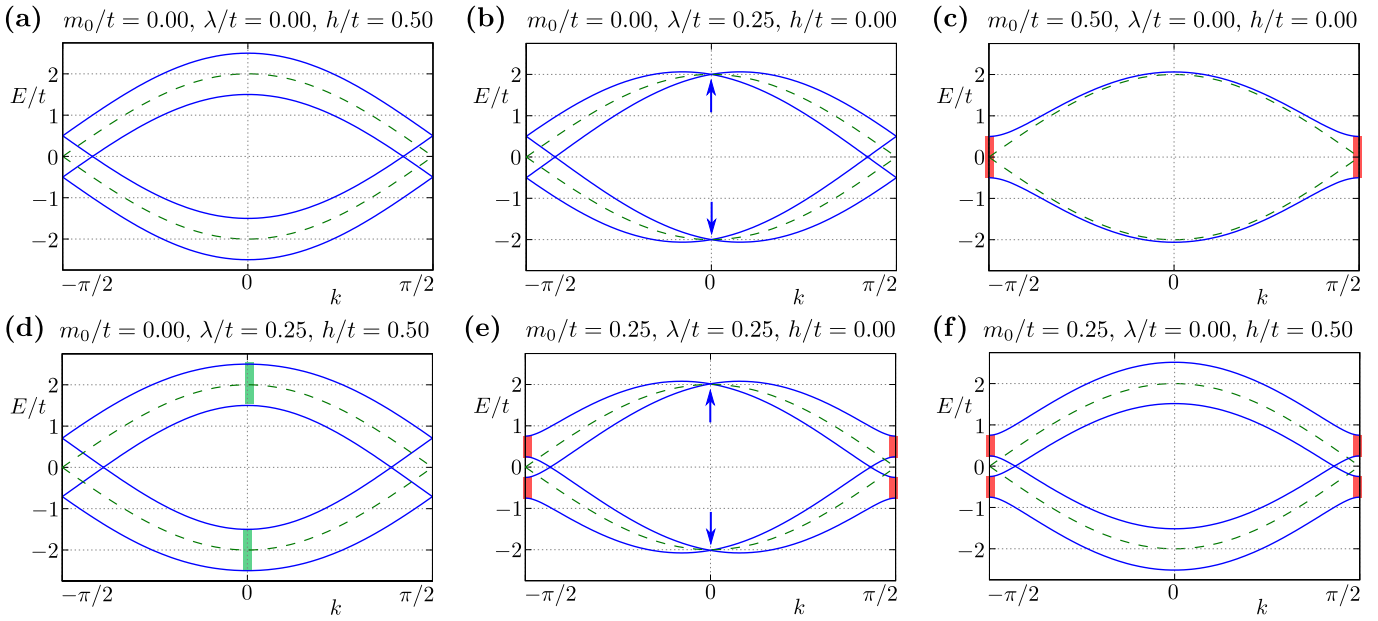

FIG. 19. Impact of the SOC and magnetic field on the spectrum of the chain without superconductivity. Results for several fixed parameters (as labeled) and chemical potential $\mu/t = 0$. Dashed green line shows folding band for "free" chain with two sites in unit cell. Green (red) markers at $k = 0$ ($k = \pm\pi/2$) indicate points with degeneracy lifted by the magnetic field (AFM order). Results obtained for several fixed parameters (as labeled) and a chemical potential $\mu/t = 0$.

hopping between sites in unit cell [135]. Such a band gap exists in the band structure independently of μ and other parameter [cf. Figs. 19(c), 19(d) and 19(f)]. Here, the spin degree of freedom remains a good quantum number, however the sublattice degree of freedom does not [136]. This yields a situation where eigenstates are a spin-dependent mixture of the A and B sublattice states. Moreover, the spatial profile displays a lattice dependent modulation of the density that is spin dependent and band dependent. Breaking time-reversal symmetry due to the AFM order still provides an analog to Kramers' theorem due to the combined time-reversal and translation symmetry—hence there are two degenerate bands with opposite spins. As a result, this degeneracy can be lifted by an external magnetic field (or by SOC).

Inclusion of such terms in pairs leads to a mixing of the aforementioned, separate, behaviors. First, a magnetic field in the presence of SOC leads to a lifting of the band degeneracy at the Γ point [indicated by the green markers in Fig. 19(d), cf. with Fig. 19(b)]. Second, AFM order and SOC shifts bands along the k axis, while the band gap changes along the E axis [Fig. 19(e)]. At the same time, the degeneracy at $\boldsymbol{k} = 0$ (indicated by blue arrows) is preserved. Still, a very strong magnetic field can lift this degeneracy (not shown). Finally, the external magnetic field in the presence of the AFM order lifts the spin-degeneracy while simultaneously preserving the band gap at $\boldsymbol{k} = \pm\pi/2$ [Fig. 19(f)].

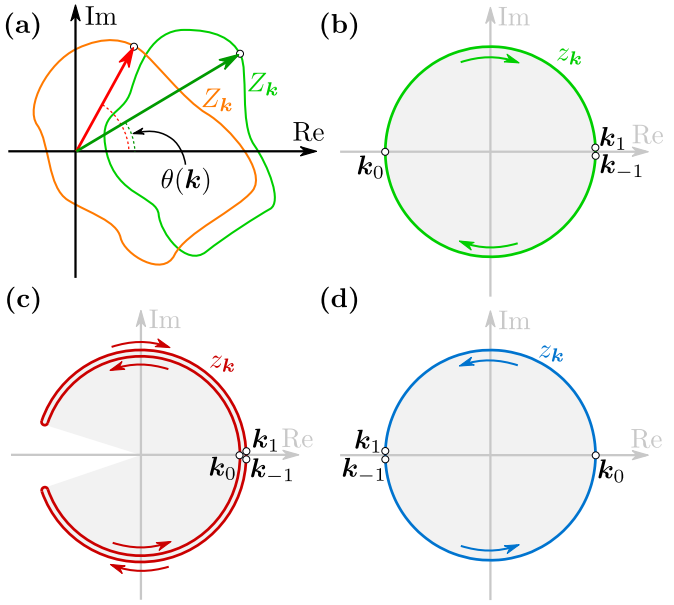

FIG. 20. (a) Graphical interpretation of the winding number w, given by Eq. (C4). $z_{\boldsymbol{k}} = Z_{\boldsymbol{k}}/|Z_{\boldsymbol{k}}|$ corresponds to a projection of some closed contour given by $Z_{\boldsymbol{k}}$ on the unit circle. In the case of the nontrivial topological phase, the contour created by $Z_{\boldsymbol{k}}$ lies on the complex plane and contains the origin. Then, periodic changes of $\boldsymbol{k}$ lead to a full winding of the phase (red circle). Contrary to this, in the trivial phase, $\theta(\boldsymbol{k})$ does not perform a full winding as a function of $\boldsymbol{k}$ (the origin is outside of the $Z_{\boldsymbol{k}}$ trajectory). Panels from (b) to (d) show exemplary results for $\mu/t = -2$, -1.25, and -0.5, respectively, for fixed $h/t = 0.5$, $\Delta/t = 0.2$, and $\lambda/t = 0.15$. TRIM ($\boldsymbol{k}_0 = 0$ and $\boldsymbol{k}_{\pm 1} = \pm\pi/2$) are depicted as white points. The behavior of the winding number in the nontrivial phase is shown in panels (b) and (d). For the trivial phase $z_{\boldsymbol{k}}$ does not describe a closed unit circle.

APPENDIX B: REAL SPACE BOGOLIUBOV-DE GENNES HAMILTONIAN

The real-space Bogoliubov-de Gennes (BdG) equations, can be written in the form $\mathcal{E}_n \Psi_{isn} = \mathbb{H}_{is,js'} \Psi_{js'n}$, where $\mathbb{H}_{is,js'}$

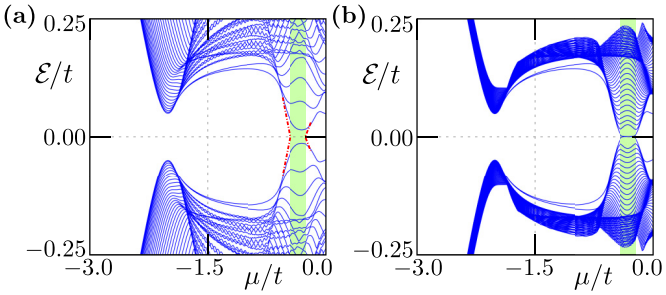

FIG. 21. Impact of the chain length on the realization of the nontrivial topological phase (marked by the green range of h). The spectrum of the system for $h/t = \pm 0.15$ and $m_0/t = 0.2$ as a function of the chemical potential μ. Results for the chain with 100 (a) and 500 (b) sites. Only the first 100 eigenvalues around the Fermi level are shown.

is the Hamiltonian in the matrix form:

$$\mathbb{H}_{is,js'} = \begin{pmatrix} H_{is,js',\uparrow} & S^{\uparrow\downarrow}_{is,js'} & \Delta_{is,js'} & 0 \\ S^{\downarrow\uparrow}_{is,js'} & H_{is,js',\downarrow} & 0 & \Delta_{is,js'} \\ \Delta^*_{is,js'} & 0 & -H^*_{is,js',\downarrow} & -S^{\downarrow\uparrow}_{is,js'} \\ 0 & \Delta^*_{is,js'} & -S^{\uparrow\downarrow}_{is,js'} & -H^*_{is,js',\uparrow} \end{pmatrix}, \tag{B1}$$

with the eigenvectors

$$\Psi_{isn} = (u_{isn\uparrow}, u_{isn\downarrow}, v_{isn\downarrow}, v_{isn\uparrow})^T. \tag{B2}$$

For the considered model (cf. Sec. II A), the matrix block elements, are given by $H_{is,js',\sigma} = -t\delta_{ij}\delta_{\langle ss'\rangle} - t\delta_{i-1,j}\delta_{\langle s,s'\rangle} - [\mu + \sigma(h + m_0(\delta_{sA} - \delta_{sB}))]\delta_{ij}\delta_{ss'}$, the superconductivity is denoted by $\Delta_{is,js'} = \Delta\delta_{ij}\delta_{ss'}$ and $S^{\sigma\sigma'}_{is,js'} = -i\lambda(\sigma_y)_{\sigma\sigma'}(\delta_{ij}\delta_{\langle ss'\rangle} - \delta_{i-1,j}\delta_{\langle ss'\rangle})$ gives the spin-orbit term.

APPENDIX C: TOPOLOGICAL INVARIANTS

The winding number w can be found starting from the standard chiral invariant [137]

$$w = \frac{1}{4\pi \mathrm{i}} \int_{-\frac{\pi}{2}}^{\frac{\pi}{2}} dk \mathrm{Tr} \mathcal{S}\tilde{\mathcal{H}}\partial_k \tilde{\mathcal{H}}^{-1}, \tag{C1}$$

which has the equivalent formulation, found after a small amount of manipulation,

$$w = \frac{1}{2\pi \mathrm{i}} \int_0^{\pi} dk \mathrm{Tr}[\partial_k \mathcal{A}(k)]\mathcal{A}^{-1}(k). \tag{C2}$$

This can be easily calculated numerically to find the chiral invariant. However in the following we will find an analytical formula for the invariant. Rewriting this as

$$w = \frac{1}{2\pi \mathrm{i}} \int_0^{\pi} dk \partial_k \ln \det [\mathcal{A}(k)], \tag{C3}$$

we see that the invariant is the winding of $\det \ln [\mathcal{A}(k)]$ across the Brillouin zone.

From the definition of Z_k and Eq. (C3) one can see that the winding number of $z_k = Z_k/|Z_k| = \exp(i\theta_k)$ is equivalently the invariant w and

$$w = \frac{-i}{2\pi} \int_{k=-\pi/2}^{k=\pi/2} \frac{dz_k}{z_k} = \frac{1}{2\pi} \int_{-\pi/2}^{\pi/2} dk \frac{d\theta_k}{dk}. \tag{C4}$$

This clearly takes only integer values (including zero) since $z_{-\pi/2} = z_{\pi/2}$. The winding number is associated with the number of times that the angle θ_k winds about the origin in the complex plane (see Fig. 20). This quantity is invariant under smooth perturbation and cannot changed unless $|Z_k|$ goes to zero due to gap closing (provided the chiral symmetry is preserved). The winding number w is the $\mathbb{Z}$ topological index.

APPENDIX D: FINITE SIZE EFFECTS

Depending on the length of the localization of the MBS, which in turn depends on the size of the gap, one may need larger system sizes in order to adequately capture the MBS. In Fig. 21, we compare the energy spectrum for system lengths of 100 and 500 sites. In the nontrivial topological phase (range of μ marked by green area), one can see that for the shorter nanowire the MBS do not fully form due to their energy splitting caused by the MBS overlapping in the nanowire [Fig. 21(a)]. However, for a longer nanowire [Fig. 21(b)] this is no longer a problem and there are well formed zero-energy states.

[1] A. Y. Kitaev, Unpaired majorana fermions in quantum wires, Phys. Usp. **44**, 131 (2001).

[2] R. Aguado, Majorana quasiparticles in condensed matter, La Rivista del Nuovo Cimento **40**, 523 (2017).

[3] R. M. Lutchyn, E. P. A. M. Bakkers, L. P. Kouwenhoven, P. Krogstrup, C. M. Marcus, and Y. Oreg, Majorana zero modes in superconductor-semiconductor heterostructures, Nat. Rev. Mater. **3**, 52 (2018).

[4] R. Pawlak, S. Hoffman, J. Klinovaja, D. Loss, and E. Meyer, Majorana fermions in magnetic chains, Prog. Part. Nucl. Phys. **107**, 1 (2019).

[5] C. Nayak, S. H. Simon, A. Stern, M. Freedman, and S. Das Sarma, Non-Abelian anyons and topological quantum computation, Rev. Mod. Phys. **80**, 1083 (2008).

[6] M. T. Deng, C. L. Yu, G. Y. Huang, M. Larsson, P. Caroff, and H. Q. Xu, Anomalous zero-bias conductance peak in a Nb-InSb nanowire-Nb hybrid device, Nano Lett. **12**, 6414 (2012).

[7] V. Mourik, K. Zuo, S. M. Frolov, S. R. Plissard, E. P. A. M. Bakkers, and L. P. Kouwenhoven, Signatures of Majorana fermions in hybrid superconductor-semiconductor nanowire devices, Science **336**, 1003 (2012).

[8] A. Das, Y. Ronen, Y. Most, Y. Oreg, M. Heiblum, and H. Shtrikman, Zero-bias peaks and splitting in an Al-InAs nanowire topological superconductor as a signature of Majorana fermions, Nat. Phys. **8**, 887 (2012).

[9] A. D. K. Finck, D. J. Van Harlingen, P. K. Mohseni, K. Jung, and X. Li, Anomalous Modulation of a Zero-Bias Peak in

a Hybrid Nanowire-Superconductor Device, Phys. Rev. Lett. **110**, 126406 (2013).

[10] F. Nichele, A. C. C. Drachmann, A. M. Whiticar, E. C. T. O'Farrell, H. J. Suominen, A. Fornieri, T. Wang, G. C. Gardner, C. Thomas, A. T. Hatke, P. Krogstrup, M. J. Manfra, K. Flensberg, and C. M. Marcus, Scaling of Majorana Zero-Bias Conductance Peaks, Phys. Rev. Lett. **119**, 136803 (2017).

[11] Ö. Gül, H. Zhang, J. D. S. Bommer, M. W. A. de Moor, D. Car, S. R. Plissard, E. P. A. M. Bakkers, A. Geresdi, K. Watanabe, T. Taniguchi, and L. P. Kouwenhoven, Ballistic Majorana nanowire devices, Nat. Nanotechnol. **13**, 192 (2018).

[12] M. T. Deng, S. Vaitiekėnas, E. B. Hansen, J. Danon, M. Leijnse, K. Flensberg, J. Nygård, P. Krogstrup, and C. M. Marcus, Majorana bound state in a coupled quantum-dot hybrid-nanowire system, Science **354**, 1557 (2016).

[13] M.-T. Deng, S. Vaitiekenas, E. Prada, P. San-Jose, J. Nygård, P. Krogstrup, R. Aguado, and C. M. Marcus, Nonlocality of Majorana modes in hybrid nanowires, Phys. Rev. B **98**, 085125 (2018).

[14] S. Nadj-Perge, I. K. Drozdov, J. Li, H. Chen, S. Jeon, J. Seo, A. H. MacDonald, B. A. Bernevig, and A. Yazdani, Observation of Majorana fermions in ferromagnetic atomic chains on a superconductor, Science **346**, 602 (2014).

[15] R. Pawlak, M. Kisiel, J. Klinovaja, T. Meier, S. Kawai, T. Glatzel, D. Loss, and E. Meyer, Probing atomic structure and Majorana wavefunctions in mono-atomic Fe chains on superconducting Pb surface, npj Quantum Inf. **2**, 16035 (2016).

[16] B. E. Feldman, M. T. Randeria, J. Li, S. Jeon, Y. Xie, Z. Wang, I. K. Drozdov, B. A. Bernevig, and A. Yazdani, High-resolution studies of the Majorana atomic chain platform, Nat. Phys. **13**, 286 (2016).

[17] M. Ruby, B. W. Heinrich, Y. Peng, F. von Oppen, and K. J. Franke, Exploring a proximity-coupled Co chain on Pb(110) as a possible Majorana platform, Nano Lett. **17**, 4473 (2017).

[18] S. Jeon, Y. Xie, J. Li, Z. Wang, B. A. Bernevig, and A. Yazdani, Distinguishing a Majorana zero mode using spin-resolved measurements, Science **358**, 772 (2017).

[19] H. Kim, A. Palacio-Morales, T. Posske, L. Rózsa, K. Palotás, L. Szunyogh, M. Thorwart, and R. Wiesendanger, Toward tailoring Majorana bound states in artificially constructed magnetic atom chains on elemental superconductors, Sci. Adv. **4**, eaar5251 (2018).

[20] B. Braunecker and P. Simon, Interplay Between Classical Magnetic Moments and Superconductivity in Quantum One-Dimensional Conductors: Toward a Self-Sustained Topological Majorana Phase, Phys. Rev. Lett. **111**, 147202 (2013).

[21] J. Klinovaja, P. Stano, A. Yazdani, and D. Loss, Topological Superconductivity and Majorana Fermions in RKKY Systems, Phys. Rev. Lett. **111**, 186805 (2013).

[22] M. M. Vazifeh and M. Franz, Self-Organized Topological State with Majorana Fermions, Phys. Rev. Lett. **111**, 206802 (2013).

[23] B. Braunecker and P. Simon, Self-stabilizing temperature-driven crossover between topological and nontopological ordered phases in one-dimensional conductors, Phys. Rev. B **92**, 241410(R) (2015).

[24] V. Kaladzhyan, P. Simon, and M. Trif, Controlling topological superconductivity by magnetization dynamics, Phys. Rev. B **96**, 020507(R) (2017).

[25] G. M. Andolina and P. Simon, Topological properties of chains of magnetic impurities on a superconducting substrate: Interplay between the Shiba band and ferromagnetic wire limits, Phys. Rev. B **96**, 235411 (2017).

[26] M. Sato, Y. Takahashi, and S. Fujimoto, Non-Abelian Topological Order in *s*-Wave Superfluids of Ultracold Fermionic Atoms, Phys. Rev. Lett. **103**, 020401 (2009).

[27] M. Sato and S. Fujimoto, Topological phases of noncentrosymmetric superconductors: Edge states, Majorana fermions, and non-Abelian statistics, Phys. Rev. B **79**, 094504 (2009).

[28] M. Sato, Y. Takahashi, and S. Fujimoto, Non-Abelian topological orders and Majorana fermions in spin-singlet superconductors, Phys. Rev. B **82**, 134521 (2010).

[29] A. Kobiałka and A. Ptok, Electrostatic formation of the Majorana quasiparticles in the quantum dot-nanoring structure, J. Phys.: Condens. Matter **31**, 185302 (2019).

[30] J. Klinovaja and D. Loss, Composite Majorana fermion wave functions in nanowires, Phys. Rev. B **86**, 085408 (2012).

[31] C. Fleckenstein, F. Domínguez, N. Traverso Ziani, and B. Trauzettel, Decaying spectral oscillations in a majorana wire with finite coherence length, Phys. Rev. B **97**, 155425 (2018).

[32] L. P. Gor'kov and E. I. Rashba, Superconducting 2d System with Lifted Spin Degeneracy: Mixed Singlet-Triplet State, Phys. Rev. Lett. **87**, 037004 (2001).

[33] K. Seo, L. Han, and C. A. R. Sá de Melo, Topological phase transitions in ultracold Fermi superfluids: The evolution from Bardeen-Cooper-Schrieffer to Bose-Einstein-condensate superfluids under artificial spin-orbit fields, Phys. Rev. A **85**, 033601 (2012).

[34] A. Ptok, K. Rodríguez, and K. J. Kapcia, Superconducting monolayer deposited on substrate: Effects of the spin-orbit coupling induced by proximity effects, Phys. Rev. Materials **2**, 024801 (2018).

[35] M. M. Desjardins, L. C. Contamin, M. R. Delbecq, M. C. Dartiailh, L. E. Bruhat, T. Cubaynes, J. J. Viennot, F. Mallet, S. Rohart, A. Thiaville, A. Cottet, and T. Kontos, Synthetic spin-orbit interaction for majorana devices, Nat. Mater. **18**, 1060 (2019).

[36] A. Yazdani, Conjuring Majorana with synthetic magnetism, Nat. Mater. **18**, 1036 (2019).

[37] J. Klinovaja, P. Stano, and D. Loss, Transition from Fractional to Majorana Fermions in Rashba Nanowires, Phys. Rev. Lett. **109**, 236801 (2012).

[38] M. Kjaergaard, K. Wölms, and K. Flensberg, Majorana fermions in superconducting nanowires without spin-orbit coupling, Phys. Rev. B **85**, 020503(R) (2012).

[39] J. Klinovaja and D. Loss, Giant Spin-Orbit Interaction Due to Rotating Magnetic Fields in Graphene Nanoribbons, Physical Review X **3**, 011008 (2013).

[40] L. N. Maurer, J. K. Gamble, L. Tracy, S. Eley, and T. M. Lu, Designing nanomagnet arrays for topological nanowires in silicon, Phys. Rev. Applied **10**, 054071 (2018).

[41] K. R. Sapkota, S. Eley, E. Bussmann, C. T. Harris, L. N. Maurer, and T. M. Lu, Creation of nanoscale magnetic fields using nano-magnet arrays, AIP Adv. **9**, 075203 (2019).

[42] V. Kornich, M. G. Vavilov, M. Friesen, M. A. Eriksson, and S. N. Coppersmith, Majorana bound states in nanowire-superconductor hybrid systems in periodic magnetic fields, Phys. Rev. B **101**, 125414 (2020).

[43] T. Zhou, N. Mohanta, J. E. Han, A. Matos-Abiague, and I. Žutić, Tunable magnetic textures in spin valves: From spintronics to Majorana bound states, Phys. Rev. B **99**, 134505 (2019).

[44] A. Matos-Abiague, J. Shabani, A. D. Kent, G. L. Fatin, B. Scharf, and I. Žutić, Tunable magnetic textures: From Majorana bound states to braiding, Solid State Commun. **262**, 1 (2017).

[45] N. Mohanta, T. Zhou, J.-W. Xu, J. E. Han, A. D. Kent, J. Shabani, I. Žutić, and A. Matos-Abiague, Electrical control of Majorana bound states using magnetic stripes, Phys. Rev. Applied **12**, 034048 (2019).

[46] L. Zhou, J. Wiebe, S. Lounis, E. Vedmedenko, F. Meier, S. Blügel, P. H. Dederichs, and R. Wiesendanger, Strength and directionality of surface Ruderman-Kittel-Kasuya-Yosida interaction mapped on the atomic scale, Nat. Phys. **6**, 187 (2010).

[47] J. Hermenau, S. Brinker, M. Marciani, M. Steinbrecher, M. dos Santos Dias, R. Wiesendanger, S. Lounis, and J. Wiebe, Stabilizing spin systems via symmetrically tailored RKKY interactions, Nat. Commun. **10**, 2565 (2019).

[48] M. Menzel, Y. Mokrousov, R. Wieser, J. E. Bickel, E. Vedmedenko, S. Blügel, S. Heinze, K. von Bergmann, A. Kubetzka, and R. Wiesendanger, Information Transfer by Vector Spin Chirality in Finite Magnetic Chains, Phys. Rev. Lett. **108**, 197204 (2012).

[49] A. Kamlapure, L. Cornils, J. Wiebe, and R. Wiesendanger, Engineering the spin couplings in atomically crafted spin chains on an elemental superconductor, Nat. Commun. **9**, 3253 (2018).

[50] M. Steinbrecher, R. Rausch, K. T. That, J. Hermenau, A. A. Khajetoorians, M. Potthoff, R. Wiesendanger, and J. Wiebe, Non-collinear spin states in bottom-up fabricated atomic chains, Nat. Commun. **9**, 2853 (2018).

[51] L. Schneider, S. Brinker, M. Steinbrecher, J. Hermenau, T. Posske, M. dos Santos Dias, S. Lounis, R. Wiesendanger, and J. Wiebe, Controlling in-gap end states by linking nonmagnetic atoms and artificially-constructed spin chains on superconductors, Nat. Commun. **11**, 4707 (2020).

[52] S. Loth, S. Baumann, C. P. Lutz, D. M. Eigler, and A. J. Heinrich, Bistability in atomic-scale antiferromagnets, Science **335**, 196 (2012).

[53] S. Yan, L. Malavolti, J. A. J. Burgess, A. Droghetti, A. Rubio, and S. Loth, Nonlocally sensing the magnetic states of nanoscale antiferromagnets with an atomic spin sensor, Sci. Adv. **3**, e1603137 (2017).

[54] L. Pedrero, M. Brando, C. Klingner, C. Krellner, C. Geibel, and F. Steglich, H-T phase diagram of $YbCo_2Si_2$ with H // [100], J. Phys.: Conf. Ser. **200**, 012157 (2010).

[55] T. Kong, S. Guo, D. Ni, and R. J. Cava, Crystal structure and magnetic properties of the layered van der Waals compound VBr_3, Phys. Rev. Mater. **3**, 084419 (2019).

[56] L. Hu, X. Wu, and J. Yang, Mn_2C monolayer: a 2D antiferromagnetic metal with high néel temperature and large spin-orbit coupling, Nanoscale **8**, 12939 (2016).

[57] K. Kim, S. Y. Lim, J.-U. Lee, S. Lee, T. Y. Kim, K. Park, G. S. Jeon, C.-H. Park, J.-G. Park, and H. Cheong, Suppression of magnetic ordering in XXZ-type antiferromagnetic monolayer $NiPS_3$, Nat. Commun. **10**, 345 (2019).

[58] M. Nakanishi, K. Yoshimura, K. Kosuge, T. Goto, T. Fujii, and J. Takada, Anomalous field-induced magnetic transitions in V_5X_8 (X=S,Se), J. Magn. Magn. Mater. **221**, 301 (2000).

[59] W. J. Hardy, J. Yuan, H. Guo, P. Zhou, J. Lou, and D. Natelson, Thickness-dependent and magnetic-field-driven suppression of antiferromagnetic order in thin V_5S_8 single crystals, ACS Nano **10**, 5941 (2016).

[60] A. Heimes, P. Kotetes, and G. Schön, Majorana fermions from Shiba states in an antiferromagnetic chain on top of a superconductor, Phys. Rev. B **90**, 060507(R) (2014).

[61] A. Heimes, D. Mendler, and P. Kotetes, Interplay of topological phases in magnetic adatom-chains on top of a rashba superconducting surface, New J. Phys. **17**, 023051 (2015).

[62] B. Kiczek and A. Ptok, Influence of the orbital effects on the Majorana quasi-particles in a nanowire, J. Phys.: Condens. Matter **29**, 495301 (2017).

[63] P. G. de Gennes, *Superconductivity of Metals and Alloys* (Addison-Wesley, 1989).

[64] A. V. Balatsky, I. Vekhter, and J.-X. Zhu, Impurity-induced states in conventional and unconventional superconductors, Rev. Mod. Phys. **78**, 373 (2006).

[65] H. Matsui, T. Sato, T. Takahashi, S.-C. Wang, H.-B. Yang, H. Ding, T. Fujii, T. Watanabe, and A. Matsuda, BCS-Like Bogoliubov Quasiparticles in High-T_c Superconductors Observed by Angle-Resolved Photoemission Spectroscopy, Phys. Rev. Lett. **90**, 217002 (2003).

[66] W. A. Hofer, A. S. Foster, and A. L. Shluger, Theories of scanning probe microscopes at the atomic scale, Rev. Mod. Phys. **75**, 1287 (2003).

[67] R. Wiesendanger, Spin mapping at the nanoscale and atomic scale, Rev. Mod. Phys. **81**, 1495 (2009).

[68] H. Oka, O. O. Brovko, M. Corbetta, V. S. Stepanyuk, D. Sander, and J. Kirschner, Spin-polarized quantum confinement in nanostructures: Scanning tunneling microscopy, Rev. Mod. Phys. **86**, 1127 (2014).

[69] J. Stenger and T. D. Stanescu, Tunneling conductance in semiconductor-superconductor hybrid structures, Phys. Rev. B **96**, 214516 (2017).

[70] R. S. K. Mong and V. Shivamoggi, Edge states and the bulk-boundary correspondence in Dirac Hamiltonians, Phys. Rev. B **83**, 125109 (2011).

[71] T. Fukui, K. Shiozaki, T. Fujiwara, and S. Fujimoto, Bulk-edge correspondence for Chern topological phases: A viewpoint from a generalized index theorem, J. Phys. Soc. Jpn. **81**, 114602 (2012).

[72] J. E. Moore and L. Balents, Topological invariants of time-reversal-invariant band structures, Phys. Rev. B **75**, 121306(R) (2007).

[73] C. Dutreix, Topological spin-singlet superconductors with underlying sublattice structure, Phys. Rev. B **96**, 045416 (2017).

[74] M. Sato and Y. Ando, Topological superconductors: a review, Rep. Prog. Phys. **80**, 076501 (2017).

[75] C.-K. Chiu, J. C. Y. Teo, A. P. Schnyder, and S. Ryu, Classification of topological quantum matter with symmetries, Rev. Mod. Phys. **88**, 035005 (2016).

[76] A. Altland and M. R. Zirnbauer, Nonstandard symmetry classes in mesoscopic normal-superconducting hybrid structures, Phys. Rev. B **55**, 1142 (1997).

[77] S. Ryu, A. P. Schnyder, A. Furusaki, and A. W. W. Ludwig, Topological insulators and superconductors: tenfold way and dimensional hierarchy, New J. Phys. **12**, 065010 (2010).
[78] S. Tewari and J. D. Sau, Topological Invariants for Spin-Orbit Coupled Superconductor Nanowires, Phys. Rev. Lett. **109**, 150408 (2012).
[79] A. Kobiałka, N. Sedlmayr, M. M. Maśka, and T. Domański, Dimerization-induced topological superconductivity in a Rashba nanowire, Phys. Rev. B **101**, 085402 (2020).
[80] G. B. Lesovik and I. A. Sadovskyy, Scattering matrix approach to the description of quantum electron transport, Phys. Usp. **54**, 1007 (2011).
[81] A. R. Akhmerov, J. P. Dahlhaus, F. Hassler, M. Wimmer, and C. W. J. Beenakker, Quantized Conductance at the Majorana Phase Transition in a Disordered Superconducting Wire, Phys. Rev. Lett. **106**, 057001 (2011).
[82] C. W. J. Beenakker, J. P. Dahlhaus, M. Wimmer, and A. R. Akhmerov, Random-matrix theory of Andreev reflection from a topological superconductor, Phys. Rev. B **83**, 085413 (2011).
[83] T. O. Rosdahl, A. Vuik, M. Kjaergaard, and A. R. Akhmerov, Andreev rectifier: A nonlocal conductance signature of topological phase transitions, Phys. Rev. B **97**, 045421 (2018).
[84] I. C. Fulga, F. Hassler, A. R. Akhmerov, and C. W. J. Beenakker, Scattering formula for the topological quantum number of a disordered multimode wire, Phys. Rev. B **83**, 155429 (2011).
[85] T.-P. Choy, J. M. Edge, A. R. Akhmerov, and C. W. J. Beenakker, Majorana fermions emerging from magnetic nanoparticles on a superconductor without spin-orbit coupling, Phys. Rev. B **84**, 195442 (2011).
[86] P. Zhang and F. Nori, Majorana bound states in a disordered quantum dot chain, New J. Phys. **18**, 043033 (2016).
[87] A. Kobiałka, P. Piekarz, A. M. Oleś, and A. Ptok, First-principles study of the nontrivial topological phase in chains of 3*d* transition metals, Phys. Rev. B **101**, 205143 (2020).
[88] F. Domínguez, J. Cayao, P. San-Jose, R. Aguado, A. L. Yeyati, and E. Prada, Zero-energy pinning from interactions in Majorana nanowires, npj Quantum Mater. **2**, 13 (2017).
[89] J. Cayao, A. M. Black-Schaffer, E. Prada, and R. Aguado, Andreev spectrum and supercurrents in nanowire-based SNS junctions containing Majorana bound states, Beilstein J. Nanotechnol. **9**, 1339 (2018).
[90] A. A. Zyuzin, D. Rainis, J. Klinovaja, and D. Loss, Correlations Between Majorana Fermions Through a Superconductor, Phys. Rev. Lett. **111**, 056802 (2013).
[91] M. Z. Hasan and C. L. Kane, Colloquium: Topological insulators, Rev. Mod. Phys. **82**, 3045 (2010).
[92] A. Bansil, H. Lin, and T. Das, Colloquium: Topological band theory, Rev. Mod. Phys. **88**, 021004 (2016).
[93] M. S. Rider, S. J. Palmer, S. R. Pocock, X. Xiao, P. Arroyo Huidobro, and V. Giannini, A perspective on topological nanophotonics: Current status and future challenges, J. Appl. Phys. **125**, 120901 (2019).
[94] F. Setiawan, K. Sengupta, I. B. Spielman, and J. D. Sau, Dynamical Detection of Topological Phase Transitions in Short-Lived Atomic Systems, Phys. Rev. Lett. **115**, 190401 (2015).
[95] P. Szumniak, D. Chevallier, D. Loss, and J. Klinovaja, Spin and charge signatures of topological superconductivity in Rashba nanowires, Phys. Rev. B **96**, 041401(R) (2017).
[96] N. Sedlmayr, J. M. Aguiar-Hualde, and C. Bena, Majorana bound states in open quasi-one-dimensional and two-dimensional systems with transverse rashba coupling, Phys. Rev. B **93**, 155425 (2016).
[97] V. Kaladzhyan and C. Bena, Formation of Majorana fermions in finite-size graphene strips, SciPost Phys. **3**, 002 (2017).
[98] P. Marra and M. Cuoco, Controlling Majorana states in topologically inhomogeneous superconductors, Phys. Rev. B **95**, 140504(R) (2017).
[99] S. Rex, I. V. Gornyi, and A. D. Mirlin, Majorana modes in emergent-wire phases of helical and cycloidal magnet-superconductor hybrids, Phys. Rev. B **102**, 224501 (2020).
[100] K. Pöyhönen, A. Westström, J. Röntynen, and T. Ojanen, Majorana states in helical Shiba chains and ladders, Phys. Rev. B **89**, 115109 (2014).
[101] M. Schmitt, P. Moras, G. Bihlmayer, R. Cotsakis, M. Vogt, J. Kemmer, A. Belabbes, P. M. Sheverdyaeva, A. K. Kundu, C. Carbone, S. Blügel, and M. Bode, Indirect chiral magnetic exchange through Dzyaloshinskii-Moriya-enhanced RKKY interactions in manganese oxide chains on ir(100), Nat. Commun. **10**, 2610 (2019).
[102] J. Herbrych, J. Heverhagen, G. Alvarez, M. Daghofer, A. Moreo, and E. Dagotto, Block-spiral magnetism: An exotic type of frustrated order, Proc. Natl. Acad. Sci. USA **117**, 16226 (2020).
[103] C. W. Groth, M. Wimmer, A. R. Akhmerov, and X. Waintal, Kwant: a software package for quantum transport, New J. Phys. **16**, 063065 (2014).
[104] M. Wimmer, A. R. Akhmerov, J. P. Dahlhaus, and C. W. J. Beenakker, Quantum point contact as a probe of a topological superconductor, New J. Phys. **13**, 053016 (2011).
[105] M. Kjaergaard, F. Nichele, H. J. Suominen, M. P. Nowak, M. Wimmer, A. R. Akhmerov, J. A. Folk, K. Flensberg, J. Shabani, C. J. Palmstrøm, and C. M. Marcus, Quantized conductance doubling and hard gap in a two-dimensional semiconductor-superconductor heterostructure, Nat. Commun. **7**, 12841 (2016).
[106] H. Zhang, C.-X. Liu, S. Gazibegovic, D. Xu, J. A. Logan, G. Wang, N. van Loo, J. D. S. Bommer, M. W. A. de Moor, D. Car, R. L. M. Op het Veld, P. J. van Veldhoven, S. Koelling, M. A. Verheijen, M. Pendharkar, D. J. Pennachio, B. Shojaei, J. S. Lee, C. J. Palmstrøm, E. P. A. M. Bakkers, S. Das Sarma, and L. P. Kouwenhoven, Quantized Majorana conductance, Nature **556**, 74 (2018).
[107] H. Zhang, D. E. Liu, M. Wimmer, and L. P. Kouwenhoven, Next steps of quantum transport in majorana nanowire devices, Nat. Commun. **10**, 5128 (2019).
[108] J. Chen, P. Yu, J. Stenger, M. Hocevar, D. Car, S. R. Plissard, E. P. A. M. Bakkers, T. D. Stanescu, and S. M. Frolov, Experimental phase diagram of zero-bias conductance peaks in superconductor/semiconductor nanowire devices, Sci. Adv. **3**, e1701476 (2017).
[109] S. Ikegaya, Y. Asano, and D. Manske, Anomalous Nonlocal Conductance as a Fingerprint of Chiral Majorana Edge States, Phys. Rev. Lett. **123**, 207002 (2019).
[110] Z. Cao, H. Zhang, H.-F. Lü, W.-X. He, H.-Z. Lu, and X. C. Xie, Decays of Majorana or Andreev Oscillations Induced by Steplike Spin-Orbit Coupling, Phys. Rev. Lett. **122**, 147701 (2019).

[111] T. D. Stanescu and S. Tewari, Robust low-energy Andreev bound states in semiconductor-superconductor structures: Importance of partial separation of component majorana bound states, Phys. Rev. B **100**, 155429 (2019).

[112] C. Moore, C. Zeng, T. D. Stanescu, and S. Tewari, Quantized zero-bias conductance plateau in semiconductor-superconductor heterostructures without topological Majorana zero modes, Phys. Rev. B **98**, 155314 (2018).

[113] A. Ptok, A. Kobiałka, and T. Domański, Controlling the bound states in a quantum-dot hybrid nanowire, Phys. Rev. B **96**, 195430 (2017).

[114] C. Reeg, O. Dmytruk, D. Chevallier, D. Loss, and J. Klinovaja, Zero-energy Andreev bound states from quantum dots in proximitized Rashba nanowires, Phys. Rev. B **98**, 245407 (2018).

[115] C. Moore, T. D. Stanescu, and S. Tewari, Two-terminal charge tunneling: Disentangling Majorana zero modes from partially separated Andreev bound states in semiconductor-superconductor heterostructures, Phys. Rev. B **97**, 165302 (2018).

[116] D. Sticlet, C. Bena, and P. Simon, Spin and Majorana Polarization in Topological Superconducting Wires, Phys. Rev. Lett. **108**, 096802 (2012).

[117] A. Haim, E. Berg, F. von Oppen, and Y. Oreg, Signatures of Majorana Zero Modes in Spin-Resolved Current Correlations, Phys. Rev. Lett. **114**, 166406 (2015).

[118] K. Björnson, S. S. Pershoguba, A. V. Balatsky, and A. M. Black-Schaffer, Spin-polarized edge currents and Majorana fermions in one- and two-dimensional topological superconductors, Phys. Rev. B **92**, 214501 (2015).

[119] M. Guigou, N. Sedlmayr, J. M. Aguiar-Hualde, and C. Bena, Signature of a topological phase transition in long SN junctions in the spin-polarized density of states, Europhys. Lett. **115**, 47005 (2016).

[120] J. J. He, T. K. Ng, P. A. Lee, and K. T. Law, Selective Equal-Spin Andreev Reflections Induced by Majorana Fermions, Phys. Rev. Lett. **112**, 037001 (2014).

[121] H.-H. Sun, K.-W. Zhang, L.-H. Hu, C. Li, G.-Y. Wang, H.-Y. Ma, Z.-A. Xu, C.-L. Gao, D.-D. Guan, Y.-Y. Li, C. Liu, D. Qian, Y. Zhou, L. Fu, S.-C. Li, F.-C. Zhang, and J.-F. Jia, Majorana Zero Mode Detected with Spin Selective Andreev Reflection in the Vortex of a Topological Superconductor, Phys. Rev. Lett. **116**, 257003 (2016).

[122] K. T. Law, P. A. Lee, and T. K. Ng, Majorana Fermion Induced Resonant Andreev Reflection, Phys. Rev. Lett. **103**, 237001 (2009).

[123] D. E. Liu, M. Cheng, and R. M. Lutchyn, Probing Majorana physics in quantum-dot shot-noise experiments, Phys. Rev. B **91**, 081405(R) (2015).

[124] D. E. Liu, A. Levchenko, and R. M. Lutchyn, Majorana zero modes choose Euler numbers as revealed by full counting statistics, Phys. Rev. B **92**, 205422 (2015).

[125] P. Devillard, D. Chevallier, and M. Albert, Fingerprints of Majorana fermions in current-correlation measurements from a superconducting tunnel microscope, Phys. Rev. B **96**, 115413 (2017).

[126] S. Smirnov, Universal Majorana thermoelectric noise, Phys. Rev. B **97**, 165434 (2018).

[127] T. Jonckheere, J. Rech, L. Raymond, A. Zazunov, R. Egger, and T. Martin, Evidence of Majorana fermions in the noise characteristic of normal metal-topological superconductor junctions, Eur. Phys. J.: Spec. Top. **229**, 577 (2020).

[128] S. Smirnov, Majorana tunneling entropy, Phys. Rev. B **92**, 195312 (2015).

[129] N. Hartman, C. Olsen, S. Lüscher, M. Samani, S. Fallahi, G. C. Gardner, M. Manfra, and J. Folk, Direct entropy measurement in a mesoscopic quantum system, Nat. Phys. **14**, 1083 (2018).

[130] J. Cayao and A. M. Black-Schaffer, Distinguishing trivial and topological zero energy states in long nanowire junctions, arXiv:2011.10411.

[131] V. Perrin, M. Civelli, and P. Simon, Discriminating Majorana from Shiba bound-states by tunneling shot-noise tomography, arXiv:2011.06893.

[132] O. A. Awoga, J. Cayao, and A. M. Black-Schaffer, Supercurrent Detection of Topologically Trivial Zero-Energy States in Nanowire Junctions, Phys. Rev. Lett. **123**, 117001 (2019).

[133] D. Bercioux and P. Lucignano, Quantum transport in rashba spin-orbit materials: a review, Rep. Prog. Phys. **78**, 106001 (2015).

[134] A. Manchon, H. C. Koo, J. Nitta, S. M. Frolov, and R. A. Duine, New perspectives for Rashba spin-orbit coupling, Nat. Mater. **14**, 871 (2015).

[135] J. K. Asbóth, L. Oroszlány, and A. Pályi, *A Short Course on Topological Insulators* (Springer, 2016), Vol. 919, p. 87.

[136] V. Baltz, A. Manchon, M. Tsoi, T. Moriyama, T. Ono, and Y. Tserkovnyak, Antiferromagnetic spintronics, Rev. Mod. Phys. **90**, 015005 (2018).

[137] V. Gurarie, Single-particle Green's functions and interacting topological insulators, Phys. Rev. B **83**, 085426 (2011).

4.2 Nonlocality of Majorana Bound States

4.2.1 Controlling the bound states in a quantum–dot hybrid nanowire

A. Ptok, A. Kobiałka, T. Domański, Phys. Rev. B **96**, 195430 (2017)

Majorana modes are formed in pairs near the edges of the system. It also allows for the *leakage* effect, where MBS transfers a part of its wave function to topologically trivial parts of the system. Motivated by the experimental study by Deng *et al.* [10], we investigated the influence of the quantum dot attached to the nanowire on the properties of MBS. Using real space calculations, we study both the emergence of MBS from coalescing ABS and its delocalisation to the quantum dot coupled to one of the nanowire's ends. We also checked the interplay between ABS and MBS – an avoided crossing feature between them relies on the strength of spin-orbit coupling but only if states on the quantum dot have the same spin as MBS. We quantified the delocalisation of MBS to the quantum dot as dependent on the majority spin character of the energy levels available on the quantum dot. For a multilevel quantum dot, MBS leakage amplifies quantum oscillations in the spatial profile. Delocalisation of MBS can be manipulated by varying the chemical potential induced by the external electrostatic gate. This led to the proposal of a nanodevice capable of distinguishing between MBS and ABS, measuring and manipulation of MBS in an experimental venue, for which we present calculations showing the proof of concept.

Author's contribution: Partial preparation numerical calculations, analysis and discussion of obtained results, partial preparation of figures, partial preparation of the manuscript, correspondence with other research groups during the prepublication period, participation in preparing the response for Referees.

Controlling the bound states in a quantum-dot hybrid nanowire

Andrzej Ptok,[1,2,*] Aksel Kobiałka,[2,†] and Tadeusz Domański[2,‡]
[1]*Institute of Nuclear Physics, Polish Academy of Sciences, ul. E. Radzikowskiego 152, PL-31342 Kraków, Poland*
[2]*Institute of Physics, Marie Curie-Skłodowska University, pl. Marii Skłodowskiej-Curie 1, PL-20031 Lublin, Poland*
(Received 10 August 2017; published 22 November 2017)

Recent experiments using the quantum dot coupled to the topological superconducting nanowire [Deng *et al.*, Science **354**, 1557 (2016)] revealed that the zero-energy bound state coalesces from the Andreev bound states. Such quasiparticle states, present in the quantum dot, can be controlled by magnetic and electrostatic means. We use a microscopic model of the quantum-dot–nanowire structure to reproduce the experimental results, applying the Bogoliubov–de Gennes technique. This is done by studying the gate voltage dependence of the various types of bound states and mutual influence between them. We show that the zero-energy bound states can emerge from the Andreev bound states in the topologically trivial phase and can be controlled using various means. In the nontrivial topological phase we show the possible resonance between these zero-energy levels with Majorana bound states. We discuss and explain this phenomenon as a result of dominant spin character of discussed bound states. Presented results can be applied in experimental studies by using the proposed nanodevice.

DOI: 10.1103/PhysRevB.96.195430

I. EXPERIMENTAL INTRODUCTION

Boundaries of the low-dimensional topological superconductors can host the zero-energy Majorana bound states (MBS) [1–3]. Topological protection and non-Abelian statistics obeyed by such exotic quasiparticles make them appealing candidates for realization of stable qubits which could be useful for quantum computing [4–10]. Intensive studies of the topological superconductors provided evidence for the MBS in various nanodevices [11–24] which are tunable by the gate potentials and magnetic field, as have been demonstrated by Deng *et al.* in Ref. [24].

In practice the topologically nontrivial phase can be induced in nanoscopic systems via the superconducting proximity effect in cooperation with some additional effects, e.g., the spin-orbit coupling (SOC) and Zeeman splitting for semiconducting nanowires [20,21]. Such phenomena have been indeed reported for InAs-Al semiconductor-superconductor nanostructures [21] or at the interface between the semiconducting InSb nanowire and the NbTiN superconductor [23]. Another possible setup for this phenomenon is a nanowire with a proximity induced superconducting gap, due to the adatom deposition on a surface of the superconductor [25]. This has been reported, i.e., in the case of Fe [19,26] or Co [27] atoms on the Pb surface.

The Andreev bound states (ABSs) induced in the nanowire spectrum can be varied by the external magnetic field [28,29]. In some range of parameters [30–32], the above critical magnetic field transition from trivial to nontrivial topological phase occurs. One pair of such ABS merges at zero energy, giving rise to the (double degenerate) MBS, which is localized near the nanowire ends.

Recent experimental results of the Copenhagen group [24], showed that the ABS/MBS can be induced in a controllable way in the quantum-dot region side-coupled to the semiconductor-superconductor hybrid nanowire. A schematic of this structure is displayed in Fig. 1. The semiconducting InAs wire was epitaxially covered by the conventional Al superconductor [33], except for a small piece of wire which was interpreted as the quantum dot (QD). The thickness of the superconducting shell should be comparable to its coherence length, as some nontrivial finite-size effects can occur if this condition is not met [34]. Upon varying the magnetic field and the gate potential there have been induced the bound states of either the Andreev (Shiba) or the exotic Majorana type, as shown by peaks in the differential conductance of the tunneling current [35–37]. In particular, the QD energy levels can be varied by the gate voltage eventually leading to emergence of the zero-energy Majorana mode.

The main purpose of this paper is to explore the Andreev and Majorana bound states of the single and multiple quantum dots coupled to the hybrid nanowire. We study their evolution with respect to the electrostatic (gate) potential, magnetic field, and the chemical potential. This paper is organized as follows. In Sec. II we introduce the model and present some computational details concerning the Bogoliubov–de Gennes technique.

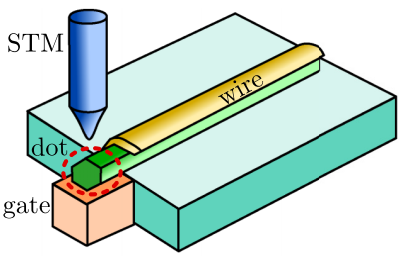

FIG. 1. Schematic representation of the experimental system discussed in Ref. [24]. InAs wire (green) is epitaxially covered by the superconducting Al (yellow). The quantum dot (InAs) is formed between the normal contact (dark orange) and the epitaxial Al shell (inside dashed circle). Magnetic field applied parallel to the wire axis can control the bound states. Measurements of the differential conductance have been done using the STM tip (blue), whereas the quantum-dot energy levels have been tuned by the gate potential.

*aptok@mmj.pl
†akob@kft.umcs.lublin.pl
‡doman@kft.umcs.lublin.pl

Next, in Sec. III we describe basic properties and main terminology in relation to the studied problem. Thorough discussion of the quasiparticle spectrum of the single QD is presented in Sec. IV. Revision of a more general system with a higher number of sites in QD, is performed in Secs. V and VI, which are devoted to the double and multisite QD cases, respectively. In Sec. VII we propose a feasible quantum device, which could enable an experimental realization of various tunable bound states. Finally, in Sec. VIII we summarize the results.

II. MODEL AND METHODS

For description of the nanostructure shown in Fig. 1, we will use a microscopic model in real space with Hamiltonian $\mathcal{H} = \mathcal{H}_w + \mathcal{H}_{\rm prox} + \mathcal{H}_{\rm soc} + \mathcal{H}_{\rm dot}$. The first term describes mobile electrons in the wire,

$$\mathcal{H}_w = \sum_{ij\sigma}\{-t\delta_{\langle i,j\rangle} - (\mu+\sigma h)\delta_{ij}\}c^\dagger_{i\sigma}c_{j\sigma}, \tag{1}$$

where t denotes a hopping integral between the nearest-neighbor sites, μ is a chemical potential, and h denotes a magnetic field parallel to the whole wire. Here $c^\dagger_{i\sigma}$ ($c_{i\sigma}$) describes the creation (annihilation) operator in site ith with spin σ. The second term accounts for the proximity effect,

$$\mathcal{H}_{\rm prox} = \sum_i \Delta(c_{i\downarrow}c_{i\uparrow} + c^\dagger_{i\uparrow}c^\dagger_{i\downarrow}), \tag{2}$$

and we assume the uniform energy gap Δ induced by the epitaxially covered classical superconductor. The spin-orbit coupling (SOC) term is given by

$$\mathcal{H}_{\rm soc} = -i\lambda\sum_{i\sigma\sigma'}c^\dagger_{i\sigma}(\sigma_y)_{\sigma\sigma'}c_{i+1,\sigma'}, \tag{3}$$

where σ_y stands for the y component of the Pauli matrix and λ is the SOC coupling along the chain. Then we treat the QD as part of a nanowire not covered by the superconductor. The last part,

$$\mathcal{H}_{\rm dot} = \sum_{i\in{\rm dot},\sigma} V_g c^\dagger_{i\sigma}c_{i\sigma}, \tag{4}$$

describes the electrostatic energy contributed by the gate potential V_g (see Fig. 2). In what follows we shall consider the quantum-dot region comprising one, two, and multiple sites coupled to the superconducting nanowire.

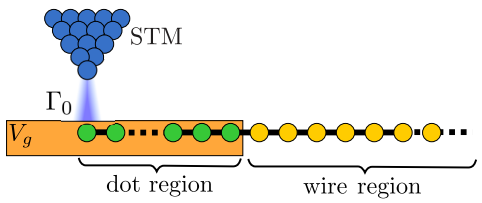

FIG. 2. Schematic idea of the described system. The sites of the quantum dot (green) are side-attached to the superconducting nanowire (yellow) with the proximity-induced electron pairing. Using the STM tip (blue) we can measure the LDOS at each site of the system. Parameter Γ_0 denotes the coupling strength between the STM tip and the probed atom.

Hamiltonian $\mathcal{H}$ of the entire chain can be diagonalized by the Bogoliubov-Valatin transformation [38],

$$c_{i\sigma} = \sum_n (u_{{\rm in}\sigma}\gamma_n - \sigma v^*_{{\rm in}\sigma}\gamma^\dagger_n), \tag{5}$$

where γ_n, $\gamma^\dagger_n$ are the quasiparticle fermionic operators and $u_{{\rm in}\sigma}$ and $v_{{\rm in}\sigma}$ are the Bogoliubov–de Gennes (BdG) eigenvectors, respectively. Such unitary transformation implies

$$\mathcal{E}_n\begin{pmatrix} u_{{\rm in}\uparrow}\\ v_{{\rm in}\downarrow}\\ u_{{\rm in}\downarrow}\\ v_{{\rm in}\uparrow}\end{pmatrix} = \sum_j\begin{pmatrix} H_{ij\uparrow} & D_{ij} & S^{\uparrow\downarrow}_{ij} & 0\\ D^*_{ij} & -H^*_{ij\downarrow} & 0 & S^{\downarrow\uparrow}_{ij}\\ S^{\downarrow\uparrow}_{ij} & 0 & H_{ij\downarrow} & D_{ij}\\ 0 & S^{\uparrow\downarrow}_{ij} & D^*_{ij} & -H^*_{ij\uparrow}\end{pmatrix}\begin{pmatrix} u_{{\rm jn}\uparrow}\\ v_{{\rm jn}\downarrow}\\ u_{{\rm jn}\downarrow}\\ v_{{\rm jn}\uparrow}\end{pmatrix}, \tag{6}$$

where $H_{ij\sigma} = -t\delta_{\langle i,j\rangle} - (\mu + \sigma h - V_G\delta_{i\in{\rm dot}})\delta_{ij}$ is the single-particle term, $D_{ij} = \Delta\delta_{ij}$ refers to the induced on-site pairing, and the SOC term (mixing the particles with different spins) is given by $S^{\sigma\sigma'}_{ij} = -i\lambda(\sigma_y)_{\sigma\sigma'}\delta_{\langle i,j\rangle}$, where $S^{\downarrow\uparrow}_{ij} = (S^{\uparrow\downarrow}_{ji})^*$.

To study our system, we will use the local density of states (LDOS) defined as $\rho_i(\omega) = -\frac{1}{\pi}\sum_\sigma {\rm Im}\langle\langle c_{i\sigma}|c^\dagger_{i\sigma}\rangle\rangle$. From numerical solution of the BdG equations (6) we obtain the Green's function $\langle\langle c_{i\sigma}|c^\dagger_{i\sigma}\rangle\rangle$, which formally gives

$$\rho_i(\omega) = \sum_{n\sigma}[|u_{{\rm in}\sigma}|^2\delta(\omega-\mathcal{E}_n) + |v_{{\rm in}\sigma}|^2\delta(\omega+\mathcal{E}_n)]. \tag{7}$$

These physical quantities can be measured experimentally in a relatively simply way [39,40]. In practice this spatially and energy-dependent spectrum can be also probed by a differential conductance $G_i(V) = dI_i(V)/dV$ of the tunneling current $I_i(V)$, which depends on the coupling between the ith atom of the wire and the STM tip [41] (indicated by Γ_0 in Fig. 2).

We have solved the BdG equations (6) for a chain with $N = 200$ sites, choosing $\Delta/t = 0.2$, $\lambda/t = 0.15$, $\mu/t = -2$. For numerical purposes we have also replaced the Dirac delta functions appearing in Eq. (7) by a Lorentzian $\delta(\omega) = \zeta/[\pi(\omega^2+\zeta^2)]$ with a small broadening $\zeta = 0.0025t$.

III. BASIC PROPERTIES

In this section, we will briefly describe basic physical properties of the nanowire without coupled QD. We will also define terminology which will be used in later sections of manuscript.

As we mentioned in Sec. I, in a case of wires with SOC and superconductivity induced by the proximity effect, for some magnetic field h_c phase transition from trivial to nontrivial topological phase occurs. In a case of a one-dimensional chain described by the Hamiltonian $\mathcal{H}$ defined in Sec. II we have $h_c = \sqrt{\Delta^2 + (2t \pm \mu)^2}$ [30,31]. For chosen parameters we have $h_c/t = 0.2$.

Change in magnetic field h leads to the typical evolution of the total density of states (DOS) for this case. Numerical calculation for chosen parameters is shown in Fig. 3. In consequence, due to the finite size effect, we can observe a

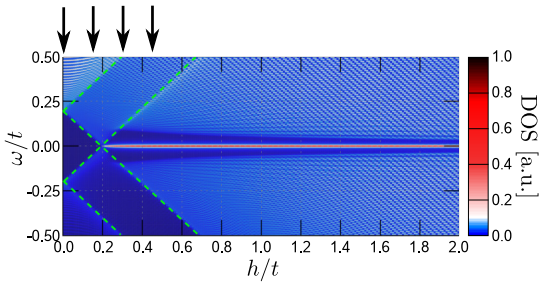

FIG. 3. Total DOS for chain in magnetic field. Result for $k_BT = 0t$, $\mu = -2t$, $\lambda = 0.15t$, and $\Delta = 0.2t$ with $V_g = 0t$. Black arrows represent specific values of h, indicated for further analysis. Green lines specify the regions of the Zeeman shifted induced superconducting gap by proximity effect.

separate line in the DOS. This line corresponds to a singular state of wire [29]. Characteristic structure of the DOS restricted by the asymptotic line (shown by the dashed green line) will be explained below. As we can see, when magnetic field crosses the critical value h_c, the previously closed superconducting gap is reopened partly as a *topological gap* [42].

Now we will introduce previously mentioned terminology, by referring to Fig. 4(a), which schematically shows a change of the DOS by magnetic field h. In the described system, the superconducting gap Δ in wire experimentally corresponds to the *hard gap* induced by proximity effects [21–23], whose value depends on the coupling between the semiconductor wire with the superconducting shell or base [43]. In consequence

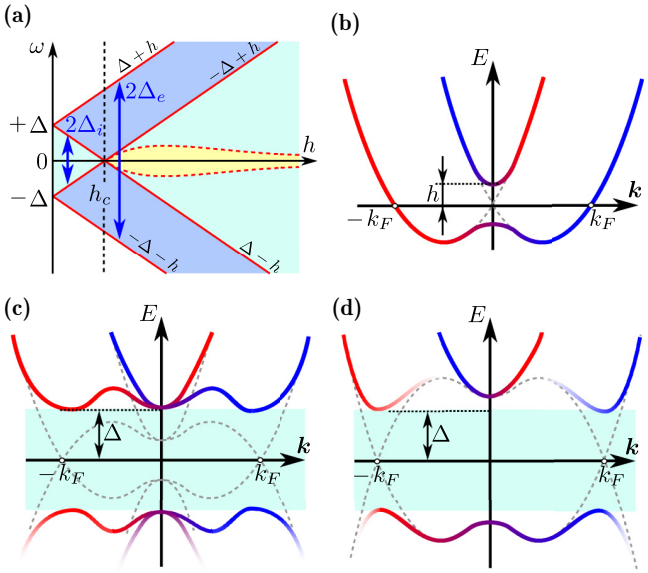

FIG. 4. (a) Schematic representation of the shifted superconducting gaps by magnetic field h, where $2\Delta_e$ and $2\Delta_i$ denote *exterior* and *interior* gaps, respectively. Region for magnetic fields smaller (bigger) than h_c describes the trivial (nontrivial) topological phase. (b)–(d) Band structure obtained in presence of the magnetic field without (b) and with (c,d) superconductivity In the case of trivial (c) and nontrivial (d) topological phases, where the green region 2Δ represents the superconducting gap. Gray dashed line represents band structure in absence of the magnetic field (b) and superconductivity (c,d).

of this, for $h = 0$ we observe a 2Δ gap in the DOS. Increasing h leads to energy levels $\omega = \pm\Delta$ shift (red lines). In this situation, similar to Ref. [42], we can define *exterior gap* $2\Delta_e = 2(\Delta + h)$ and *interior gap* $2\Delta_i = 2(\Delta - h)$ as an energy spacing between external and internal asymptotic line, respectively (blue double-arrows). For $0 < h < h_c$ the *interior* gap decreases, creating *soft gap* with value smaller than *hard gap*. Finally, *interior* superconducting gap is closed in h_c, while for $h > h_c$ *topological gap* reopens (yellow region between dashed red lines). Note that increasing the SOC leads to increased *topological gap* [5].

Experimentally observed *hard gap* depends on magnetic field [12], which is approximately described by the BCS-like relation $\Delta(h) \simeq \Delta\sqrt{1-(h/h_{c2})^2}$ [44], where h_{c2} denotes upper critical magnetic field of superconductor (magnetic field in which *hard gap* will be closed). This dependence effectively leads to experimentally observed suppression of in-gap bound states. However, we assume constant value of Δ, which does not change interpretation of the presented results.

Phase transition from trivial to nontrivial phase, characterized by $\mathbb{Z}_2$ topological invariant [45–47], can be described in relation to band structure of infinite wire with periodic boundary conditions [Figs. 4(b)–4(d)] [12,42,48,49]. In the absence of the superconducting gap, the external magnetic field h leads to the gap opening and lifts spin degeneracy at momentum $k = 0$ [Fig. 4(b)]. Induction of the superconductivity in the wire opens additional gap around the Fermi level $E = 0$ (horizontal axis). The relation between Δ and h, corresponding to the gap opening due to superconductivity and magnetic field, respectively, defines the topologically trivial [Fig. 4(c)] and nontrivial [Fig. 4(d)] regimes. In the trivial topological phase $h < h_c$ [Fig. 4(c)], a new gap at the Fermi momentum $\pm k_F$ emerges and also increases gap at the $k = 0$ because $\Delta > h$ (in accord with "positive" value of the *interior gap* $2\Delta_i$). The situation looks differently in a nontrivial topological phase regime $h > h_c$ [Fig. 4(d)], when $\Delta < h$ (what corresponds to a "negative" value of $2\Delta_i$). In this situation, opening of the superconducting gap at $\pm k_F$ does not change the character of the gap at $k = 0$. Moreover, from a formal point of view, in our system a nontrivial *p-wave* pairing between quasiparticles from this same band is induced. This possibility has been described before [30,31,50–54].

However, in the absence of the boundary conditions (finite wire), discussion of the band structure is unreasonable because momentum is not a good quantum number. Moreover, energy of *bound states* occurring at the *boundaries* of the wire, has symmetrical shape with respect to Fermi energy $\omega = 0$. Nonzero magnetic field applied in the system leads to emergence of ABS in-gap states (with energies $\Delta > |\omega| > \Delta - h$) and ABS with lowest energy defines the boundary of the *interior gap*. Increasing h to a value above h_c allows the MBS to form from the two lowest energy ABSs. Simultaneously, when the lowest energy ABSs merged into MBS, the *topological gap* is created between the new lowest energy ABSs.

In the nontrivial topological phase ($h > h_c$) the zero-energy MBS can be experimentally observed, i.e., in the form of zero-bias peaks in the tunneling conductance measurement [36,40,55,56]. In this type of experiment, the MBS is observed in the form of the zero-bias conductance peak $G_0 = 2e^2/h$ at zero temperature. However, in the finite temperature regime

conductance is significantly reduced, which has been observed experimentally [18] and discussed theoretically [44,56–59]. Therefore, local density of states presented here is a good indicator for the differential conductance [37], however, it strongly depends on temperature and coupling between tip and nanowire [18,49,58–62].

Moreover, the MBS are physically localized at the end of the wire. Length of the wire plays an important role in the realization of MBS wave-function oscillation in space, which is connected to the MBS nonlocality [63]. When considering a sufficiently short wire, overlapping of the two Majorana wave functions is too extensive and the "true" zero-energy MBS cannot be realized, as the MBS annihilate [64–66]. This system requires a meticulously made nanowire [67], because any disorder has a destructive role on the topological phase [47,68–71]. However, local impurity can lead to MBS separation into the pair of new MBS at the *newly* created boundaries of the homogeneous system in topological states [66,72–75].

As we mentioned in Sec. I, the ABSs can be experimentally controlled. Moreover, for some experimental parameter the ABS can coalesce [24] into a *zero-energy bound state* (ZEBS). This feature is realized only in the nontrivial topological phase ($h < h_c$). Because the ZEBS and MBS are zero-energy states, we must mention the differences between those two similar kinds of bound states. First, magnetic field in which ZEBS ($h < h_c$) coalesce is smaller than the one required for MBS to emerge ($h > h_c$). Second, what is more important from a practical point of view, ZEBS do not obey the non-Abelian statistics which is a consequence of different parity with respect to MBS [9,70].

IV. SINGLE QUANTUM DOT

Let us now inspect the superconducting wire comprising $N = 200$ sites with one additional site, representing the normal QD. Evolution of this QD spectrum with respect to the gate voltage V_g is illustrated in Fig. 5 for several magnetic fields h. In the absence of the magnetic field [Fig. 5(a)] and for $V_g/t \leqslant -1.8$ the QD quasiparticles show up in LDOS as the characteristic *devil's staircase* [red ellipse in Fig. 5(a)]. This avoided crossing structure occurs as a consequence of hybridization of the QD energy level with a finite number of the nanowire energy levels. In the regime $V_g/t \in (-1.8, 0.8)$ there appear two ABSs inside the *hard gap*, which never cross each other (as is indicated by the pink double-arrow).

For the $h < h_c$ in the trivial topological phase [Fig. 5(b)], we observe the Zeeman splitting of the initially single spin-degenerate QD levels [white arrows in Fig. 5(b)]. In consequence, the majority spin character for both levels has been disjointed (character of "left" and "right" levels corresponds to majority spin $\downarrow$ and $\uparrow$ quasiparticles, respectively). Moreover, when magnetic field is strong enough, the ABS can cross each other creating ZEBS at two different values of V_g, depending on h (indicated by the green arrows). Characteristic spin-split structure has been also observed [21,76–79].

For strong magnetic field $h > h_c$, at the nontrivial topological phase [Figs. 5(c) and 5(d)], the MBS emerge in the nanowire. Let us remark that such Majorana quasiparticles, for some range of parameters, coexist with the conventional ABS inside the *topological gap*, whose spectral weights depend

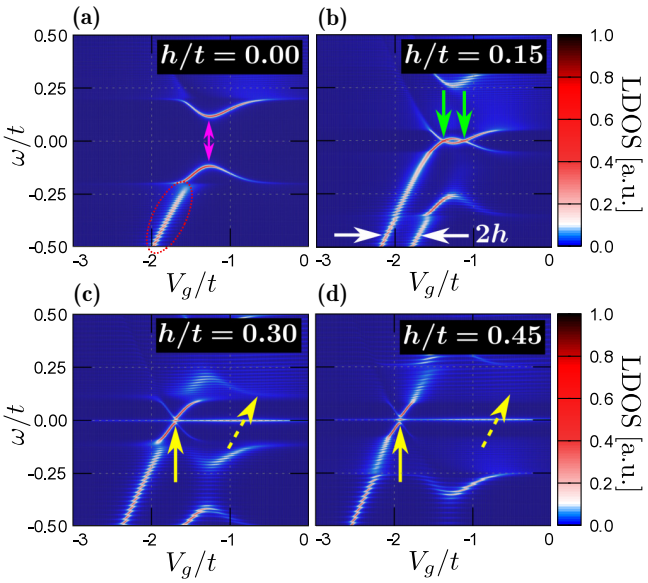

FIG. 5. Evolution of the quantum-dot spectral function with respect to V_g for several magnetic fields, indicated by the black arrows in Fig. 3. Results are obtained for $k_BT = 0t$, $\mu = -2t$, $\lambda = 0.15t$, $\Delta = 0.2t$. Red ellipse in (a) indicates the *devil's staircase* structure.

on h and V_g. Modification of the QD energy level with dominant σ-spin character by V_g leads to two different kinds of resonance with MBS. In the case of the $\uparrow$-like state (in the region indicated by the yellow dashed arrow) *leak* of the MBS into the QD has been observed, whereas for the $\downarrow$-like state there is only a relatively weak resonance (yellow arrows).

It should be mentioned that the possible crossing of the ABS in the absence of the magnetic field is possible when ratio coupling between the QD and nanowire would induce a *hard gap* (in our case t/Δ) that is smaller than one [78]. This scenario can be also realized at the quantum phase transition in the correlated quantum dot [63,78–80] but such an issue is beyond the scope of the present study. For parameters chosen in our system we have $t/\Delta \gg 1$ and the gap between two ABSs inside the *hard gap* could not observed (Fig. 6). In the case studied here, the minimum of the gap mentioned above occurs at $V_g \sim -1.3t$, whereas its extreme value 2Δ is reached either

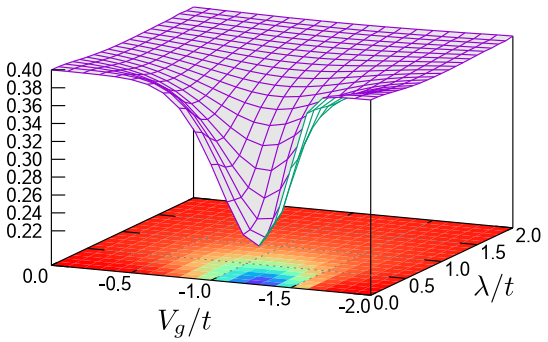

FIG. 6. Effective gap between the ABS (inside the *hard gap*) versus the spin-orbit coupling λ and the gate potential V_g. Results are obtained for the single quantum dot at zero temperature for $\mu = -2t$, $\Delta = 0.2t$, and $h = 0$.

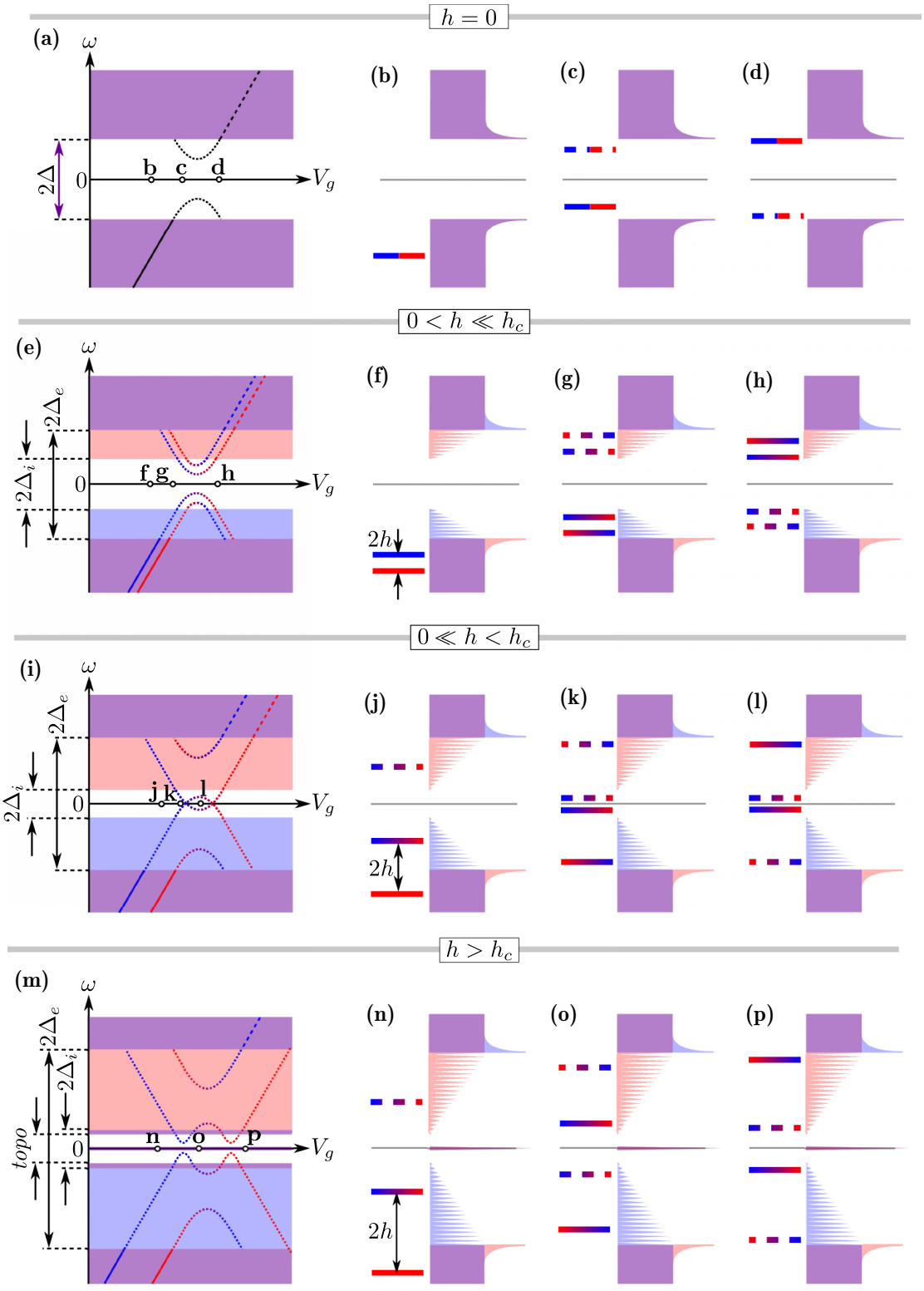

FIG. 7. Schematic representation of the resonance of the dot energy levels and the nanowire with increasing magnetic field (from top to bottom). For every case in the most-left column, solid, dashed, and dotted lines represent occupied, unoccupied, and Andreev bound states, respectively. Moreover, the gray dashed axis line shows the Fermi level and letters on those axes in the most-left column denote the specific gate potential V_g on the quantum dot. In the rest of the columns a solid (dashed) line indicates quasiparticles with dominant particle (hole) character. Colors (red/blue/violet) illustrate the dominant spin ($\uparrow/\downarrow$/degenerate case) of energetic levels. ABSs (f)–(h), (j)–(l), and (n)–(p) inside the external gap become a *mixture* of spins, due to the spin-orbit coupling, hence the transition in colors representing energy levels. Labels 2Δ, $2\Delta_i$, $2\Delta_e$, and *topo* represent the *hard gap*, *interior gap*, *exterior gap*, and *topological gap*, respectively, which have been introduced in Sec. III.

away when gate potential is insignificant or for the strong SOC λ. As we can see in Fig. 5, the ABS crossing can be achieved for some fixed gate potential V_g, in the presence of the magnetic field h which is equal to one-half of the gap between the ABS when magnetic field is absent.

A. Resonance of the quantum-dot levels with Majorana bound states

Let us now explain in detail the asymmetry in the resonance of the QD energy levels with nonowire energy levels, presented previously in Fig. 5. We will do this using the schematic representation of the QD energy levels and nanowire total DOS shown in Fig. 7 and terminology introduced in Sec. III. In the absence of magnetic field [Figs. 7(a)–7(d)], manipulation of gate voltage V_g changes the spin degenerate dot energetic levels with respect to the Fermi level ($\omega = 0$). When states are localized below the superconducting *hard* gap [Fig. 7(b)] we can observe the *devil's staircase* structure. This structure is formed as a consequence of coupling between the QD and nanowire energetic levels–spin conserved (t) and spin-flip (λ) hoppings. ABSs emerge when the QD energy levels are near or inside the *hard gap* [Figs. 7(c) and 7(d)]. The spectral weight of the ABS is leaking from the occupied to the nonoccupied (c → d) levels, converting its character [i.e., see also Fig. 5(a)]. Initially, the negative energy ABS is particle dominated, whereas the positive energy one is hole dominated [Fig. 7(c)]. As the change in V_g progresses, occupation of states is inverted [Fig. 7(d)]. For any nonzero magnetic field h [Figs. 7(e)–7(p)] spin degeneracy is lifted by the Zeeman shift. When $0 < h < h_c$, sharp structures of the ABS are observed in the *hard gap*, creating the *soft gap* which is equal to the *interior gap* ($2\Delta_i$) for this value of magnetic field. If the h is sufficiently small [Fig. 7(e)], the ABS does not cross the Fermi level. When both QD energy levels are localized below the *exterior gap* [Fig. 7(f)], then we observe two separate levels with different spin majority character [see Fig. 5(b)]. As we increase V_g, observed mirrored ABS resonances invert its dominant character from particle to hole (g → h). For high enough magnetic field (but still smaller than h_c) [Figs. 7(i)–7(l)] the ABSs start to cross at zero-energy level. In consequence ABSs coalesce into ZEBS at the Fermi level and the *interior gap* narrows [Fig. 7(i)]. For some value of V_g [Fig. 7(j)] only one pair of ABSs exists inside the *exterior gap* while the ↑ dominant spin level of the QD resides below this gap. Before first coalescing of ABSs [Fig. 7(k)] we observe a situation similar to Fig. 7(g). However, for V_g between points of ABS coalescence (l) energy levels invert. In a case of the $h > h_c$ [Figs. 7(m)–7(p)] the *topological gap* opens and the MBS emerge at $\omega = 0$. In this nontrivial topological phase (with $h > \Delta$) the dot-energy level is shifted enough to treat it independently. For V_g at the point [Fig. 7(n)] the QD energy levels with ↑(↓) dominant spin character are located deep below (near) the *topological gap*. In consequence we observe "in-topological-gap" ABS detached from the ↓-spin QD energy level, which suits minority spin in the whole system. Increase of V_g (o → p) leads to a position of the QD energy level with majority ↑(↓)-spin character near (far above) the *topological gap*, respectively. Additionally, dominant spin component reverses during the topological phase transition [81].

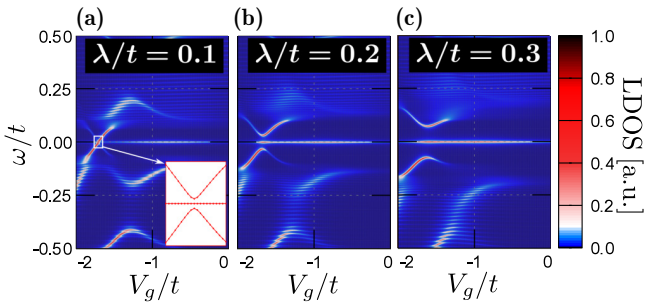

FIG. 8. Effect of the spin-orbit coupling λ on the induced Majorana and Andreev bound states. (a) Inset shows the quasiparticle energies for the zoomed region. Results are obtained for $k_BT = 0t$, $\mu = -2t$, $h = 0.3t$, and $\Delta = 0.2t$.

We must have in mind that quasiparticles with the ↑(↓)-spin character has a dominant (inferior) role in the whole system due to the Zeeman splitting. In this sense MBS at zero-energy level have ↑ spin polarization [9]. Stemming from this, only remaining ↑ dominant spin character energy levels can resonate with the MBS. Following this condition and keeping in mind that the SOC is sufficiently strong in the system, a characteristic structure of avoided crossing occurs, halting the ABS emerged from the inferior ↓-spin QD energy level to cross the zero-energy level. Simultaneously, the ↑-spin dominant QD energy level can resonate with the MBS, which can be clearly seen as an increasing of the spectral weight of the MBS along the dashed arrows in Figs. 5(c) and 5(d).

As a result of the QD coupling to the wire by spin-conserved t and spin-flip λ hopping, the resonance of the QD energy levels with minority ↓-spin character and MBS with ↑ polarization, depends strongly on the spin-orbit coupling. Role of the spin-orbit influence on this behavior is shown Fig. 8, where we compare the resonance of the QD energy levels with the zero-energy MBS for several values of the SOC λ. For any nonzero value of λ, the system supports both the MBS and ABS, coexisting inside the *topological* gap. It can be noticed, that the ABS become gapped [see the inset in Fig. 8(a)] and their avoided crossing behavior becomes significant with an increase of SOC strength λ. At the same time, the MBS gain more and more spectral weight. Furthermore, we also observe constructive influence of the SOC λ on the *devil's staircase* structure, existing outside the *topological* gap. In relation to the previous paragraph, this is a consequence of spin-flip hybridization between QD and wire, supporting the resonance of the ABS and opposite spin character MBS.

B. Different types of zero-energy bound states

We have shown that the ABS can coexist with MBS and sometimes their energies are identical (resonant). Such resonance depends on the quantum-dot energy level, which can by modified by the global Fermi level (i.e., the chemical potential μ), the gate voltage V_g, and the magnetic field h. These quantities affect the ABS and for trivial topological phase ($h < h_c$) lead to emergence of the ZEBS. Here we should remind one that the ZEBS and the MBS are zero-energy states, but emerge in different topological phases (trivial and

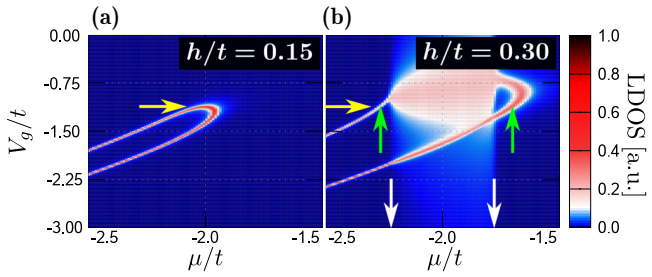

FIG. 9. Modification of the zero-energy LDOS on the quantum-dot site by change μ and V_g in the cases of the phase not supporting (a) and supporting (b) realization of the MBS. Results for $k_BT = 0t$, $\lambda = 0.15t$, and $\Delta = 0.2t$.

nontrivial, respectively). It is illustrated in Fig. 9, where we plot the LDOS of the dot region for $\omega = 0$ versus μ and V_g.

These results refer to the following cases: (i) $h < h_c$, when MBS are not realized for any parameter of the system [Fig. 9(a)]; (ii) $h > h_c$, when for some values of μ, the system can host the MBS [Fig. 9(b); the MBS supporting regime exists between white arrows]. In the first case we can find such regions, where ABSs coalesce into ZEBS [red kink in Fig. 9(a)]. For the latter case, upon varying μ (or h) we can distinguish two regimes: supporting (between white arrows) and nonsupporting (outside white arrows) emergence of the MBS. Inside the first region we can see realization of the (asymmetric) resonance of the QD energy levels with the MBS hosted at the ends of the nanowire. In the second region, similar to previously discussed, we can only see a crossing of the ABS in the ZEBS form. The difference between such resonances has been discussed in previous sections.

The following results are discussed for the cross section of Fig. 9 along $V_g = -1.125t$ indicated by the yellow arrow. Figure 10 shows the LDOS of the QD as a function of the (global) chemical potential μ. We can clearly see that upon varying of μ the coalescing ABS give rise to ZEBS [Fig. 10(a), green arrow]. However, for the nontrivial topological phase [Fig. 10(b)], ZEBS appear only beyond the MBS-supported regime [green arrows outside the region marked by white arrows in Fig. 10(b)]. These results are complementary to Fig. 9(b). Inside this regime there exists the topologically

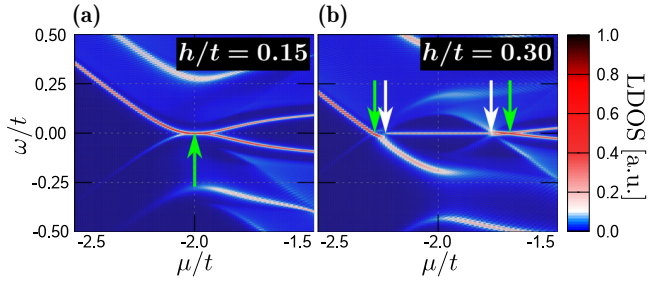

FIG. 10. LDOS on the quantum dot versus the chemical potential μ for the cases not supporting (a) and supporting (b) realization of the MBS. The gate potential is $V_g = -1.125t$ as indicated by the right green arrow in Fig. 5(b). Results are obtained for $k_BT = 0t$, $\lambda = 0.15t$, and $\Delta = 0.2t$.

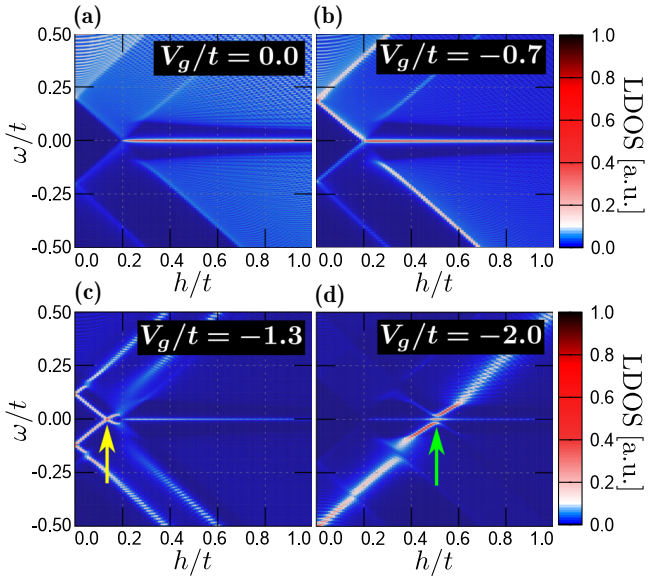

FIG. 11. Evolution of the quantum-dot spectrum with respect to magnetic field h for several gate potentials V_g, as indicated. Results are obtained for $k_BT = 0$, $\mu = -2t$, $\lambda = 0.15t$, and $\Delta = 0.2t$.

protected Majorana states, while for other parameters the ABSs create a new gap around $\omega = 0$.

Further important effects can be seen if we investigate the influence of magnetic field (Fig. 11). As we mentioned previously, h detunes the energy levels of the states with opposite spin character. This is true for the whole studied system. We remind one that, in general, for $h < h_c$ we can observe the ABS or the ZEBS coalesced from ABS, like indicated by yellow arrow in Fig. 11(c), what is in agreement with experimental results [24], whereas the zero-energy MBS can be realized only for $h > h_c$. Similarly to the previous result, increase in h reveals asymmetry in resonance between the QD energy levels with dominant σ-spin character and MBS, what has been explained in Sec. IV A. In some range of gate potential V_g (compare with Fig. 5), with changed h, the dominant $\uparrow$- or $\downarrow$-spin character of the QD energy levels are revealed. In the case of the energy levels with spin majority character ($\uparrow$), resonance between the QD energy level and MBS is favored by spin-conserving hopping [Figs. 11(a) and 11(b)]. For the energy levels with minority character ($\downarrow$), resonance of the QD level and the MBS is more energetically expensive due the fact that the spin-flip hopping λ is smaller than spin-conserved hopping t. As a result, we can observe emergence of the ABS in-topological gap [Fig. 11(d)] and weak resonance with the MBS (green arrow), depending on λ (see Fig. 8). When the QD energy levels penetrate the *hard gap* as the ABS [in weak magnetic field, Fig. 11(c)], the ZEBS is formed (yellow arrow).

V. DOUBLE-SITE QUANTUM DOT

Similar analysis can be performed for the system comprising two additional sites (double-site quantum dot) side-attached to the hybrid nanowire. In this case, we observe two pairs of the ABS appearing in the spectrum of such dots

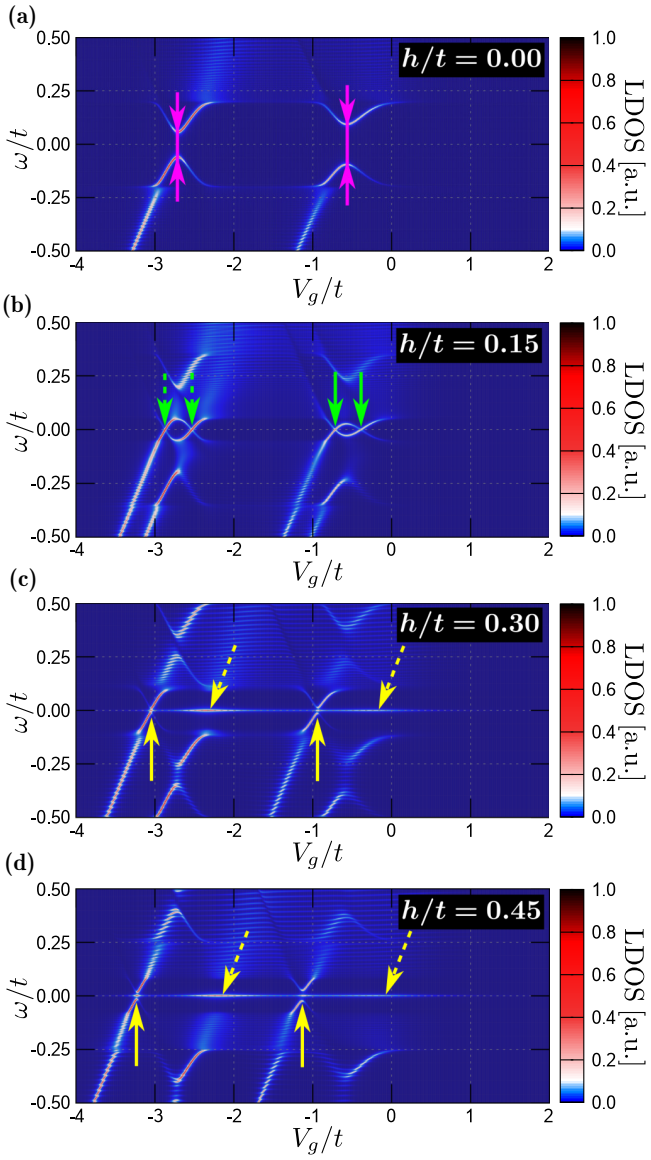

FIG. 12. Evolution of the double quantum-dot LDOS with respect to the gate voltage V_g for several magnetic fields, indicated by the white arrows in Fig. 3. Results are obtained for $k_BT = 0t$, $\mu = -2t$, $\lambda = 0.15t$, and $\Delta = 0.2t$.

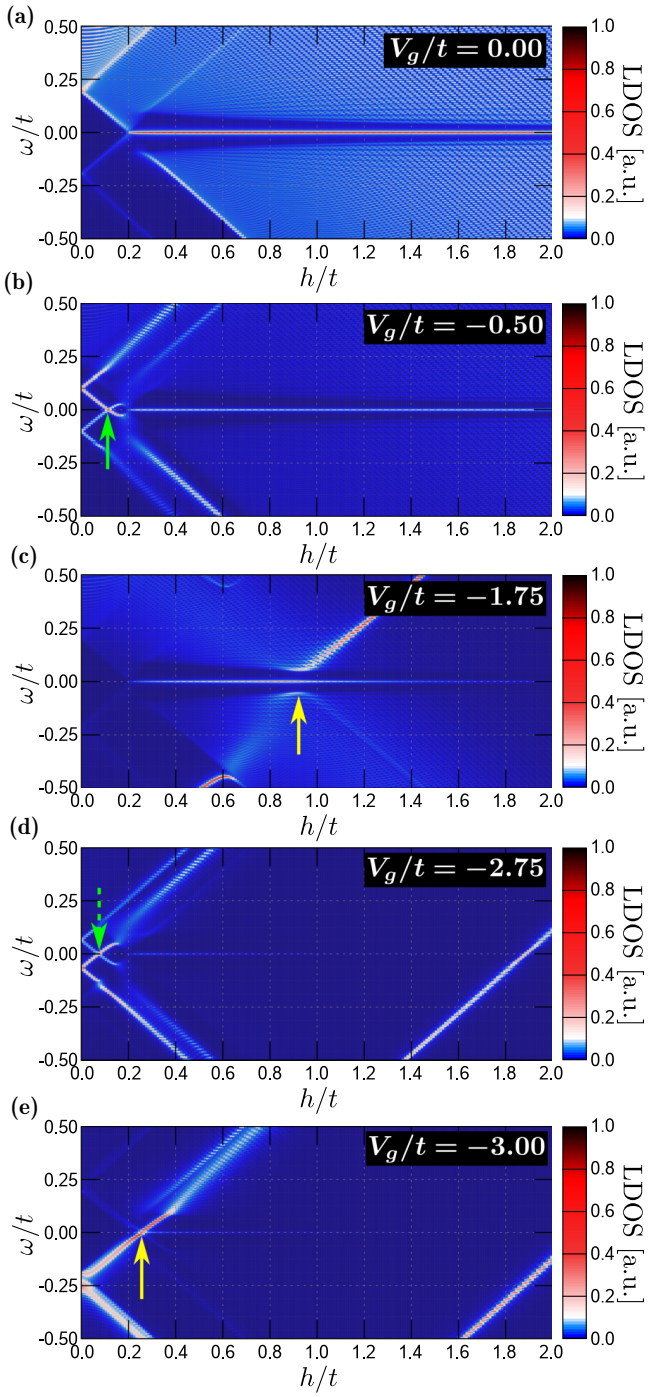

FIG. 13. Influence of the magnetic field h on the LDOS of the double quantum dot for different values of the gate voltage V_g, as indicated. Result are obtained for $k_BT = 0t$, $\mu = -2t$, $\lambda = 0.15t$, and $\Delta = 0.2t$.

(Fig. 12). We notice that for $h = 0$ these pairs of ABSs are split by different energy gaps [indicated by the pink arrows in Fig. 12(a)]. For this reason, within a range of weak magnetic field $h < h_c$ we can observe either one or two pairs of the spin-split ZEBS [marked by the solid and dashed green arrows in Fig. 12(b)]. In the regime of nontrivial topological phase (for $h > h_c$) we see emergence of the zero-energy MBS [yellow solid and dashed arrows in Figs. 12(c) and 12(d)]. When the MBS (with ↑ majority spin character of the system) hosted on the wire, coincides with the minority spin character (↓) double-site QD energy levels [yellow solid arrows in Figs. 12(c) and 12(d)], we can observe its existence in the *topological gap* while ABSs do not cross at zero-energy level. In other words, the ABS separate from the zero-energy Majorana mode as a consequence of weak coupling between QD and the strong one in the wire due to the spin-flip hopping λ. Regarding the case of energy levels with ↑-spin character (dashed yellow arrows), their bound states do not enter the *topological gap* but resonate with the MBS at the zero-energy level. Figure 13 shows the double quantum-dot spectrum as a function of the magnetic field h for several values of the gate voltage V_g. Again, we notice that V_g controls the spectral

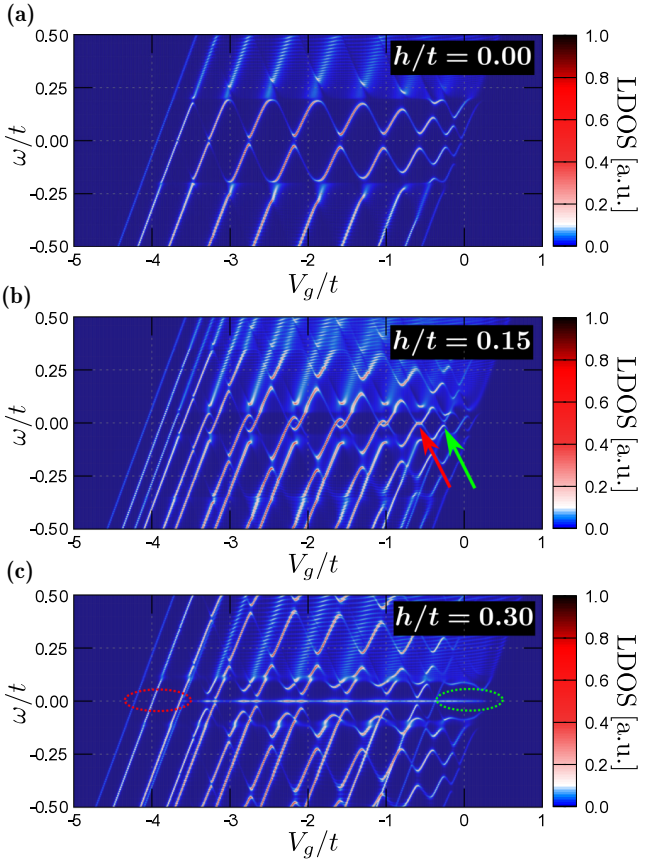

FIG. 14. Gate voltage dependence of the LDOS obtained at zero temperature for the quantum dot comprising 10 sites, using $\mu = -2t$, $\lambda = 0.15t$, and $\Delta = 0.2t$. (c) Red (green) dotted ellipses correspond to the region where only the quantum-dot energy levels with $\downarrow$ ($\uparrow$)-spin character exist.

weight of the Majorana mode leaking into the QD region in the nontrivial topological phase (above the critical magnetic field $h > h_c$).

VI. MULTISITE QUANTUM DOT

In realistic quantum systems the ABS can sometimes originate from a multitude of the energy levels existing in a subgap regime. We shall model such a situation here, considering a piece of the nanowire (sketched in Fig. 2) whose energy levels can be identified as the finite number of lattice sites in this complex structure. Such systems can be realized experimentally, e.g., in the carbon nanotube superconducting device [76]. Similar effects can be relevant to the experiment reported by Deng *et al.* [24]. Another possible realization could refer to the multilevel structure obtained by the modern experimental technique, designing the quantum dot with atomic precision [82]. Due to the proximity effect, we can expect appearance of the N pairs ABS [21,22,24,76], where N is the number of the sites in the QD region. In our calculations for the multilevel dot we shall focus on $N = 10$ sites.

Figure 14 shows variation of the normal nanowire spectrum with respect to the gate voltage V_g for several magnetic fields h, as indicated. For $h = 0$ [Fig. 14(a)] we observe N quasiparticle branches, which become doubled at low energies (due to particle-hole mixing). For the weak magnetic field $h < h_c$ [Fig. 14(b)] we can observe the Zeeman splitting of the initial quasiparticle branches. In a low energy regime these bound states eventually reveal either a crossing (red arrow) or avoided crossing (green arrow), depending on the gate voltage V_g. Finally, when hybrid-nanowire transitions to nontrivial topological phase $h > h_c$, we can observe resonance of the QD energy levels with MBS hosted in the nanowire [Fig. 14(c)], similarly to previous results, but different form for levels with majority or minority spin character.

In consequence of the asymmetric resonances of the QD energy levels with minority and majority spin types, we observe different behaviors of these levels in the subgap region [Fig. 14(c)]. The QD energy levels with the minority spin ($\downarrow$) character are insensitive to the existence of the MBS zero-energy level in the wire (red dotted ellipse), while in the case of majority spin ($\uparrow$) complete resonance is observed (green dotted ellipse). In the case of the intermediate V_g regime (between red and green dotted ellipses), the spectral weight of the MBS weakly oscillates with a varying V_g as a consequence of various interplay between the QD energy levels, depending on their dominant spin component.

From a practical point of view it is important to know what are the spatial profiles of the zero-energy bound states of the nanowire, due to their dependence on the magnetic field. For $h < h_c$ they correspond to crossings of the ZEBS whereas for $h > h_c$ they refer to the MBS, respectively. As mentioned in Sec. III, the zero-energy MBS is characterized as the localized, oscillating in space, wave function formed at the end of the wire. Similarly, the ABS wave functions are localized in the QD region of the studied system. In both cases these zero-energy bound states can leak from the QD to the nanowire region (in the case of the ZEBS) or *vice versa* (when MBS is present), via the hybridization between both parts. Figure 15 presents the spatially dependent spectral weight of the zero-energy ($\omega = 0$) quasiparticles. Let us remark that $i \in \langle 1,10 \rangle$ in this case correspond to the multisite QD connected to the hybrid nanowire. For some value of the magnetic field smaller than h_c [Fig. 15(a)], but bigger than the gap between ABS in the absence of the magnetic field, we can observe several crossings of the ABS (visible as red lines). These ZEBS are localized mainly in the QD region and leak into the nanowire region. The situation looks different in a nontrivial topological phase [Fig. 15(b)], where the MBS are present. In consequence, when QD energy levels change (controlled by gate voltage V_g), we can observe a shift of the MBS initially localized in the end of the wire to the dot region.

By inspecting Fig. 15 we can also notice spatial oscillations of the zero-energy quasiparticles, both in the trivial ($h < h_c$) and nontrivial ($h > h_c$) topological phases. This behavior is observable near the edges (spectrum of the entire system is shown in Fig. 16). In the trivial topological phase [Fig. 16(a)] such oscillations appear mainly in the QD and leak partially to the wire (green dotted ellipse). The situation changes completely for the nontrivial superconducting state [Fig. 16(b)], where the MBS oscillations (red arrows) exist on both sides of the interface and leak to the QD region (green dotted ellipse). In the second case the spatial oscillations are very pronounced, as has been mentioned in Sec. III.

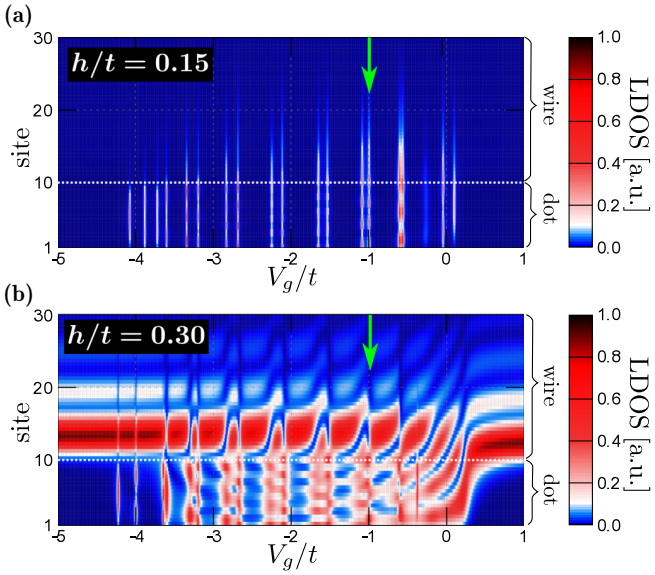

FIG. 15. Spatial profiles of the ABS and/or MBS obtained at $\omega = 0$ for the normal nanowire, comprising 10 sites. (a) The ABS of the trivial superconducting state ($h < h_c$); (b) Illustration of the spatial profiles of the MBS in the topologically nontrivial superconducting state ($h > h_c$). Results are obtained for $k_BT = 0t$, $\mu = -2t$, $\lambda = 0.15t$, and $\Delta = 0.2t$. Dotted white line shows the boundary between the quantum dot and wire regions.

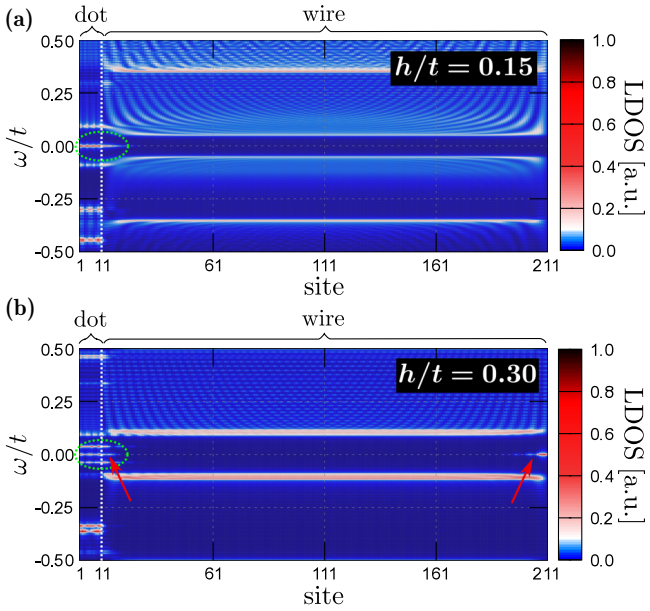

FIG. 16. LDOS along the quantum-dot hybrid nanowire in the cases of the phase not supporting (a) and supporting (b) realization of the MBS. Dot regions are localized below site 11, while the superconducting wire is above site 10. Results for $k_BT = 0t$, $\mu = -2t, \lambda = 0.15t$, and $\Delta = 0.2t$. Bias voltages are fixed as $V_g = -0.99$, which corresponds to one of the ABS-resonance levels shown in Fig. 15 as green arrows. The dotted white line shows the boundary between the quantum-dot and wire regions. Red arrows show a pair of MBS.

VII. QUANTUM DEVICE WITH TUNABLE ANDREEV AND MAJORANA BOUND STATES

Finally we propose an experimentally feasible device (sketched in Fig. 17) for controllable realization of various types of the bound states using electrostatic means. Motivation to realization of the device in the proposed form, is provided by the results from previous sections, which suggest multiple possible outcomes: (i) realization and controlling of ZEBS from coalescing ABS (for $h < h_c$); (ii) ZEBS leakage from the QD to the nanowire region (for $h < h_c$); (iii) MBS leakage from the nanowire to the QD region (for $h > h_c$). In analogy to the setup used by Deng *et al.* [24] we suggest using the semiconducting wire whose external parts are epitaxially covered by the superconductors (SC1 and SC2). Such a system resembles the typical SNS junction [83], however, we omit the phase dependence as superconductors SC1 and SC2 can be taken as made from the same material. The central piece (which is not covered by superconductors) is treated as the multilevel QD in which energy levels can be varied by the gate potential V_g (orange region, similar to Fig. 1). Pairs of gates at the ends of the wire (pink), play a crucial role in this setup as they employ the means to measure and verify the existence of zero-bias MBS peaks, e.g., in a differential conductance discussed in Sec. III. The change of the (global) chemical potential μ can be realized by changing the voltage at the base (green). By applying the STM tip to the central QD region, one can probe the different types of bound states in the differential conductance for each individual site. We have in mind that the whole device should be in the external magnetic field, directed along the wire. Moreover, in generality the SC1 and SC2 may be different materials. As a consequence of this, only one part of the nanowire can pass to the nontrivial topological phase, supporting the realization of the MBS, which should be observed as a zero-bias peak in the differential conductance between pairs of the gates, i.e., G1-G1′ and G2-G2′ (or G3-G3′ and G4-G4′). On the other hand, simultaneous measurements carried out by pairs of the gates and the STM can verify the possibility of the bound states leaking from the QD to the nanowire region or *vice versa*.

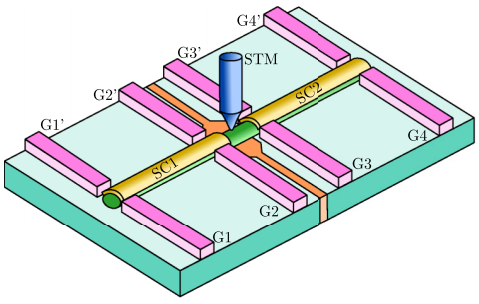

FIG. 17. Sketch of the proposed device for a tunable realization of the Andreev or Majorana bound states. Semiconducting wire (green) is epitaxially covered by two pieces of the superconducting material (SC1 and SC2). The uncovered part of the wire is the multisite quantum dot, for which energy levels are constrained by the underlying gate (pink). The side-attached pairs of gates (i.e., G1-G1′, G2-G2′, etc.) can be used to measure, e.g., differential conductance. Using the STM tip (blue) one can detect the bound states present in the quantum-dot region.

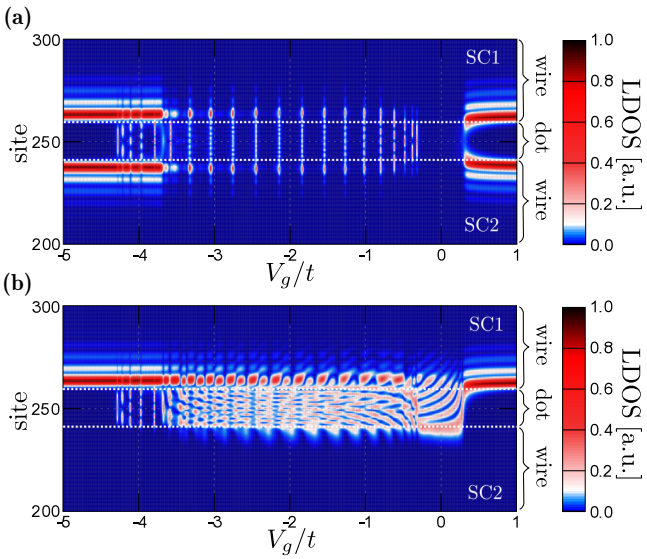

FIG. 18. Spectral weight of the zero-energy quasiparticles induced in the multilevel quantum dot (sites from 240 to 260) coupled the two nanowires (see Fig. 17). Results are obtained for $k_BT = 0t$, $\mu = -2t, \lambda = 0.15t$, and $h = 0.3t$ assuming either $\Delta = 0.2t$ for both superconducting wires (a) or $\Delta = 0.2t$ for the sites $i > 260$ and $\Delta = 0.4t$ for the sites $i < 240$, respectively. The dotted white line shows the boundary between the quantum-dot and wire regions.

The STM-type measurement in the central region of the proposed device, also can be useful for studying or checking the nature of the realized bound states. It has been recently emphasized that the Majorana quasiparticles can be distinguished from the usual Andreev states by the spin-polarized spectroscopy called the selective equal spin Andreev reflections (SESARs) [84] or spin selective Andreev reflection (SSAR) [85,86]. This type of spectroscopy, unambiguously distinguishes between the "true" and "fake" Majorana quasiparticles [87,88], which has been used successfully for, e.g., the detection of a zero-bias peak in the $Bi_2Te_3/NbSe_2$ heterostructure [89,90] or in the case of the magnetic atom chain [17,27,91–93].

Now we will show and discuss numerical results, which should be realized in the device described above. We considered the QD comprising 20 sites ($240 < i < 260$). Figure 18 shows the zero-energy quasiparticle spectrum for two situations: (i) when both nanowires are in the nontrivial topological phase [Fig. 18(a)], and (ii) when one part (SC1) is the nontrivial topological phase, whereas the other one (SC2) is not [Fig. 18(b)]. In both cases the zero-energy QD levels are available for some discrete values of the gate potential V_g, approximately in the voltage regime of $-4.5 \leqslant V_g/t \leqslant -0.5$. What is also important, in both cases, outside this range of V_g we can observe a hosting of the MBS in the SC1 region (and in the SC2 region in the first case). ZEBS available on the QD and MBS hosted in the wires, can be lead to a resonance between them in a controlled fashion. As a consequence we can check features described in previous sections, a difference in resonance of the MBS with the QD energy levels with majority or minority spin character [asymmetry in Fig. 18(a) around V_g equals $-4t$ and $0t$]. Another possibility is an

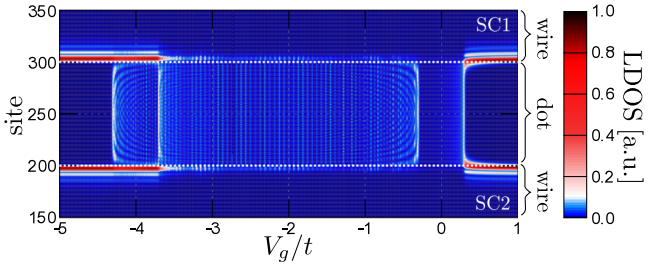

FIG. 19. This same as in Fig. 18(a) but for the broader central quantum-dot region, comprising 100 sites ($200 \leqslant i \leqslant 300$). Dotted white lines show the boundary between the quantum-dot and wire regions.

experimental study of the leaking of the MBS from one part of the device to the second one via the QD region. Moreover, here we have two possibilities: (i) when MBS is hosted in both wires [Fig. 18(a)], this causes an *interference* between two different Majorana quasiparticles [94,95], and (ii) when only one wire hosts the MBS [Fig. 18(b)], this gives the possibility of studying the MBS leakage from the first to the second wire in the ZEBS form [Fig. 18(b)]. A similar suggestion can be found in Ref. [96], where the authors described the expected experimental result of conductance spectroscopy in a nontopological-topological superconductor junction, which is a building block of our proposed device. In both cases, measurement of the differential conductance between pairs of gates (i.e., G1-G1′, etc.) in the described device, can be helpful to verify the realization of the zero-energy-type bound states in the form of the zero-bias peak or the ABS in the case of nonzero bias.

It should be mentioned that our calculation shows an important role of the finite number of available QD energy levels (compare, e.g., Figs. 18(a) and 19). Suggested measurement should be more apparent for QD with a smaller number of energy levels (which in our case corresponds to number of sites in the dot region).

VIII. SUMMARY

Recent experiments suggest the possibility of realization of the zero-energy bound state in a hybrid-nanowire structure (Sec. I), which can be interpreted as a Majorana bound state, with its characteristic features (Sec. III). Motivated by the results obtained by Deng *et al.* [24], who reported the possibility of inducing the bound states in the quantum dot in a controllable way, we described the experimental setup (quantum-dot hybrid nanowire structure), using the microscopic model (Sec. II) and solving it in real space by the Bogoliubov–de Gennes technique.

In Sec. IV we studied properties of the system with the one-site quantum dot adjoined to the nanowire. In particular, we analyzed the following: (i) possible influence of gate voltage V_g on the bound state realized in the quantum dot, and (ii) mutual relation between bound states in the quantum dot and the nanowire region. We showed that the Andreev bound states, observed for some value of the magnetic field inside the *hard* superconducting gap, can coalesce in a controllable way, creating zero-energy bound states. In relation to this, the zero-energy Majorana bound states can be realized only when

magnetic field is sufficiently large. Our results are in agreement with those presented in Ref. [24].

Mutual influence of those two types of bound states is possible as a consequence of shared existence at the zero-energy level. Therefore, it is possible for bound states to leak from the quantum dot to the nanowire region or *vice versa*. Moreover, we showed an asymmetry between resonance of the Majorana bound state and the quantum-dot energy levels. We explained both results as a consequence of (i) change in dominant spin character of quantum-dot energy levels by magnetic field (the majority ↑ and minority ↓ spin character), and (ii) different resonance between the Majorana bound states (with ↑ character) and the quantum-dot energy levels (corresponding to ↑ and ↓).

This can also be observed as an influence of the spin-orbit coupling on the relation between the Andreev bound state, which penetrates the *topological gap* and zero-energy Majorana bound states. Increase in the spin-orbit coupling leads to an avoided crossing of the Andreev bound state with a dominant ↓-spin character and is accompanied by transfer of the spectral weight to the Majorana bound state. This effect is not observed when the quantum-dot energy level has ↑-spin character.

Those results also can be observed in a more general structure with the multisite quantum dot (e.g., two-site or multisite quantum dot described in Sec. V and Sec. VI, respectively). In this more realistic picture of the quantum dot, we found that the Majorana bound state can resonate with several quantum-dot energy levels with dominant ↑-spin character, which is visible as a series of the discrete quantum levels in the quasiparticle spectrum. We showed that the Majorana bound states leak from the wire to the quantum-dot region and observed the pronounced quantum oscillations in their spatial profiles. These effects indicate a tendency towards spatial broadening of the Majorana modes.

In Sec. VII we proposed a quantum device in the form of a semiconductor nanowire, whose two parts are covered by the superconductor. The remaining uncovered part can be treated as a quantum dot, with a finite number of available energy levels. This type of device can be used in the realization of described properties, i.e., interplay between different types of bound states. In the regime of the parameter supporting the realization of the Majorana quasiparticles, the presented nanodevice can help to distinguish the differences in resonance between zero-energy bound states with a different dominant spin character. We hope that such a device would be stimulating for further studies of the Majorana quasiparticles and their *interactions* with other kinds of bound states.

Experimental results obtained by Deng *et al.* [24] have been intensively discussed by many groups studying the tunneling conductance [44,57–59]. However, the zero-bias conductance peak does not provide definitive evidence for Majorana zero modes [44]. In relation to this, the zero mode occurring as a consequence of the usual Andreev bound state (in a trivial topological phase) is generally expected to produce a zero-bias conductance peak of height varying between 0 to $4e^2/h$. We must have in mind, however, influence of additional physical effects (e.g., finite temperature [58]) leading to reduction of the conductance value, as mentioned in Sec. III. This type of behavior is important in distinguishing the zero-energy feature related to the "trivial" Andreev from the "nontrivial" Majorana bound states [44].

To this end, let us highlight the main findings of our paper. Interplay between the quantum-dot and nanowire energy levels strongly depend on the *topological state* of the system (cf. Fig. 9). In the case of the trivial topological phase, the dot energy level creates zero-energy bound states via Andreev bound states only for some specific values of the gate potential and magnetic field. Contrary to this, in the nontrivial topological phase the Majorana zero-energy bound states can be observed in a wide range of parameters. We also inspected *leakage* of the Majorana bound states from the nanowire to quantum-dot region. In relation to the previous work addressing interplay between the quantum-dot energy levels with a nonlocality of the Majorana zero modes [63], we discussed influence of the coupling in spin-conserved and in spin-flip channels between the quantum dot and the nanowire. We showed that this process strongly depends on the dominant spin component of the quantum-dot energy states. Similar behavior has been discussed in the context of spin-dependent coupling between the quantum dot and the nanowire [97]. Moreover, we have proposed an experimentally feasible device for studying such a *leakage* effect and detecting the Majorana quasiparticles. This device can be helpful in experimental verification of the described behavior and in practical realization of the true Majorana qubits [98]. Realizations of this proposed device could be well controlled electrostatically, in which the Majorana bound states could emerge or disappear in the quantum-dot region. Similarities have been previously suggested for quantum computing based on the Majorana quasiparticles [99].

Note added. During the reviewing process of this article, we became aware of Ref. [100], describing detection of the topological phase transition in nanowires using the quantum dot analogous to the properties described by us in Sec. IV.

ACKNOWLEDGMENTS

We kindly thank Sz. Głodzik, J. Klinovaja, M. P. Nowak, M. M. Maśka, J. Tworzydło, and D. P. Wójcik for careful reading of the manuscript, valuable comments, and discussions. We also thank M. T. Deng for consultation and remarks on Sec. VII. This work was supported by the National Science Centre (NCN, Poland) under Grants No. UMO-2016/20/S/ST3/00274 (A.P.) and No. DEC-2014/13/B/ST3/04451 (A.K. and T.D.).

[1] N. Read and D. Green, Paired states of fermions in two dimensions with breaking of parity and time-reversal symmetries and the fractional quantum Hall effect, Phys. Rev. B **61**, 10267 (2000).

[2] A. Y. Kitaev, Unpaired Majorana fermions in quantum wires, Phys.-Usp. **44**, 131 (2001).

[3] L. Fu and C. L. Kane, Superconducting Proximity Effect and Majorana Fermions at the Surface of a Topological Insulator, Phys. Rev. Lett. **100**, 096407 (2008).

[4] Ch. Nayak, S. H. Simon, A. Stern, M. Freedman, and S. Das Sarma, Non-Abelian anyons and topological quantum computation, Rev. Mod. Phys. **80**, 1083 (2008).

[5] J. D. Sau, S. Tewari, R. M. Lutchyn, T. D. Stanescu, and S. Das Sarma, Non-Abelian quantum order in spin-orbit-coupled semiconductors: Search for topological Majorana particles in solid-state systems, Phys. Rev. B **82**, 214509 (2010).

[6] J. Alicea, Y. Oreg, G. Refael, F. von Oppen, and M. P. A. Fisher, Non-Abelian statistics and topological quantum information processing in 1D wire networks, Nat. Phys. **7**, 412 (2011).

[7] D. Rainis and D. Loss, Majorana qubit decoherence by quasiparticle poisoning, Phys. Rev. B **85**, 174533 (2012).

[8] B. van Heck, A. R. Akhmerov, F. Hassler, M. Burrello, and C. W. J. Beenakker, Coulomb-assisted braiding of Majorana fermions in a Josephson junction array, New J. Phys. **14**, 035019 (2012).

[9] D. Sticlet, C. Bena, and P. Simon, Spin and Majorana Polarization in Topological Superconducting Wires, Phys. Rev. Lett. **108**, 096802 (2012).

[10] D. Aasen, M. Hell, R. V. Mishmash, A. Higginbotham, J. Danon, M. Leijnse, T. S. Jespersen, J. A. Folk, Ch. M. Marcus, K. Flensberg, and J. Alicea, Milestones Toward Majorana-Based Quantum Computing, Phys. Rev. X **6**, 031016 (2016).

[11] V. Mourik, K. Zuo, S. M. Frolov, S. R. Plissard, E. P. A. M. Bakkers, and L. P. Kouwenhoven, Signatures of Majorana fermions in hybrid superconductor-semiconductor nanowire devices, Science **336**, 1003 (2012).

[12] A. Das, Y. Ronen, Y. Most, Y. Oreg, M. Heiblum, and H. Shtrikman, Zero-bias peaks and splitting in an Al-InAs nanowire topological superconductor as a signature of Majorana fermions, Nat. Phys. **8**, 887 (2012).

[13] M. T. Deng, C. L. Yu, G. Y. Huang, M. Larsson, P. Caroff, and H. Q. Xu, Anomalous zero-bias conductance peak in a Nb-InSb nanowire-Nb hybrid device, Nano Lett. **12**, 6414 (2012).

[14] L. P. Rokhinson, X. Liu, and J. K. Furdyna, The fractional a.c. Josephson effect in a semiconductor-superconductor nanowire as a signature of Majorana particles, Nat. Phys. **8**, 795 (2012).

[15] H. O. H. Churchill, V. Fatemi, K. Grove-Rasmussen, M. T. Deng, P. Caroff, H. Q. Xu, and C. M. Marcus, Superconductor-nanowire devices from tunneling to the multichannel regime: Zero-bias oscillations and magnetoconductance crossover, Phys. Rev. B **87**, 241401 (2013).

[16] A. D. K. Finck, D. J. Van Harlingen, P. K. Mohseni, K. Jung, and X. Li, Anomalous Modulation of a Zero-Bias Peak in a Hybrid Nanowire-Superconductor Device, Phys. Rev. Lett. **110**, 126406 (2013).

[17] B. E. Feldman, M. T. Randeria, J. Li, S. Jeon, Y. Xie, Z. Wang, I. K. Drozdov, B. Andrei Bernevig, and A. Yazdani, High-resolution studies of the Majorana atomic chain platform, Nat. Phys. **13**, 286 (2017).

[18] F. Nichele, A. C. C. Drachmann, A. M. Whiticar, E. C. T. O'Farrell, H. J. Suominen, A. Fornieri, T. Wang, G. C. Gardner, C. Thomas, A. T. Hatke, P. Krogstrup, M. J. Manfra, K. Flensberg, and Ch. M. Marcus, Scaling of Majorana Zero-Bias Conductance Peaks, Phys. Rev. Lett. **119**, 136803 (2017).

[19] S. Nadj-Perge, I. K. Drozdov, J. Li, H. Chen, S. Jeon, J. Seo, A. H. MacDonald, B. A. Bernevig, and A. Yazdani, Observation of Majorana fermions in ferromagnetic atomic chains on a superconductor, Science **346**, 602 (2014).

[20] P. Krogstrup, N. L. B. Ziino, W. Chang, S. M. Albrecht, M. H. Madsen, E. Johnson, J. Nygård, C. M. Marcus, and T. S. Jespersen, Epitaxy of semiconductor–superconductor nanowires, Nat. Mater. **14**, 400 (2015).

[21] W. Chang, M. S. Albrecht, S. T. Jespersen, F. Kuemmeth, P. Krogstrup, J. Nygård, and M. C. Marcus, Hard gap in epitaxial semiconductor–superconductor nanowires, Nat. Nanotech. **10**, 232 (2015).

[22] S. M. Albrecht, A. P. Higginbotham, M. Madsen, F. Kuemmeth, T. S. Jespersen, J. Nygård, P. Krogstrup, and C. M. Marcus, Exponential protection of zero modes in Majorana islands, Nature (London) **531**, 206 (2016).

[23] Ö. Gül, H. Zhang, F. K. de Vries, J. van Veen, K. Zuo, V. Mourik, S. Conesa-Boj, M. P. Nowak, D. J. van Woerkom, M. Quintero-Pérez, M. C. Cassidy, A. Geresdi, S. Koelling, D. Car, S. R. Plissard, E. P. A. M. Bakkers, and L. P. Kouwenhoven, Hard superconducting gap in InSb nanowires, Nano Lett. **17**, 2690 (2017).

[24] M. T. Deng, S. Vaitiekenas, E. B. Hansen, J. Danon, M. Leijnse, K. Flensberg, J. Nygård, P. Krogstrup, and C. M. Marcus, Majorana bound state in a coupled quantum-dot hybrid-nanowire system, Science **354**, 1557 (2016).

[25] A. Yazdani, B. A. Jones, C. P. Lutz, M. F. Crommie, and D. M. Eigler, Probing the local effects of magnetic impurities on superconductivity, Science **275**, 1767 (1997).

[26] R. Pawlak, M. Kisiel, J. Klinovaja, T. Meier, S. Kawai, T. Glatzel, D. Loss, and E. Meyer, Probing atomic structure and Majorana wavefunctions in mono-atomic Fe chains on superconducting Pb surface, npj Quantum Inf. **2**, 16035 (2016).

[27] M. Ruby, B. W. Heinrich, Y. Peng, F. von Oppen, and K. J. Franke, Exploring a proximity-coupled Co chain on Pb(110) as a possible Majorana platform, Nano Lett. **17**, 4473 (2017).

[28] D. Chevallier, D. Sticlet, P. Simon, and C. Bena, Mutation of Andreev into Majorana bound states in long superconductor-normal and superconductor-normal-superconductor junctions, Phys. Rev. B **85**, 235307 (2012).

[29] D. Chevallier, P. Simon, and C. Bena, From Andreev bound states to Majorana fermions in topological wires on superconducting substrates: A story of mutation, Phys. Rev. B **88**, 165401 (2013).

[30] M. Sato and S. Fujimoto, Topological phases of noncentrosymmetric superconductors: Edge states, Majorana fermions, and non-Abelian statistics, Phys. Rev. B **79**, 094504 (2009).

[31] M. Sato, Y. Takahashi, and S. Fujimoto, Non-Abelian topological orders and Majorana fermions in spin-singlet superconductors, Phys. Rev. B **82**, 134521 (2010).

[32] J. Chen, P. Yu, J. Stenger, M. Hocevar, D. Car, S. R. Plissard, E. P. A. M. Bakkers, T. D. Stanescu, and S. M. Frolov, Experimental phase diagram of zero-bias conductance peaks in superconductor/semiconductor nanowire devices, Sci. Adv. **3**, e1701476 (2017).

[33] S. Gazibegovic, D. Car, H. Zhang, S. C. Balk, J. A. Logan, M. W. A. de Moor, M. C. Cassidy, R. Schmits, D. Xu, G. Wang, P. Krogstrup, R. L. M. Op het Veld, K. Zuo, Y. Vos, J. Shen, D. Bouman, B. Shojaei, D. Pennachio, J. S. Lee, P. J. van Veldhoven, S. Koelling, M. A. Verheijen, L. P. Kouwenhoven, Ch. J. Palmstrøm, and E. P. A. M. Bakkers, Epitaxy of advanced nanowire quantum devices, Nature (London) **548**, 434 (2017).

[34] Ch. Reeg, D. Loss, and J. Klinovaja, Finite-size effects in a nanowire strongly coupled to a thin superconducting shell, Phys. Rev. B **96**, 125426 (2017).
[35] E. Prada, P. San-Jose, and R. Aguado, Transport spectroscopy of NS nanowire junctions with Majorana fermions, Phys. Rev. B **86**, 180503 (2012).
[36] D. Chevallier and J. Klinovaja, Tomography of Majorana fermions with STM tips, Phys. Rev. B **94**, 035417 (2016).
[37] J. Stenger and T. D. Stanescu, Tunneling conductance in semiconductor-superconductor hybrid structures, arXiv: 1703.02543.
[38] P. G. de Gennes, *Superconductivity of Metals and Alloys* (Addison-Wesley, Boston, 1989).
[39] H. Matsui, T. Sato, T. Takahashi, S.-C. Wang, H.-B. Yang, H. Ding, T. Fujii, T. Watanabe, and A. Matsuda, BCS-Like Bogoliubov Quasiparticles in High-T_c Superconductors Observed by Angle-Resolved Photoemission Spectroscopy, Phys. Rev. Lett. **90**, 217002 (2003).
[40] J. Figgins and D. K. Morr, Differential Conductance and Quantum Interference in Kondo Systems, Phys. Rev. Lett. **104**, 187202 (2010).
[41] J. Tersoff and D. R. Hamann, Theory of the scanning tunneling microscope, Phys. Rev. B **31**, 805 (1985).
[42] J. Klinovaja and D. Loss, Composite Majorana fermion wave functions in nanowires, Phys. Rev. B **86**, 085408 (2012).
[43] W. S. Cole, S. Das Sarma, and T. D. Stanescu, Effects of large induced superconducting gap on semiconductor Majorana nanowires, Phys. Rev. B **92**, 174511 (2015).
[44] Ch.-X. Liu, J. D. Sau, T. D. Stanescu, and S. Das Sarma, Andreev bound states versus Majorana bound states in quantum-dot–nanowire-superconductor hybrid structures: Trivial versus topological zero-bias conductance peaks, Phys. Rev. B **96**, 075161 (2017).
[45] C. L. Kane and E. J. Mele, Z_2 Topological Order and the Quantum Spin Hall Effect, Phys. Rev. Lett. **95**, 146802 (2005).
[46] X.-L. Qi and S.-Ch. Zhang, Topological insulators and superconductors, Rev. Mod. Phys. **83**, 1057 (2011).
[47] P. Zhang and F. Nori, Majorana bound states in a disordered quantum dot chain, New J. Phys. **18**, 043033 (2016).
[48] Y. Oreg, G. Refael, and F. von Oppen, Helical Liquids and Majorana Bound States in Quantum Wires, Phys. Rev. Lett. **105**, 177002 (2010).
[49] Ch. Reeg and D. L. Maslov, Transport signatures of topological superconductivity in a proximity-coupled nanowire, Phys. Rev. B **95**, 205439 (2017).
[50] L. P. Gor'kov and E. I. Rashba, Superconducting 2D System with Lifted Spin Degeneracy: Mixed Singlet-Triplet State, Phys. Rev. Lett. **87**, 037004 (2001).
[51] Ch. Zhang, S. Tewari, R. M. Lutchyn, and S. Das Sarma, $p_x + ip_y$ Superfluid from S-Wave Interactions of Fermionic Cold Atoms, Phys. Rev. Lett. **101**, 160401 (2008).
[52] J. Alicea, Majorana fermions in a tunable semiconductor device, Phys. Rev. B **81**, 125318 (2010).
[53] K. Seo, L. Han, and C. A. R. Sá de Melo, Topological phase transitions in ultracold Fermi superfluids: The evolution from Bardeen-Cooper-Schrieffer to Bose-Einstein-condensate superfluids under artificial spin-orbit fields, Phys. Rev. A **85**, 033601 (2012).
[54] T. Yu and M. W. Wu, Gapped triplet p-wave superconductivity in strong spin-orbit-coupled semiconductor quantum wells in proximity to s-wave superconductor, Phys. Rev. B **93**, 195308 (2016).
[55] M. Gibertini, F. Taddei, M. Polini, and R. Fazio, Local density of states in metal-topological superconductor hybrid systems, Phys. Rev. B **85**, 144525 (2012).
[56] J. Liu, A. C. Potter, K. T. Law, and P. A. Lee, Zero-Bias Peaks in the Tunneling Conductance of Spin-Orbit-Coupled Superconducting Wires with and without Majorana End States, Phys. Rev. Lett. **109**, 267002 (2012).
[57] B. van Heck, R. M. Lutchyn, and L. I. Glazman, Conductance of a proximitized nanowire in the Coulomb blockade regime, Phys. Rev. B **93**, 235431 (2016).
[58] Ch.-X. Liu, J. D. Sau, and S. Das Sarma, Role of dissipation in realistic Majorana nanowires, Phys. Rev. B **95**, 054502 (2017).
[59] J. Danon, E. B. Hansen, and K. Flensberg, Conductance spectroscopy on Majorana wires and the inverse proximity effect, Phys. Rev. B **96**, 125420 (2017).
[60] P. Devillard, D. Chevallier, and M. Albert, Fingerprints of majorana fermions in current-correlation measurements from a superconducting tunnel microscope, Phys. Rev. B **96**, 115413 (2017).
[61] Ch.-X. Liu, F. Setiawan, J. D. Sau, and S. Das Sarma, Phenomenology of the soft gap, zero-bias peak, and zero-mode splitting in ideal Majorana nanowires, Phys. Rev. B **96**, 054520 (2017).
[62] F. Setiawan, Ch.-X. Liu, J. D. Sau, and S. Das Sarma, Electron temperature and tunnel coupling dependence of zero-bias and almost-zero-bias conductance peaks in Majorana nanowires, arXiv:1708.09039.
[63] E. Prada, R. Aguado, and P. San-Jose, Measuring Majorana nonlocality and spin structure with a quantum dot, Phys. Rev. B **96**, 085418 (2017).
[64] A. C. Potter and P. A. Lee, Multichannel Generalization of Kitaev's Majorana End States and a Practical Route to Realize Them in Thin Films, Phys. Rev. Lett. **105**, 227003 (2010).
[65] S. Das Sarma, J. D. Sau, and T. D. Stanescu, Splitting of the zero-bias conductance peak as smoking gun evidence for the existence of the Majorana mode in a superconductor-semiconductor nanowire, Phys. Rev. B **86**, 220506 (2012).
[66] X.-J. Liu, Soliton-induced Majorana fermions in a one-dimensional atomic topological superfluid, Phys. Rev. A **91**, 023610 (2015).
[67] H. Zhang, Ö. Gül, S. Conesa-Boj, M. P. Nowak, M. Wimmer, K. Zuo, V. Mourik, F. K. de Vries, J. van Veen, M. W. A. de Moor, J. D. S. Bommer, D. J. van Woerkom, D. Car, S. R. Plissard, E. P. A. M. Bakkers, M. Quintero-Pérez, M. C. Cassidy, S. Koelling, S. Goswami, K. Watanabe, T. Taniguchi, and L. P. Kouwenhoven, Ballistic superconductivity in semiconductor nanowires, Nat. Commun. **8**, 16025 (2017).
[68] Ch. Moore, T. D. Stanescu, and S. Tewari, Majorana bound states in non-homogeneous semiconductor nanowires, arXiv:1611.07058.
[69] W. S. Cole, J. D. Sau, and S. Das Sarma, Proximity effect and Majorana bound states in clean semiconductor nanowires coupled to disordered superconductors, Phys. Rev. B **94**, 140505 (2016).
[70] S. S. Hegde and S. Vishveshwara, Majorana wave-function oscillations, fermion parity switches, and disorder in Kitaev chains, Phys. Rev. B **94**, 115166 (2016).

[71] O. A. Awoga, K. Björnson, and A. M. Black-Schaffer, Disorder robustness and protection of Majorana bound states in ferromagnetic chains on conventional superconductors, Phys. Rev. B **95**, 184511 (2017).

[72] X.-J. Liu and P. D. Drummond, Manipulating Majorana fermions in one-dimensional spin-orbit-coupled atomic Fermi gases, Phys. Rev. A **86**, 035602 (2012).

[73] Y. Xu, L. Mao, B. Wu, and Ch. Zhang, Dark Solitons with Majorana Fermions in Spin-Orbit-Coupled Fermi Gases, Phys. Rev. Lett. **113**, 130404 (2014).

[74] M. M. Maśka, A. Gorczyca-Goraj, J. Tworzydło, and T. Domański, Majorana quasiparticles of an inhomogeneous Rashba chain, Phys. Rev. B **95**, 045429 (2017).

[75] A. Ptok, A. Cichy, and T. Domański, Quantum engineering of Majorana quasiparticles in one-dimensional optical lattices, arXiv:1706.04155.

[76] J.-D. Pillet, C. H. L. Quay, P. Morfin, C. Bena, A. L. Yeyati, and P. Joyez, Andreev bound states in supercurrent-carrying carbon nanotubes revealed, Nat. Phys. **6**, 965 (2010).

[77] T. Dirks, T. L. Hughes, S. Lal, B. Uchoa, Y.-F. Chen, C. Chialvo, P. M. Goldbart, and N. Mason, Transport through Andreev bound states in a graphene quantum dot, Nat. Phys. **7**, 386 (2011).

[78] J.-D. Pillet, P. Joyez, R. Žitko, and M. F. Goffman, Tunneling spectroscopy of a single quantum dot coupled to a superconductor: From Kondo ridge to Andreev bound states, Phys. Rev. B **88**, 045101 (2013).

[79] E. J. H. Lee, X. Jiang, M. Houzet, R. Aguado, Ch. M. Lieber, and S. De Franceschi, Spin-resolved Andreev levels and parity crossings in hybrid superconductor-semiconductor nanostructures, Nat. Nanotech. **9**, 79 (2014).

[80] J. Barański and T. Domański, In-gap states of a quantum dot coupled between a normal and a superconducting lead, J. Phys.: Condens. Matter **25**, 435305 (2013).

[81] P. Szumniak, D. Chevallier, D. Loss, and J. Klinovaja, Spin and charge signatures of topological superconductivity in Rashba nanowires, Phys. Rev. B **96**, 041401 (2017).

[82] S. Folsch, J. Martinez-Blanco, J. Yang, K. Kanisawa, and S. C. Erwin, Quantum dots with single-atom precision, Nat. Nanotech. **9**, 505 (2014).

[83] J. Cayao, E. Prada, P. San-Jose, and R. Aguado, SNS junctions in nanowires with spin-orbit coupling: Role of confinement and helicity on the subgap spectrum, Phys. Rev. B **91**, 024514 (2015).

[84] J. J. He, T. K. Ng, P. A. Lee, and K. T. Law, Selective Equal-Spin Andreev Reflections Induced by Majorana Fermions, Phys. Rev. Lett. **112**, 037001 (2014).

[85] L.-H. Hu, Ch. Li, D.-H. Xu, Y. Zhou, and F.-Ch. Zhang, Theory of spin-selective Andreev reflection in the vortex core of a topological superconductor, Phys. Rev. B **94**, 224501 (2016).

[86] H.-H. Sun, K.-W. Zhang, L.-H. Hu, Ch. Li, G.-Y. Wang, H.-Y. Ma, Z.-A. Xu, Ch.-L. Gao, D.-D. Guan, Y.-Y. Li, C. Liu, D. Qian, Y. Zhou, L. Fu, S.-Ch. Li, F.-Ch. Zhang, and J.-F. Jia, Majorana Zero Mode Detected with Spin Selective Andreev Reflection in the Vortex of a Topological Superconductor, Phys. Rev. Lett. **116**, 257003 (2016).

[87] R. Chirla and C. P. Moca, Fingerprints of Majorana fermions in spin-resolved subgap spectroscopy, Phys. Rev. B **94**, 045405 (2016).

[88] M. M. Maśka and T. Domański, Spin-polarized Andreev tunneling through the Rashba chain, arXiv:1706.01468.

[89] J.-P. Xu, M.-X. Wang, Z. L. Liu, J.-F. Ge, X. Yang, C. Liu, Z. A. Xu, D. Guan, Ch. L. Gao, D. Qian, Y. Liu, Q.-H. Wang, F.-Ch. Zhang, Q.-K. Xue, and J.-F. Jia, Experimental Detection of a Majorana Mode in the Core of a Magnetic Vortex Inside a Topological Insulator-Superconductor $Bi_2Te_3/NbSe_2$ Heterostructure, Phys. Rev. Lett. **114**, 017001 (2015).

[90] H. Li, T. Zhou, J. He, H.-W. Wang, H. Zhang, H.-Ch. Liu, Y. Yi, Ch. Wu, K. T. Law, H. He, and J. Wang, Origin of bias-independent conductance plateaus and zero-bias conductance peaks in $Bi_2Se_3/NbSe_2$ hybrid structures, Phys. Rev. B **96**, 075107 (2017).

[91] S. Jeon, Y. Xie, J. Li, Z. Wang, B. A. Bernevig, and A. Yazdani, Distinguishing a Majorana zero mode using spin-resolved measurements, Science **358**, 772 (2017).

[92] J. Li, S. Jeon, Y. Xie, A. Yazdani, and B. A. Bernevig, The Majorana spin in magnetic atomic chain systems, arXiv:1709.05967.

[93] K. Björnson and A. M. Black-Schaffer, Probing chiral edge states in topological superconductors through spin-polarized local density of state measurements, arXiv:1709.09061.

[94] A. Yamakage and M. Sato, Interference of Majorana fermions in NS junctions, Phys. E **55**, 13 (2014).

[95] J. Barański, A. Kobiałka, and T. Domański, Spin-sensitive interference due to Majorana state on the interface between normal and superconducting leads, J. Phys.: Condens. Matter **29**, 075603 (2017).

[96] F. Setiawan, W. S. Cole, J. D. Sau, and S. Das Sarma, Conductance spectroscopy of nontopological-topological superconductor junctions, Phys. Rev. B **95**, 020501 (2017).

[97] S. Hoffman, D. Chevallier, D. Loss, and J. Klinovaja, Spin-dependent coupling between quantum dots and topological quantum wires, Phys. Rev. B **96**, 045440 (2017).

[98] L. H. Guessi, F. A. Dessotti, Y. Marques, L. S. Ricco, G. M. Pereira, P. Menegasso, M. de Souza, and A. C. Seridonio, Encrypting Majorana fermion qubits as bound states in the continuum, Phys. Rev. B **96**, 041114 (2017).

[99] S. Hoffman, C. Schrade, J. Klinovaja, and D. Loss, Universal quantum computation with hybrid spin-majorana qubits, Phys. Rev. B **94**, 045316 (2016).

[100] D. Chevallier, P. Szumniak, S. Hoffman, D. Loss, and J. Klinovaja, Topological phase detection in Rashba nanowires with a quantum dot, arXiv:1710.05576.

4.2.2 Leakage of the Majorana Quasiparticles in Rashba Nanowire Deposited on Superconducting–Normal Substrate

A. Kobiałka, A. Ptok, Acta Phys. Pol. A **135**, 64 (2019)

Building upon the previous paper, we check what happens if we elongate the quantum dot region into a size comparable to the nanowire. We obtain a system where half of a nanowire is nontrivial and the other half is trivial, which is deposited on an insulator instead of superconductor. By changing the global chemical potential for the normal part of the system, we can shift the energy states creating a barrier that prevents MBS delocalisation. This changes when the majority spin levels in the normal part align with MBS spin, allowing for delocalisation. As a result, a clear picture of MBS leakage into the trivial region is revealed. One of MBS which is highly delocalized, seemingly disappears from the spectrum due to the spreading of MBS wave function in the whole trivial region.

Author's contribution: Partial preparation of numerical and analytical calculations, partial preparation of figures, analysis and discussion of obtained results, partial preparation of the manuscript, preparing the response for Referees.

Proceedings of the 18th National Conference on Superconductivity, Krynica Morska, Poland, October 8–13, 2017

Leakage of the Majorana Quasiparticles in Rashba Nanowire Deposited on Superconducting–Normal Substrate

A. Kobiałka[a,*] and A. Ptok[b]

[a]Institute of Physics, M. Curie-Skłodowska University, pl. M. Skłodowskiej-Curie 1, PL-20031 Lublin, Poland
[b]Institute of Nuclear Physics, Polish Academy of Sciences, E. Radzikowskiego 152, PL-31342 Kraków, Poland

Recent experiments show the possibility of realization of the Majorana quasiparticles at the end of the low dimensional structures. In this type of systems, interplay between spin–orbit coupling, superconductivity and magnetic field leads to the emergence of the Majorana bound states in the topologically non-trivial phase. Here, we study the nanowire located partially at the normal and superconducting base, using microscopic model of this structure and the Bogoliubov–de Gennes technique. We discuss the possibility of the *leakage* of the Majorana bound state, located at the part above superconducting substrate to the part above normal material. We have shown that this is possible only for some specific potential applied to the normal part.

DOI: 10.12693/APhysPolA.135.64

PACS/topics: Majorana bound states, Bogoliubov–de Gennes technique

1. Introduction

The Majorana bound states (MBS) are emergent phenomena existing in solid state physics. Since its experimental validation, there has been a shift of interest in the scientific community, as the proposed ideas regarding realization of the Majorana quantum computers started to look promising [1–4]. Recently, realisation of the MBS have been reported in hybrid semiconductor–superconductor nanowire [5–9] and in ferromagnetic chain at the superconductor surface [10–12]. Being a topological state, MBS robustness against external influence is essential in overcoming the problem of decoherence of quantum state, one of the main halting points in realization of quantum computing [13]. Implementation of such system requires three main ingredients: induced superconductivity, strong spin–orbit interaction and external magnetic field. Together, all of the above result in topological phase shift to non-trivial phase as the Cooper pairs pairing type changes from *s-wave* to *p-wave* [14–18]. This is due to the pairing of electrons from different Rashba bands, therefore having non-opposite momentum $\boldsymbol{k}$. As a result, this allows for the Andreev bound states (ABS) residing inside superconducting gap to coalesce into MBS on zero energy under conditions mentioned above [19–24].

The Majorana states emerge on the edges of low dimensional systems. However, contrary to the $\Delta = t$ instance of Kitaev toy model [25], MBS are not localized exactly on the last sites of theoretical nanowire but are spread about the edge as its wave function is spread as well [26]. If there exists a part of the nanowire that does not share the topological character with a non-trivial part, the MBS can *leak* into this region even though it does not meet the topologically non-trivial criteria [8, 22, 27]. To test these phenomena we propose a nanowire deposited on the surface composed of normal (N) and superconducting (S) regions (Fig. 1).

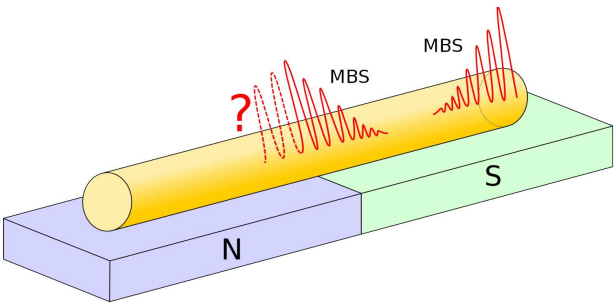

Fig. 1. Schematic representation of investigated system. A semiconductor nanowire (yellow cylinder) is deposited on two kinds of substrates: normal (N) and superconducting (S). Red curve represents our question regarding the effect of the Majorana wave function leakage into the part of the nanowire in normal part of the setup.

The part of nanowire deposited on the normal part of substrate acts as an topologically trivial elongation of nanowire due to the absence of superconducting gap Δ. Such elongation should influence the leakage of MBS wave function as it is flowing into the additional region of nanowire, hosting dozens of available states for the Majorana wave function to leak into [28–30].

The main purpose of this paper is to investigate the leakage phenomena of the MBS from one part of the system to another. We will study this using the system schematically shown in Fig. 1 — a semiconductor nanowire (with strong spin–orbit coupling) located partially on the normal/superconducting base. We study evolution of the MBS by investigation of the local density of states (LDOS) with respect to the electrostatic

*corresponding author; e-mail: akob@kft.umcs.lublin.pl

potential V_N on the normal part of system and magnetic field h directed along the wire. This paper is constructed as follows: firstly, we described a Hamiltonian model and lay out used techniques in Sect. 2. Afterwards, in Sect. 3 we present our numerical calculations and interpretations of obtained results. Finally, we summarize our findings in Sect. 4.

2. Model and technique

For description of the setup described by Fig. 1, we will use a microscopic model in real space with Hamiltonian $\mathcal{H} = \mathcal{H}_{\rm wire} + \mathcal{H}_{\rm SOC} + \mathcal{H}_{\rm prox} + \mathcal{H}_N$. Firstly, we describe the mobile electrons in the wire by

$$\mathcal{H}_{\rm wire} = \sum_{ij\sigma} \left[-t\delta_{\langle i,j\rangle} - (\mu + \sigma h)\,\delta_{ij}\right] c^\dagger_{i\sigma} c_{j\sigma}, \tag{1}$$

where $c^\dagger_{i\sigma}$ ($c_{i\sigma}$) describes creation (annihilation) operator of the electron with spin σ in site i-th, t denotes a hopping integral between the nearest-neighbor sites, whereas μ is a chemical potential. Here h describes the magnetic field parallel to the wire in the Zeeman form, which is necessary to the realization of the MBS. We neglected the orbital effects which have destructive impact on the MBS [31, 32]. The spin–orbit coupling (SOC) in the whole wire can be expressed by

$$\mathcal{H}_{\rm SOC} = -\mathrm{i}\lambda \sum_{i\sigma\sigma'} c^\dagger_{i\sigma} \hat{\sigma}_y^{\sigma\sigma'} c_{i+1\sigma'} + \text{h.c.}, \tag{2}$$

where $\hat{\sigma}_y$ is the second Pauli matrix.

As we mentioned, we are assuming the nanowire deposited on the superconducting (S) and normal (N) substrates (Fig. 1). In consequence of the proximity effects in a part of nanowire in vicinity of the S, the superconducting energy gap Δ is induced in the wire in the following way:

$$\mathcal{H}_{\rm prox} = \sum_{i\in \rm S} \Delta \left(c_{i\downarrow} c_{i\uparrow} + c^\dagger_{i\uparrow} c^\dagger_{i\downarrow}\right). \tag{3}$$

Similarly, in the part of the wire in vicinity of the N, the occupation of the nanowire is changed electrostatically by the V_N voltage applied to the N part

$$\mathcal{H}_N = \sum_{i\in \rm N} V_N \left(c^\dagger_{i\uparrow} c_{i\uparrow} + c^\dagger_{i\downarrow} c_{i\downarrow}\right). \tag{4}$$

The Hamiltonian $\mathcal{H}$ can be exactly diagonalized by transformation [22]:

$$c_{i\sigma} = \sum_n \left(u_{in\sigma}\gamma_n - \sigma v^*_{in\sigma}\gamma^\dagger_n\right), \tag{5}$$

where γ_n and $\gamma^\dagger_n$ are the quasiparticle fermionic operators, while $u_{in\sigma}$ and $v_{in\sigma}$ are the eigenvectors. This leads to the Bogoliubov–de Gennes (BdG) equations [33]:

$$\mathcal{E}_n \psi_{in} = \sum_j \begin{pmatrix} H_{ij\uparrow} & D_{ij} & S^{\uparrow\downarrow}_{ij} & 0 \\ D^*_{ij} & -H^*_{ij\downarrow} & 0 & S^{\downarrow\uparrow}_{ij} \\ S^{\downarrow\uparrow}_{ij} & 0 & H_{ij\downarrow} & D_{ij} \\ 0 & S^{\uparrow\downarrow}_{ij} & D^*_{ij} & -H^*_{ij\uparrow} \end{pmatrix} \psi_{jn}, \tag{6}$$

where $\psi_{in} = (u_{in\uparrow}, v_{in\downarrow}, u_{in\downarrow}, v_{in\uparrow})^T$. Here, the single-particle term $H_{ij\sigma} = -t\delta_{\langle i,j\rangle} - (\mu + \sigma h)\,\delta_{ij} + \forall_{i\in \rm N} V_N \delta_{ij}$ and the spin–orbit coupling term $S^{\sigma\sigma'}_{ij} = -i\lambda\hat{\sigma}_y^{\sigma\sigma'}$. The expression $D_{ij} = \forall_{i\in \rm S}\Delta\delta_{ij}$ describes the superconducting gap. We employ the eigenvectors and eigenvalues of transformed Hamiltonian $\mathcal{H}$ solving the BdG equations, which allow to calculate the local density of states (LDOS) [34]:

$$\rho_{i\sigma}(\omega) = \sum_n \left[|u_{in\sigma}|^2 \delta(\omega - \mathcal{E}_n) + |v_{in\sigma}|^2 \delta(\omega + \mathcal{E}_n)\right]. \tag{7}$$

3. Numerical results and discussion

In this section we shall describe the physical properties of the investigated system and the phenomena occurring as a result of the voltage V_N manipulation. Calculations has been performed in the system with 300 sites with fixed $\mu/t = -2$, $\lambda/t = 0.15$, $\Delta/t = 0.2$ and $k_{\rm B}T/t = 0$.

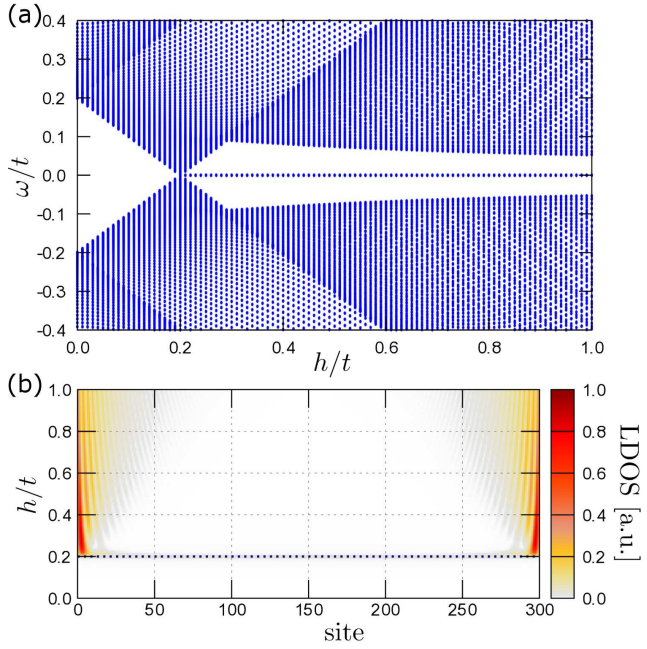

Fig. 2. (a) Energy levels of nanowire as a function of magnetic field h. The zero energy state corresponds to the doubly-degenerate Majorana bound states. (b) Zero energy LDOS of nanowire on given site, as a function of the magnetic field h. MBS emerge at the ends of the nanowire, as the system undergoes a transition from topologically trivial to non-trivial phase ($h_c = 0.2t$).

We shall begin with a brief description of the studied system in the absence of the N part of nanowire. In the low dimensional system with SOC, superconductivity and magnetic field a topological phase transition can occur as the magnetic field crosses a critical threshold value of $h_c = \sqrt{\Delta^2 + (2t \pm \mu)^2}$ [16, 35, 36]. With the increase of magnetic field value h, we obtain the standard Hamiltonian spectrum (Fig. 2a). For chosen parameters, the critical magnetic field threshold occurs for $h_c/t = 0.2$. For this value of magnetic field ($h = h_c$), the gap of the

system closes and reopens, therefore changing the topological state of system. As a result of this, the Andreev bound states originating in symmetric (with respect to the Fermi level) energies coalesce at zero energy creating an MBS [4, 21, 22]. Zero energy states correspond to the states localized on the edge of nanowire, which is shown in zero-energy LDOS (Fig. 2b). After a passing through the magnetic field threshold we can observe non-zero LDOS concentrated at the ends of nanowire. Additionally, increase in the Zeeman field *dissolves* this edge state even further, due to the decrease of topological gap and changing the Majorana states oscillation in space.

In the above calculations we assumed that the superconducting gap Δ is independent of the magnetic field. However, we must have in mind that the experimental value of the superconducting gap changes with magnetic field in a following way $\Delta(h) \simeq \Delta\sqrt{1-(h/h_{c2})^2}$ [21]. As a result, for the magnetic field h_{c2} superconducting gap $\Delta(h)$ closes and the system transits to the normal state. Consequently, topological gap vanishes as well and therefore MBS would exist only for $h_c < h < h_{c2}$. In further results we use constant values of Δ and h, thus condition mentioned above does not influence the calculations.

Now, we will describe the results in a case of the nanowire located partially in the S (sites $\in \langle 1, 150\rangle$) and the N (sites $\in \langle 151, 300\rangle$) base. Due to fact that the system has to be under the influence of spin–orbit coupling, spin is not a valid quantum number anymore. Instead we consider states in terms of spin dominant character.

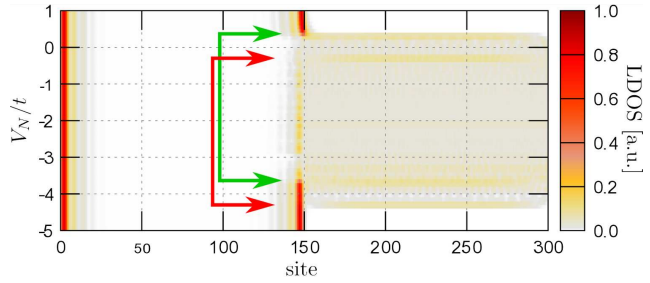

Fig. 3. Influence of voltage V_N on the normal part of nanowire LDOS at zero energy. Energies V_N between red (green) arrows correspond to the energies of states with dominant $\downarrow$ ($\uparrow$) spin character.

At the end of the nanowire, for a case of the non-trivial topological phase (Fig. 2b), the typical Majorana wave function oscillation occurs [28, 37]. Similar results can be observed for any value of voltage V_N (Fig. 3). This changes drastically near the N/S interface (in the center of the nanowire). Existence of the interface between normal and superconducting part enables the Majorana wave function to *leak* to the rest of nanowire (in our case from left to right). Applying a potential to the normal part of the nanowire changes the energy of available states. In the range indicated by green arrows, electrostatical potential shifts the energy of normal levels in such manner that some states cross the Fermi level. If the majority character of states shifted by voltage coincides with MBS "spin" [38], then MBS can leak to the normal part of nanowire. We must have in mind that the magnetic field h shifts the energy of the $\uparrow/\downarrow$ states in the N part. In consequence, the states with $\uparrow$ ($\downarrow$) dominant character are located between green (red) arrows on V_N in Fig. 3. Moreover, in regions below green (above red) arrows of the potential V_N, only the states with $\downarrow$ ($\uparrow$) spin dominant character are available at the zero energy. At the same time, dominant spin in the S region is still $\uparrow$ (for $h > 0$). In consequence of this, for V_N around $0t$ (between green and red upper arrows) we can observe leakage of the MBS from the left (S) region to the right (N) region. This behavior are not observed for V_N around $-4t$.

Settings described above correspond to the eigenvalues presented in Fig. 4. We can see the interplay between zero-energy MBS and in-gap ABS states originating in nanowire. Significant asymmetry of ABS as a function of potential V_N can be observed in regions between red and green arrows. This is a result of the availability of spin dominant levels aligned (left region) and misaligned (right region) with MBS spin and therefore can lead to MBS leakage (in the left region between red and green arrows).

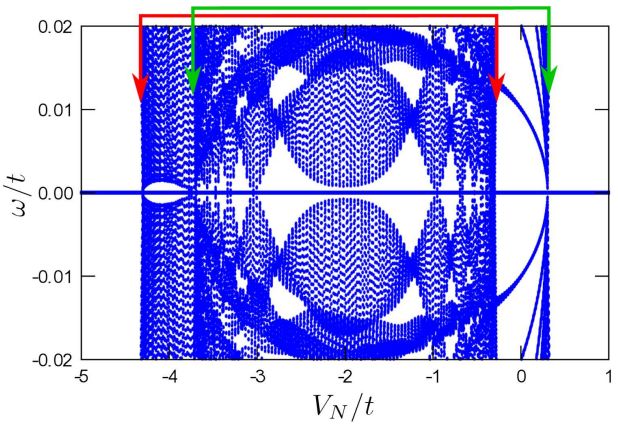

Fig. 4. Low energy eigenvalues of the system as a function of the normal part voltage V_N. Potential V_N between red (green) arrows corresponds to the energies of states with dominant $\downarrow$ ($\uparrow$) spin character. Outside that region the only residing states are ABS.

The MBS emerge in the system for any value V_N. However, its localization at the end of the S part is changed. This can be seen explicitly in a LDOS along the whole wire for chosen V_N (Fig. 5). In a case of the spin $\downarrow$ majority character (part (a)), MBS is stationary localized at the ends of the topologically non-trivial part of the nanowire (green ellipses). MBS leaks only very slightly into the states of opposite spin majority, therefore the LDOS around the end of S part of nanowire does not diminish drastically. We observe two symmetrical MBS

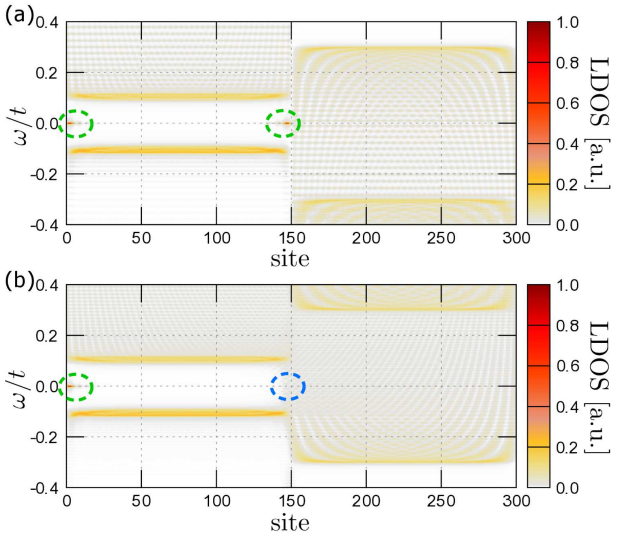

Fig. 5. LDOS of nanowire for V_N equal to $-4t$ (a) and $0t$ (b).

with comparable spectral weight in the S region. Contrary to that (part (b)), only one of the MBS can be clearly distinguished (green ellipse), while second one is delocalized along N part of the wire (blue ellipse). This is a result of leakage of one of the MBS to the spin ↑ majority normal nanowire state and can be understood as the enhancement of the LDOS at $\omega = 0t$ with qualitatively denser distribution of states than in Fig. 5a. The normal part of system plays a role of an "new" edge of topologically non-trivial part and behaves like such enabling the Majorana wave function oscillation in its region. As a consequence, spectral weight of right MBS is partially transferred to the normal part of wire, creating the pairs of the MBS with strongly non-symmetric spectral weight (cf. green and blue ellipses at part Fig. 5b).

4. Summary

Recent experimental studies introduced the phenomenon of MBS leakage, due to the spreading of the Majorana wave function along the wire to the attached structures [8]. It shows an interesting opportunity for both fundamental studies and application in quantum computing due to the ease of manipulation of the potential on quantum dot [22, 23]. In this paper we ask a question regarding conditions of the leakage and how does it correspond to the localization of MBS on the ends of topologically non-trivial nanowire. We proposed a system to test this feature.

In typical situation, the MBS exhibits spatial oscillations in LDOS spectrum related to the oscillations of the Majorana wave function in space. Tuning the chemical potential of normal part of the nanowire by electrostatic means, shifts the states on the Fermi level of the spin dominant character aligned with the MBS "spin" and can lead to the leakage of one of the bound states from non-trivial to topologically trivial part of the wire. Moreover, the localization of the zero-energy state is diminished sufficiently enough to be indistinguishable from the background zero energy ABS (in trivial part of nanowire). This creates a system of effective topological nanowire with strongly non-symmetric spectral weight, where only one of the MBS can be clearly distinguished due to the severe leakage of the other MBS to the normal part of the system. We strongly believe that the experimental realization of this type system can be helpful in distinguishing trivial (Andreev) and non-trivial (Majorana) zero energy bound states.

Acknowledgments

This work was supported by the National Science Centre (NCN, Poland) under grants DEC-2014/13/B/ST3/04451 (A.K.) and UMO-2017/25/B/ST3/02586 (A.P.).

References

[1] C. Nayak, S.H. Simon, A. Stern, M. Freedman, S. Das Sarma, *Rev. Mod. Phys.* **80**, 1083 (2008).

[2] D. Aasen, M. Hell, R.V. Mishmash, A. Higginbotham, J. Danon, M. Leijnse, T.S. Jespersen, J.A. Folk, C.M. Marcus, K. Flensberg, J. Alicea, *Phys. Rev. X* **6**, 031016 (2016).

[3] T. Karzig, C. Knapp, R.M. Lutchyn, P. Bonderson, M.B. Hastings, C. Nayak, J. Alicea, K. Flensberg, S. Plugge, Y. Oreg, C.M. Marcus, M.H. Freedman, *Phys. Rev. B* **95**, 235305 (2017).

[4] S. Hoffman, C. Schrade, J. Klinovaja, D. Loss, *Phys. Rev. B* **94**, 045316 (2016).

[5] V. Mourik, K. Zuo, S.M. Frolov, S.R. Plissard, E.P.A.M. Bakkers, L.P. Kouwenhoven, *Science* **336**, 1003 (2012).

[6] M.T. Deng, C.L. Yu, G.Y. Huang, M. Larsson, P. Caroff, H.Q. Xu, *Nano Lett.* **12**, 6414 (2012).

[7] A. Das, Y. Ronen, Y. Most, Y. Oreg, M. Heiblum, H. Shtrikman, *Nat. Phys.* **8**, 887 (2012).

[8] M.T. Deng, S. Vaitiekenas, E.B. Hansen, J. Danon, M. Leijnse, K. Flensberg, J. Nygård, P. Krogstrup, C.M. Marcus, *Science* **354**, 1557 (2016).

[9] F. Nichele, A.C.C. Drachmann, A.M. Whiticar, E.C.T. O'Farrell, H.J. Suominen, A. Fornieri, T. Wang, G.C. Gardner, C. Thomas, A.T. Hatke, P. Krogstrup, M.J. Manfra, K. Flensberg, C.M. Marcus, *Phys. Rev. Lett.* **119**, 136803 (2017).

[10] S. Nadj-Perge, I.K. Drozdov, J. Li, H. Chen, S. Jeon, J. Seo, A.H. MacDonald, B.A. Bernevig, A. Yazdani, *Science* **346**, 602 (2014).

[11] R. Pawlak, M. Kisiel, J. Klinovaja, T. Meier, S. Kawai, T. Glatzel, D. Loss, E. Meyer, *npj Quant. Inform.* **2**, 16035 (2016).

[12] S. Jeon, Y. Xie, J. Li, Z. Wang, B.A. Bernevig, A. Yazdani, *Science* **358**, 772 (2017).

[13] S.M. Albrecht, A.P. Higginbotham, M. Madsen, F. Kuemmeth, T.S. Jespersen, J. Nygård, P. Krogstrup, C.M. Marcus, *Nature* **531**, 206 (2016).

[14] C. Zhang, S. Tewari, R.M. Lutchyn, S. Das Sarma, *Phys. Rev. Lett.* **101**, 160401 (2008).

[15] C.H.L. Quay, T.L. Hughes, J.A. Sulpizio, L.N. Pfeiffer, K.W. Baldwin, K.W. West, D. Goldhaber Gordon, R. de Picciotto, *Nat. Phys.* **6**, 336 (2010).

[16] M. Sato, Y. Takahashi, S. Fujimoto, *Phys. Rev. B* **82**, 134521 (2010).

[17] K. Seo, L. Han, C.A.R. Sá de Melo, *Phys. Rev. A* **85**, 033601 (2012).

[18] S. Heedt, N. Traverso Ziani, F. Crépin, W. Prost, S. Trellenkamp, J. Schubert, D. Grützmacher, B. Trauzettel, T. Schäpers, *Nat. Phys.* **13**, 563 (2017).

[19] D. Chevallier, D. Sticlet, P. Simon, C. Bena, *Phys. Rev. B* **85**, 235307 (2012).

[20] D. Chevallier, P. Simon, C. Bena, *Phys. Rev. B* **88**, 165401 (2013).

[21] C.-X. Liu, J.D. Sau, T.D. Stanescu, S. Das Sarma, *Phys. Rev. B* **96**, 075161 (2017).

[22] A. Ptok, A. Kobiałka, T. Domański, *Phys. Rev. B* **96**, 195430 (2017).

[23] E. Prada, R. Aguado, P. San-Jose, *Phys. Rev. B* **96**, 085418 (2017).

[24] S.D. Escribano, A.L. Yeyati, E. Prada, *Beilstein J. Nanotechnol.* **9**, 2171 (2018).

[25] A.Y. Kitaev, *Phys.-Usp.* **44**, 131 (2001).

[26] C. Fleckenstein, F. Domínguez, N.T. Ziani, B. Trauzettel, *Phys. Rev. B* **97**, 155425 (2018).

[27] E. Vernek, P.H. Penteado, A.C. Seridonio, J.C. Egues, *Phys. Rev. B* **89**, 165314 (2014).

[28] J. Klinovaja, D. Loss, *Phys. Rev. B* **86**, 085408 (2012).

[29] E. Prada, P. San-Jose, R. Aguado, *Phys. Rev. B* **86**, 180503 (2012).

[30] M. Guigou, N. Sedlmayr, J.M. Aguiar-Hualde, C. Bena, *EPL* **115**, 47005 (2016).

[31] B. Kiczek, A. Ptok, *J. Phys. Condens. Matter* **29**, 495301 (2017).

[32] M.P. Nowak, P. Wójcik, *Phys. Rev. B* **97**, 045419 (2018).

[33] P.G. de Gennes, *Superconductivity of Metals and Alloys*, Addison-Wesley, 1989.

[34] H. Matsui, T. Sato, T. Takahashi, S.-C. Wang, H.B. Yang, H. Ding, T. Fujii, T. Watanabe, A. Matsuda, *Phys. Rev. Lett.* **90**, 217002 (2003).

[35] M. Sato, S. Fujimoto, *Phys. Rev. B* **79**, 094504 (2009).

[36] M. Sato, Y. Takahashi, S. Fujimoto, *Phys. Rev. Lett.* **103**, 020401 (2009).

[37] S.S. Hegde, S. Vishveshwara, *Phys. Rev. B* **94**, 115166 (2016).

[38] D. Sticlet, C. Bena, P. Simon, *Phys. Rev. Lett.* **108**, 096802 (2012).

4.2.3 Delocalisation of Majorana quasiparticles in plaquette–nanowire hybrid system

A. Kobiałka, T. Domański, A. Ptok, Sci. Rep. **9**, 12933 (2019)

In this paper, we propose a fusion of 1D nanowire and 2D plaquette, creating a system with *mixed dimensionality*. We investigate the combination of nontrivial nanowire with trivial and nontrivial plaquettes. Our 2D part in the nontrivial regime is not able to host any zero modes (chirally propagating MZM), although it contains a plethora of ingap states that localize at the edges or corners of the system. Therefore, to introduce MBS into the 2D plaquette, we joined both systems together. In the case where the nanowire is connected to the trivial plaquette, we obtain a small delocalisation of the MBS that was previously located in the junction point. However, in the case where every part of the system was in the nontrivial regime, MBS leakage was extremely large and resulted in MBS wave function delocalizing to the furthest regions of the system. We also checked the impact of the location of a junction point on the spreading of the wave function as well as various 2D shapes of plaquette. Additionally, we proposed a SESAR technique, which could help in the experimental verification of MBS nonlocality and leakage. It is also worth noting that similar studies of mixed dimensionality followed our research.

Author's contribution: Partial preparation of numerical calculations, partial preparation of figures, analysis and discussion of obtained results, partial preparation of the manuscript, participation in preparing the response for Referees.

SCIENTIFIC REPORTS
nature research

OPEN

Delocalisation of Majorana quasiparticles in plaquette–nanowire hybrid system

Received: 25 March 2019
Accepted: 31 July 2019
Published online: 10 September 2019

Aksel Kobiałka[1], Tadeusz Domański[1] & Andrzej Ptok[2]

Interplay between superconductivity, spin-orbit coupling and magnetic field can lead to realisation of the topologically non–trivial states which in finite one dimensional nanowires are manifested by emergence of a pair of zero-energy Majorana bound states. On the other hand, in two dimensional systems the chiral edge states can appear. We investigate novel properties of the bound states in a system of *mixed dimensionality*, composed of one-dimensional nanowire connected with two-dimensional plaquette. We study this system, assuming either its part or the entire structure to be in topologically non–trivial superconducting state. Our results show delocalisation of the Majorana modes, upon leaking from the nanowire to the plaquette with some tendency towards its corners.

Recent nanotechnological progress allows for fabrication of artificial nanostructures[1], where unique quantum phenomena and new states of matter[2] could be observed. Prominent examples are the Majorana bound states (MBS) emerging on quasi-one-dimensional structures, e.g. semiconducting–superconducting hybrid nanowire[3–10] or nanochains of magnetic atoms deposited on superconducting surface[11–16]. Such MBS are characterized by particle–antiparticle indistinguishability and their non–Abelian statistics[17], which makes them promising entity for realisation of the topological quantum computing[18,19].

Proximity-induced superconductivity combined with the magnetic field and the spin-orbit coupling (SOC) drives the system from its topologically trivial to non–trivial superconducting phase[20]. Such transition occurs at critical magnetic field h_c, dependent on the SOC strength and dimensionality of the system[21–23]. Spectroscopically it is manifested by a coalescence of one pair of the Andreev (finite-energy) bound states into the Majorana (zero–energy) quasiparticles[24,25].

Emergence of the degenerate Majorana modes from the Andreev bound states has been also reported in hybrid structures, comprising the quantum dots side-attached to the topological superconducting nanowires[7]. Initial theoretical prediction of such MBS *leakage* on the quantum dot region[26] has been investigated by various groups[27–35]. In these hybrid structures the wavefunction of Majorana quasiparticle is spread onto a region of the normal quantum dot–superconducting nanowire interface[20,24,35–38], diluting the spatial distribution of its spectral weight. This issue has been a subject of intensive experimental and theoretical studies[39].

In one-dimensional structures the Majorana quasiparticles localise at the sample boundaries[40] or near internal defects[32,41,42]. Contrary to that, for quasi two-dimensional systems there have been predicted chiral edge modes[43–46] enabling the Majoranas to be delocalised, both in the real and momentum spaces[32]. Evidence for such dispersive Majorana modes have been recently provided by STM measurements for magnetic islands deposited on superconducting substrates[47–50]. Another route to achieve the topological superconductivity and MBS in two-dimensional systems relies on the phase biased planar Josephson junctions, which confine the narrow strip of electron gas subject to the Rashba interaction and magnetic field[51,52].

In general, realisation of the MBS might not be restricted solely to systems with simple geometries[46,53,54], therefore, we propose the setup of *mixed dimensionality*, comprising one-dimensional nanowire coupled to two-dimensional plaquette (Fig. 1). This situation resembles the recently investigated nanostructures, where quasi-one-dimensional wires are attached to larger structures[8]. Here, we study the subgap spectrum of this system, focusing on spatial profiles of the Majorana modes leaking from the nanowire into the adjoined plaquette. We explore the quasiparticle spectra of this setup for representative values of the chemical potentials of both constituents (tunable by electrostatic potentials), which control topological nature of their superconducting phase.

[1]Institute of Physics, M. Curie-Skłodowska University, pl. M. Skłodowskiej-Curie 1, 20-031, Lublin, Poland. [2]Institute of Nuclear Physics, Polish Academy of Sciences, ul. W. E. Radzikowskiego 152, 31-342, Kraków, Poland. Correspondence and requests for materials should be addressed to A.K. (email: akob@kft.umcs.lublin.pl) or T.D. (email: doman@kft.umcs.lublin.pl) or A.P. (email: aptok@mmj.pl)

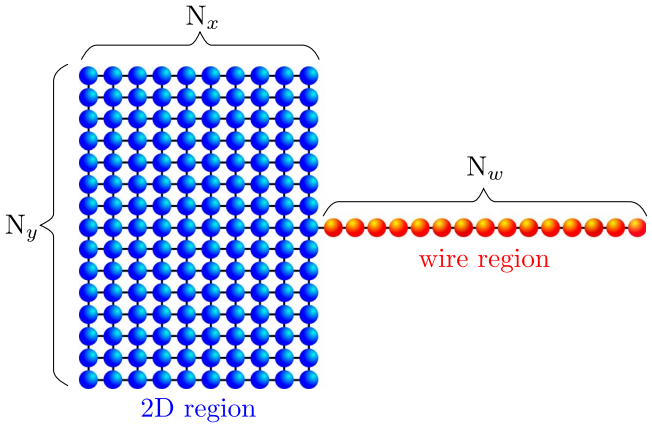

Figure 1. Scheme of the hybrid structure, where a semiconducting Rashba nanowire (comprising N_w sites) is connected to 2D cluster (whose dimensions are $N_x \times N_y$). This system is deposited on a surface of the superconducting substrate.

Our study gives an insight into non–local character of the Majorana quasiparticles. Proposed system can be realized experimentally in form of semiconducting–superconducting nanostrucure[8], while results obtained in this paper can be verified experimentally.

The paper is organised as follows. First we introduce the microscopic model and present computational details. Next, we describe the numerical results obtained for each constituent and for the entire hybrid structure in various topological states. Beyond the scope of numerical calculations, we also described the proposal for experimental verification of out theoretical predictions. Finally, we summarise the results in last section.

Model and Method

The nanostructure shown in Fig. 1 can be modelled by the real space Hamiltonian $\mathcal{H} = \mathcal{H}_{kin} + \mathcal{H}_{sc} + \mathcal{H}_{soc}$. The first term describes the kinetic energy:

$$\mathcal{H}_{kin} = \sum_{ij\sigma}\left\{-t\delta_{\langle i,j\rangle} - (\mu_i + \sigma h)\delta_{ij}\right\}c^{\dagger}_{i\sigma}c_{j\sigma}, \tag{1}$$

where t denotes the hopping integral between nearest-neighbour sites and $c^{\dagger}_{i\sigma}$ ($c_{i\sigma}$) describes creation (annihilation) of electron on i-th site with spin σ. In general, the chemical potential μ_i can be tuned *in-situ* by some external gate voltage. For simplicity, however, we assume it to be constant over the entire 2D plaquette ($\forall_{i\in 2D}\ \mu_i = \mu_{2d}$) and in the 1D nanowire ($\forall_{i\in w}\ \mu_i = \mu_w$). We assume the Zeeman magnetic field h to be parallel along the wire and neglect any orbital effects[55]. The second term

$$\mathcal{H}_{sc} = \Delta\sum_i (c_{i\downarrow}c_{i\uparrow} + c^{\dagger}_{i\uparrow}c^{\dagger}_{i\downarrow}), \tag{2}$$

accounts for the proximity induced on-site pairing, where Δ is the uniform energy gap in the system. The spin–orbit coupling (SOC) is given by[56–59]

$$\mathcal{H}_{soc} = \lambda\sum_{i\sigma\sigma'}(ic^{\dagger}_{i\sigma}\sigma_x^{\sigma\sigma'}c_{i+\hat{y},\sigma'} - ic^{\dagger}_{i\sigma}\sigma_y^{\sigma\sigma'}c_{i+\hat{x},\sigma'} + \text{H. c. }), \tag{3}$$

where σ_i are the Pauli matrices and λ stands for the Rashba potential. Since the nanowire is oriented along $\hat{x}$ axis, only the second part of SOC term survives.

Hamiltonian $\mathcal{H}$ of the hybrid structure can be diagonalised by the Bogoliubov–Valatin transformation[60]

$$c_{i\sigma} = \sum_n (u_{in\sigma}\gamma_n - \sigma v^{*}_{in\sigma}\gamma^{\dagger}_n), \tag{4}$$

where γ_n, $\gamma^{\dagger}_n$ are the new *quasi*-particle fermionic operators and $u_{in\sigma}$, $v_{in\sigma}$ are the corresponding eigenvectors. From this transformation (4) we get the Bogoliubov–de Gennes (BdG) equations

$$\mathcal{E}_n\begin{pmatrix} u_{in\uparrow}\\ v_{in\downarrow}\\ u_{in\downarrow}\\ v_{in\uparrow}\end{pmatrix} = \sum_j \begin{pmatrix} H_{ij\uparrow} & D_{ij} & S^{\uparrow\downarrow}_{ij} & 0\\ D^{*}_{ij} & -H^{*}_{ij\downarrow} & 0 & S^{\downarrow\uparrow}_{ij}\\ S^{\downarrow\uparrow}_{ij} & 0 & H_{ij\downarrow} & D_{ij}\\ 0 & S^{\uparrow\downarrow}_{ij} & D^{*}_{ij} & -H^{*}_{ij\uparrow}\end{pmatrix}\begin{pmatrix} u_{jn\uparrow}\\ v_{jn\downarrow}\\ u_{jn\downarrow}\\ v_{jn\uparrow}\end{pmatrix}, \tag{5}$$

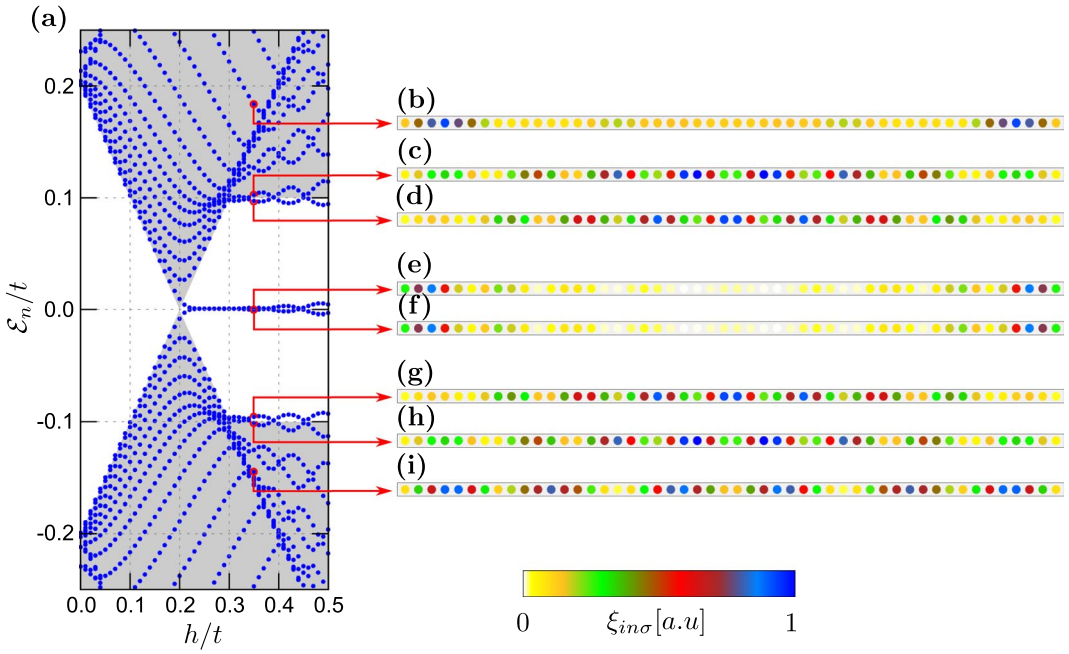

Figure 2. Low energy spectrum of the 1D nanowire (**a**) and the spatially resolved probabilities $\xi_{in} = \sum_\sigma \xi_{in\sigma}$ for the quasiparticle energies $\mathcal{E}_n$ indicated by the red arrows (**b**–**i**). Results are obtained for $N_x = N_y = 0$, $N_w = 50$ and $\mu_w = -2.0t$.

where $H_{ij\sigma} = -t\delta_{\langle i,j\rangle} - (\mu_i + \sigma h)\delta_{ij}$ is the single-particle term, $D_{ij} = \Delta\delta_{ij}$ refers to the superconducting gap, and $S_{ij}^{\sigma\sigma'} = -i\lambda(\sigma_y)_{\sigma\sigma'}\delta_{\langle i,j\rangle}$ is the SOC term (which mixes particles with different spins), where $S_{ij}^{\downarrow\uparrow} = (S_{ji}^{\uparrow\downarrow})^*$ and $S_{ji}^{\uparrow\uparrow} = S_{ij}^{\downarrow\downarrow} = 0$.

From numerical solution of the BdG Eq. (5) we determine the Green's function $\langle\langle c_{i\sigma}|c_{i\sigma}^\dagger\rangle\rangle$ and compute the local density of states (LDOS) defined as $\rho_{i,\sigma}(\omega) = -\frac{1}{\pi}\mathrm{Im}\langle\langle c_{i\sigma}|c_{i\sigma}^\dagger\rangle\rangle$. In the present case we have

$$\rho_{i,\sigma}(\omega) = \sum_n \xi_{in\sigma}[\delta(\omega - \mathcal{E}_n) + \delta(\omega + \mathcal{E}_n)], \tag{6}$$

where the spectral weights

$$\xi_{in\sigma} = |u_{in\sigma}|^2\theta(-\mathcal{E}_n) + |v_{in\sigma}|^2\theta(\mathcal{E}_n) \tag{7}$$

refer to probability of the n-th quasiparticle energy and spin σ to exist at i-th site of the system[61].

Numerical Results

In what follows, we study the hybrid setup consisting of $N = N_x \times N_y + N_w$ sites, which is $N_x \times N_y$ sites of the 2D–plaquette and N_w sites in of 1D–nanowire. For numerical computations we choose $\Delta/t = 0.2$ and $\lambda/t = 0.15$. In presence of the spin-orbit coupling and the Zeeman effect the on-site electron pairing evolves into the inter-site (p–wave) superconducting phase[23,62–64]. Its topological form occurs above the critical magnetic field $h_c = \sqrt{\Delta^2 + (-W \pm \mu)^2}$ [21,22], where W is half of the bandwidth (equal to $2t$ and $4t$ for 1D and 2D system, respectively). Upon increasing the magnetic field h, the superconducting gap closes at h_c and reopens when entering the topological region. Our calculations are done for the finite-size system, therefore the quasiparticle spectra are discretised. As a useful guide-to-eye, in panels (a) of Figs 2–6 we have marked the continuous spectrum of the bulk system by grey colour.

Described system can be experimentally implemented in the form of the semiconducting–superconducting hybrid nanostructure. In such heterostructure the realistic parameters can be estimated as[4,5,65]: superconducting gap $\Delta \simeq 250\,\mu$eV, SOC strength $\lambda \simeq 0.25\,\mathrm{eV}\cdot$Å, and effective mass of electrons $m^* \approx 0.15\,m_e$. Topological phase transition in the nanowire is observed for $h \sim 0.15$ t, when magnetic field starts to exceed Δ. Independently from realistic values of physical quantities, parameter values assumed in our calculations allow for clear exhibition of behavior and physical properties of described system.

Separate components of the system. Here, we briefly describe the quasiparticles for each component of the hybrid structure separately. Let us start with the 1D chain. For $\forall_i\ \mu_w = -2.0t$ and assuming the magnetic field $h = 0.35t$ the nanowire would be in its non–trivial topological state. Figure 2(b)–(i) show the spatial distribution for representative quasiparticle states whose energies are indicted by the arrows. The quasiparticles from outside the topological gap [panels (b)–(d) and (g)–(i)] are spread all over the nanowire, whereas two states residing inside the topological gap [panels (e) and (f) in Fig. 2] are clearly localised near the nanowire ends. Such

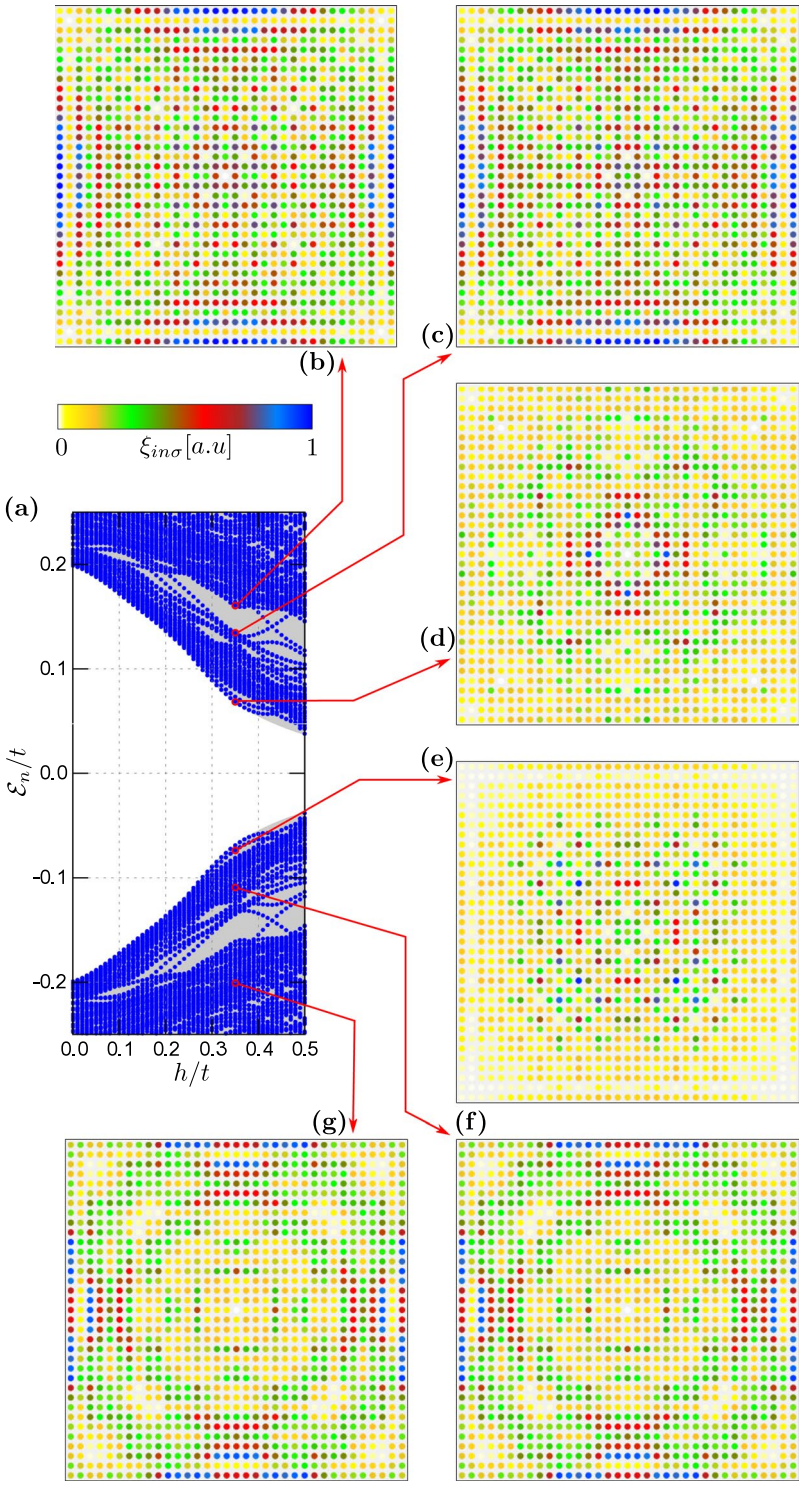

Figure 3. Low energy spectrum of the 2D plaquette obtained in topologically trivial state for $\forall_i\ \mu_i = -2.0t$ (**a**). Panels (b–g) display spatial profiles of the quasiparticle for several eigenvalues $\mathcal{E}_n$. Results are obtained for $h/t = 0.35$, assuming $N_x = N_y = 35$ and $N_w = 0$.

zero-energy quasiparticles exist only in the topological region, above the critical magnetic field $h_c = 0.2t$, and can be identified as the MBS. Let us notice, that quasiparticles at energies $\pm\mathcal{E}_n$ have the same spatial patterns [cf. panels (e) and (f), (d) and (g), or (c) and (h)], due to electron–hole symmetry of the BdG equations.

Let's now focus on properties of the plaquette. Figure 3 shows the spectrum and displays the profiles of selected quasiparticles obtained for $\forall_i\ \mu_i = -2.0t$ when the 2D-region is in a trivial superconducting phase. Under such circumstances, there is no evidence for any in--gap quasiparticles regardless of h. Figure 4 presents

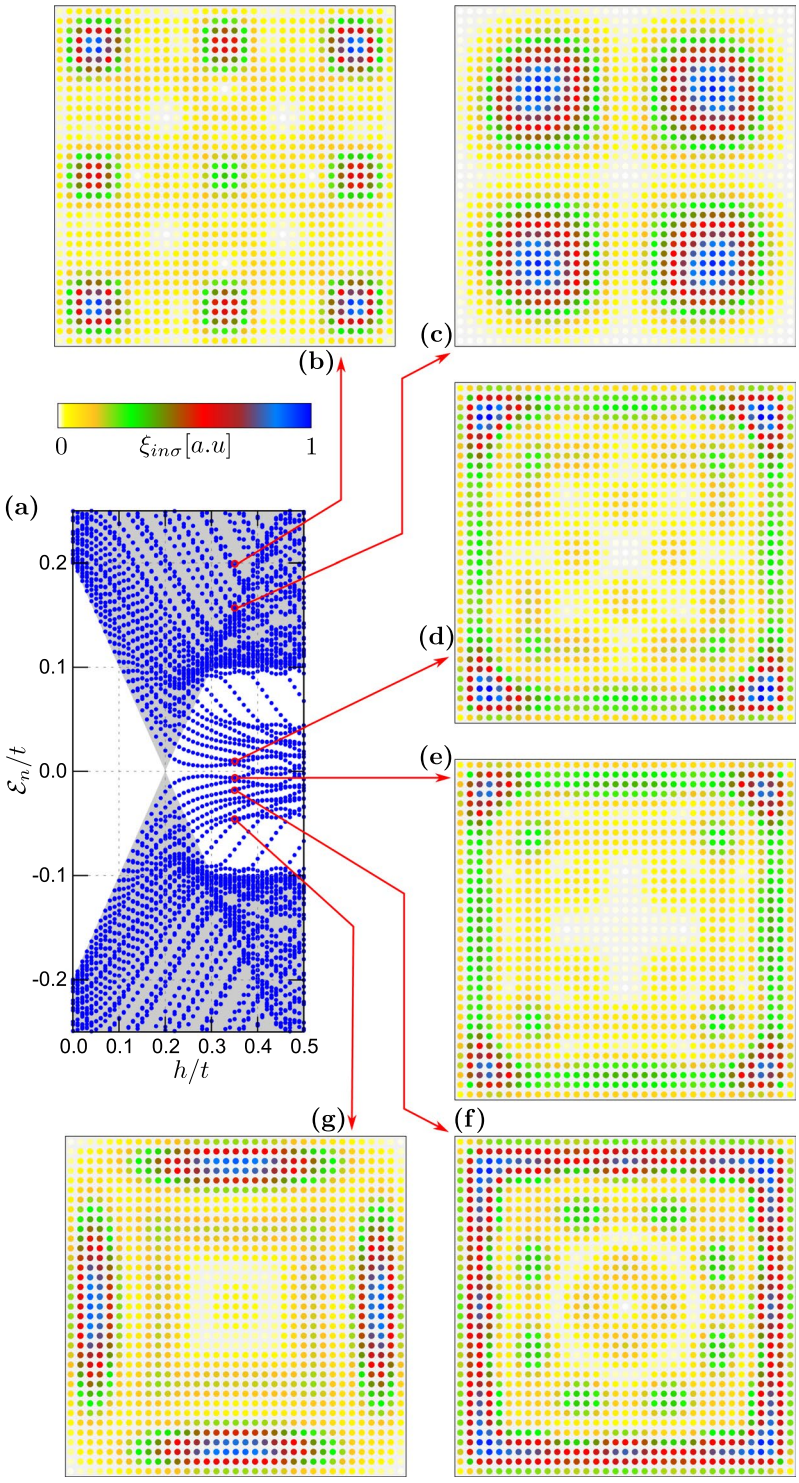

Figure 4. Low energy spectrum of the 2D plaquette obtained in topologically non--trivial state for $\forall_i\ \mu_i = -4.0t$ (**a**). All other model parameters are the same as in Fig. 3.

the results obtained $\forall_i\ \mu_i = -4.0t$, corresponding to the non--trivial superconducting phase. By inspecting the quasiparticles outside the topological gap [panels (b)–(c)] we observe their nearly uniform distribution in the plaquette without clear signatures of any edge phenomena. On the other hand, the quasiparticle states existing inside the topological gap [panels (d)–(g)] reveal a tendency towards their localisation near the sample boundaries[43–46].

It is worth noting, that the in both cases, the transition from trivial to topological phase is associated with closing of the soft-superconducting gap at some critical magnetic field h_c[21–23]. For chosen parameters, in the

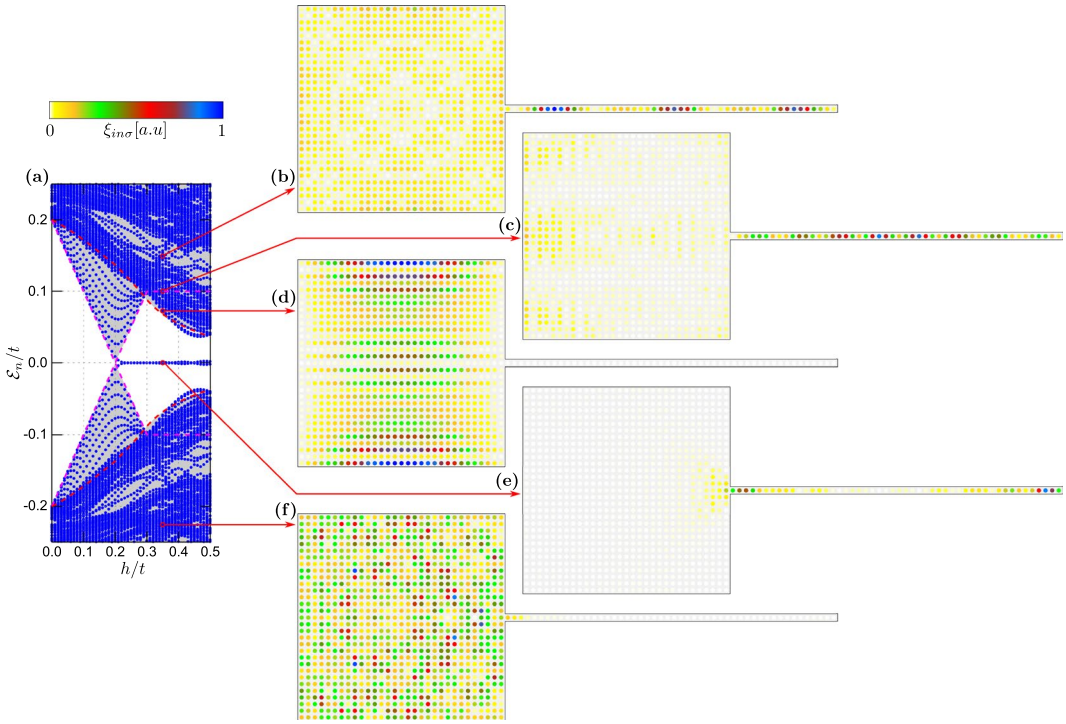

Figure 5. Spectrum of the plaquette–nanowire hybrid system obtained for $N_x = N_y = 31$ and $N_w = 50$, $h = 0.35t$, assuming $\mu_{2D} = \mu_w = -2.0t$. In this case, only the nanowire is in the non--trivial topological superconducting phase.

1D-nanowire (Fig. 2a) and 2D-plaquette (Fig. 4a) these fields are equal and given as $h_c/t \simeq 0.2$. For magnetic field $h > h_c$ new topological gap is reopened. This allows for simultaneous emergence of in--gap states in the both constituents of finite system (with edges).

Appearance of the MBS in the nanowire can be associated with changes of topological $\mathbb{Z}_2$ index[66]. Furthermore, we know that the MBS must always appear in pairs in the nanowires. Contrary to this, in the 2D-plaquette we observe plenty of in–gap states whose energies differ from zero. Strictly speaking, we do not observe the completely localised Majorana states in such 2D systems. This situation changes qualitatively, however, in the plaquette–nanowire hybrid system.

Plaquette-nanowire hybrid. Let us first consider the case, when only part of our hybrid setup is in the topologically non–trivial superconducting phase. This can be realised e.g. for the chemical potential $\mu_{2D} = \mu_w = -2t$ (Fig. 5). For the chosen model parameters, the critical magnetic field of the nanowire is $h_c = 0.2t$. In this case the quasiparticle spectrum shows a collection of levels, originating from the 1D and 2D regions [cf. with Figs 2 and 4]. By increasing the magnetic field the original gap closes at $h = h_c$ and at stronger magnetic fields the nanowire part is in the non–trivial topological phase. In consequence, we observe emergence of just one pair of the nearly–zero–energy bound states originating from the 1D part of our setup [Fig. 5(e)]. One of these quasiparticles is localised at interface with the nanowire region and partly leaks into the 2D plaquette. Other (finite-energy) quasiparticles are distributed either over the plaquette [Fig. 5(d)] or over both regions of the setup [Fig. 5(b,c)].

Below, we describe the results for the system, in which both 1D and 2D regions simultaneously undergo a transition to non–trivial topological phase. This situation can be achieved by fine tuning the site dependent chemical potentials – choosing $\mu_w = -2t$ and $\mu_{2D} = -4t$ yields a transition to topological phase for the entire system at $h_c = 0.2t$. Numerical results for this case are shown in Fig. 6. By inspecting the lowest in--gap states for $h > h_c$ we observe their localisation near the boundaries of the system, i.e. at a free-standing end of the nanowire (right-hand side of the system) and in corners of the plaquette. On the other hand, the states from the electron band regions are nearly uniformly spread over the whole structure [Fig. 6(f)].

It is worth noting that both parts of the system have comparable topological gap. Due to existence of the common topological non--trivial state, all the in--gap states tend to be localised at the sample edges. The quasiparticle state appearing at zero energy is predominantly localised in the right hand end of the wire [Fig. 6(d)], whereas its co-partner (initially localised at the left side of nanowire) partly *leaks* onto the adjoined 2D-region and appears predominantly in the corners of the plaquette. Contrary to the previous case [displayed in Fig. 5(e)] the MBS are strongly delocalised and redistributed. The other finite–energy states appear either near the wire-plaquette boundary [see Fig. 6(c,e)] or at the edges of the plaquette.

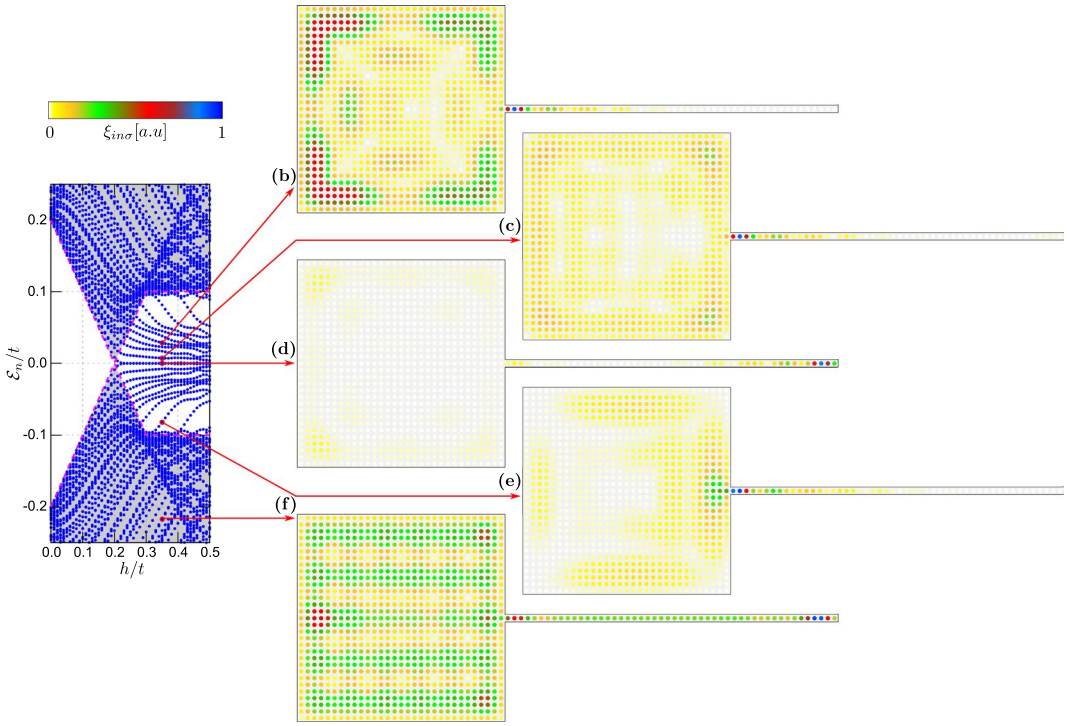

Figure 6. Spectrum of the plaquette–nanowire hybrid system obtained for $N_x = N_y = 31$ and $N_w = 50$, $h = 0.35t$, assuming $\mu_{2D} = -4.0t$ and $\mu_w = -2.0t$, which guarantee that both constituents are in the non–trivial topological phase.

Role of finite size effects. Here, we address influence of the finite-size of our hybrid structure. In Fig. 7 we show the eigenvalues for three different sizes of the system as a function of the chemical potential μ_{2D}. Let us remark, that plaquette is in the non–trivial topological phase for $\mu_{2D}/t - 4.0$. Emergence of the in--gap states is well visible in all cases as can be seen by the horizontal zero-energy lines that correspond to the quasiparticles originating from the nanowire (for which we have fixed the chemical potential at $\mu_w/t = -2$). If a nanowire is very short, the MBS overlap with each other, forming the bonding and anti-bonding states [Fig. 7(a)]. Consequence of such overlapping wavefunctions have been studied by a number of authors[67–69]. In some analogy to this behaviour, also variation of the plaquette size $N_x \times N_y$ can lead to rearrangement of the quasiparticle states, depending on μ_{2D}. In particular, it may reduce a number of the in–gap states which appear near the sample edges.

Nanowire coupled to plaquette's corner. We have also checked numerically, that spatial patterns of the MBS leaking from 1D to 2D parts do not depend strongly on a particular location of the contact point between these constituents. In Fig. 8 we illustrate this effect, considering the hybrid structure where the nanowire is attached to a corner of the plaquette. In this situation the delocalised MBS accumulates near three other corners of the plaquette, yet some of its remnants are still observable at the interface with nanowire. Irrespectively of the particular contact point, MBS is again strongly delocalised [cf. Fig. 6(d)].

Proposal for Empirical Detection

Quasiparticles of the topologically non–trivial superconducting state appearing at zero energy at boundaries of one and two-dimensional parts in our hybrid structure could be experimentally probed by the scanning tunnelling microscopy (STM). Its low-energy and spin-polarised version, relying on the *selective equal–spin Andreev reflection* (SESAR), has been proposed[70] as a unique tool for probing the Majorana quasiparticles manifested by the zero-bias tunnelling conductance. This kind of STM measurements, using ferromagnetic tip, has been already sucessfully used in the study of the Majorana bound states in the monoatomic ferromagnetic chain deposited at the superconducting surface[15].

Let us briefly explain how such SESAR spectroscopy could probe the spatial distribution of the localised and delocalised Majorana quasiparticles in our hybrid structure. Applying voltage V between the conducting STM tip and the superconducting nanowire-plaquette system induces the charge transport of a given spin σ carriers. On microscopic level, electrons arriving from the STM tip would be converted into the inter-site pairs, reflecting holes of the same spin polarisation back to the tip. The resulting current can be expressed by the Landauer–Büttiker formula[71]:

$$I^{\sigma}_{i,i+1}(V) = \frac{e}{h}\int T^{\sigma}_{i,i+1}(\omega)[f(\omega - eV) - f(\omega + eV)]d\omega, \tag{8}$$

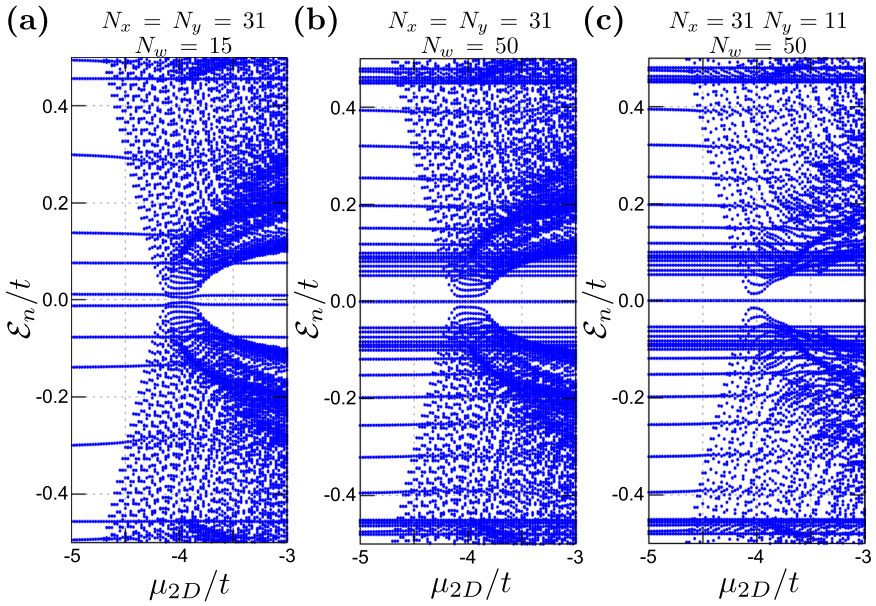

Figure 7. Spectrum of the plaquette–nanowire hybrid as a function of μ_{2D} for various sizes of 1D and 2D components (as indicated) obtained for $h/t = 0.25$ and $\mu_w/t = -2$.

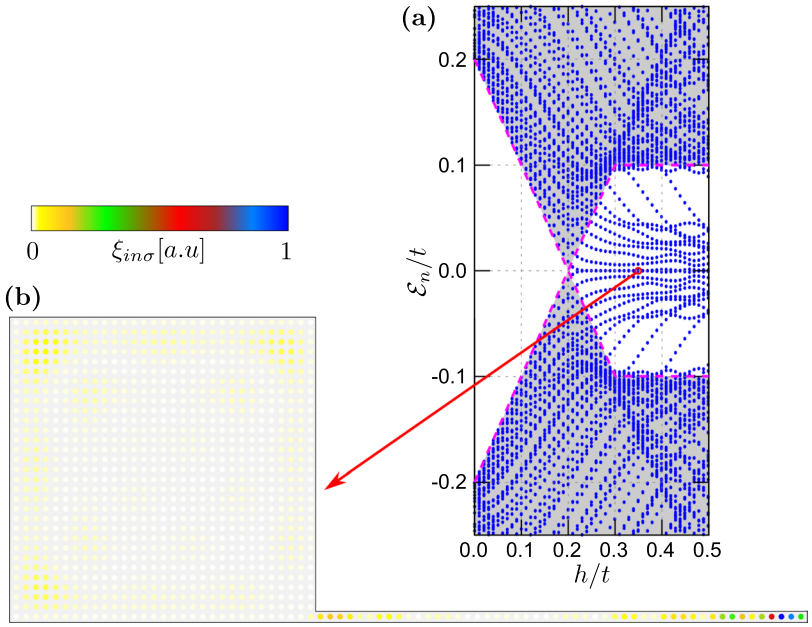

Figure 8. Spectrum of the plaquette–nanowire hybrid obtained for $N_x = N_y = 31$, $N_w = 50$, in the case when the nanowire is connected to the corner of the 2D-region.

where the transmittance for a given pair of the neighbouring sites is $T^{\sigma}_{i,i+1}(\omega) = |\Gamma^{\sigma}_N|^2 |\langle\langle \hat{d}_{i\sigma};\ \hat{d}_{i+1\sigma}\rangle\rangle|^2$ with Γ^{σ}_N denoting the spin-dependent hybridisation between the STM tip and individual sites of our hybrid structure. We assume it to be uniform, which should be reasonable assumption as long as distance between the STM tip and the probed system is kept constant.

At low temperatures the conductance simplifies to

$$G^{\sigma}_{i,i+1}(V) \equiv \frac{d}{dV} I^{\sigma}_{i,i+1}(V) \simeq \frac{2e^2}{h} T^{\sigma}_{i,i+1}(\omega = eV). \tag{9}$$

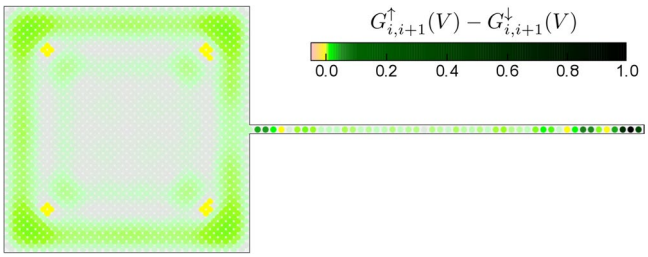

Figure 9. Difference of the zero-bias tunnelling conductance between ↑ and ↓ charge carriers obtained in units of $2e^2/h$, assuming both parts of our hybrid system to be in topologically non–trivial superconducting phase.

Figure 9 shows a difference of the spin polarised conductance $G^{\uparrow}_{i,i+1}(V) - G^{\downarrow}_{i,i+1}(V)$ obtained at zero bias $V = 0$. Transmittance $T^{\sigma}_{i,i+1}(\omega)$ of the SESAR has been computed for all pairs of the neighboring sites, both in the nanowire and in the nanoscopic plaquette using the off-diagonal Green's function determined from the BdG diagonalization procedure. Each point presented at Fig. 9 corresponds to the central place between the neighboring i and $i+1$ sites, both in x and y directions. We clearly see that this polarised zero-bias conductance is strongly enhanced near the localised Majorana mode at the end of nanowire and can also allow for detection of its delocalised partner, whose spectral weight is smeared along the boundaries of 2D-plaquette. Additionally, it should be noted that the magnitude of spin polarised conductance is locally 100 times lower in plaquette than in nanowire.

Other proposal for probing the delocalised mode could be also based on measurements of the edge currents[44,72,73], however we can hardly judge its practical feasability. Such local supercurrents between the topologically trivial and non–trivial parts of the proximitized systems have been also addressed in ref.[74] and several important aspects concerning the topological superconductivity of 2D systems have been discussed in refs[75] and[76].

Summary

We have investigated quasiparticle spectra of the hybrid system, comprising the 1D-nanowire attached to the 2D-plaquette, both proximitized to the s-wave superconductor. Depending on the electron energies in these constituents (which should be tunable by external gate potentials), the spin-orbit interactions along with the magnetic field could induce the topologically non–trivial superconducting phase, either (i) only in the nanowire or (ii) in the entire setup. Selfconsistent numerical determination of the quasiparticle spectra has revealed, that under such circumstances the zero-energy Majorana quasiparticles would be (i) localised near the ends of 1D-nanowire or (ii) one of them would leak into the plaquette region. For the latter case we have inspected the spatial profile of the delocalised Majorana mode and found its signatures distributed along boundaries of the 2D-plaquette, with some preference towards its corners. We have shown that, spatial profiles of both the localised and delocalised Majorana quasiparticles could be probed by the polarised scanning tunnelling measurements, where such quasiparticles would be detectable via the Andreev scattering mechanism.

Proposed hybrid structure (and similar ones) could open new perspectives for studying the topological superconducting phase in complex geometries of mixed dimensionality and might shed an insight into itinerancy of the emerging Majorana modes[46,77]. Furthermore, such delocalisation of the Majorana modes could be practically used for realisation of their braiding by attaching a few nanowires to the plaquette region.

Additional note. Our proposal refers to the semiconductor–superconductor hybrid nanostructure. However, after the initial version of this manuscript has been submitted, similar concept have been proposed in context of the recent experiments concerning the magnetic nanoflakes[77]. This proposal is strongly associated with realization of the zero energy bound state around two dimensional magnetic structure[47,49].

References

1. Santos, A., Deen, M. J. & Marsal, L. F. Low-cost fabrication technologies for nanostructures: state-of-the-art and potential. *Nanotechnology* **26**, 042001, https://doi.org/10.1088/0957-4484/26/4/042001 (2015).
2. Soumyanarayanan, A., Reyren, N., Fert, A. & Panagopoulos, C. Emergent phenomena induced by spin-orbit coupling at surfaces and interfaces. *Nature* **539**, 509, https://doi.org/10.1038/nature19820 (2016).
3. Deng, M. T. *et al.* Anomalous zero-bias conductance peak in a Nb–InSb nanowire–Nb hybrid device. *Nano Lett.* **12**, 6414, https://doi.org/10.1021/nl303758w (2012).
4. Mourik, V. *et al.* Signatures of Majorana fermions in hybrid superconductor-semiconductor nanowire devices. *Science* **336**, 1003, https://doi.org/10.1126/science.1222360 (2012).
5. Das, A. *et al.* Zero-bias peaks and splitting in an Al–InAs nanowire topological superconductor as a signature of Majorana fermions. *Nat. Phys.* **8**, 887, https://doi.org/10.1038/nphys2479 (2012).
6. Finck, A. D. K., Van Harlingen, D. J., Mohseni, P. K., Jung, K. & Li, X. Anomalous modulation of a zero-bias peak in a hybrid nanowire-superconductor device. *Phys. Rev. Lett.* **110**, 126406, https://doi.org/10.1103/PhysRevLett.110.126406 (2013).
7. Deng, M. T. *et al.* Majorana bound state in a coupled quantum-dot hybrid-nanowire system. *Science* **354**, 1557, https://doi.org/10.1126/science.aaf3961 (2016).
8. Nichele, F. *et al.* Scaling of Majorana zero-bias conductance peaks. *Phys. Rev. Lett.* **119**, 136803, https://doi.org/10.1103/PhysRevLett.119.136803 (2017).
9. Lutchyn, R. M. *et al.* Majorana zero modes in superconductor-semiconductor heterostructures. *Nat. Rev. Mater.* **3**, 52, https://doi.org/10.1038/s41578-018-0003-1 (2018).

10. Gül, O. *et al*. Ballistic Majorana nanowire devices. *Nat. Nanotechnol.* **13**, 192, https://doi.org/10.1038/s41565-017-0032-8 (2018).
11. Nadj-Perge, S. *et al*. Observation of Majorana fermions in ferromagnetic atomic chains on a superconductor. *Science* **346**, 602, https://doi.org/10.1126/science.1259327 (2014).
12. Pawlak, R. *et al*. Probing atomic structure and Majorana wavefunctions in mono-atomic Fe chains on superconducting Pb surface. *Npj Quantum Information* **2**, 16035, https://doi.org/10.1038/npjqi.2016.35 (2016).
13. Feldman, B. E. *et al*. High-resolution studies of the Majorana atomic chain platform. *Nat. Phys.* **13**, 286, https://doi.org/10.1038/nphys3947 (2016).
14. Ruby, M., Heinrich, B. W., Peng, Y., von Oppen, F. & Franke, K. J. Exploring a proximity-coupled Co chain on Pb (110) as a possible Majorana platform. *Nano Lett.* **17**, 4473, https://doi.org/10.1021/acs.nanolett.7b01728 (2017).
15. Jeon, S. *et al*. Distinguishing a Majorana zero mode using spin-resolved measurements. *Science* **358**, 772, https://doi.org/10.1126/science.aan3670 (2017).
16. Kim, H. *et al*. Toward tailoring Majorana bound states in artificially constructed magnetic atom chains on elemental superconductors. *Sci. Adv*. **4**, https://doi.org/10.1126/sciadv.aar5251 (2018).
17. Nayak, C., Simon, S. H., Stern, A., Freedman, M. & Das Sarma, S. Non-Abelian anyons and topological quantum computation. *Rev. Mod. Phys.* **80**, 1083, https://doi.org/10.1103/RevModPhys.80.1083 (2008).
18. Aasen, D. *et al*. Milestones toward Majorana-based quantum computing. *Phys. Rev. X* **6**, 031016, https://doi.org/10.1103/PhysRevX.6.031016 (2016).
19. Karzig, T. *et al*. Scalable designs for quasiparticle-poisoning-protected topological quantum computation with Majorana zero modes. *Phys. Rev. B* **95**, 235305, https://doi.org/10.1103/PhysRevB.95.235305 (2017).
20. Klinovaja, J. & Loss, D. Composite Majorana fermion wave functions in nanowires. *Phys. Rev. B* **86**, 085408, https://doi.org/10.1103/PhysRevB.86.085408 (2012).
21. Sato, M. & Fujimoto, S. Topological phases of noncentrosymmetric superconductors: Edge states, Majorana fermions, and non-Abelian statistics. *Phys. Rev. B* **79**, 094504, https://doi.org/10.1103/PhysRevB.79.094504 (2009).
22. Sato, M., Takahashi, Y. & Fujimoto, S. Non-Abelian topological order in *s*-wave superfluids of ultracold fermionic atoms. *Phys. Rev. Lett.* **103**, 020401, https://doi.org/10.1103/PhysRevLett.103.020401 (2009).
23. Sato, M., Takahashi, Y. & Fujimoto, S. Non-Abelian topological orders and Majorana fermions in spin-singlet superconductors. *Phys. Rev. B* **82**, 134521, https://doi.org/10.1103/PhysRevB.82.134521 (2010).
24. Chevallier, D., Sticlet, D., Simon, P. & Bena, C. Mutation of Andreev into Majorana bound states in long superconductor-normal and superconductor-normal-superconductor junctions. *Phys. Rev. B* **85**, 235307, https://doi.org/10.1103/PhysRevB.85.235307 (2012).
25. Chevallier, D., Simon, P. & Bena, C. From Andreev bound states to Majorana fermions in topological wires on superconducting substrates: A story of mutation. *Phys. Rev. B* **88**, 165401, https://doi.org/10.1103/PhysRevB.88.165401 (2013).
26. Vernek, E., Penteado, P. H., Seridonio, A. C. & Egues, J. C. Subtle leakage of a Majorana mode into a quantum dot. *Phys. Rev. B* **89**, 165314, https://doi.org/10.1103/PhysRevB.89.165314 (2014).
27. Liu, C.-X., Sau, J. D., Stanescu, T. D. & Das Sarma, S. Andreev bound states versus Majorana bound states in quantum dot-nanowire-superconductor hybrid structures: Trivial versus topological zero-bias conductance peaks. *Phys. Rev. B* **96**, 075161, https://doi.org/10.1103/PhysRevB.96.075161 (2017).
28. Hoffman, S., Chevallier, D., Loss, D. & Klinovaja, J. Spin-dependent coupling between quantum dots and topological quantum wires. *Phys. Rev. B* **96**, 045440, https://doi.org/10.1103/PhysRevB.96.045440 (2017).
29. Ptok, A., Kobiałka, A. & Domański, T. Controlling the bound states in a quantum–dot hybrid nanowire. *Phys. Rev. B* **96**, 195430, https://doi.org/10.1103/PhysRevB.96.195430 (2017).
30. Chevallier, D., Szumniak, P., Hoffman, S., Loss, D. & Klinovaja, J. Topological phase detection in Rashba nanowires with a quantum dot. *Phys. Rev. B* **97**, 045404, https://doi.org/10.1103/PhysRevB.97.045404 (2018).
31. Stenger, J. P. T., Woods, B. D., Frolov, S. M. & Stanescu, T. D. Control and detection of Majorana bound states in quantum dot arrays. *Phys. Rev. B* **98**, 085407, https://doi.org/10.1103/PhysRevB.98.085407 (2018).
32. Kobiałka, A. & Ptok, A. Electrostatical formation of the Majorana quasiparticles in the quantum dot–nanoring structure. *J. Phys.: Condens. Matter* **31**, 185302, https://doi.org/10.1088/1361-648X/ab03bf (2019).
33. Moore, C., Stanescu, T. D. & Tewari, S. Two-terminal charge tunneling: Disentangling Majorana zero modes from partially separated Andreev bound states in semiconductor-superconductor heterostructures. *Phys. Rev. B* **97**, 165302, https://doi.org/10.1103/PhysRevB.97.165302 (2018).
34. Górski, G., Baranski, J., Weymann, I. & Domanski, T. Interplay between correlations and Majorana mode in proximitized quantum dot. *Sci. Rep.* **8**, 15717, https://doi.org/10.1038/s41598-018-33529-1 (2018).
35. Fleckenstein, C., Domnguez, F., Traverso Ziani, N. & Trauzettel, B. Decaying spectral oscillations in a Majorana wire with finite coherence length. *Phys. Rev. B* **97**, 155425, https://doi.org/10.1103/PhysRevB.97.155425 (2018).
36. Gibertini, M., Taddei, F., Polini, M. & Fazio, R. Local density of states in metal-topological superconductor hybrid systems. *Phys. Rev. B* **85**, 144525, https://doi.org/10.1103/PhysRevB.85.144525 (2012).
37. Guigou, M., Sedlmayr, N., Aguiar-Hualde, J. M. & Bena, C. Signature of a topological phase transition in long sn junctions in the spin-polarized density of states. *EPL* **115**, 47005, https://doi.org/10.1209/0295-5075/115/47005 (2016).
38. Kobiałka, A. & Ptok, A. Leakage of the Majorana quasiparticles in Rashba nanowire deposited on superconducting–normal substrate. *Acta Phys. Pol. A* **135**, 64, https://doi.org/10.12693/APhysPolA.135.64 (2019).
39. Deng, M.-T. *et al*. Nonlocality of Majorana modes in hybrid nanowires. *Phys. Rev. B* **98**, 085125, https://doi.org/10.1103/PhysRevB.98.085125 (2018).
40. Kitaev, A. Y. Unpaired Majorana fermions in quantum wires. *Phys.-Usp.* **44**, 131, https://doi.org/10.1070/1063-7869/44/10S/S29 (2001).
41. Maśka, M. M., Gorczyca-Goraj, A., Tworzydło, J. & Domański, T. Majorana quasiparticles of an inhomogeneous Rashba chain. *Phys. Rev. B* **95**, 045429, https://doi.org/10.1103/PhysRevB.95.045429 (2017).
42. Ptok, A., Cichy, A. & Domański, T. Quantum engineering of Majorana quasiparticles in one-dimensional optical lattices. *J. Phys.: Condens. Matter* **30**, 355602, https://doi.org/10.1088/1361-648X/aad659 (2018).
43. Röntynen, J. & Ojanen, T. Topological superconductivity and high Chern numbers in 2D ferromagnetic Shiba lattices. *Phys. Rev. Lett.* **114**, 236803, https://doi.org/10.1103/PhysRevLett.114.236803 (2015).
44. Björnson, K., Pershoguba, S. S., Balatsky, A. V. & Black-Schaffer, A. M. Spin-polarized edge currents and Majorana fermions in one- and two-dimensional topological superconductors. *Phys. Rev. B* **92**, 214501, https://doi.org/10.1103/PhysRevB.92.214501 (2015).
45. Li, J. *et al*. Two-dimensional chiral topological superconductivity in Shiba lattices. *Nat. Commun.* **7**, 12297, https://doi.org/10.1038/ncomms12297 (2016).
46. Rachel, S., Mascot, E., Cocklin, S., Vojta, M. & Morr, D. K. Quantized charge transport in chiral Majorana edge modes. *Phys. Rev. B* **96**, 205131, https://doi.org/10.1103/PhysRevB.96.205131 (2017).
47. Ménard, G. C. *et al*. Two-dimensional topological superconductivity in Pb/Co/Si(111). *Nat. Commun.* **8**, 2040, https://doi.org/10.1038/s41467-017-02192-x (2017).
48. He, Q. L. *et al*. Chiral Majorana fermion modes in a quantum anomalous Hall insulator–superconductor structure. *Science* **357**, 294, https://doi.org/10.1126/science.aag2792 (2017).
49. Palacio-Morales, A. *et al*. Atomic-scale interface engineering of Majorana edge modes in a 2D magnet-superconductor hybrid system. arXiv:1809.04503 (2018).

50. Ménard, G. C. *et al*. Isolated pairs of Majorana zero modes in a disordered superconducting lead monolayer. *Nature Commun.* **10**, 2587, https://doi.org/10.1038/s41467-019-10397-5 (2019).
51. Fornieri, A. *et al*. Evidence of topological superconductivity in planar Josephson junctions. *Nature* **569**, 89, https://doi.org/10.1038/s41586-019-1068-8 (2019).
52. Ren, H. *et al*. Topological superconductivity in a phase-controlled Josephson junction. *Nature* **569**, 93, https://doi.org/10.1038/s41586-019-1148-9 (2019).
53. Björnson, K. & Black-Schaffer, A. M. Majorana fermions at odd junctions in a wire network of ferromagnetic impurities. *Phys. Rev. B* **94**, 100501, https://doi.org/10.1103/PhysRevB.94.100501 (2016).
54. Stanescu, T. D. & Das Sarma, S. Building topological quantum circuits: Majorana nanowire junctions. *Phys. Rev. B* **97**, 045410, https://doi.org/10.1103/PhysRevB.97.045410 (2018).
55. Kiczek, B. & Ptok, A. Influence of the orbital effects on the Majorana quasi -particles in a nanowire. *J. Phys.: Condens. Matter* **29**, 495301, https://doi.org/10.1088/1361-648X/aa93ab (2017).
56. Li, Z., Covaci, L., Berciu, M., Baillie, D. & Marsiglio, F. Impact of spin-orbit coupling on the Holstein polaron. *Phys. Rev. B* **83**, 195104, https://doi.org/10.1103/PhysRevB.83.195104 (2011).
57. Li, Z., Covaci, L. & Marsiglio, F. Impact of dresselhaus versus Rashba spin-orbit coupling on the Holstein polaron. *Phys. Rev. B* **85**, 205112, https://doi.org/10.1103/PhysRevB.85.205112 (2012).
58. Smith, E. D. B., Tanaka, K. & Nagai, Y. Manifestation of chirality in the vortex lattice in a two-dimensional topological superconductor. *Phys. Rev. B* **94**, 064515, https://doi.org/10.1103/PhysRevB.94.064515 (2016).
59. Goertzen, S. L., Tanaka, K. & Nagai, Y. Self-consistent study of Abelian and non-Abelian order in a two-dimensional topological superconductor. *Phys. Rev. B* **95**, 064509, https://doi.org/10.1103/PhysRevB.95.064509 (2017).
60. de Gennes, P. G. *Superconductivity of metals and alloys* (Addison-Wesley, 1989).
61. Głodzik, S. & Ptok, A. Bound states induced by the ferromagnetic dimer in a triangular lattice. *Acta Phys. Pol. A* **135**, 60, https://doi.org/10.12693/APhysPolA.135.60 (2019).
62. Zhang, C., Tewari, S., Lutchyn, R. M. & Das Sarma, S. $p_x + ip_y$ superfluid from *s*-wave interactions of fermionic cold atoms. *Phys. Rev. Lett.* **101**, 160401, https://doi.org/10.1103/PhysRevLett.101.160401 (2008).
63. Seo, K., Han, L. & Sá de Melo, C. A. R. Topological phase transitions in ultracold Fermi superfluids: The evolution from Bardeen-Cooper-Schrieffer to Bose-Einstein-condensate superfluids under artificial spin-orbit fields. *Phys. Rev. A* **85**, 033601, https://doi.org/10.1103/PhysRevA.85.033601 (2012).
64. Ptok, A., Rodrguez, K. & Kapcia, K. J. Superconducting monolayer deposited on substrate: Effects of the spin-orbit coupling induced by proximity effects. *Phys. Rev. Materials* **2**, 024801, https://doi.org/10.1103/PhysRevMaterials.2.024801 (2018).
65. Rokhinson, L. P., Liu, X. & Furdyna, J. K. The fractional a.c. Josephson effect in a semiconductor-superconductor nanowire as a signature of Majorana particles. *Nat. Phys.* **8**, 795, https://doi.org/10.1038/nphys2429 (2012).
66. Kane, C. L. & Mele, E. J. Z_2 topological order and the quantum spin Hall effect. *Phys. Rev. Lett.* **95**, 146802, https://doi.org/10.1103/PhysRevLett.95.146802 (2005).
67. Ben-Shach, G. *et al*. Detecting Majorana modes in one-dimensional wires by charge sensing. *Phys. Rev. B* **91**, 045403, https://doi.org/10.1103/PhysRevB.91.045403 (2015).
68. Escribano, S. D., Yeyati, A. L. & Prada, E. Interaction-induced zero-energy pinning and quantum dot formation in Majorana nanowires. *Beilstein J. Nanotechnol.* **9**, 2171, https://doi.org/10.3762/bjnano.9.203 (2018).
69. Peñaranda, F., Aguado, R., San-Jose, P. & Prada, E. Quantifying wave-function overlaps in inhomogeneous majorana nanowires. *Phys. Rev. B* **98**, 235406, https://doi.org/10.1103/PhysRevB.98.235406 (2018).
70. He, J. J., Ng, T. K., Lee, P. A. & Law, K. T. Selective equal-spin Andreev reflections induced by Majorana fermions. *Phys. Rev. Lett.* **112**, 037001, https://doi.org/10.1103/PhysRevLett.112.037001 (2014).
71. Maśka, M. M. & Domański, T. Polarization of the Majorana quasiparticles in the Rashba chain. *Sci. Rep.* **7**, 16193, https://doi.org/10.1038/s41598-017-16323-3 (2017).
72. Pershoguba, S. S., Björnson, K., Black-Schaffer, A. M. & Balatsky, A. V. Currents induced by magnetic impurities in superconductors with spin-orbit coupling. *Phys. Rev. Lett.* **115**, 116602, https://doi.org/10.1103/PhysRevLett.115.116602 (2015).
73. Mohanta, N., Kampf, A. P. & Kopp, T. Supercurrent as a probe for topological superconductivity in magnetic adatom chains. *Phys. Rev. B* **97**, 214507, https://doi.org/10.1103/PhysRevB.97.214507 (2018).
74. Cayao, J. & Black-Schaffer, A. M. Finite length effect on supercurrents between trivial and topological superconductors. *Eur. Phys. J. Spec. Top.*, https://doi.org/10.1140/epjst/e2018-800101-0 (2018).
75. Sedlmayr, N., Aguiar-Hualde, J. M. & Bena, C. Majorana bound states in open quasi-one-dimensional and two-dimensional systems with transverse Rashba coupling. *Phys. Rev. B* **93**, 155425, https://doi.org/10.1103/PhysRevB.93.155425 (2016).
76. Potter, A. C. & Lee, P. A. Multichannel generalization of Kitaev's Majorana end states and a practical route to realize them in thin films. *Phys. Rev. Lett.* **105**, 227003, https://doi.org/10.1103/PhysRevLett.105.227003 (2010).
77. Mascot, E., Cocklin, S., Rachel, S. & Morr, D. K. Quantum engineering of Majorana fermions. arXiv:1811.06664 (2018).

Acknowledgements

We thank N. Sedlmayr for useful remarks. A.P. is grateful to Laboratoire de Physique des Solides (CNRS, Université Paris-Sud) for hospitality during a part of the work on this project. This projects is supported by the National Science Centre (NCN, Poland) under grants UMO-2017/27/B/ST3/01911 (A.K.), UMO-2018/29/B/ST3/00937 (T.D.), and UMO-2017/25/B/ST3/02586 (A.P.).

Author Contributions

A.P. initialized and coordinated the project. A.P. and A.K. contributed equally to posing the problem, the Bogoliubov–de Gennes approach and the numerical calculations. T.D. described the application of SESAR technique and interpreted the results of it. A.K. performed numerical calculations for the SESAR technique. All authors consulted the results. A.P. and A.K. prepared the first version of the paper. All authors contributed to its final form.

Additional Information

Competing Interests: The authors declare no competing interests.

Publisher's note: Springer Nature remains neutral with regard to jurisdictional claims in published maps and institutional affiliations.

4.2.4 Majorana Bound State Leakage to Impurity in Su–Schrieffer–Heeger–Rashba Scenario

A. Kobiałka, A. Ptok, Acta Phys. Pol. A **138**, 673 (2020)

In this paper, we extend our discussion of SSH model within Rashba nanowire by introducing a quantum dot coupled to the nanowire. We find that both topological branches present in the system, a typical and a dimerized one, differ in the sign of asymmetry of spin polarization. Such difference is a result of different starting order of bands before the inversion which signifies the transition to nontrivial state. Moreover, the existence of quantum dot allows for MBS leakage which is in this case influenced by ABS emergence. This behaviour depends on the topological state of the system and can be observed as *pinning* of zero energy states to the quantum dot. Such states imitating MBS can be distinguished from true MBS if both ends of nanowire are probed.

Author's contribution: Research idea, preparation of numerical and analytical calculations, preparation of figures, analysis and discussion of obtained results, preparation of manuscript, participation in preparing the response for Referees.

Proceedings of the 19th National Conference on Superconductivity, Bronisławów, Poland, October 6–11, 2019

Majorana Bound State Leakage to Impurity in Su–Schrieffer–Heeger–Rashba Scenario

A. Kobiałka[a,*] and A. Ptok[b]

[a] *Institute of Physics, Maria Curie-Skłodowska University, Pl. M. Skłodowskiej-Curie 1, 20-031 Lublin, Poland*
[b] *Institute of Nuclear Physics, Polish Academy of Sciences, W.E. Radzikowskiego 152, 31-342 Kraków, Poland*

Doi: 10.12693/APhysPolA.138.673 *e-mail: akob@kft.umcs.lublin.pl

We show the anomalous features of the Majorana bound state leakage in the situation where topological Rashba nanowire is dimerized according to the Su–Schrieffer–Heeger scenario and an impurity is present at one of the ends of the system. We find that two topological branches: the usual, indigenous to the Rashba nanowire, and the dimerized one, existing as a result of the Su–Schrieffer–Heeger dimerization of the nanowire, have different asymmetry of spin polarization that can be explained by the opposite order of bands taking part in topological transitions. Additionally, the introduction of an impurity to the dimerized nanowire influences the leakage of the Majorana bound states into the trivial impurity due to the emergence of the Andreev bound states that behave differently depending on whether the system is or is not in a topological phase. This results in the pinning of zero energy states to the impurity site for some range of parameters.

topics: Su–Schrieffer–Heeger, SSH, Rashba nanowire, Majorana bound states

1. Introduction

Systems exhibiting an existence of the Majorana bound states (MBS) are very promising for the emergence of a new branch of quantum computing — topological quantum computing, relying on topological superconductors. Quantum computing is a steadily growing field of both physics and nanotechnology, however, a working example of its topological counterpart is still yet to be presented. A presumed advantage of topological quantum computing over a "regular" one is the property of fault-tolerant computing [1]. In order to achieve this, non-Abelian quasiparticles [2] have to be employed, hence the interest in MBS which are believed to possess such properties [3].

Recently, such quasiparticles have been experimentally uncovered in numerous examples, both in one-dimensional (1D) systems (e.g., in the form of zero-energy bound states localized at the ends of nanowires deposited upon a surface due to interplay between spin–orbit coupling, superconductivity and magnetic field) [4–15] or two-dimensional (2D) systems (e.g., edge states around a superconducting island) [16–18].

Dimerization alone can allow for a topological transition, even if a superconductor is not present in the system [19]. For instance, in the Su–Schrieffer–Heeger (SSH) model [19, 20], two different bonds between atoms are assumed which makes the atoms dimerize due to the Peierls instability. This phenomenon generated some interest but mainly the combination of the Kitaev [2] and SSH models [21–27] was used. Therefore, we combine the aforementioned SSH dimerization with the Rashba nanowire properties in order to obtain a Su–Schrieffer–Heeger–Rashba (SSHR) model.

MBS, as the edge phenomena, tend to leak to the furthest elements of the system, even if those parts (e.g., impurity) do not manifest any topologically non-trivial nature [28–31]. At this point, we check how the leakage of MBS behaves when impurity is attached to the end of the dimerized Rashba nanowire, within the SSH scenario (see Fig. 1), depending on the order of the bond strength and thus the type of the bond between the last two sites in the system.

This paper is organized as follows: in Sect. 2 the SSH model of the dimerized Rashba nanowire and methods is introduced, in Sect. 3 results obtained by numerical calculation are discussed and in Sect. 4 the results are summerized.

2. Methodology

We consider an SSH analogue of the Rashba nanowire, where the 1D semiconducting nanowire which is deposited on a superconducting substrate (Fig. 1) is modified with an alternating order of weak and strong bonds (or vice versa) that emulate

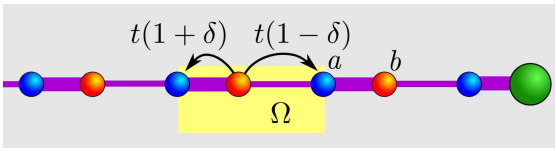

Fig. 1. Schematics of the dimerized nanowire proximitized to the isotropic superconductor. Modulation of the hopping integral δ corresponds to the shifts in positions between the neighboring a and b sites in the unit cell Ω (marked by the yellow frame). Sites on selected sublattices a and b are marked by blue and red colors, respectively, while green corresponds to an additional impurity site connected to the end of the nanowire.

an SSH scenario. We model the distance between the neighboring sites a, b (forming the unit cell Ω) by the modulation δ of the hopping integral that effectively changes the probability of electron transport between the neighboring sites. Similar modulations also affect the spin–orbit Rashba interactions. In a natural way, the SSH model describes a system with two sublattices (sites of a- and b-type).

2.1. Microscopic model

Our system can be described by the Hamiltonian $\mathcal{H} = \mathcal{H}_0 + \mathcal{H}_{\rm so} + \mathcal{H}_{\rm prox}$. The first term

$$\mathcal{H}_0 = -\sum_{i\sigma}\left[t(1+\delta)c^\dagger_{ia\sigma}c_{ib\sigma} + t(1-\delta)c^\dagger_{ia\sigma}c_{i-1b\sigma} + \text{h.c.}\right] - \sum_{s\in\Omega}\sum_{i,\sigma}(\mu+\sigma h)\,c^\dagger_{is\sigma}c_{is\sigma}, \tag{1}$$

describes an SSH-like nanowire. The operator $c^\dagger_{is\sigma}$ ($c_{is\sigma}$) denotes the creation (annihilation) of the electron with spin σ in i-th unit cell and sublattice s (e.g., site a or b), μ is the chemical potential, h denotes the magnetic field in the Zeeman form and $(1 \pm \delta)$ is a periodic variation of hopping integral t between the nearest neighboring sites, i.e., between sites in different sublattices. We also assume similar modulation for the spin–orbit Rashba interaction term

$$\mathcal{H}_{\rm so} = -i\sum_{i\sigma\sigma'}\Big[\lambda(1+\delta)c^\dagger_{ia\sigma}(\sigma_y)_{\sigma\sigma'}c_{ib\sigma'} + \lambda(1-\delta)c^\dagger_{ia\sigma}(\sigma_y)_{\sigma\sigma'}c_{i-1b\sigma'}\Big] + h.c., \tag{2}$$

where σ_y is the second Pauli matrix and λ describes the strength of the spin–orbit coupling. The last term models a BCS-like superconducting gap that arises from the proximity effect, i.e., the deposition of a nanowire on a superconducting surface [32]:

$$\mathcal{H}_{\rm prox} = \sum_{is}\left(\Delta c^\dagger_{is\uparrow}c^\dagger_{is\downarrow} + \Delta^* c_{is\downarrow}c_{is\uparrow}\right). \tag{3}$$

Impurity is treated as an additional site connected to the nanowire that is not affected by the proximity effect $\Delta_{\rm imp} = 0$.

In a typical situation of a homogeneous nanowire, the transition from the trivial to non-trivial topological phase occurs for some critical value of magnetic field [33–35]:

$$h_c^2 = (2t-\mu)^2 + |\Delta|^2. \tag{4}$$

With the increase of magnetic field, the quasiparticle spectrum closes and reopens as a new topologically non-trivial gap at $h = h_c$ [36]. In the case of the dimerized SSH nanowire, the emergence of a non-trivial phase depends on the existence of additional parameters (e.g., λ and δ). Then, the value of h_c depends on model parameters in a non-trivial manner and can be determined analytically (more details can be found in [37]) but still, in the limit of $\delta \to 0$, the condition (4) remains unchanged.

2.2. Formalism

The model Hamiltonian $\mathcal{H}$ can be numerically diagonalized by the Bogoliubov–Valatin transformation [38]:

$$c_{is\sigma} = \sum_n\left(u_{isn\sigma}\gamma_n - \sigma v^*_{isn\bar\sigma}\gamma^\dagger_n\right), \tag{5}$$

where γ_n and $\gamma^\dagger_n$ are the "new" quasiparticle fermionic operators. This transformation yields the Bogoliubov–de Gennes equations, i.e., $\mathcal{E}_n\Psi_{isn} = \sum_{js'}\mathbb{H}_{is,js'}\Psi_{js'n}$, where the Hamiltonian $\mathbb{H}_{is,js'}$ is given in the matrix form as

$$\mathbb{H}_{is,js'} = \begin{pmatrix} H_{is,js',\uparrow} & D_{is,js'} & S^{\uparrow\downarrow}_{is,js'} & 0 \\ D^*_{is,js'} & -H^*_{is,js',\downarrow} & 0 & S^{\downarrow\uparrow}_{is,js'} \\ S^{\downarrow\uparrow}_{is,js'} & 0 & H_{is,js',\downarrow} & D_{is,js'} \\ 0 & S^{\uparrow\downarrow}_{is,js'} & D^*_{is,js'} & -H^*_{is,js',\uparrow} \end{pmatrix} \tag{6}$$

while eigenvector

$$\Psi_{isn} = (u_{isn\uparrow}, v_{isn\downarrow}, u_{isn\downarrow}, v_{isn\uparrow})^T. \tag{7}$$

The matrix block elements (taking into account both sublattices) are given here by

$$H_{is,js',\sigma} = -t(1+\delta)\delta_{ij}\delta_{\langle ss'\rangle} - t(1-\delta)\delta_{i-1,j}\delta_{\langle s,s'\rangle} - (\mu+\sigma h)\delta_{ij}\delta_{ss'}. \tag{8}$$

In turn, the on-site superconducting gap is denoted as $D_{is,js'} = \Delta\delta_{ij}\delta_{ss'}$, while

$$S^{\sigma\sigma'}_{is,js'} = -\mathrm{i}\lambda(\sigma_y)_{\sigma\sigma'} \times\left[(1+\delta)\,\delta_{ij}\delta_{\langle ss'\rangle} - (1-\delta)\,\delta_{i-1,j}\delta_{\langle ss'\rangle}\right] \tag{9}$$

stands for the spin–orbit Rashba term. Now, we must keep in mind that the indexes i and s change values over a number of unit cells and sublattice indexes, respectively. From this, $\mathbb{H}_{is,js'}$ is a square matrix with the size of $4\mathcal{N}\times 4\mathcal{N}$, where $\mathcal{N}$ denotes a number of sites in the system. In the absence of impurity, $\mathcal{N}$ is equal to the double of cells number N_Ω.

From the solution of the BdG equations, we can determine the spin-resolved local density of states

(LDOS) $\rho_{is\sigma}(\omega) = -\frac{1}{\pi}\mathrm{Im}\langle\langle c_{is\sigma}|c^{\dagger}_{is\sigma}\rangle\rangle$ which can be expressed as [39]:

$$\rho_{is\sigma}(\omega) = \sum_n |u_{isn\sigma}|^2\delta\left(\omega - \mathcal{E}_n\right) + |v_{isn\sigma}|^2\delta\left(\omega + \mathcal{E}_n\right) \quad (10)$$

Also, the spin polarization asymmetry (SPA) of LDOS

$$\delta\rho_{is}(\omega) = \rho_{is\uparrow}(\omega) - \rho_{is\downarrow(\omega)} \quad (11)$$

can give additional information, e.g., about spin polarization of the bound state [40]. In numerical calculations, we replace the Dirac delta function by Lorentzian $\delta(\omega) = \zeta/[\pi(\omega^2 + \zeta^2)]$ with a small broadening $\zeta/t = 0.001$.

Total LDOS $\rho_{is\uparrow}(\omega) + \rho_{is\downarrow}(\omega)$ in a low temperature limit gives information about the differential conductance $G(\omega)$ [41–43]. Similarly, SPA LDOS $\delta\rho_{is}$ can give information about spin polarization of the bound states. Both quantities can be measured in a relatively simple way by using a scanning tunneling microscope (STM) [44–46]. Experiments with a magnetic tip give information about the magnetic structure of the bound states in atomic scale [47–49]. From the theoretical point of view, previous studies in spinfull models have shown that MBS have spin polarization [28, 29, 40, 50]. From this, an existence of topological bound states can be probed via the previously mentioned spin-polarized STM measurements [44–46] (which has been done, e.g., in ferromagnetic atom chains [10, 11]). This type of measurements can be useful in distinguishing between the ordinary Andreev bound states (ABS) and topological MBS in hybrid nanostructures [51].

A similar analysis of the system can be performed in the momentum space (more details are given in [37]). The studies are based on the spin-resolved spectral function

$$\mathcal{A}_{\boldsymbol{k}\sigma}(\omega) = -\frac{1}{\pi}\mathrm{Im}\langle\langle c_{\boldsymbol{k}\sigma}|c^{\dagger}_{\boldsymbol{k}\sigma}\rangle\rangle, \quad (12)$$

from which the band structure and its SPA $\delta\mathcal{A}_{\boldsymbol{k}}(\omega) = \mathcal{A}_{\boldsymbol{k}\uparrow}(\omega) - \mathcal{A}_{\boldsymbol{k}\downarrow}(\omega)$ can be found [52]. Similarly to LDOS, these quantities can be measured via the angle-resolved photoemission spectroscopy (ARPES) technique [53], even in nanostructures [54]. The existence of the topological phase in the system leads to the observation of the band inversion, clearly visible in the spin polarization of bands. This is typical not only of the case of the topological insulator [52, 55] but also of other systems in which the topological phase emerges [29, 56, 57].

3. Numerical results

In this section, we discuss the leakage of MBS to the impurity within the dimerized SSH nanowire. As for the parameters used in calculation, we took a nanowire composed of $N_\Omega = 100$ cells, i.e., $\mathcal{N} = 200$ sites and an additional impurity being the 201st site (unless stated otherwise). An alternating order of bonds is preserved in the junction between the nanowire and impurity. Nanowire is characterized by $\Delta/t = 0.2$ and $\lambda/t = 0.15$. Any change in chemical potential μ affects the entire system, both the nanowire and impurity. At this point, it should be mentioned that the described results do not depend on the size of the nanowire. Additionally, throughout the entire paper, we take $h = 0.3t > h_c$ which ensures that the homogeneous system is in the non-trivial phase. If not stated differently, when the nanowire has an odd number of sites, it begins with a weak $(1-\delta)t$ bond and ends with a strong $(1+\delta)t$ bond.

The existence of hopping modulation has a negative impact on the usual non-trivial phase. However, for the dimerization-dependent branch it is essential for its existence. Let us start with discussing the influence of the impurity on the Rashba nanowire.

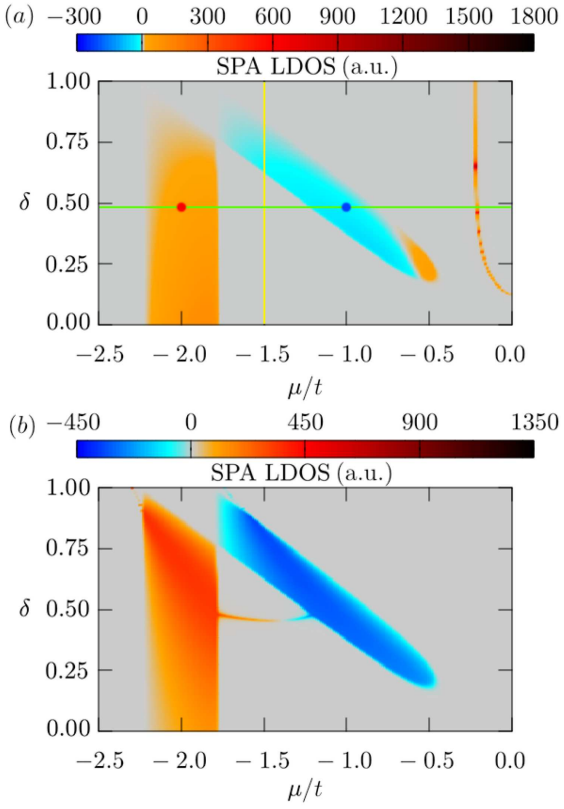

Fig. 2. SPA LDOS for zero energy μ–δ phase space of the first site (a) of the system and impurity site (b). The first site is connected to the rest of the nanowire with a weak bond, while the impurity site is connected by a strong bond. In the case of (b), the impurity is connected with a strong bond, which allows for forming of the bridge-like structure. Eigenvalues for parameters along the green and yellow lines at (a) are shown in Fig. 3. Red and blue dots correspond to SPA $\delta\mathcal{A}_{\boldsymbol{k}}(\omega)$ for different topological phases (cf. Fig. 5a and 5b respectively). Results for the system with $\mathcal{N} = 201$ sites and $h/t = 0.3$.

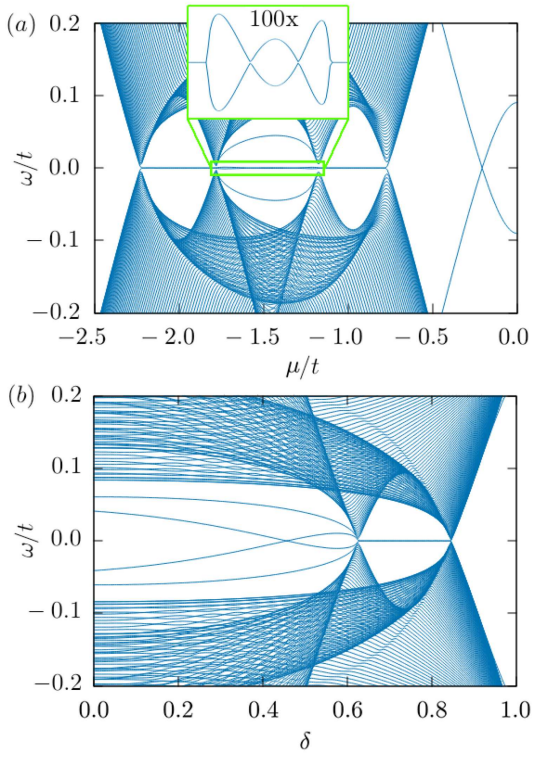

Fig. 3. Spectrum of the system for fixed $\delta = 0.46$ (a) and $\mu/t = -1.5$ (b) which corresponds to the green horizontal and yellow vertical lines in Fig. 2a, respectively. Results in the absence of impurity are presented in Fig. 8 in [37].

In Fig. 2, we show a color map of SPA LDOS for $\omega = 0$ as a function of the chemical potential μ and hopping modulation δ. The nanowire is in the presence of the impurity which is connected to the system with a strong bond $(1 + \delta)$. In Fig. 2, regions centered around $\mu = 2t$ (near the bottom of the band) show parameters of the system which allow for hosting of MBS in the system. This range of parameters, where the non-trivial phase exists, can be associated with a typical limit in the homogeneous system [33–35]. Additional modulation of hopping introduced by δ does not change the topological character of the system in $\delta \to 0$. However, bond modulation creates an additional topological branch which allows for the existence of MBS in a broader range of parameters, in accordance with (4). This additional dimerized branch incorporates regions within the band where for some range of modulation of hopping integrals a non-trivial phase appears in which MBS can emerge. The abrupt change of SPA of the system between two branches of a topological phase can be explained by the reordering of bands that takes place with each band closure at the moment of a topological transition [58]. When the bands close at the transition from a topologically non-trivial to a trivial state $\mu \simeq 1.8t$, they reopen in the opposite order during the transition to a non-trivial state (within a dimerized topological branch) [58]. Due to the interplay between the magnetic field and SOC, the change of spin polarization occurs. In Fig. 2a, we can see a phase space for the first site of the nanowire, linked to the main part of the nanowire with a weak bond $(1 - \delta)$. This allows for visualization of a characteristic feature for the investigated system, a parabola at $\mu/t \in (-0.22, 0.22)$ (as plots are μ-symmetric) which is a manifestation of states of the first site of the nanowire, crossing at zero energy. Another distinctive feature is shown in Fig. 2b, where we can see a SPA LDOS space for the impurity (being the last site of the nanowire) which is linked to the main part of the nanowire with a strong bond $(1 + \delta)$.

The existence of bridge-like features can be understood from the analysis of the system spectrum presented in Fig. 3. There, a bridge-like feature emerges due to the existence of ABS, connecting separate topological phases. It is the result of crossing the Fermi level by the eigenvalues of states associated with the existence of impurity, coupled to the nanowire by a strong bond. There is no analogue of strong bond feature for the last site when it is not an impurity. In Fig. 3a, we can see eigenvalues for $\delta = 0.46$ (green line in Fig. 2a), crossing the bridge-like structure. Here, the two zero energy Majorana states are separated by a trivial bow tie-like ABS feature (inset). These in-gap states are also clearly visible in the SPA LDOS analyses and are strongly associated with the localization of ABS from one site of the nanowire — near the impurity, as seen in Fig. 4. As it may be observed, this structure is in fact a manifestation of zero energy crossing of ABS. Similar behavior can be observed in the case of the spectrum of the system from $\mu/t = -1.5$ (yellow line in Fig. 2a), shown in Fig. 3b.

In contrast to MBS in an isotropic chain ($\delta = 0$), in our results SPA LDOS of MBS have the opposite value in a different part of the phase space (Fig. 2). This behavior is strongly associated with the influence of δ on the band structure and its spin polarization (Fig. 5). The exact analysis of the band structure where MBS exist [29] shows that the Majorana quasiparticle inherits spin polarization of bands nearest the zero energy, i.e., the Fermi level. Here, from studying the band structure, we can observe that MBS in the main branch have a typical spin polarization $\uparrow$ (Fig. 5a). In this case, the emergence of the topological phase is associated with the band inversion around $k = 0$. On the contrary, SPA of MBS in dimerization-dependent branch is $\downarrow$, namely the opposite. This is a consequence of the band inversion of the nearly fully filled bands around $k = \pi$ point (Fig. 5b). Summarizing, in our case SPA LDOS yielded unexpected results if compared to the aforementioned results.

The crossing point shows accidental nature of a bridge-like feature of zero energy ABS. Thanks to this, it is certain that the region connecting two topological branches does not hold MBS, as this would result not only in a zero energy state typical

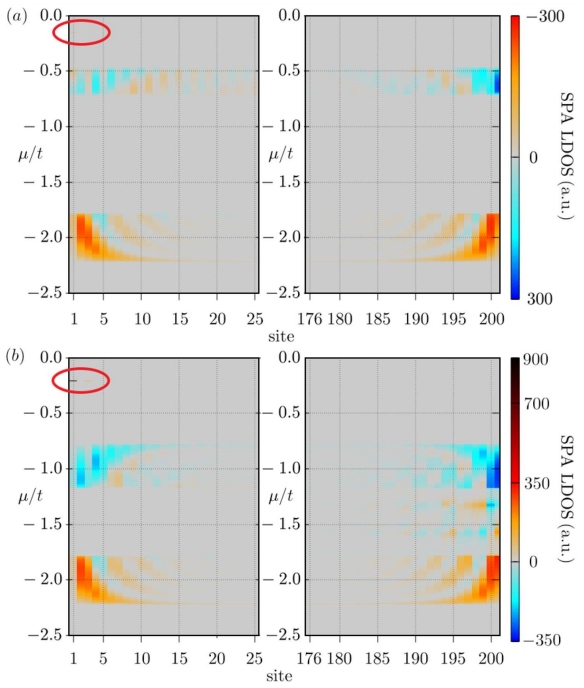

Fig. 4. Real space distribution of asymmetry of SPA of MBS as a function of the chemical potential, at the ends of the nanowire. Results for parameters like in Fig. 2 along $\delta = 0.24$ (a) and $\delta = 0.46$ (b). The central feature for $\mu/t \simeq -1.5$ shows the distribution of SPA LDOS along the bridge-like structure from Fig. 2. Regions within the red oval show instances of a weak bond parabola state forming on the first site. Here, our system consists of $\mathcal{N} = 200$ sites.

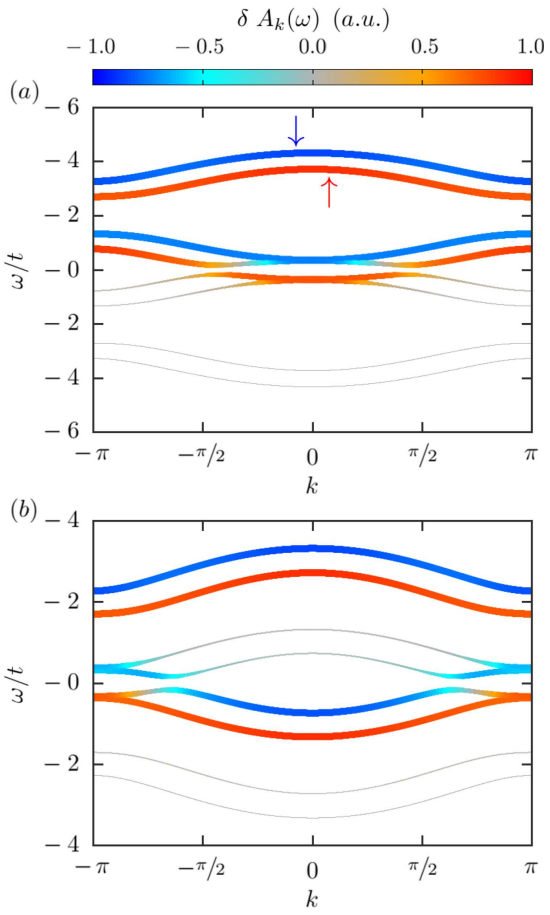

Fig. 5. SPA of the spectral function $\delta\mathcal{A}_{\boldsymbol{k}}(\omega)$. Results for (a) $\mu/t = -2$ and (b) $\mu/t = -1$, with fixed $\delta = 0.46$ (see red and blue dots in Fig. 2a, respectively). The color corresponds to spin polarization (marked with corresponding arrows) and the width of line to the total spectral function $\mathcal{A}_{\boldsymbol{k}\uparrow}(\omega) + \mathcal{A}_{\boldsymbol{k}\downarrow}(\omega)$.

of MBS but additionally with an avoided crossing of ABS. On the other hand, if the nanowire is pristine (no impurity), near-zero energy states that do not mutate into MBS after the topological transition would not show any avoided crossing or bow tie behavior but instead they will follow MBS and diverge out of the topological regime.

Now, we discuss the zero-energy SPA LDOS shown in Fig. 4. In the case of a non-trivial phase, MBS are localized at both ends of the nanowire. These states are characterized by the oscillation of SPA LDOS in space. As we can see, in both branches of the non-trivial phase LDOS is characterized by the opposite SPA. The largest localization of the state is visible at the impurity site (right-hand side), i.e., $\mu/t \approx -2$ for the main branch and $\mu/t \approx -0.75$ for the dimerized branch, while ABS are pinned to the impurity. For the intermediate region $\mu/t \approx -1.5$, we observe the localization of the state mostly at impurity, which is associated with the aforementioned ABS that were manifested as a bridge-like structure in the phase space and, correspondingly, a bow tie region in eigenvalues of Fig. 3. As we move away from the impurity towards the middle of the nanowire, a bridge-like feature will fade away and show no SPA within a distance of ≈ 20 sites. Additionally, we can observe instances of weak bond parabola states forming on the first site (red ovals). These states are characterized by high SPA LDOS and correspond to ABS forming on the edge site which is weakly connected to the rest of the nanowire.

We should also discuss an important problem of interplay between trivial energy levels (of quantum dot or impurity) with energy levels of SSHR chain which contains MBS in a topological regime. In a typical case, when additional impurity is connecting to the trivial superconducting system, the ordinary in-gap Andreev bound states emerge [59]. The situation is more interesting when impurity is connected to the superconducting system in a topological phase. For instance, this issue was experimentally studied by Deng et al. [60], in a fabricated nanowire with a quantum dot at one end. Topologically trivial bound states were seen to coalesce into MBS as the magnetic field was increased. A theoretical study of this behavior showed that the interplay between trivial ABS and

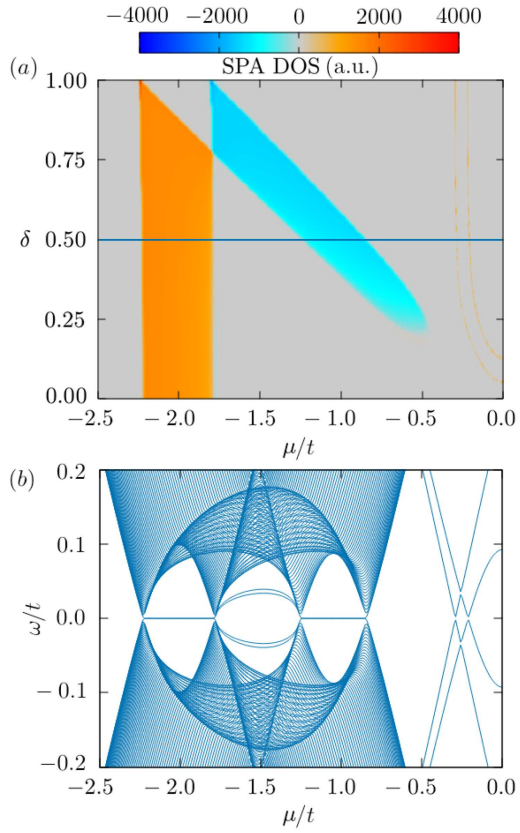

Fig. 6. (a) SPA for zero energy DOS phase spaces as a function of μ and δ, in the case when the nanowire begins with a weak bond and connects with a weak bond to impurity (as seen in Fig. 2). Here, our system consists of $\mathcal{N} = 200$ sites. (b) Eigenvalues for the cross-section of (a), along the blue line ($\delta = 0.5$, as seen in Fig. 3).

topological MBS strongly depend on spin polarization of ABS [28, 56, 61, 62], due to positive spin polarization of MBS [29]. In such a case, the avoided crossing or resonance of the ABS energy levels can be observed [63–65]. Moreover, this behavior can be helpful in distinguishing MBS from ABS [66–68]. At this point, we must have in mind that the boundary of the topological regime of a one-dimensional nanowire is given by relation (4) [56, 69]. In this regime, MBS have the same spin polarization [29]. Contrary to this, in the discussed SSHR model, a topological phase diagram has a more complicated form — due to the existence of the main and dimerization-dependent branches (see Fig. 3) [37]. Here, the spin polarization of MBS depends on parameters of the system, i.e., in the main (dimerized) branch it is positive (negative). Unfortunately, this can lead to ambiguity in distinguishing between ABS and MBS.

Finally, we analyze the results for the system with the even (200 in total) number of sites. In such a case, the nanowire begins with a weak bond and connects with a weak bond to impurity (Fig. 6). The number of sites does not affect the results in any other way than just the order of weak/strong bonds. Here, we can see a familiar phase space with two additional parabolas in zero-energy SPA LDOS (Fig. 6a) forming at $\mu < 0.3t$. The μ-position of the starting point for the outer parabola is linearly dependent on the value of the magnetic field. As for the inner parabola, it forms only if the system exists in a non-trivial phase, after the gap closing ($h > h_c$), similar to the bridge-like feature. If the nanowire started and ended with a strong bond, a bridge-like feature identical to the one from Fig. 2b would appear. However, the fact of both bonds being the same would not affect the bridge in any way, in contrast to the situation with a weak bond.

4. Summary

In this paper, we have shown that the Majorana bound state leakage in the Rashba nanowire which is dimerized according to the SSH scenario might behave anomalously, when an additional impurity is in the vicinity of the nanowire. We find that topological branches, the usual and the dimerized ones, have different SPA that can be explained by the opposite order of bands taking part in topological transitions which are closest to the Fermi level. Moreover, the introduction of impurity along the dimerized nanowire influences the leakage profile of the Majorana state into the trivial impurity. Coupling of impurity to the nanowire leads to the emergence of the trivial Andreev bound states, strongly localized around the impurity. In the case of the one-site impurity, this can lead to the emergence of states crossing the Fermi level. As a consequence, we observe trivial zero-energy states in the form of a bridge-like structure, connecting two branches of the non-trivial topological phases. Stemming from this, measurements of both ends of the nanowire in search of MBS could resolve an ambiguity created by a potential existence of impurities in the nanowire.

Acknowledgments

We thank Pascal Simon and Nicholas Sedlmayr for inspiring discussions. This work was supported by the National Science Centre (NCN, Poland) under grants UMO-2031/N/ST3/01746 (A.K.) and UMO-2017/25/B/ST3/02586 (A.P.).

References

[1] D. Aasen, M. Hell, R.V. Mishmash et al., *Phys. Rev. X* **6**, 031016 (2016).

[2] A.Y. Kitaev, *Phys.-Usp.* **44**, 131 (2001).

[3] Ch. Nayak, S.H. Simon, A. Stern, M. Freedman, S. Das Sarma, *Rev. Mod. Phys.* **80**, 1083 (2008).

[4] V. Mourik, K. Zuo, S.M. Frolov, S.R. Plissard, E.P.A.M. Bakkers, L.P. Kouwenhoven, *Science* **336**, 1003 (2012).

[5] A. Das, Y. Ronen, Y. Most, Y. Oreg, M. Heiblum, H. Shtrikman, *Nat. Phys.* **8**, 887 (2012).

[6] S. Nadj-Perge, I.K. Drozdov, J. Li, H. Chen, S. Jeon, J. Seo, A.H. MacDonald, B.A. Bernevig, A. Yazdani, *Science* **346**, 602 (2014).

[7] R. Pawlak, M. Kisiel, J. Klinovaja, T. Meier, S. Kawai, T. Glatzel, D. Loss, E. Meyer, *Npj Quant. Informat.* **2**, 16035 (2016).

[8] M.T. Deng, S. Vaitiekenas, E.B. Hansen, J. Danon, M. Leijnse, K. Flensberg, J. Nygård, P. Krogstrup, C.M. Marcus, *Science* **354**, 1557 (2016).

[9] F. Nichele, A.C.C. Drachmann, A.M. Whiticar, *Phys. Rev. Lett.* **119**, 136803 (2017).

[10] S. Jeon, Y. Xie, J. Li, Z. Wang, B.A. Bernevig, A. Yazdani, *Science* **358**, 772 (2017).

[11] H. Kim, A. Palacio-Morales, T. Posske, L. Rózsa, K. Palotás, L. Szunyogh, M. Thorwart, R. Wiesendanger, *Sci. Adv.* **4**, aar5251 (2018).

[12] R.M. Lutchyn, E.P.A.M. Bakkers, L.P. Kouwenhoven, P. Krogstrup, C.M. Marcus, Y. Oreg, *Nat. Rev. Mater.* **3**, 52 (2018).

[13] Ö. Gül, H. Zhang, J.D.S. Bommer, *Nat. Nanotechnol.* **13**, 192 (2018).

[14] A. Fornieri, A.M. Whiticar, F. Setiawan et al., *Nature* **569**, 89 (2019).

[15] H. Ren, F. Pientka, S. Hart et al., *Nature* **569**, 93 (2019).

[16] G.C. Ménard, S. Guissart, Ch. Brun et al., *Nat. Commun.* **8**, 2040 (2017).

[17] G.C. Ménard, A. Mesaros, Ch. Brun, F. Debontridder, D. Roditchev, P. Simon, T. Cren, *Nat. Commun.* **10**, 2587 (2019).

[18] A. Palacio-Morales, E. Mascot, S. Cocklin, H. Kim, S. Rachel, D.K. Morr, R. Wiesendanger, *Sci. Adv.* **5**, eaav6600 (2019).

[19] W.P. Su, J.R. Schrieffer, A.J. Heeger, *Phys. Rev. Lett.* **42**, 1698 (1979).

[20] A.J. Heeger, S. Kivelson, J.R. Schrieffer, W.P. Su, *Rev. Mod. Phys.* **60**, 781 (1988).

[21] R. Wakatsuki, M. Ezawa, Y. Tanaka, N. Nagaosa, *Phys. Rev. B* **90**, 014505 (2014).

[22] Y. Wang, J.-J. Miao, H.-K. Jin, S. Chen, *Phys. Rev. B* **96**, 205428 (2017).

[23] M. Ezawa, *Phys. Rev. B* **96**, 121105 (2017).

[24] G.Y. Chitov, *Phys. Rev. B* **97**, 085131 (2018).

[25] W.C. Yu, P.D. Sacramento, Y.C. Li, D.G. Angelakis, H.-Q. Lin, *Phys. Rev. B* **99**, 115113 (2019).

[26] Ch.-B. Hua, R. Chen, D.-H. Xu, B. Zhou, *Phys. Rev. B* **100**, 205302 (2019).

[27] S. Tamura, S. Nakosai, A.M. Black-Schaffer, Y. Tanaka, J. Cayao, *Phys. Rev. B* **101**, 214507 (2020).

[28] A. Ptok, A. Kobiałka, T. Domański, *Phys. Rev. B* **96**, 195430 (2017).

[29] A. Kobiałka, A. Ptok, *J. Phys. Condens. Matter* **31**, 185302 (2019).

[30] A. Kobiałka, A. Ptok, *Acta Phys. Pol. A* **135**, 64 (2019).

[31] A. Kobiałka, T. Domański, A. Ptok, *Sci. Rep.* **9**, 12933 (2019).

[32] W. Chang, S.M. Albrecht, T.S. Jespersen, F. Kuemmeth, P. Krogstrup, J. Nygård, C.M. Marcus, *Nat. Nanotechnol.* **10**, 232 (2015).

[33] M. Sato, S. Fujimoto, *Phys. Rev. B* **79**, 094504 (2009).

[34] M. Sato, Y. Takahashi, S. Fujimoto, *Phys. Rev. Lett.* **103**, 020401 (2009).

[35] M. Sato, Y. Takahashi, S. Fujimoto, *Phys. Rev. B* **82**, 134521 (2010).

[36] J.E. Moore, L. Balents, *Phys. Rev. B* **75**, 121306 (2007).

[37] A. Kobiałka, N. Sedlmayr, M.M. Maśka, T. Domański, *Phys. Rev. B* **101**, 085402 (2020).

[38] P.G. de Gennes, *Superconductivity of Metals and Alloys*, Addison-Wesley, 1989.

[39] H. Matsui, T. Sato, T. Takahashi, S.-C. Wang, H.-B. Yang, H. Ding, T. Fujii, T. Watanabe, A. Matsuda, *Phys. Rev. Lett.* **90**, 217002 (2003).

[40] D. Sticlet, C. Bena, P. Simon, *Phys. Rev. Lett.* **108**, 096802 (2012).

[41] J. Figgins, D.K. Morr, *Phys. Rev. Lett.* **104**, 187202 (2010).

[42] D. Chevallier, J. Klinovaja, *Phys. Rev. B* **94**, 035417 (2016).

[43] J. Stenger, T.D. Stanescu, *Phys. Rev. B* **96**, 214516 (2017).

[44] W.A. Hofer, A.S. Foster, A.L. Shluger, *Rev. Mod. Phys.* **75**, 1287 (2003).

[45] R. Wiesendanger, *Rev. Mod. Phys.* **81**, 1495 (2009).

[46] H. Oka, O.O. Brovko, M. Corbetta, V.S. Stepanyuk, D. Sander, J. Kirschner, *Rev. Mod. Phys.* **86**, 1127 (2014).

[47] F. Meier, Lihui Z., J. Wiebe, R. Wiesendanger, *Science* **320**, 82 (2008).

[48] S.M. Hus, X.-G. Zhang, G.D. Nguyen, W. Ko, A.P. Baddorf, Y.P. Chen, A.-P. Li, *Phys. Rev. Lett.* **119**, 137202 (2017).

[49] S. Rolf-Pissarczyk, S. Yan, L. Malavolti, J.A.J. Burgess, G. McMurtrie, S. Loth, *Phys. Rev. Lett.* **119**, 217201 (2017).

[50] M.M. Maśka, T. Domański, *Sci. Rep.* **7**, 16193 (2017).

[51] P. Devillard, D. Chevallier, M. Albert, *Phys. Rev. B* **96**, 115413 (2017).

[52] A. Bansil, H. Lin, T. Das, *Rev. Mod. Phys.* **88**, 021004 (2016).

[53] A. Damascelli, Z. Hussain, Z.-X. Shen, *Rev. Mod. Phys.* **75**, 473 (2003).

[54] P.C. Snijders, H.H. Weitering, *Rev. Mod. Phys.* **82**, 307 (2010).

[55] M.Z. Hasan, C.L. Kane, *Rev. Mod. Phys.* **82**, 3045 (2010).

[56] P. Szumniak, D. Chevallier, D. Loss, J. Klinovaja, *Phys. Rev. B* **96**, 041401 (2017).

[57] D. Sticlet, C. Pascu Moca, B. Dóra, *Phys. Rev. B* **102**, 075437 (2020).

[58] Supplemental Material in: Ref. [36].

[59] A.V. Balatsky, I. Vekhter, J.-X. Zhu, *Rev. Mod. Phys.* **78**, 373 (2006).

[60] M.T. Deng, S. Vaitiekenas, E.B. Hansen, J. Danon, M. Leijnse, K. Flensberg, J. Nygård, P. Krogstrup, C.M. Marcus, *Science* **354**, 1557 (2016).

[61] E. Prada, R. Aguado, P. San-Jose, *Phys. Rev. B* **96**, 085418 (2017).

[62] S. Hoffman, D. Chevallier, D. Loss, J. Klinovaja, *Phys. Rev. B* **96**, 045440 (2017).

[63] E. Vernek, P.H. Penteado, A.C. Seridonio, J.C. Egues, *Phys. Rev. B* **89**, 165314 (2014).

[64] J. Barański, A. Kobiałka, T. Domański, *J. Phys. Condens. Matter* **29**, 075603 (2016).

[65] T. Zienkiewicz, J. Barański, G. Górski, T. Domański, *J. Phys. Condens. Matter* **32**, 025302 (2019).

[66] Ch.-X. Liu, J.D. Sau, S. Das Sarma, *Phys. Rev. B* **97**, 214502 (2018).

[67] L.S. Ricco, M. de Souza, M.S. Figueira, I.A. Shelykh, A.C. Seridonio, *Phys. Rev. B* **99**, 155159 (2019).

[68] O.A. Awoga, J. Cayao, A.M. Black-Schaffer, *Phys. Rev. Lett.* **123**, 117001 (2019).

[69] P. Zhang, F. Nori, *New J. Phys.* **18**, 043033 (2016).

4.2.5 Probing the chirality of one–dimensional Majorana edge states around a two–dimensional nanoflake in a superconductor

A. Ptok, D.J. Alspaugh, S. Głodzik, A. Kobiałka, A.M. Oleś, P. Simon, P. Piekarz, Phys. Rev. B **102**, 245405 (2020)

Here, we change our usual venue of 1D systems into 2D magnetic nanoflake deposited on superconducting surfaces. Usually, the transition to nontrivial phase happens after surpassing the critical Zeeman energy required for reopening of gap in the system. As this is not a valid approach for magnetic islands, we proposed a scheme based on the tuning of chemical potential. This allows for the formation of chiral edge currents along the border of the system, whose existence depends upon the system parameters. From the analytical calculations obtained for a circular nanoflake, we derived the spectrum of the system depending on the total angular momentum. We proposed a real space indicator, which allows to characterize the topological state of the system locally. This shows a separation of our probed system into three parts: the nanoflake in the center, *domain wall* around which chiral currents propagate and bulk, outside. Additionally, we propose a STM setup composed of two tips which enables a nonlocal differential conductance measurement of chiral bond currents in the domain wall. As a result, we can not only measure those currents but also find their direction of propagation, which depends mainly on the type of particles forming the current and their spin.

Author's contribution: Analysis and discussion of obtained results, partial preparation of the manuscript, participation in preparing the response for Referees.

Probing the chirality of one-dimensional Majorana edge states around a two-dimensional nanoflake in a superconductor

Andrzej Ptok,[1,*] David J. Alspaugh,[2,†] Szczepan Głodzik,[3] Aksel Kobiałka,[3] Andrzej M. Oleś,[4,5] Pascal Simon,[6,‡] and Przemysław Piekarz[1,§]

[1]*Institute of Nuclear Physics, Polish Academy of Sciences, ulica W. E. Radzikowskiego 152, PL-31342 Kraków, Poland*
[2]*Department of Physics and Astronomy, Louisiana State University, Baton Rouge, Louisiana 70803-4001, USA*
[3]*Institute of Physics, Maria Curie-Skłodowska University, Plac Marii Skłodowskiej-Curie 1, PL-20031 Lublin, Poland*
[4]*Institute of Theoretical Physics, Jagiellonian University, Profesora Stanisława Łojasiewicza 11, PL-30348 Kraków, Poland*
[5]*Max Planck Institute for Solid State Research, Heisenbergstrasse 1, D-70569 Stuttgart, Germany*
[6]*Université Paris-Saclay, CNRS, Laboratoire de Physique des Solides, F-91405 Orsay, France*

(Received 24 August 2020; revised 12 November 2020; accepted 12 November 2020; published 3 December 2020)

The interplay between superconductivity, magnetic field, and spin-orbit coupling can lead to the realization of nontrivial topological phases. Recent experiments have found signatures of such phases in magnetic nanoflakes formed by nanostructures coupled to a superconducting substrate. These heterostructures comprise a topologically nontrivial region surrounded by a trivial one due to the finite magnetic exchange field induced by the magnetic nanoflake. The analysis of the topological phase diagram of such a system shows that a similar phase separation occurs by tuning the chemical potential of the nanoflake. In this paper, we study such a possibility in detail, analyzing the spatial extent of the edge modes circulating around the nanoflake and discussing some practical implementations. We also show how the chirality of Majorana edge states can be probed using scanning tunneling spectroscopy with a double-tip setup.

DOI: 10.1103/PhysRevB.102.245405

I. INTRODUCTION

The quest for the realization of Majorana zero modes (MZMs), driven by the pursuit of both fundamental physics and their potential application to fault-tolerant topological quantum computation [1–5], is steering active research in engineering p-wave superconductivity. Non-Abelian braiding is an essential step towards topological quantum computing, though it has not yet been experimentally achieved with MZMs. Due to the localized nature of MZMs, their braiding will necessarily involve both coupling and manipulation processes.

However, it has been suggested that non-Abelian braiding is not only restricted to MZMs but can also be implemented with one-dimensional (1D) chiral Majorana fermions [6]. Chiral Majorana fermions can manifest themselves as quasiparticle edge states of a two-dimensional (2D) topological p-wave superconductor [4,7]. Signatures of 1D chiral Majorana quasiparticles were recently observed in 2D heterostructures consisting of a quantum anomalous Hall insulator bar in contact with a superconductor [8]. Additionally, recent progress in atomic-scale engineering [9–13] is opening up new perspectives for the practical implementation of chiral Majorana fermions by spatially building nontrivial topological phases separated from trivial ones. Recent progress includes Co islands grown on a Si substrate covered by a monolayer of Pb [9] and nanoscale Fe islands of monoatomic height on a Re surface [14]. Due to the nontrivial topological phase transition resulting from a gap closure, in-gap edge states surrounding the topological superconducting (SC) domain are observed. In both experiments, these in-gap states are strongly delocalized around the islands and have been interpreted as signatures of chiral Majorana fermions.

In 2D superconductors with Rashba spin-orbit coupling (SOC), the transition to a nontrivial phase can be induced by an external Zeeman magnetic field [15–17]. The boundary between the trivial and nontrivial topological phases is given by $h_c^2 = \mu^2 + \Delta^2$ [see Fig. 1(a)], where h_c stands for the critical Zeeman field for given values of the doping μ and the SC gap Δ. In the aforementioned experimental results, the Zeeman magnetic energy arises from the presence of magnetic dopants interacting with the substrate, while the SOC and the SC gap are intrinsic to the subsystem. Looking at the phase diagram presented in Fig. 1(a), one observes that a line which connects points A and B in the (μ, h) plane could correspond to an inhomogeneous system in real space, where a nonmagnetic trivial domain (point A) surrounds or borders a topological magnetic domain (point B).

In this paper, we instead choose to explore an alternative route. We consider an inhomogeneous system but with a constant magnetic Zeeman energy, which would reside on the C-D line in Fig. 1(a). The transition to the topological domain occurs due to a change in the chemical potential μ. Such a

*aptok@mmj.pl
†dalspa1@lsu.edu
‡pascal.simon@u-psud.fr
§piekarz@wolf.ifj.edu.pl

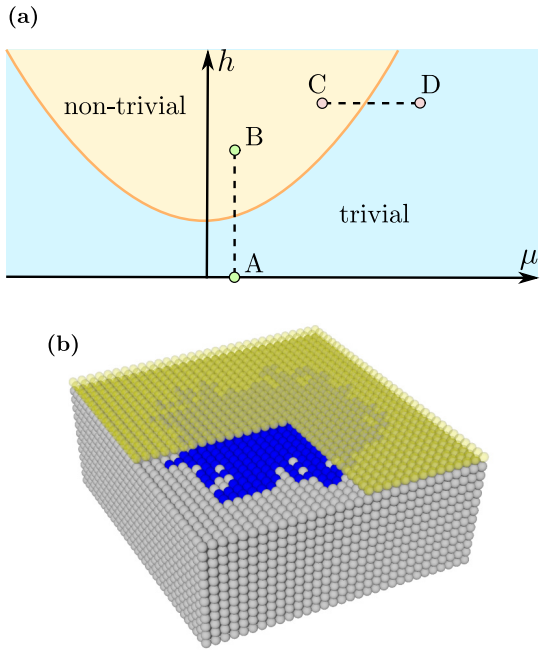

FIG. 1. (a) Schematic representation of the topological phase diagram as a function of the chemical potential μ and magnetic Zeeman energy h. (b) Schematic view of the studied system. A superconducting (SC) layer (yellow transparent atoms) is deposited on a magnetic substrate (gray atoms). The nanoflake is formed by nonmagnetic atoms located at random sites either between the substrate and the SC layer as shown or above the SC layer. For a constant SC gap Δ, the boundary between the topologically trivial (blue region) and nontrivial (yellow region) phases is given by a parabola, $h_c^2 = \Delta^2 + \mu^2$ [orange line in (a)].

system could be constructed experimentally in many different ways: one option would be to substitute the magnetic atoms in the Co island [9] by nonmagnetic ones and add a magnetic field parallel to the SC Pb monolayer [Fig. 1(b)]. Another promising approach is to use the versatility offered by 2D van der Waals heterostructures [18]. A possible way to generate a homogeneous Zeeman exchange energy in the proximity of a superconductor could be engineered by stacking recently synthesized 2D magnetic materials [19,20] with a transition metal dichalcogenide superconductor such as $NbSe_2$. A nonmagnetic island can be obtained by evaporating some alkaline adatoms to enforce charge transfer.

This paper is organized as follows: In Sec. II, we first start with a circular geometry for the nanoflake and derive the dispersive chiral Majorana edge states analytically in the continuum limit. We also discuss the spatial extent of the chiral Majorana modes in the transverse direction. In Sec. III we compare our results obtained in the continuum limit to exact diagonalization of a tight-binding model on a lattice. In Sec. IV, we propose and study a setup in order to measure the chirality of the Majorana edge states using two ferromagnetic tips. Finally, we present a summary of our results and give conclusions in Sec. V.

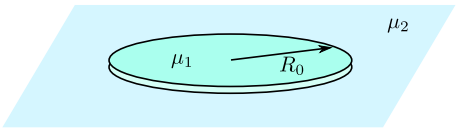

FIG. 2. Schematic representation of the discussed system in the thermodynamic limit with a circular nanoflake deposited on a substrate.

II. NANOFLAKE WITH CIRCULAR GEOMETRY

We begin by considering a nanoflake with circular symmetry as depicted in Fig. 2. For simplification and without loss of generality, we can also assume a smooth boundary of the nanoflake. Keeping in mind the circular symmetry, the Hamiltonian will commute with the zth component of the total angular momentum operator $J_z \equiv L_z + S_z$. We may then find the energies of the bound state wave functions localized at the edge of the nanoflake in terms of the m_J quantum numbers. This method allows us to determine the existence of chiral subgap states within our system and has successfully been used in the studies of other 2D systems with circular symmetry such as graphene [21].

Thus, the real-space normal state Hamiltonian has the form

$$H(\boldsymbol{r}, \nabla) = \left(-\frac{\nabla^2}{2m} - \mu(\boldsymbol{r})\right)\sigma_0 + \alpha(\boldsymbol{\sigma} \times -i\nabla)_z + h\sigma_z,$$

where σ_i (for $i = \{0, x, y, z\}$) are the Pauli matrices acting in spin space. Here, the system is 2D with $\mathbf{r} \equiv (x, y)$, and the chemical potential is given by

$$\mu(r) = \begin{cases} \mu_1 & r < R_0, \\ \mu_2 & r \geqslant R_0. \end{cases} \tag{2}$$

We may also define the discontinuity $\delta\mu = \mu_2 - \mu_1$ at the boundary (see Fig. 2). In other words, $\delta\mu$ corresponds to the spatial variation of the chemical potential induced by the nanoflake. The Bogoliubov–de Gennes (BdG) Hamiltonian may then be expressed as

$$\mathcal{H} = \frac{1}{2}\int d\boldsymbol{r}\, \Psi^\dagger(\boldsymbol{r}) \begin{pmatrix} H(\boldsymbol{r}, \nabla) & i\sigma_y\Delta \\ -i\sigma_y\Delta & -H^T(\boldsymbol{r}, -\nabla) \end{pmatrix} \Psi(\boldsymbol{r}), \tag{3}$$

where $\Psi(\boldsymbol{r}) \equiv (\psi_\uparrow(\boldsymbol{r}), \psi_\downarrow(\boldsymbol{r}), \psi_\uparrow^\dagger(\boldsymbol{r}), \psi_\downarrow^\dagger(\boldsymbol{r}))^T$ is the Nambu spinor, with $\psi_\sigma(\boldsymbol{r})$ being electron field operators which destroy an electron with spin σ at location $\boldsymbol{r}$.

Due to the circular symmetry of the nanoflake [or, more precisely, the scalar chemical potential $\mu(\boldsymbol{r}) = \mu(r)$], the BdG Hamiltonian commutes with the zth component of the total angular momentum operator $J_z = L_z + S_z$. It follows that the Hamiltonian and J_z share the same eigenstates. The eigenstates of J_z, with the half-integer eigenvalues m_J, are given by

$$\varphi_{m_J} = \begin{pmatrix} u_{m_J\uparrow}(r)\, e^{i(m_J-1/2)\theta} \\ u_{m_J\downarrow}(r)\, e^{i(m_J+1/2)\theta} \\ v_{m_J\uparrow}(r)\, e^{i(m_J+1/2)\theta} \\ v_{m_J\downarrow}(r)\, e^{i(m_J-1/2)\theta} \end{pmatrix}. \tag{4}$$

To focus on states with small total angular momenta, we take a low-energy approximation and neglect the kinetic energy term in the Hamiltonian [22]. By writing the $u_{m_J\sigma}(r)$ and $v_{m_J\sigma}(r)$

functions in terms of the modified Bessel functions of the first and second kinds, we may then solve for the bound state wave functions localized at $r = R_0$. The details of this approach can be found in the Supplemental Material (SM) [23], and the resulting wave functions have the form

$$\varphi_{m_J} = \begin{cases} \varphi_{m_J 1} & r < R_0, \\ \varphi_{m_J 2} & r \gtrsim R_0, \end{cases} \tag{5}$$

where

$$\varphi_{m_J 1} = \sum_{\eta=\pm} N_{m_J 1\eta} \begin{pmatrix} a_{m_J 1\eta} I_{m_J-\frac{1}{2}}(k_{m_J 1\eta} r) e^{i(m_J-\frac{1}{2})\theta} \\ b_{m_J 1\eta} I_{m_J+\frac{1}{2}}(k_{m_J 1\eta} r) e^{i(m_J+\frac{1}{2})\theta} \\ c_{m_J 1\eta} I_{m_J+\frac{1}{2}}(k_{m_J 1\eta} r) e^{i(m_J+\frac{1}{2})\theta} \\ I_{m_J-\frac{1}{2}}(k_{m_J 1\eta} r) e^{i(m_J-\frac{1}{2})\theta} \end{pmatrix} \tag{6}$$

and

$$\varphi_{m_J 2} = \sum_{\eta=\pm} N_{m_J 2\eta} \begin{pmatrix} a_{m_J 2\eta} e^{i(m_J-\frac{1}{2})\pi} K_{m_J-\frac{1}{2}}(k_{m_J 2\eta} r) e^{i(m_J-\frac{1}{2})\theta} \\ b_{m_J 2\eta} e^{i(m_J+\frac{1}{2})\pi} K_{m_J+\frac{1}{2}}(k_{m_J 2\eta} r) e^{i(m_J+\frac{1}{2})\theta} \\ c_{m_J 2\eta} e^{i(m_J+\frac{1}{2})\pi} K_{m_J+\frac{1}{2}}(k_{m_J 2\eta} r) e^{i(m_J+\frac{1}{2})\theta} \\ e^{i(m_J-\frac{1}{2})\pi} K_{m_J-\frac{1}{2}}(k_{m_J 2\eta} r) e^{i(m_J-\frac{1}{2})\theta} \end{pmatrix}. \tag{7}$$

Here, $I(z)$ and $K(z)$ are the modified Bessel functions of the first and second kinds, respectively. The a, b, and c parameters along with the normalizations are derived within the SM [23], while the radial momenta which control the spatial extent of the bound states wave functions are given by

$$k_{m_J j\eta} = \frac{1}{\alpha}\sqrt{h^2 - E_{m_J}^2 + \Delta^2 - \mu_j^2 + 2\eta\sqrt{E_{m_J}^2\mu_j^2 + \Delta^2(h-\mu_j)(h+\mu_j)}}, \tag{8}$$

where $j = 1, 2$ and $\eta = \pm$. For each of the φ_{m_J} bound states localized at $r = R_0$, the total radial spatial extent ξ_{m_J} of the wave functions are thus determined by

$$\xi_{m_J} = \max\left\{k_{m_J 1+}^{-1}, k_{m_J 1-}^{-1}, k_{m_J 2+}^{-1}, k_{m_J 2-}^{-1}\right\}. \tag{9}$$

The energy spectrum of these bound states vs the m_J quantum numbers is presented in Fig. 3, while the spatial profile of the wave functions is given in Fig. 4 for two different characteristic sets of parameters. The number of in-gap states is quantized due to the finite perimeter of the nanoflake, and their energy spacing depends on intrinsic parameters. In the first set of parameters, we find eight in-gap states, while we have four in-gap states in the second set. We choose the strength of the Zeeman field such that the topological gap,

$$\Delta_{\text{top}} = \left|h - \sqrt{\Delta^2 + \mu^2}\right|, \tag{10}$$

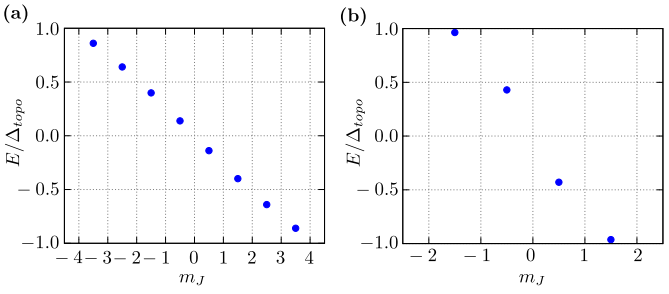

FIG. 3. Spectrum of the in-gap dispersive states as a function of the total angular momentum quantum number m_J. Results are presented for two different sets of parameters: (a) $\mu_1 = 0.2$ meV, $\mu_2 = 0.4$ meV, $\Delta = 0.3$ meV and (b) $\mu_1 = 0.1$ meV, $\mu_2 = 0.2$ meV, $\Delta = 0.2$ meV. We take $R_0 = 10$ nm and $\alpha = 0.25$ meV nm.

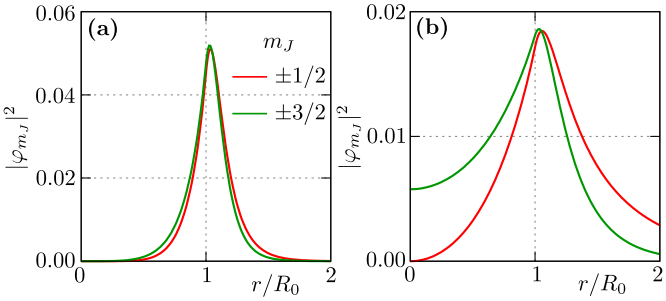

FIG. 4. Localization of the in-gap bound states around the edge of the nanoflake for different values of the total angular momentum m_J. (a) and (b) correspond to the same sets of parameter values as detailed in Fig. 3.

is equal inside and outside the nanoflake. From our first set of data we obtain $\Delta_{\text{top}} = 0.070$ meV, while for our second set we obtain $\Delta_{\text{top}} = 0.0296$ meV. The existence of only one branch of states in the topological gap signals that they are chiral (here left-handed). This in turn supports the hypothesis of a phase separation in space with a chiral Majorana edge state circulating around the nanoflake.

We also note that these dispersive states are not perfectly linear but instead exhibit a slightly cubic behavior. Comparing both sets of parameters, we see that the larger the discontinuity $|\delta\mu| = |\mu_1 - \mu_2|$ is, the more localized the edge states are. This behavior is expected; indeed, the in-gap Majorana states are pinned at the domain wall, which is controlled by the spatial variation of the chemical potential.

III. TIGHT-BINDING FORMULATION

In order to confirm our calculations performed in the continuum limit and to go beyond the circular symmetry assumption for a nanoflake, we have also performed numerical calculations on a lattice based on a tight-binding description. Our system can be described by the following tight-binding Hamiltonian:

$$\mathcal{H} = \mathcal{H}_{\text{kin}} + \mathcal{H}_{\text{SO}} + \mathcal{H}_{\text{prox}} + \mathcal{H}_{\text{flake}}. \tag{11}$$

The first term corresponds to a free particle on a 2D square lattice,

$$\mathcal{H}_{\text{kin}} = \sum_{ij\sigma} [-t + (4t - \mu - \sigma h)\delta_{ij}]\, c^{\dagger}_{i\sigma} c_{j\sigma}. \tag{12}$$

Here, t is the hopping integral between nearest-neighbor sites [24], μ is the chemical potential (calculated from the bottom of the band), and h can be regarded either as a genuine Zeeman energy or as a magnetic exchange energy depending on the situation under consideration. In all cases, we treat it as an effective magnetic field in what follows. The second term describes the in-plane SOC,

$$\mathcal{H}_{\text{SO}} = -i\alpha \sum_{ij\sigma\sigma'} c^{\dagger}_{i+\boldsymbol{d}_j\sigma} [(\boldsymbol{d}_j \times \hat{\boldsymbol{\sigma}}) \cdot \hat{z}]_{\sigma\sigma'} c_{i\sigma'}, \tag{13}$$

where vectors $\boldsymbol{d}_i \in \{\pm\hat{x}, \pm\hat{y}\}$ stand for the locations of the neighbors of the ith site, while $\hat{\boldsymbol{\sigma}} = (\sigma_x, \sigma_y, \sigma_z)$ is the vector with the Pauli matrices being its components. A SC gap can be induced in the layer through the proximity effect—this process is described through the third term by the BCS-like form

$$\mathcal{H}_{\text{prox}} = \Delta \sum_i (c^{\dagger}_{i\uparrow} c^{\dagger}_{i\downarrow} + \text{H.c.}). \tag{14}$$

The last term in Eq. (10) denotes the influence of the nanoflake at the particle distribution,

$$\mathcal{H}_{\text{flake}} = -\sum_i V_i c^{\dagger}_{i\sigma} c_{i\sigma}. \tag{15}$$

We assume that every atom comprising the nanoflake changes the energy levels of the rest of the sites; that is, we assume a long-range impurity potential given by $V_i = V_0 \sum_m \exp(-R_{mi}/\lambda)$, where the summation is carried out over all adatoms in a given configuration $\mathcal{V}$ [25]. Here, λ denotes the characteristic length of decay of the impurity potential.

The Hamiltonian $\mathcal{H}$ can be diagonalized by the unitary transformation,

$$c_{i\sigma} = \sum_n (u_{in\sigma}\gamma_n - \sigma v^{*}_{in\sigma}\gamma^{\dagger}_n), \tag{16}$$

which leads to BdG equations [26] of the form

$$\mathcal{E}_n \Phi_{in} = \sum_j \mathbb{H}_{ij} \Phi_{jn}, \tag{17}$$

with eigenvectors $\Phi_{in} = (u_{in\uparrow}, v_{in\downarrow}, u_{in\downarrow}, v_{in\uparrow})^T$. Here,

$$\mathbb{H}_{ij} = \begin{pmatrix} H_{ij\uparrow} & D_{ij} & S^{\uparrow\downarrow}_{ij} & 0 \\ D^{*}_{ij} & -H^{*}_{ij\downarrow} & 0 & S^{\downarrow\uparrow}_{ij} \\ S^{\downarrow\uparrow}_{ij} & 0 & H_{ij\downarrow} & D_{ij} \\ 0 & S^{\uparrow\downarrow}_{ij} & D^{*}_{ij} & -H^{*}_{ij\uparrow} \end{pmatrix} \tag{18}$$

is the Hamiltonian in matrix form, with matrix elements $H_{ij\sigma} = -t\sum_j \delta_{\langle i,j\rangle} + (4t - \mu - \sigma h - V_i)\delta_{ij}$ as the kinetic term, $D_{ij} = \Delta\delta_{ij}$ describing the SC correlations, and $S^{\sigma\sigma'}_{ij} = -i\alpha\sum_j [(\boldsymbol{d}_j \times \hat{\boldsymbol{\sigma}}) \cdot \hat{z}]_{\sigma\sigma'}\delta_{\langle i,j\rangle}$ standing for the matrix representation of the spin-orbit coupling. More details of this method can be found, e.g., in Ref. [27].

A. Numerical results

We report the calculations performed using an $N_x \times N_y = 59 \times 59$ square lattice with periodic boundary conditions. Omitting generality, in the calculations presented in this section we use a nanoflake with a circular shape and a radius $R_0 = 15.1$, which covers about 20% of the total area. We present results for a nanoflake characterized by $\lambda = 1$ and $V_0/t = -0.06$. In subsequent calculations, we take $\alpha/t = 0.15$, $\Delta/t = 0.3$, and $\mu/t = 0.4$. If not mentioned explicitly in the text, the value of the magnetic Zeeman field h was chosen so that the boundary between the trivial and nontrivial phases remains in the center of the artificial domain wall (typically, $h/t \simeq 0.4$).

1. Density of states

From the solutions of the BdG equations, we first calculate the local density of states (LDOS) [28],

$$\rho_i(\omega) = \sum_{\sigma n} [|u_{in\sigma}|^2 \delta(\omega - \mathcal{E}_n) + |v_{in\sigma}|^2 \delta(\omega + \mathcal{E}_n)], \tag{19}$$

where we replace the Dirac function $\delta(\omega)$ by a Lorentzian, $\delta(\omega) = \zeta/[\pi(\omega^2 + \zeta^2)]$, with a small broadening $\zeta = 0.003t$. Figure 5 shows an example of the LDOS for a chosen path (along the nanoflake with $y = 30$). The nontrivial domain is separated from the trivial phase by in-gap states strongly localized along the edge of the nanoflake (see Fig. 6). The domain wall is visible in the form of two sets of LDOS peaks with oscillating intensity near $\omega/t \simeq 0$, which are a result of the discrete nature of the in-gap state's spectrum. The LDOS in our system does not exhibit an sfX-shaped crossing through the energy gap around the nanoflake edge, in contrast to the results presented in Refs. [9,29]. Nevertheless, our results are in agreement with experimental results presented in Ref. [14]. As a consequence, we do not observe the two-ring

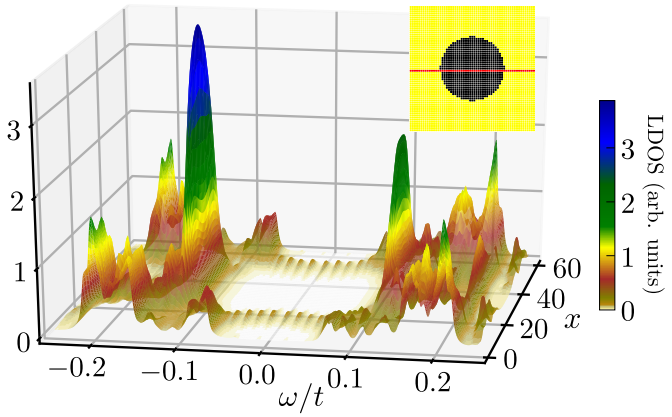

FIG. 5. Local density of states along the line presented in the inset.

localization like in Refs. [9,29] but a one-ring structure along the nanoflake boundary like in Ref. [14].

The localization of the in-gap states is shown Fig. 6. As we can see, the edge states are localized around the nanoflake at the border between the trivial and topological phases. All states create localized states with a circular shape with the same radius (equal approximately to 17), while the radius of the nanoflake is $R_0 \simeq 15.1$ (shown by the dot-dashed line). The difference in these results with respect to the ones discussed in the continuum limit is a consequence of the smearing of the domain wall given by V_i.

The total density of states (DOS) of the system per site is given by a summation of the LDOS over the whole 2D space, i.e., $\rho(\omega) = 1/N \sum_i \rho_i(\omega)$. Here, we can separate the sum into three different terms,

$$\sum_i \rightarrow \sum_{i\in\text{Nanoflake}} + \sum_{i\in\text{DW}} + \sum_{i\in\text{Bulk}}, \tag{20}$$

a contribution from the sites belonging to the nanoflake, a contribution from the domain wall (DW), and a contribution from the bulk states [see the inset in Fig. 7(b)]. As in Ref. [30], we can define the functions $\mathcal{C}_i$ in order to

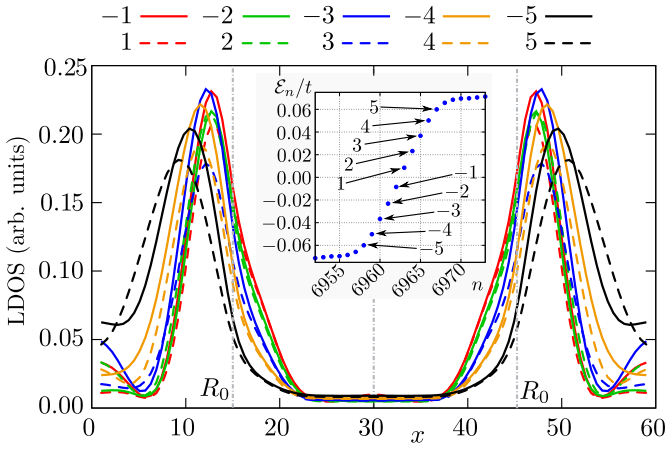

FIG. 6. LDOS of several in-gap eigenstates along the center of the nanoflake ($y = 30$). The radius $R_0 = 15.1$ is shown by a gray line (see Fig. 4). The inset shows a spectrum of the system and a description of the eigenstates (see Fig. 3). Numbers from −5 to 5 enumerate the ten states near the Fermi level. Solid and dashed lines correspond to negative and positive eigenvalues.

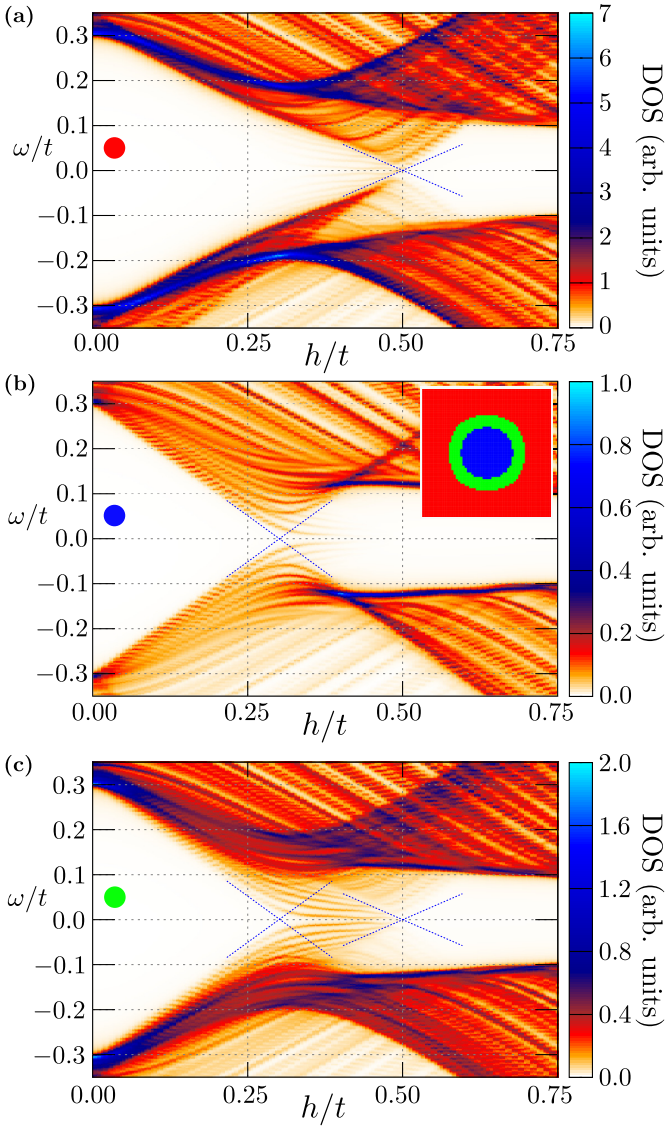

FIG. 7. Partial density of states for different regions: (a) bulk, (b) nanoflake, and (c) domain wall. Blue dashed lines serve as a guide to the eye and present the linear continuation of the gap closing.

classify the states in real space. These functions are equal to 1 when a site i belongs to a given region and 0 otherwise. We assume that the nanoflake (bulk) region is located in sites where the nanoflake changes (does not change) the chemical potential significantly, i.e., $|V_i| < 0.95 \max\{|V_i|\}$ ($|V_i| > 0.05 \max\{|V_i|\}$). Otherwise, we treat the site as a part of the DW region, i.e., when $0.95 \max\{|V_i|\} \leqslant |V_i| \leqslant 0.05 \max\{|V_i|\}$. These conditions can be smoothed arbitrarily without changing the results qualitatively (see Figs. S6 and S7 in the SM [23]).

We use this recipe to present the partial density of states (PDOS), which is defined as follows:

$$\tilde{\rho}(\omega) = \sum_i \mathcal{C}_i \, \rho_i(\omega). \tag{21}$$

The contribution of the bulk (nanoflake), presented in Fig. 7(a) [Fig. 7(b)], looks like the familiar DOS of a pure 2D Rashba spin-orbit coupled superconductor, in which the gap closing

is followed by a reopening of the topological gap. Dashed blue lines serve as a guide to the eye, showing the linear continuation of the last negative and first positive eigenvalues. The value of the magnetic field h for which these dashed lines cross zero energy indicates the phase transition from the trivial to nontrivial phase.

For effective fields larger than this crossing point, in both cases we observe a topological gap opening around $\omega/t \simeq \pm 0.1$. Contrary to this, the DW PDOS [Fig. 7(c)] resembles a nontrivial 2D system with edges [31]. Between critical fields for bulk and nanoflake regions (dashed blue lines crossing the Fermi level), we observe the in-gap states associated only with the DW, which confirms the existence of bound states localized along the DW. Additionally, with the increase of h, the contribution of these states to the total DOS is shifted from the DW to bulk region (see Fig. S8 in the SM [23]).

2. *Nontrivial topological domains and topological phase diagram*

A magnetic field h leads to a closing of the trivial SC gap and reopening of a new nontrivial topological gap. This occurs at the critical energy $h_c^2 = \mu^2 + \Delta^2$ [15–17] ($h_c/t \simeq 0.5$ for our choice of parameters). In our system, the value of the chemical potential varies from site to site i.e., $\mu_i = \mu + V_i$. This nonhomogeneity can lead to a situation in which the above condition is met only locally [32–34]. We can therefore construct a space-dependent indicator [35] that describes the spatial distribution of the nontrivial topological phase,

$$\chi_i = \sqrt{(\mu + V_i)^2 + \Delta^2} - h. \tag{22}$$

Thus, a positive (negative) sign of χ_i indicates the topologically trivial (nontrivial) phase. Indeed, from the analysis of χ_i under an increase of the magnetic field h (see Fig. S9 in the SM [23]), we find that the nontrivial phase exists in the system when $\chi_i < 0$.

From the above analysis, it follows that the spatial dependence of the χ_i indicator gives correct information about the emergence of the nontrivial topological domain inside the nanoflake. Using this condition, we construct a topological phase diagram in the two-parameter space defined by the chemical potential μ and the effective magnetic field h shown in Fig. 8(a).

First, we recall that the trivial and nontrivial topological phases are separated by a parabolic boundary $h_c^2 = \mu^2 + \Delta^2$ in the homogeneous system. In our system, the nanoflake introduces a nonhomogeneity in μ to the system; thus, the boundary splits due to the existence of two regions in space where topological phases can emerge. As a consequence, the boundary in the phase diagram evolves into a stripe, whose width is given by $\max |V_i|$. Thus, in the limit $V_0 \to 0$ (a homogeneous system without any nanoflake), the "stripe" would narrow down into a line $h_c(\mu)$, as seen in Fig. 1.

Second, the region of the stripe separating the phases (dashed lines) coincides with the value of the gap δE, calculated as the energy difference between the eigenvalues closest to Fermi level [Fig. 8(b)]. The existence of a nontrivial domain in the system is a result of the occurrence of in-gap states with exponentially small eigenenergies (described by δE). The deviation from the near-zero value of δE in the central

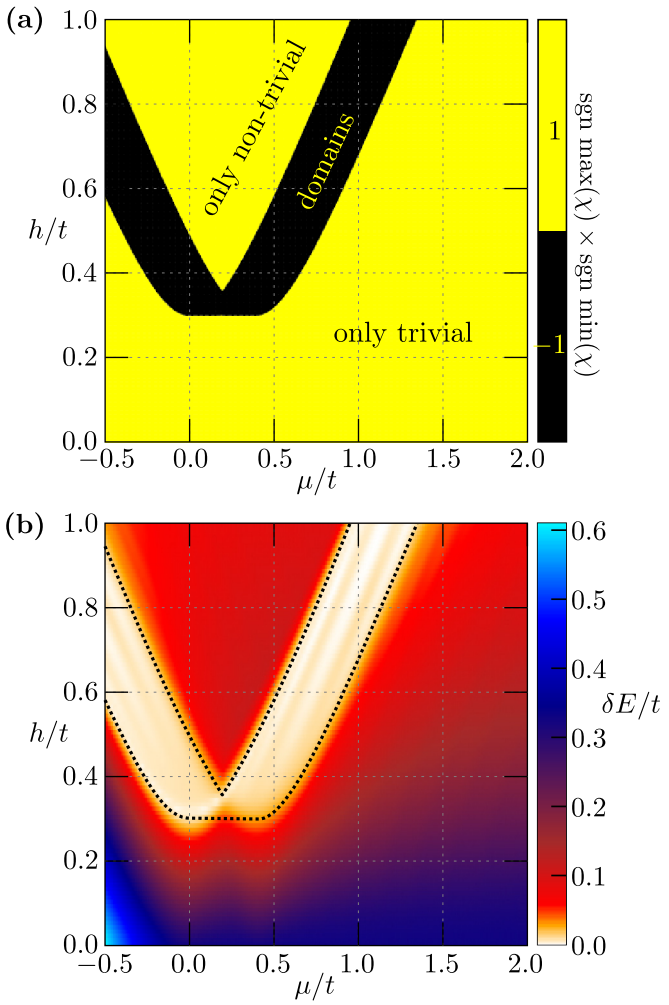

FIG. 8. Topological phase diagram in the (μ, h) plane: (a) as obtained from the indicator χ_i defined in Eq. (21) and (b) the value of the energy gap δE. Note that the values in the bottom left corner are very high and exceed the scale of the plot.

part of the "domain region" is a consequence of the finite-size effect that is pronounced near the topological transition in lower magnetic fields, similar to the 1D Rashba nanowires.

3. *Bond current*

When the system has boundaries [31,36] or if artificial barriers are introduced [34,37], in-gap states localize on the edges of the system. The in-gap states are localized in a collection of preferable locations, independent of the broadening of domain wall. These well-localized in-gap states provide a contribution to the bond current which can be expressed as the local charge flow and is obtained from the Heisenberg equation [38–40],

$$\imath\hbar \frac{\partial \langle n_i \rangle}{\partial t} = \langle [\mathcal{H}, n_i] \rangle. \tag{23}$$

The current vector field can be represented as a sum of the spin-dependent currents, $I_i = \sum_{i\sigma} I_{i\sigma}$, where $I_{i\sigma} = \partial_t \langle n_{i\sigma} \rangle$ can be expressed by the BdG eigenvectors [40,41].

In Fig. 9, we present the real-space map of the bond current. The color of the arrows denotes their magnitude $\propto |I_i|$. Once again, the width of the domain wall (controlled by λ) is reflected by an observable; however, this time it is through

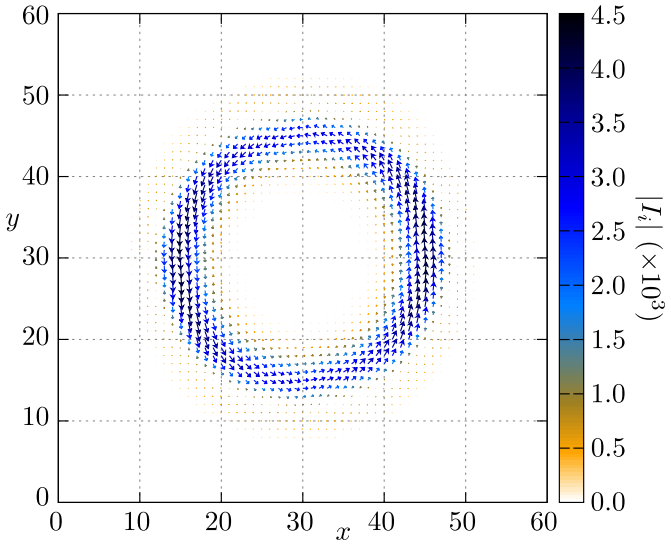

FIG. 9. Vector map of the bond current in the described system. Color corresponds to the absolute value of the current $|I_i|$ (right scale).

the area in which there is a significant flow of charge (see Fig. S3 in the SM [23]). These low-energy modes bear a close resemblance to the surface states of three-dimensional topological insulators (TIs) [42,43]. Due to the SOC-induced band inversion and bulk-boundary correspondence, the 2D surface of a TI hosts metallic states which disperse through the band gap. Generally, band inversion is a result of the nontrivial phase transition, but here, "surface states" are limited to the boundary of the nanoflake, which serves as an edge of the system. The current vector field presented in Fig. 9 is the sum of the contributions of the spin-↑ and spin-↓ currents.

Due to the breaking of time reversal symmetry, the spin-↑ component dominates and thus resembles the "quasihelical" situation described in Ref. [9]. It is worth noting that a magnetic impurity or a ferromagnetic island proximity coupled to a SOC superconductor will exhibit a finite spin polarization, thus giving rise to persistent currents [38–40] as a result of the magnetoelectric effect. This type of bond current along the nanoflake can be observed experimentally, e.g., in the differential conductance measurements [14,44].

B. Numerical results for irregular nanoflake

In order to go beyond the circular limit discussed in previous paragraphs, we locate the substituted atoms at random sites of the lattice as nearest neighbors of an initial atom, located at the center of the surface. This method results in a nanoflake with a *rugged* boundary (see Fig. 1) between the substituted (blue) and substrate (gray) atoms, which is similar to experimental setups [9,14]. However, artificial construction of nanoflakes could be characterized by a more regular shape too. In practice, in the SM [23], we show that the main properties of the system do not depend qualitatively on the shape of the nanoflake. Therefore, all properties described before remain when the flake becomes irregular.

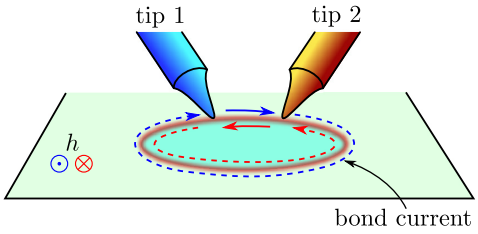

FIG. 10. Setup of a double-tip experiment probing the chirality of the edge states. In the presence of the external magnetic field h in the ↑ ⊙ (red) or ↓ ⊗ (blue) direction, the chiral bond current flows clockwise (blue arrows) or counterclockwise (red arrows) along the boundary of the system. Thus, the double-tip measurement of nonlocal differential conductance G_{12} depends on the chirality of the edge state, i.e., on the direction of the magnetic field and the bond current.

IV. PROPOSAL TO EXPERIMENTALLY MEASURE THE CHIRALITY USING SCANNING TUNNELING MICROSCOPY

Our experimental proposal is based on the double-tip measurement technique [45–47]. The in-gap edge states localized around the nanoflake can give a *nonlocal* response between two spatially separated tips, which is schematically shown in Fig. 10. A similar transconductance technique was successfully used to measure an in-gap surface band [48].

We performed the calculation of the local and nonlocal differential conductance using the KWANT [49] code to numerically obtain the scattering matrix [50–52]:

$$S = \begin{pmatrix} S_{11} & S_{12} \\ S_{21} & S_{22} \end{pmatrix}, \quad S_{ij} = \begin{pmatrix} S_{ij}^{ee} & S_{ij}^{eh} \\ S_{ij}^{he} & S_{ij}^{hh} \end{pmatrix}. \tag{24}$$

Here, $S_{ij}^{\alpha\beta}$ is the block of the scattering amplitudes of incident particles of type β in tip j to particles of type α in tip i. Then, the differential conductance matrix is given as [53]

$$G_{ij}(E) \equiv \frac{\partial I_i}{\partial V_j} = \frac{e^2}{h}\left(T_{ij}^{ee} - T_{ij}^{he} - \delta_{ij} N_i^e\right), \tag{25}$$

where I_i is the current entering terminal i from the scattering region and V_j is the voltage applied to terminal j and N_i^e is the number of electron modes at energy E in terminal i. Finally, the energy transmission is

$$T_{ij}^{\alpha\beta} = \mathrm{Tr}\left(\left[S_{ij}^{\alpha\beta}\right]^\dagger S_{ij}^{\alpha\beta}\right). \tag{26}$$

The nonlocal response is constituted by two processes: (i) a direct electron transfer between the leads and (ii) the crossed Andreev reflection (CAR) of an electron from one tip into a hole in the second tip [54,55]. In typical cases, the CAR contribution dominates the electron transfer [56,57], and such processes are responsible for the Cooper pair splitter [58]. Here, we show that this technique has a potential application in measuring the chirality of the edge state. In order to achieve this goal, we suggest the use of two ferromagnetic tips described by the Hamiltonian

$$\mathcal{H}_{\mathrm{tip}}^i = \sum_{k\sigma} (\varepsilon_{k\sigma} - \sigma M_i) c_{k\sigma}^\dagger c_{k\sigma}, \tag{27}$$

where $\varepsilon_{k\sigma}$ is the dispersion relation of the free electrons in the tips, while M_i is the magnetization of the ith tip.

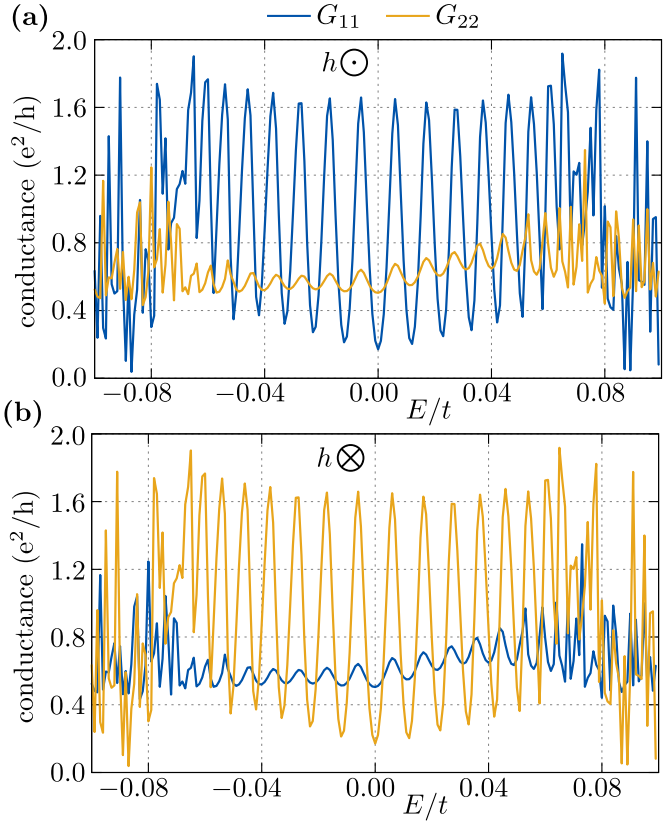

FIG. 11. The local conductances G_{11} and G_{22} are shown by blue and red lines for (a) positive and (b) negative magnetic field $h/t = \pm 0.4$. Here, we take two ferromagnetic (FM) tips with $M_1 = -M_2 = 3.0t$. The direction of the magnetic field applied to the system is shown at the top.

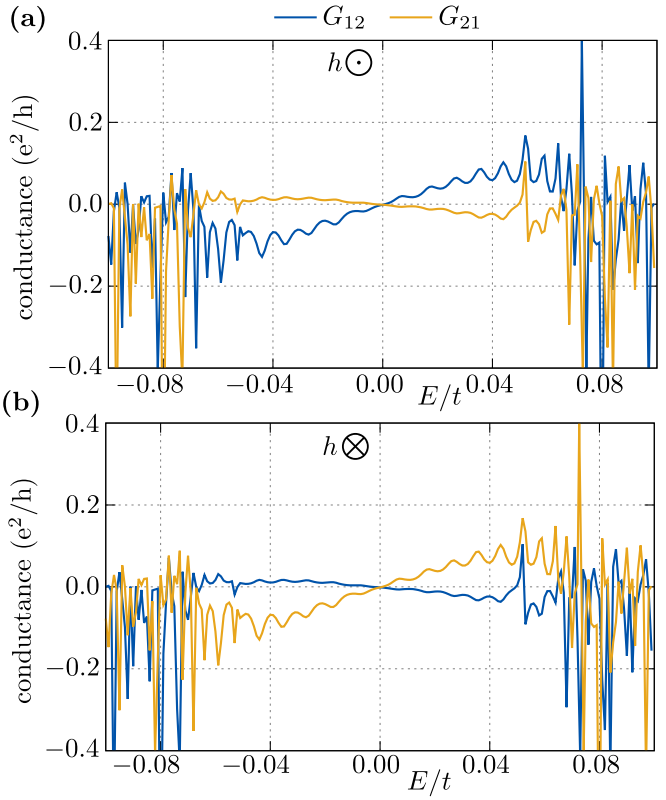

FIG. 12. The same as Fig. 11, but in the case of the nonlocal conductances G_{12} and G_{21}, shown by red and blue lines, respectively. The direction of the magnetic field applied to the system is shown at the top.

We assume that the tips have opposite magnetizations, i.e., $M_1 = -M_2$. The tips are separated from the plane of the system by the barrier potential. We assume a system like that shown schematically in Fig. 10; that is, tips are located exactly above the nanoflake edge in a nonsymmetric position. As a result, the distance between the first and second tips differs when measured clockwise and counterclockwise (along the edge state channel at the border of the nanoflake).

In our system, we can find the local (G_{11} and G_{22}) as well as nonlocal (G_{12} and G_{21}) differential conductances (Figs. 11 and 12, respectively). The local conductance G_{ii} can be treated as a probe of the existence of states in the system [59,60]. In this sense, each state gives a positive signal in G_{ii}, independent of the direction of the magnetic field h [see the Figs. 11(a) and 11(b)]. As we can see, in our case we observe several in-gap states. Due to the use of ferromagnetic tips we observe nonequality of G_{11} and G_{22} (blue and red lines, respectively).

The nonlocal conductances G_{12} and G_{21} (Fig. 12) describe different situations. In order for CAR processes to occur, electrons from both tips need to have opposite spins to create a Cooper pair and simultaneously eject a hole from the other tip. Due to the applied external magnetic field the incident electrons from the edge bond current would have the same spin as the electrons from the first tip they encounter. The electron with opposite spin should come from the other tip (which has opposite magnetization) and emit a hole with the same spin to constitute a CAR process. Thanks to this nonlocal phenomenon, we can easily determine the direction of the edge state propagation as the nonlocal conductance coincides with the direction of the chiral bond current. Thus, if the sign of the magnetic field changes, the direction of the edge state propagation reverts too; G_{12} becomes G_{21} due to the spatial symmetry of the system. However, tips are not perfectly magnetized; therefore, the nonlocal conductance measurement in the direction opposite the chiral bond current remains nonzero (e.g., G_{21} for the $\odot$ direction of the magnetic field). As the edge state bond current constitutes both spins, particles with spins not aligned with the tip magnetization scatter off the tip (see wave function localizations in Fig. 13). If the magnetic field is not present in the system, in-gap nonlocal conductance vanishes (not shown), and peaks at the edge of the superconducting gap appear [53]. Differences between the absolute values of nonlocal conductances are the consequence of the nonsymmetric position of the tips. The change from a negative to positive slope near the gap can be interpreted as a crossover from subgap transport dominated by crossed Andreev reflection to a charge imbalance above the gap [61]. Additionally, the nonlocal conductance strongly depends on the distance between the tips [53].

To explain the above results, we analyzed the propagating modes in the system (Fig. 13). The nonlocal transport corresponds to the situation where an incident electron from one tip is transmitted through the edge modes as the chiral mode and is scattered into the second tip. Such propagating modes can be represented in the form of a wave function,

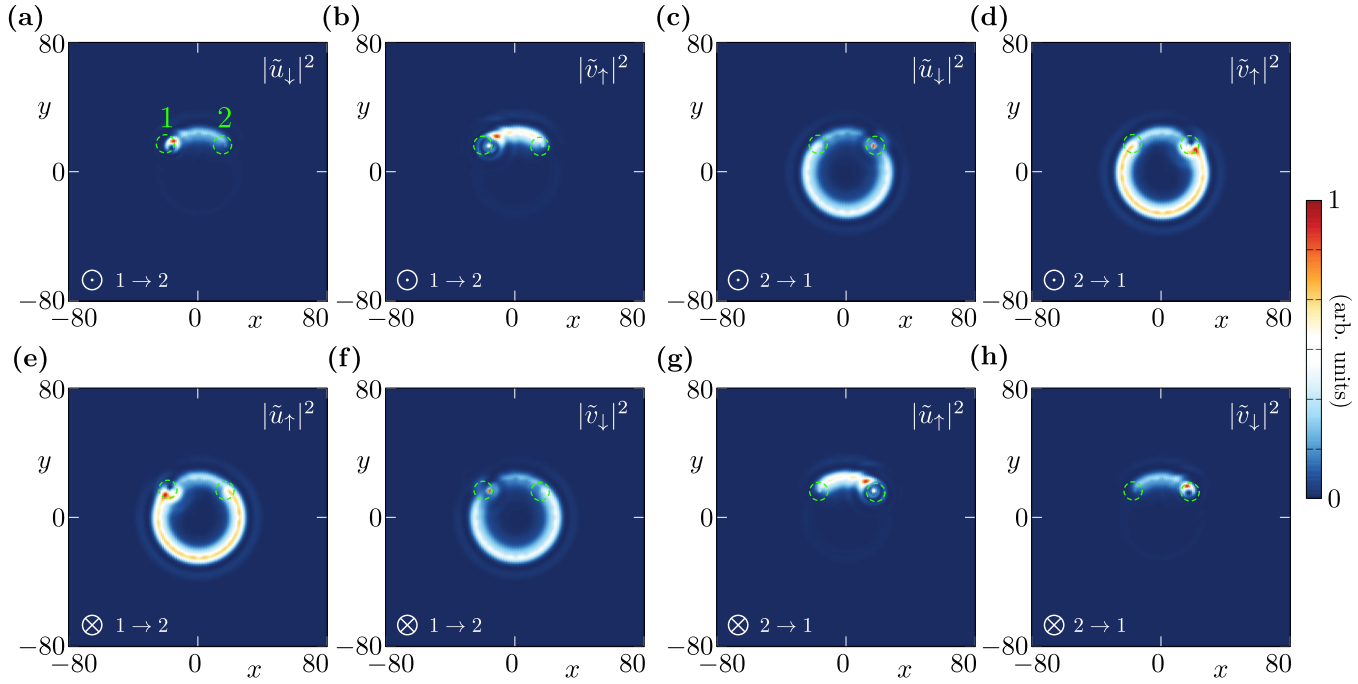

FIG. 13. Spatial profile of the wave functions (particle- and hole-like components, given by u and v, respectively) having the largest contribution to propagating modes at energy $0.02t$. Top (bottom) panels show results in the case of a positive (negative) value of magnetic field and are depicted by $\odot$ ($\otimes$). The first and second columns correspond to propagating modes from the first to second tip ($1 \rightarrow 2$), while the third and fourth columns correspond to propagating modes from the second to first tip ($2 \rightarrow 1$). Scanning tunneling microscopy tips are labeled in (a). Yellow dashed lines represent the region of the system bordered by the potential barrier.

$\psi(\boldsymbol{r}) = (\tilde{u}_\downarrow, \tilde{u}_\uparrow, \tilde{v}_\downarrow, \tilde{v}_\uparrow)^T$, where $\tilde{u}$ and $\tilde{v}$ correspond to its electron- and holelike components, respectively. Here, ψ is composed mostly of $\downarrow$-electron and $\uparrow$-hole components [62]. Regions with a nonzero probability of localization correspond to the particle remnants of scattering processes, whose distribution coincides with the direction of edge state propagation. As we mentioned above, with relatively small voltage bias, the nonlocal transport is dominated by CAR processes (which was envisioned by the antiparallel magnetization of G_{12} and G_{21}). In the case of the "positive" $\odot$ magnetic field, we observe propagation from the first to the second tip in the clockwise direction [Figs. 13(a) and 13(b)] for both electron and hole components of the wave function. Then, if we check the mode propagation from the second to the first tip [Figs. 13(c) and 13(d)], we can see that the chirality of the propagating modes is preserved and clockwise. In the case of the magnetic field with the inverted direction, we observe modes propagating in the direction opposite to the one previously mentioned (used in the bottom pannels in Fig. 13). Without any surprise, the mode propagation direction in this case is also preserved.

Summarizing, the nonlocal conductance is not just a fingerprint of the existence of the chiral mode [62] but also a tool to measure its chirality.

V. SUMMARY AND CONCLUSIONS

Recent experimental results have presented the possibility of the emergence of nontrivial topological phases in magnetic nanostructures coupled to superconducting substrates [9,14]. In this paper, we have explored the artificial implementation of topological phase transitions induced by the local modification of the chemical potential. In this respect, we performed analytic calculations valid in the continuum limit in the case of a nanoflake with a circular geometry and found the spectrum of the system as a function of the total angular momentum. We have also studied how the transverse spatial extent of the wave function of the chiral Majorana state localized around the nanoflake depends upon the system parameters. We then performed similar calculations for a finite-size geometry using a tight-binding formulation. In-gap states correspond to prominent peaks in the LDOS only in a distinct region of space, identified as the domain wall, which should be observed relatively simply through scanning tunneling microscopy experiments.

Next, we introduced a real-space indicator, which locally characterizes the topological phase. Indeed, for a few sets of parameters, results obtained from this indicator were in agreement with those obtained in the continuum limit. In the case analyzed here, the effective magnetic field leads to the realization of a nontrivial phase only in distinct regions of the system, creating a nontrivial superconducting dome surrounded by a trivial superconducting phase. This phase separation could be observed through the measurement of a bond chiral current, which is connected to the existence of strongly localized in-gap states. We have shown that this current circulates around the nanoflake. Additionally, with the help of the indicator, we have found the topological phase diagram of

the system. We have shown that an artificial phase separation can be induced for a finite range of effective magnetic field. The boundary of this phase separation is strongly related to the effective magnetic field, which determines the transition between trivial and nontrivial phases

In the last part of our work, we proposed an experimental method to measure the chirality of the edge states based on a double-tip measurement of the nonlocal differential conductivity. We have found that the nonlocal transport properties between the two tips allow one to determine the chirality of the edge state. Although challenging, this type of experiment should be accessible with the present technology.

ACKNOWLEDGMENTS

We would like to thank T. Cren for interesting discussions. This work was supported by the National Science Centre (NCN, Poland) under Grants No. 2017/24/C/ST3/00276 (A.P.), No. 2017/27/N/ST3/01762 (S.G.), No. 2018/31/N/ST3/01746 (A.K.), No. 2016/23/B/ST3/00839 (A.M.O.), and No. 2017/25/B/ST3/02586 (P.P.). A.M.O. is grateful for the Alexander von Humboldt Foundation Fellowship (Humboldt-Forschungspreis). A.P. appreciates also funding in the frame of scholarships of the Minister of Science and Higher Education (Poland) for outstanding young scientists (2019 edition, No. 818/STYP/14/2019).

[1] A. Yu. Kitaev, Fault-tolerant quantum computation by anyons, Ann. Phys. (NY) **303**, 2 (2003).

[2] Ch. Nayak, S. H. Simon, A. Stern, M. Freedman, and S. Das Sarma, Non-Abelian anyons and topological quantum computation, Rev. Mod. Phys. **80**, 1083 (2008).

[3] J. Alicea, Y. Oreg, G. Refael, F. von Oppen, and M. P. A. Fisher, Non-Abelian statistics and topological quantum information processing in 1d wire networks, Nat. Phys. **7**, 412 (2011).

[4] J. Alicea, New directions in the pursuit of Majorana fermions in solid state systems, Rep. Prog. Phys. **75**, 076501 (2012).

[5] D. Aasen, M. Hell, R. V. Mishmash, A. Higginbotham, J. Danon, M. Leijnse, T. S. Jespersen, J. A. Folk, Ch. M. Marcus, K. Flensberg, and J. Alicea, Milestones Toward Majorana-Based Quantum Computing, Phys. Rev. X **6**, 031016 (2016).

[6] B. Lian, X.-Q. Sun, A. Vaezi, X.-L. Qi, and S.-Ch. Zhang, Topological quantum computation based on chiral Majorana fermions, Proc. Natl. Acad. Sci. USA **115**, 10938 (2018).

[7] X.-L. Qi and S.-Ch. Zhang, Topological insulators and superconductors, Rev. Mod. Phys. **83**, 1057 (2011).

[8] Q. L. He, L. Pan, A. L. Stern, E. C. Burks, X. Che, G. Yin, J. Wang, B. Lian, Q. Zhou, E. S. Choi, K. Murata, X. Kou, Z. Chen, T. Nie, Q. Shao, Y. Fan, S.-Ch. Zhang, K. Liu, J. Xia, and K. L. Wang, Chiral Majorana fermion modes in a quantum anomalous Hall insulator–superconductor structure, Science **357**, 294 (2017).

[9] G. C. Ménard, S. Guissart, Ch. Brun, R. T. Leriche, M. Trif, F. Debontridder, D. Demaille, D. Roditchev, P. Simon, and T. Cren, Two-dimensional topological superconductivity in Pb/Co/Si(111), Nat. Commun. **8**, 2040 (2017).

[10] R. Drost, T. Ojanen, A. Harju, and P. Liljeroth, Topological states in engineered atomic lattices, Nat. Phys. **13**, 668 (2017).

[11] H. Kim, A. Palacio-Morales, T. Posske, L. Rózsa, K. Palotás, L. Szunyogh, M. Thorwart, and R. Wiesendanger, Toward tailoring Majorana bound states in artificially constructed magnetic atom chains on elemental superconductors, Sci. Adv. **4**, eaar5251 (2018).

[12] A. Kamlapure, L. Cornils, J. Wiebe, and R. Wiesendanger, Engineering the spin couplings in atomically crafted spin chains on an elemental superconductor, Nat. Commun. **9**, 3253 (2018).

[13] G. C. Ménard, A. Mesaros, Ch. Brun, F. Debontridder, D. Roditchev, P. Simon, and T. Cren, Isolated pairs of Majorana zero modes in a disordered superconducting lead monolayer, Nat. Commun. **10**, 2587 (2019).

[14] A. Palacio-Morales, E. Mascot, S. Cocklin, H. Kim, S. Rachel, D. K. Morr, and R. Wiesendanger, Atomic-scale interface engineering of Majorana edge modes in a 2D magnet-superconductor hybrid system, Sci. Adv. **5**, eaav6600 (2019).

[15] M. Sato and S. Fujimoto, Topological phases of noncentrosymmetric superconductors: Edge states, Majorana fermions, and non-Abelian statistics, Phys. Rev. B **79**, 094504 (2009).

[16] M. Sato, Y. Takahashi, and S. Fujimoto, Non-Abelian Topological Order in *s*-Wave Superfluids of Ultracold Fermionic Atoms, Phys. Rev. Lett. **103**, 020401 (2009).

[17] M. Sato, Y. Takahashi, and S. Fujimoto, Non-Abelian topological orders and Majorana fermions in spin-singlet superconductors, Phys. Rev. B **82**, 134521 (2010).

[18] K. S. Novoselov, A. Mishchenko, A. Carvalho, and A. H. Castro Neto, 2D materials and van der Waals heterostructures, Science **353**, aac9439 (2016).

[19] K. S. Burch, D. Mandrus, and J.-G. Park, Magnetism in two-dimensional van der Waals materials, Nature (London) **563**, 47 (2018).

[20] Ch. Gong and X. Zhang, Two-dimensional magnetic crystals and emergent heterostructure devices, Science **363**, eaav4450 (2019).

[21] M. M. Asmar and S. E. Ulloa, Spin-Orbit Interaction and Isotropic Electronic Transport in Graphene, Phys. Rev. Lett. **112**, 136602 (2014).

[22] Y. Oreg, G. Refael, and F. von Oppen, Helical Liquids and Majorana Bound States in Quantum Wires, Phys. Rev. Lett. **105**, 177002 (2010).

[23] See Supplemental Material at http://link.aps.org/supplemental/10.1103/PhysRevB.102.245405 for details of the analytical calculations and additional numerical results for the nanoflake with irregular shape. In the second case, the numerical results for different sets of values λ and V_0 are presented.

[24] In the case of a homogeneous 2D system, this gives the dispersion relation $\mathcal{E}_{\boldsymbol{k}} = -2t[\cos(k_x) + \cos(k_y)]$. Then, the minimal available energy is equal to $-4t$.

[25] M. M. Maśka, Ż. Śledź, K. Czajka, and M. Mierzejewski, Inhomogeneity-Induced Enhancement of the Pairing Interac-

tion in Cuprate Superconductors, Phys. Rev. Lett. **99**, 147006 (2007).

[26] P. G. De Gennes, *Superconductivity of Metals and Alloys*, Advanced Books Classics Series (Westview Press, Boca Raton, 1999).

[27] A. V. Balatsky, I. Vekhter, and J.-X. Zhu, Impurity-induced states in conventional and unconventional superconductors, Rev. Mod. Phys. **78**, 373 (2006).

[28] H. Matsui, T. Sato, T. Takahashi, S.-C. Wang, H.-B. Yang, H. Ding, T. Fujii, T. Watanabe, and A. Matsuda, BCS-Like Bogoliubov Quasiparticles in High-T_c Superconductors Observed by Angle-Resolved Photoemission Spectroscopy, Phys. Rev. Lett. **90**, 217002 (2003).

[29] K. Björnson and A. M. Black-Schaffer, Probing chiral edge states in topological superconductors through spin-polarized local density of state measurements, Phys. Rev. B **97**, 140504(R) (2018).

[30] K. Björnson and A. M. Black-Schaffer, Probing vortex Majorana fermions and topology in semiconductor/superconductor heterostructures, Phys. Rev. B **91**, 214514 (2015).

[31] A. Kobiałka, T. Domański, and A. Ptok, Delocalisation of Majorana quasiparticles in plaquette–nanowire hybrid system, Sci. Rep. **9**, 12933 (2019).

[32] X.-J. Liu and H. Hu, Topological superfluid in one-dimensional spin-orbit-coupled atomic Fermi gases, Phys. Rev. A **85**, 033622 (2012).

[33] X.-J. Liu and P. D. Drummond, Manipulating Majorana fermions in one-dimensional spin-orbit-coupled atomic Fermi gases, Phys. Rev. A **86**, 035602 (2012).

[34] A. Ptok, A. Cichy, and T. Domański, Quantum engineering of Majorana quasiparticles in one-dimensional optical lattices, J. Phys.: Condens. Matter **30**, 355602 (2018).

[35] T. Zhou, N. Mohanta, J. E. Han, A. Matos-Abiague, and I. Žutić, Tunable magnetic textures in spin valves: From spintronics to Majorana bound states, Phys. Rev. B **99**, 134505 (2019).

[36] J. Röntynen and T. Ojanen, Topological Superconductivity and High Chern Numbers in 2D Ferromagnetic Shiba Lattices, Phys. Rev. Lett. **114**, 236803 (2015).

[37] A. Kobiałka and A. Ptok, Electrostatic formation of the Majorana quasiparticles in the quantum dot-nanoring structure, J. Phys.: Condens. Matter **31**, 185302 (2019).

[38] S. S. Pershoguba, K. Björnson, A. M. Black-Schaffer, and A. V. Balatsky, Currents Induced by Magnetic Impurities in Superconductors with Spin-Orbit Coupling, Phys. Rev. Lett. **115**, 116602 (2015).

[39] J. Li, T. Neupert, Z. Wang, A. H. MacDonald, A. Yazdani, and B. A. Bernevig, Two-dimensional chiral topological superconductivity in Shiba lattices, Nat. Commun. **7**, 12297 (2016).

[40] K. Björnson, S. S. Pershoguba, A. V. Balatsky, and A. M. Black-Schaffer, Spin-polarized edge currents and Majorana fermions in one- and two-dimensional topological superconductors, Phys. Rev. B **92**, 214501 (2015).

[41] Sz. Głodzik and T. Domański, In-gap states of magnetic impurity in quantum spin Hall insulator proximitized to a superconductor, J. Phys.: Condens. Matter **32**, 235501 (2020).

[42] M. Z. Hasan and C. L. Kane, Colloquium: Topological insulators, Rev. Mod. Phys. **82**, 3045 (2010).

[43] C.-Z. Chang and M. Li, Quantum anomalous Hall effect in time-reversal-symmetry breaking topological insulators, J. Phys.: Condens. Matter **28**, 123002 (2016).

[44] I. K. Drozdov, A. Alexandradinata, S. Jeon, S. Nadj-Perge, H. Ji, R. J. Cava, B. A. Bernevig, and A. Yazdani, One-dimensional topological edge states of bismuth bilayers, Nat. Phys. **10**, 664 (2014).

[45] I. Shiraki, F. Tanabe, R. Hobara, T. Nagao, and S. Hasegawa, Independently driven four-tip probes for conductivity measurements in ultrahigh vacuum, Surf. Sci. **493**, 633 (2001).

[46] M. Kolmer, P. Olszowski, R. Zuzak, Sz. Godlewski, Ch. Joachim, and M. Szymonski, Two-probe STM experiments at the atomic level, J. Phys.: Condens. Matter **29**, 444004 (2017).

[47] B. Voigtländer, V. Cherepanov, S. Korte, A. Leis, D. Cuma, S. Just, and F. Lüpke, Invited review article: Multi-tip scanning tunneling microscopy: Experimental techniques and data analysis, Rev. Sci. Instrum. **89**, 101101 (2018).

[48] M. Kolmer, P. Brandimarte, J. Lis, R. Zuzak, Sz. Godlewski, H. Kawai, A. Garcia-Lekue, N. Lorente, T. Frederiksen, Ch. Joachim, D. Sanchez-Portal, and M. Szymonski, Electronic transport in planar atomic-scale structures measured by two-probe scanning tunneling spectroscopy, Nat. Commun. **10**, 1573 (2019).

[49] Ch. W. Groth, M. Wimmer, A. R. Akhmerov, and X. Waintal, KWANT: A software package for quantum transport, New J. Phys. **16**, 063065 (2014).

[50] G. B. Lesovik and I. A. Sadovskyy, Scattering matrix approach to the description of quantum electron transport, Phys. Usp. **54**, 1007 (2011).

[51] A. R. Akhmerov, J. P. Dahlhaus, F. Hassler, M. Wimmer, and C. W. J. Beenakker, Quantized Conductance at the Majorana Phase Transition in a Disordered Superconducting Wire, Phys. Rev. Lett. **106**, 057001 (2011).

[52] I. C. Fulga, F. Hassler, A. R. Akhmerov, and C. W. J. Beenakker, Scattering formula for the topological quantum number of a disordered multimode wire, Phys. Rev. B **83**, 155429 (2011).

[53] T. Ö. Rosdahl, A. Vuik, M. Kjaergaard, and A. R. Akhmerov, Andreev rectifier: A nonlocal conductance signature of topological phase transitions, Phys. Rev. B **97**, 045421 (2018).

[54] J. M. Byers and M. E. Flatté, Probing Spatial Correlations with Nanoscale Two-Contact Tunneling, Phys. Rev. Lett. **74**, 306 (1995).

[55] G. Deutscher and D. Feinberg, Coupling superconducting-ferromagnetic point contacts by Andreev reflections, Appl. Phys. Lett. **76**, 487 (2000).

[56] G Falci, D Feinberg, and F. W. J Hekking, Correlated tunneling into a superconductor in a multiprobe hybrid structure, Europhys. Lett. **54**, 255 (2001).

[57] D. Beckmann, H. B. Weber, and H. v. Löhneysen, Evidence for Crossed Andreev Reflection in Superconductor-Ferromagnet Hybrid Structures, Phys. Rev. Lett. **93**, 197003 (2004).

[58] L. G. Herrmann, F. Portier, P. Roche, A. Levy Yeyati, T. Kontos, and C. Strunk, Carbon Nanotubes as Cooper-Pair Beam Splitters, Phys. Rev. Lett. **104**, 026801 (2010).

[59] J. Chen, P. Yu, J. Stenger, M. Hocevar, D. Car, S. R. Plissard, E. P. A. M. Bakkers, T. D. Stanescu, and S. M. Frolov, Experimental phase diagram of zero-bias conductance peaks in superconductor/semiconductor nanowire devices, Sci. Adv. **3**, e1701476 (2017).

[60] H. Zhang *et al.*, Quantized Majorana conductance, Nature (London) **556**, 74 (2018).

[61] M. S. Kalenkov and A. D. Zaikin, Crossed Andreev reflection and spin-resolved non-local electron transport, in *Fundamentals of Superconducting Nanoelectronics*, edited by A. Sidorenko (Springer, Berlin, 2011), pp. 67–100.

[62] S. Ikegaya, Y. Asano, and D. Manske, Anomalous Nonlocal Conductance as a Fingerprint of Chiral Majorana Edge States, Phys. Rev. Lett. **123**, 207002 (2019).

Bibliography

[1] A. Kobiałka, N. Sedlmayr, M. M. Ma śka, and T. Doma ński, *Dimerization-induced topological superconductivity in a Rashba nanowire*, Phys. Rev. B **101**, 085402 (2020) DOI: 10.1103/PhysRevB.101.085402

[2] A. Kobiałka, N. Sedlmayr, and A. Ptok, *Majorana bound states in a superconducting Rashba nanowire in the presence of antiferromagnetic order*, Phys. Rev. B **103**, 125110 (2021) DOI: 10.1103/PhysRevB.103.125110

[3] A. Kobiałka and A. Ptok, *Electrostatic formation of the Majorana quasiparticles in the quantum dot-nanoring structure*, J. Phys.: Condens. Matter **31**, 185302 (2019) DOI: 10.1088/1361-648x/ab03bf

[4] A. Kobiałka, P. Piekarz, A. M. Ole ś, and A. Ptok, *First-principles study of the nontrivial topological phase in chains of* 3*d transition metals*, Phys. Rev. B **101**, 205143 (2020) DOI: 10.1103/PhysRevB.101.205143

[5] A. Ptok, A. Kobiałka, and T. Domański, *Controlling the bound states in a quantum-dot hybrid nanowire*, Phys. Rev. B **96**, 195430 (2017) DOI: 10.1103/PhysRevB.96.195430

[6] A. Kobiałka and A. Ptok, *Majorana Bound State Leakage to Impurity in Su-Schrieffer-Heeger-Rashba Scenario*, Acta Phys. Pol. A **138**, 673 (2020) DOI: 10.12693/aphyspola.138.673

[7] A. Kobiałka and A. Ptok, *Leakage of the Majorana Quasiparticles in Rashba Nanowire Deposited on Superconducting–Normal Substrate*, Acta Phys. Pol. A **135**, 64 (2019) DOI: 10.12693/aphyspola.135.64

[8] A. Kobiałka, T. Domański, and A. Ptok, *Delocalisation of Majorana quasiparticles in plaquette–nanowire hybrid system*, Scientific Reports **9**, 12933 (2019) DOI: 10.1038/s41598-019-49227-5

[9] A. Ptok, D. J. Alspaugh, S. Głodzik, A. Kobiałka, A. M. Oleś, P. Simon, and P. Piekarz, *Probing the chirality of one-dimensional Majorana edge states around a two-dimensional nanoflake in a superconductor*, Phys. Rev. B **102**, 245405 (2020) DOI: 10.1103/PhysRevB.102.245405

[10] M. T. Deng, S. Vaitiekenas, E. B. Hansen, J. Danon, M. Leijnse, K. Flensberg, J. Nygård, P. Krogstrup, and C. M. Marcus, *Majorana bound state in a coupled quantum-dot hybrid-nanowire system*, Science **354**, 1557 (2016) DOI: 10.1126/science.aaf3961

CHAPTER 5

Final thoughts

In this thesis, being the cumulation of my work done over the last five years, I focused on timely elements of Majorana physics: their emergence and nonlocality. It resulted in a series of nine papers in which we studied both of the mentioned phenomena related to the Majorana behaviour. My contribution to these papers was taking part in numerical and analytical calculations, discussing and analysing obtained results with my co–authors and finally, cooperating with my co–authors on preparation of manuscripts. Knowledge about the emergence of Majorana bound states is crucial for proposing solutions for the application of this phenomenon in experiment and technology. Experimental premises have already suggested the existence of Majorana bound states, however there are still some unexplored venues which may strengthen these claims. Theoretical research concerning the emergence of MBS might prove beneficial for this aspect of experimental investigation. In our emergence studies, we showed that MBS can exist outside of the usual bottom–of–the–band regime of Oreg–Lutchyn model. However, in such a case, this model has to be extended by some additional feature like SSH–like dimerization or antiferromagnetism. Additionally, we showed the importance of the substrate for DFT calculations of 1D $3d$ transition metal chains, by showing discrepancies between free standing and deposited chains. We also proposed a ring shaped system where the MBS could emerge due to the barrier forming on quantum dot region. The other part of this thesis concerning Majorana nonlocality is again closely related to the application in real world. It is this phenomenon that allows for robust storing of quantum information, which can pave a safe way for quantum computing into mainstream applications. In this case, the investigation of Majorana bound state affinity for ends of the structures they reside in, is important for a successful approach to braiding. In regards to the

nonlocality, we showed that MBS delocalize to the attached additional regions, even if they are in trivial topological phase. For 0D case, this change is noticeable and tuning the energy of the quantum dot allows for the manipulation of MBS. For 1D case, leakage of MBS to trivial system is substantial as nearly all of the Majorana spectral weight delocalizes to the trivial region. Lastly, in 2D case, delocalisation of MBS to the attached plaquette strongly depends on the topological state of the 2D region. Additionally, we checked the nonlocal conductance of edge states propagating around magnetic island. We proposed a system where those currents can be measured and distinguished with respect to their direction of propagation. Concluding, the physics branch related to Majorana bound states is still full of possible routes for development in both theory and experiment. Still, both of them need to work in synergy, in order to have a meaningful impact on human civilisation.

CHAPTER 6

List of publications and acknowledgement of funding

12. **A.K.**, N. Sedlmayr, A. Ptok, "Majorana bound states in a superconducting Rashba nanowire deposited on an antiferromagnetic surface",
Phys. Rev. B **103**, 125110 (2021)

11. A. Ptok, D. J. Alspaugh, S. Głodzik, **A.K.**, A. M. Oleś, P. Simon, P. Piekarz "Probing the chirality of 1D Majorana edge states around a 2D nanoflake in a superconductor",
Phys. Rev. B **102**, 245405 (2020)

10. **A.K.**, A. Ptok, "Majorana bound states and zero-bias conductance peaks in superconductor/semiconductor nanowire devices",
Acta Phys. Pol. A. **138**, 681 (2020)

09. **A.K.**, A. Ptok, "Majorana Bound State leakage to impurity in Su-Schrieffer-Heeger-Rashba scenario",
Acta Phys. Pol. A. **138**, 673 (2020)

08. **A.K.**, P. Piekarz, A.M Oleś, A Ptok, "First-principles study of the nontrivial topological phase in chains of transition metals",
Phys. Rev. B **101**, 205143 (2020)

07. **A.K.**, N. Sedlmayr, M.M. Maśka, T. Domański, "Dimerization-induced topological superconductivity in a Rashba nanowire",
Phys. Rev. B **101**, 085402 (2020)

06. **A.K.**, T. Domański, A. Ptok, "Delocalisation of Majorana quasiparticles in plaquette–nanowire hybrid system",

Sci. Rep. **9**, 12933 (2019)

05. **A.K.**, A. Ptok, "Electrostatic formation of the Majorana quasiparticles in the quantum dot-nanoring structure",
J. Phys.: Condens. Matter **31** 185302 (2019)

04. **A.K.**, A. Ptok, "Leakage of the Majorana quasiparticles in Rashba nanowire deposited on superconducting–normal substrate",
Acta Phys. Pol. A **135**, 64 (2019)

03. S. Głodzik, **A.K.**, A. Gorczyca-Goraj, A. Ptok, G. Górski, M.M. Maśka, T. Domański, "Interplay between pairing and correlations in spin-polarized bound states",
Beilstein J. Nanotechnol. **9**, 1370, (2018)

02. A. Ptok, **A.K.**, T. Domański, "Controlling the bound states in a quantum-dot hybrid nanowire",
Phys. Rev. B **96**, 195430 (2017)

01. J. Barański, **A.K.**, T. Domański, "Spin-sensitive interference due to Majorana state on the interface between normal and superconducting leads",
J. Phys.: Condens. Matter **29**, 075603 (2016)

During my PhD studies, my work was supported by the following grants from National Centre of Science (NCN):

- OPUS 2014/13/B/ST3/04451 (PI: prof. Tadeusz Domański)
- OPUS 2017/27/B/ST3/01911 (PI: prof. Tadeusz Domański)
- PRELUDIUM 2017/27/N/ST3/01762.